Springer Series in Chemical Physics 106

Kaoru Yamanouchi
Gerhard G. Paulus
Deepak Mathur *Editors*

Progress in Ultrafast Intense Laser Science X

Springer

PUILS

JILS

Springer Series in Chemical Physics

Volume 106

For further volumes:
http://www.springer.com/series/11752

The purpose of this series is to provide comprehensive up-to-date monographs in both well established disciplines and emerging research areas within the broad fields of chemical physics and physical chemistry. The books deal with both fundamental science and applications, and may have either a theoretical or an experimental emphasis. They are aimed primarily at researchers and graduate students in chemical physics and related fields.

Kaoru Yamanouchi · Gerhard G. Paulus ·
Deepak Mathur
Editors

Progress in Ultrafast Intense Laser Science

Volume X

Springer

Editors
Kaoru Yamanouchi
Department of Chemistry
University of Tokyo
Tokyo, Japan

Deepak Mathur
Tata Institute of Fundamental Research
Mumbai, India

Gerhard G. Paulus
Institute of Optics and Quantum Electronics
Friedrich Schiller University Jena
Jena, Germany

ISSN 0172-6218 Springer Series in Chemical Physics
ISBN 978-3-319-00520-1 ISBN 978-3-319-00521-8 (eBook)
DOI 10.1007/978-3-319-00521-8
Springer Cham Heidelberg New York Dordrecht London

Library of Congress Control Number: 2006927806

© Springer International Publishing Switzerland 2014
This work is subject to copyright. All rights are reserved by the Publisher, whether the whole or part of the material is concerned, specifically the rights of translation, reprinting, reuse of illustrations, recitation, broadcasting, reproduction on microfilms or in any other physical way, and transmission or information storage and retrieval, electronic adaptation, computer software, or by similar or dissimilar methodology now known or hereafter developed. Exempted from this legal reservation are brief excerpts in connection with reviews or scholarly analysis or material supplied specifically for the purpose of being entered and executed on a computer system, for exclusive use by the purchaser of the work. Duplication of this publication or parts thereof is permitted only under the provisions of the Copyright Law of the Publisher's location, in its current version, and permission for use must always be obtained from Springer. Permissions for use may be obtained through RightsLink at the Copyright Clearance Center. Violations are liable to prosecution under the respective Copyright Law.
The use of general descriptive names, registered names, trademarks, service marks, etc. in this publication does not imply, even in the absence of a specific statement, that such names are exempt from the relevant protective laws and regulations and therefore free for general use.
While the advice and information in this book are believed to be true and accurate at the date of publication, neither the authors nor the editors nor the publisher can accept any legal responsibility for any errors or omissions that may be made. The publisher makes no warranty, express or implied, with respect to the material contained herein.

Printed on acid-free paper

Springer is part of Springer Science+Business Media (www.springer.com)

Preface

We are pleased to present the tenth volume of Progress in Ultrafast Intense Laser Science. As the frontiers of ultrafast intense laser science rapidly expand ever outward, there continues to be a growing demand for an introduction to this interdisciplinary research field that is at once widely accessible and capable of delivering cutting-edge developments. Our series aims to respond to this call by providing a compilation of concise review-style articles written by researchers at the forefront of this research field, so that researchers with different backgrounds as well as graduate students can easily grasp the essential aspects.

As in previous volumes of PUILS, each chapter of this book begins with an introductory part, in which a clear and concise overview of the topic and its significance is given, and moves onto a description of the authors' most recent research results. All chapters are peer-reviewed. The articles of this tenth volume cover a diverse range of the interdisciplinary research field, and the topics may be grouped into four categories: electron scattering by atoms in intense laser fields (Chap. 1), atoms and molecules in ultrashort pulsed EUV and X-ray light fields (Chaps. 2–5), filamentation induced by intense laser fields (Chaps. 6 and 7), and physics in super-intense laser fields (Chaps. 8 and 9).

From the third volume, the PUILS series has been edited in liaison with the activities of the Center for Ultrafast Intense Laser Science at the University of Tokyo, which has also been responsible for sponsoring the series and making the regular publication of its volumes possible. From the fifth volume, the Consortium on Education and Research on Advanced Laser Science, the University of Tokyo, has joined this publication activity as one of the sponsoring programs. The series, designed to stimulate interdisciplinary discussion at the forefront of ultrafast intense laser science, has also collaborated since its inception with the annual symposium series of ISUILS (http://www.isuils.jp/), sponsored by JILS (Japan Intense Light Field Science Society).

We would like to take this opportunity to thank all of the authors who have kindly contributed to the PUILS series by describing their most recent work at the frontiers of ultrafast intense laser science. We also thank the reviewers who have read the submitted manuscripts carefully. One of the co-editors (KY) thanks Ms. Chie Sakuta for her help with the editing processes. Last but not least, our gratitude goes out to Dr. Claus Ascheron, Physics Editor of Springer-Verlag at Heidelberg, for his kind support.

We hope this volume will convey the excitement of ultrafast intense laser science to the readers, and stimulate interdisciplinary interactions among researchers, thus paving the way to explorations of new frontiers.

Tokyo, Japan Kaoru Yamanouchi
Jena, Germany Gerhard G. Paulus
Mumbai, India Deepak Mathur

Contents

Contributors

Skirmantas Alisauskas Photonics Institute, Vienna University of Technology, Vienna, Austria

Andrius Baltuska Photonics Institute, Vienna University of Technology, Vienna, Austria

Annelise R. Beck Ultrafast X-ray Science Laboratory, Chemical Sciences Division, Lawrence Berkeley National Laboratory, Berkeley, CA, USA; Department of Chemistry, University of California, Berkeley, CA, USA

M. Justine Bell Ultrafast X-ray Science Laboratory, Chemical Sciences Division, Lawrence Berkeley National Laboratory, Berkeley, CA, USA; Department of Chemistry, University of California, Berkeley, CA, USA

Yohann Brelet Laboratoire d'Optique Appliquée, ENSTA Paristech/CNRS/Ecole Polytechnique, Palaiseau, France

Francesca Calegari CNR-IFN, Dipartimento di Fisica Politecnico, Milan, Italy

Ya Cheng State Key Laboratory of High Field Laser Physics, SIOM, CAS, Shanghai, China

See-Leang Chin Department of Physics & Center for Optics, Photonics and Laser, Laval University, Québec City, Canada

Wei Chu State Key Laboratory of High Field Laser Physics, SIOM, CAS, Shanghai, China

Arnaud Couairon Centre de Physique Théorique, CNRS, Ecole Polytechnique, Palaiseau, France

Antonino Di Piazza Max Planck Institute for Nuclear Physics (MPIK), Heidelberg, Germany

Louis F. DiMauro Department of Physics, The Ohio State University, Columbus, OH, USA

Magali Durand Laboratoire d'Optique Appliquée, ENSTA Paristech/CNRS/Ecole Polytechnique, Palaiseau, France

Benjamin Forestier Laboratoire d'Optique Appliquée, ENSTA Paristech/CNRS/Ecole Polytechnique, Palaiseau, France

Yusuke Furukawa Laser Technology Laboratory, RIKEN ASI, Saitama, Wako-shi, Japan

Omri Har-Shemesh Max Planck Institute for Nuclear Physics (MPIK), Heidelberg, Germany

Aurélien Houard Laboratoire d'Optique Appliquée, ENSTA Paristech/CNRS/Ecole Polytechnique, Palaiseau, France

Amélie Jarnac Laboratoire d'Optique Appliquée, ENSTA Paristech/CNRS/Ecole Polytechnique, Palaiseau, France

Reika Kanya Department of Chemistry, School of Science, the University of Tokyo, Tokyo, Bunkyo-ku, Japan

Daniil Kartashov Photonics Institute, Vienna University of Technology, Vienna, Austria

Stephen R. Leone Ultrafast X-ray Science Laboratory, Chemical Sciences Division, Lawrence Berkeley National Laboratory, Berkeley, CA, USA; Department of Chemistry, University of California, Berkeley, CA, USA; Department of Physics, University of California, Berkeley, CA, USA

Guihua Li State Key Laboratory of High Field Laser Physics, SIOM, CAS, Shanghai, China

Yi Liu Laboratoire d'Optique Appliquée, ENSTA Paristech/CNRS/Ecole Polytechnique, Palaiseau, France

Hiroki Mashiko Ultrafast X-ray Science Laboratory, Chemical Sciences Division, Lawrence Berkeley National Laboratory, Berkeley, CA, USA; Material Quantum Optical Physics Research Group, Optical Science Laboratory, NTT Basic Research Laboratory, Kanagawa, Atsugi-shi, Japan

Sebastian Meuren Max Planck Institute for Nuclear Physics (MPIK), Heidelberg, Germany

Katsumi Midorikawa Laser Technology Laboratory, RIKEN ASI, Saitama, Wako-shi, Japan

Yuya Morimoto Department of Chemistry, School of Science, the University of Tokyo, Tokyo, Bunkyo-ku, Japan

André Mysyrowicz Laboratoire d'Optique Appliquée, ENSTA Paristech/CNRS/Ecole Polytechnique, Palaiseau, France

Yasuo Nabekawa Laser Technology Laboratory, RIKEN ASI, Saitama, Wako-shi, Japan

Daniel M. Neumark Ultrafast X-ray Science Laboratory, Chemical Sciences Division, Lawrence Berkeley National Laboratory, Berkeley, CA, USA; Department of Chemistry, University of California, Berkeley, CA, USA

Jielei Ni State Key Laboratory of High Field Laser Physics, SIOM, CAS, Shanghai, China

Mauro Nisoli Dipartimento di Fisica Politecnico, Milan, Italy

David Novoa Centro de Láseres Pulsados, CLPU, Villamayor, Spain

Audrius Pugzlys Photonics Institute, Vienna University of Technology, Vienna, Austria

Christoph A. Roedig Department of Physics, The Ohio State University, Columbus, OH, USA

Luis Roso Centro de Láseres Pulsados, CLPU, Villamayor, Spain

Giuseppe Sansone Dipartimento di Fisica Politecnico, Milan, Italy

Daniele Tommasini Department of Applied Physics, University of Vigo, Ourense, Spain

Huailiang Xu State Key Laboratory on Integrated Optoelectronics, College of Electronic Science and Engineering, Jilin University, Changchun, China

Zhizhan Xu State Key Laboratory of High Field Laser Physics, SIOM, CAS, Shanghai, China

Kaoru Yamanouchi Department of Chemistry, School of Science, the University of Tokyo, Tokyo, Bunkyo-ku, Japan

Jinping Yao State Key Laboratory of High Field Laser Physics, SIOM, CAS, Shanghai, China

Bin Zeng State Key Laboratory of High Field Laser Physics, SIOM, CAS, Shanghai, China

Chapter 1
Laser-Assisted Electron Scattering and Diffraction in Ultrashort Intense Laser Fields

Reika Kanya, Yuya Morimoto, and Kaoru Yamanouchi

Abstract Recent progress in experimental studies of laser-assisted electron scattering (LAES) in ultrashort intense laser fields is reviewed. After a brief survey of theoretical backgrounds of the LAES process and earlier LAES experiments started in 1970's, new phenomena induced by LAES experiments in ultrashort intense laser fields and expected applications of these experiments are discussed. A new experimental setup designed for measurements of LAES induced by ultrashort intense laser fields is described. Experimental results of energy spectra, angular distributions, and laser polarization dependence of the LAES signals are presented with corresponding results of numerical simulations. A light-dressing effect appearing in the LAES signals to be obtained under our experimental conditions is also examined by numerical calculations. In addition, as an application of the LAES process, the determination of instantaneous geometrical structure of molecules by a novel technique of laser-assisted electron diffraction is introduced.

1.1 Introduction

1.1.1 Electron-Atom Collisions in Laser Fields

Through elastic scattering process between an electron and an atom occurring in a laser field, the kinetic energy of the scattered electron (E_f) can be shifted by multiples of photon energy ($\hbar\omega$), i.e., $E_f = E_i + n\hbar\omega$, where E_i is the initial kinetic energy and $n = 0, \pm 1, \pm 2, \ldots$. This process is called "laser-assisted electron scattering (LAES)" or "free-free transition." In some cases, the energy gain process ($n > 0$)

R. Kanya (✉) · Y. Morimoto · K. Yamanouchi
Department of Chemistry, School of Science, the University of Tokyo, 7-3-1 Hongo, Bunkyo-ku, Tokyo 113-0033, Japan
e-mail: kanya@chem.s.u-tokyo.ac.jp

Y. Morimoto
e-mail: morimoto@chem.s.u-tokyo.ac.jp

K. Yamanouchi
e-mail: kaoru@chem.s.u-tokyo.ac.jp

K. Yamanouchi et al. (eds.), *Progress in Ultrafast Intense Laser Science X*,
Springer Series in Chemical Physics 106, DOI 10.1007/978-3-319-00521-8_1,

and energy loss ($n < 0$) process are separately called "inverse bremsstrahlung" and "stimulated bremsstahlung," respectively, referring to the bremsstrahlung, which is the light emission induced by a sudden acceleration of incident electrons by an atomic potential. As an elementary process in astronomy, plasma physics, and intense laser physics, the LAES plays important roles in the infrared opacity of the solar atmosphere, the plasma heating, and the laser-induced rescattering in intense laser fields. The LAES process can also be regarded as a special kind of three-body collision, where a laser photon acts as a simple third-body in the electron-atom collision process.

Such energy gain and loss of scattered electrons by $n\hbar\omega$ can also be induced through "inelastic" scattering processes, which are called simultaneous electron-photon excitation (SEPE) or laser-assisted electron inelastic scattering in a similar manner as in the LAES process. Especially, the energy gain and loss by $n\hbar\omega$ associated with electron impact ionizations are called "laser-assisted electron impact ionization" or "laser-assisted $(e, 2e)$" processes. Experimental and theoretical studies on these inelastic phenomena were reviewed by Mason [1].

1.1.2 Theory of the LAES Process

Theoretical framework of the LAES process was proposed first by Bunkin and Fedorov in 1966 [2]. Under the first Born approximation for the scattering process between a target atom and an electron expressed as an eigenfunction of a free electron in an electromagnetic field, i.e., Gordon-Volkov wavefunction [3, 4], they derived the differential cross section for net n-photon absorption, $d\sigma^{(n)}_{\mathrm{BFA}}/d\Omega$, as

$$\frac{d\sigma^{(n)}_{\mathrm{BFA}}}{d\Omega} = \frac{|\boldsymbol{p}_f|}{|\boldsymbol{p}_i|} J_n^2(\boldsymbol{\alpha}_0 \cdot \boldsymbol{s}) \frac{d\sigma_{\mathrm{FBA}}(\boldsymbol{s})}{d\Omega}, \tag{1.1}$$

where $J_n(x)$ is the n-th order Bessel function of the first kind, $\boldsymbol{p}_i$ and $\boldsymbol{p}_f$ are initial and final electron momenta, respectively, $d\sigma_{\mathrm{FBA}}(\boldsymbol{s})/d\Omega$ is a differential cross section of elastic scattering without laser fields derived by the first Born approximation, $\boldsymbol{s}$ is a scattering vector defined by $(\boldsymbol{p}_i - \boldsymbol{p}_f)/\hbar$, and $\boldsymbol{\alpha}_0$ is defined as

$$\boldsymbol{\alpha}_0 \equiv \frac{e}{m\omega^2}\boldsymbol{\varepsilon}, \tag{1.2}$$

where e is unit charge, m is mass of an electron, and $\boldsymbol{\varepsilon}$ is an electric amplitude vector of the laser field. The absolute value of $\boldsymbol{\alpha}_0$, $|\boldsymbol{\alpha}_0|$, corresponds to the quiver radius, i.e., the amplitude of the classical motion of an electron in the electromagnetic field. In the Bunkin-Fedorov approximation (BFA), the interaction between an atom and a laser field is neglected, and the electron-atom interaction is treated within the first Born approximation, which is a good approximation for the forward scattering of high-energy electrons, and the non-perturbative interaction between an electron and a laser field is explicitly treated by using the Gordon-Volkov wavefunctions for the incident and scattered electrons. Equation (1.1) shows that the differential cross section for the $n = 0$ LAES process is also modified by the laser field. Because the scattered electrons of this $n = 0$ LAES process have an overlap in the kinetic energy with the electrons scattered by an elastic scattering process without laser fields, the scattering processes in which $E_i = E_f$ is satisfied are referred to commonly as "$n = 0$ scattering" in the present paper.

In 1973, Kroll and Watson derived the differential cross section of LAES process by taking into account the non-perturbative interaction between an electron and an atom [5]. In the Kroll-Watson approximation (KWA), the formula of the differential cross section for net n-photon absorption, $d\sigma_{\mathrm{KWA}}^{(n)}/d\Omega$, takes a similar form to (1.1), and is written as

$$\frac{d\sigma_{\mathrm{KWA}}^{(n)}}{d\Omega} = \frac{|\boldsymbol{p}_f|}{|\boldsymbol{p}_i|} J_n^2(\boldsymbol{\alpha}_0 \cdot \boldsymbol{s}) \frac{d\sigma_{\mathrm{el}}(\tilde{E}_i; \boldsymbol{s})}{d\Omega}, \tag{1.3}$$

where $d\sigma_{\mathrm{el}}(\tilde{E}_i; \boldsymbol{s})/d\Omega$ is the differential cross section of elastic electron scattering, $\tilde{\boldsymbol{p}}_i - \hbar\boldsymbol{s} \leftarrow \tilde{\boldsymbol{p}}_i$, occurring without laser fields with an incident electron whose initial momentum, $\tilde{\boldsymbol{p}}_i$, and initial kinetic energy, $\tilde{E}_i$, are defined as

$$\tilde{\boldsymbol{p}}_i \equiv \boldsymbol{p}_i + \frac{nm\omega}{(\boldsymbol{\alpha}_0 \cdot \boldsymbol{s})} \boldsymbol{\alpha}_0, \tag{1.4}$$

$$\tilde{E}_i \equiv \frac{|\tilde{\boldsymbol{p}}_i|^2}{2m}, \tag{1.5}$$

respectively. Equation (1.3) means that the differential cross section of the LAES process is calculated from $d\sigma_{\mathrm{el}}(E_i; \boldsymbol{s})/d\Omega$, which can be given by conventional scattering experiments without a laser field, or obtained from a database provided, for example, by NIST [6]. The Kroll-Watson formula can also be applied to the slow-electron scattering and the backward scattering. However, the formation of light-dressed states of target atoms could not be described because the interaction between an atom and a laser field is neglected.

Mittleman et al. [7–10] developed a theoretical framework for an electron-atom scattering in the presence of a laser field whose frequency is near resonant to the atomic transition. Zon [11, 12] proposed a simple and convenient model by describing the laser-atom interaction as the polarization of electron clouds of target atoms induced by the off-resonant laser fields. Later, Byron et al. [13, 14] studied the effect of the formation of light-dressed atoms by treating the laser-atom interaction by a first-order time-dependent perturbation theory and the electron-atom interaction by the first Born approximation. Non-perturbative interactions between laser fields and atoms in high-energy electron-atom scattering processes can be treated in Born-Floquet theory proposed by Faisal [15], or non-Hermitian Born-Floquet theory developed by Dörr et al. [16], while R-matrix Floquet theory [17, 18] and close-coupling Floquet theory [19] are applicable for low-energy scattering process, in which the non-perturbative electron-atom interaction is included in addition to the non-perturbative laser-atom interaction. In addition, other theoretical methods were also proposed on the basis of a variety of models and approximations as reviewed in [20].

1.1.3 Experimental Studies of the LAES

The first observation of LAES was reported by Andrick and Langhans in 1976 [21], who observed $n = \pm 1$ LAES signals in the electron-Ar collision process under a continuous laser filed ($\lambda = 10.6\ \mu\text{m}$, $I = 6 \times 10^4\ \text{W/cm}^2$) generated by cw-$CO_2$ laser. In the next year, Weingartshofer et al. reported multiphoton-LAES signals up to $n = \pm 3$ in the electron-Ar scattering with a pulsed-CO_2 laser ($\lambda = 10.6\ \mu\text{m}$, $I = 10^9\ \text{W/cm}^2$, $\Delta t = 2\ \mu\text{s}$) [22]. Compared to the theoretical studies, only a small number of experimental studies [1, 23] have been reported probably because LAES measurements are very difficult. Until 2010, the kinetic energies of an incident electron beam in LAES experiments had been in the low energy range, $4\ \text{eV} < E_i < 80\ \text{eV}$, and all the laser light sources were cw-CO_2 lasers [21, 24–27] or pulsed-CO_2 lasers with the minimum pulse duration of the order of microseconds [22, 28–38], except a study with cw-CO laser ($I = 10^3\ \text{W/cm}^2$, $\lambda = 5.3\ \mu\text{m}$) [39]. Consequently, in these experimental studies, the laser field intensities were in the rather moderate range ($<10^9\ \text{W/cm}^2$) and the photon energies were too small to induce electronic transitions of target atoms. Therefore, no evidences of the formation of the light-dressed states of target atoms were identified in these traditional LAES experiments, as concluded by several theoretical estimations [40–42].

Interestingly, in 1970's, Hertel et al. reported their results of laser-induced superelastic scattering experiments, i.e., the electron scattering experiments in which target atoms are resonantly excited by cw-laser fields [43, 44]. These experiments are regarded as electron scattering by light-dressed atoms occurring when the laser-electron interaction is negligibly small. This is the opposite situation to the conventional LAES experiments, in which light-dressed electrons are scattered by non-dressed target atoms. So far, no experimental report has been made on "scattering of light-dressed electrons by light-dressed atoms."

1.1.4 LAES Experiment in Femtosecond Intense Laser Fields

In 2010, we observed LAES signals induced by femtosecond near-infrared intense laser fields ($I = 1.8 \times 10^{12}\ \text{W/cm}^2$, $\lambda = 800\ \text{nm}$, $\Delta t = 200\ \text{fs}$) in the elastic scattering of 1 keV electrons by Xe atoms [45]. This is the first observation of LAES by femtosecond laser pulses. Compared to the conventional LAES experiments, such as the latest LAES experiment with a pulsed-CO_2 laser ($I = 4 \times 10^8\ \text{W/cm}^2$, $\lambda = 10.6\ \mu\text{m}$, $\Delta t = 3\ \mu\text{s}$, $E_i = 22\ \text{eV}$) [38], the experimental conditions in our study [45] were completely different in the following four points; (i) the photon energy is 13 times higher, (ii) the laser intensity is 4.5×10^3 times higher, (iii) the laser pulse duration is 1.5×10^7 times shorter, and (iv) the kinetic energy of the incident electrons is 45 times larger than the latest conventional LAES study [38].

The large differences in the photon energy and the laser intensity will enable us to perform experiments on LAES by light-dressed atoms. Several theoretical studies predicted that a peak structure will appear at the zero scattering angle in the angular distributions of LAES signals when target atoms form light-dressed electronic states [11, 13], and the intensity of the peak appearing in the small scattering angle region increases drastically when a substantial electronic-state mixing occurs through resonant interactions between laser fields and atoms [16, 18, 19]. Therefore, LAES occurring in intense near-infrared laser fields should carry information on light-dressed states of target atoms having ultrashort lifetimes in intense laser fields. On the other hand, ultrashort laser pulses for LAES experiments enable us to achieve high temporal resolutions, and LAES by molecules with high-energy electrons can carry information on geometrical structure of molecules as in electron diffraction of gas-phase molecules. This means that LAES by molecules will lead to “a new time-resolved electron diffraction method” with the temporal resolution of femtoseconds [45].

After the first observation of the LAES signals induced by 200 fs laser pulses [45], a LAES experiment with 50 fs laser pulses was reported in 2011 also by our group [46], and another near-infrared LAES experiment was reported in 2011 by deHarak et al., where Nd:YAG laser ($\Delta t = 6$ ns, $\lambda = 1064$ nm) was used for generating laser fields of the order of 10^9 W/cm^2 [47]. It can be said that experimental studies of the LAES process are now entering into a new stage 34 years after the first conventional LAES experiment [21].

In the present article, the recent progress of the LAES experiments in femtosecond intense laser fields is reviewed, and promising applications of LAES processes to “probing of light-dressed states” and “gas electron diffraction” are discussed by referring to our numerical simulations.

1.2 Experimental Setup

Details of the experimental setup were described in [46]. Figure 1.1 shows the schematic of our setup for femtosecond-LAES experiments. The apparatus consists of a femtosecond laser system, an electron beam source, a sample gas nozzle, a toroidal-type electron energy analyzer, and an imaging detector. Scattered electrons generated by the collision among the three beams, i.e., the electron beam, the atom beam, and the laser beam, are introduced into the electron energy analyzer and are detected by the imaging detector.

By taking the leading term of the Bessel functions in (1.1) or (1.3), intensities of the LAES signals in BFA and KWA are approximately proportional to $\Delta t(\lambda^4 I)^{|n|}$. This means that the signal intensities per laser-shot for the $n = \pm 1$ transitions in LAES should decrease by a factor of 1×10^{-8} when the laser field conditions change from “$\Delta t = 3$ µs, $\lambda = 10.6$ µm, $I = 4 \times 10^8$ W/cm^2” to “$\Delta t = 200$ fs, $\lambda = 800$ nm, $I = 1.8 \times 10^{12}$ W/cm^2,” which correspond to the conditions employed in the latest conventional LAES experiment with CO$_2$ laser [38] and our first femtosecond-LAES experiment [45], respectively. Therefore, a drastic improvement in the detection efficiency is necessary for the measurements of the LAES signals

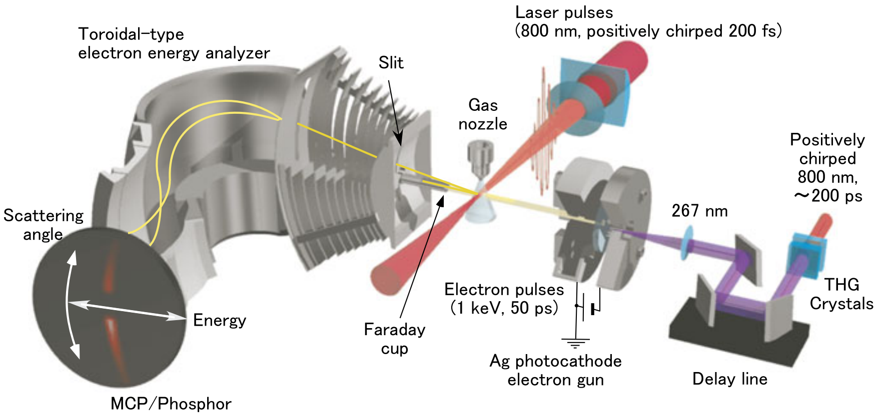

Fig. 1.1 The schematic of the experimental setup of LAES [46]

in ultrashort intense laser fields. Furthermore, because of the limited spatial overlap and the velocity mismatch between the electron pulse and the femtosecond laser pulse [48], the fraction of scattering events in the laser field is estimated to be only 0.4 %, and majority of the scattering events (99.6 %) are those occurring in the absence of the laser fields under the experimental conditions, in which a pulsed 1 keV electron beam collides with a sample gas beam of ∼1 mm diameter at right angles and a 200 fs laser pulse is introduced perpendicularly to both the electron and sample beams. Thus, it is difficult to discriminate the femtosecond-LAES signals in the energy spectra of the scattered electrons from the neighboring huge peak of $n = 0$ scattering signals. Moreover, intensities of the LAES signals will be similar in magnitude to noise signals originating from stray photons, photoelectrons, photoions, and metastable neutral atoms generated by the irradiation of intense near-infrared laser pulses. In order to overcome the experimental difficulties mentioned above, the following three components are newly introduced into our LAES apparatus, i.e., (i) the electron beam source with a photocathode-type pulsed electron gun, (ii) the high repetition-rate and high power Ti:sapphire laser system, and (iii) the toroidal-type electron energy analyzer equipped with the two-dimensional detector.

The electron pulses are generated from the photocathode-type pulsed electron gun by irradiating the photocathode with UV laser pulses, which are the third harmonics of 800 nm light split from the main 800 nm pulses before a pulse compressor of the laser system. The synchronization between the electron pulse and the intense IR laser pulse for the LAES process is achieved by adjusting the optical delay between the UV laser pulses and the intense IR laser pulses. The pulse duration of the electron pulses were found to be ∼50 ps by the shadow graph method [46]. Huge background signals originating from elastic scattering without laser fields can be suppressed by using these ultrashort incident electron pulses. The generated monochromatic electron pulse of 1 keV kinetic energy collides with a Xe gas in a near-infrared intense laser field ($\Delta t = 200$ fs, $\lambda = 800$ nm, $I = 1.8 \times 10^{12}$ W/cm^2) at the scattering point in the vacuum chamber. The scattered electrons are introduced

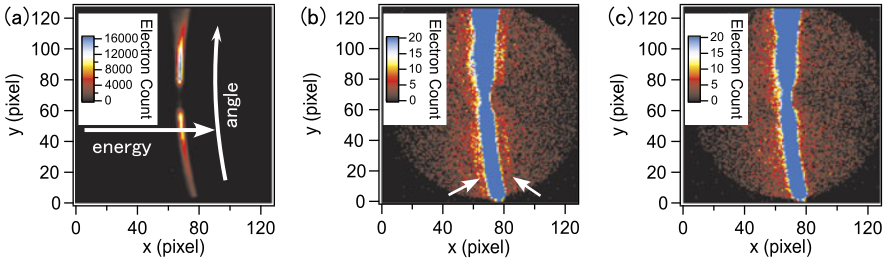

Fig. 1.2 (**a**) The raw image of electron scattering signals recorded when vertically polarized laser pulses were introduced at the timing of the electron scattering by Xe atoms. (**b**) The amplified image of (**a**). (**c**) The raw image of background signals in the same intensity scale as (**b**) [45]

into the toroidal-type electron energy analyzer through a 0.8 mm slit. Simultaneous detection of the angular and energy distributions is achieved by the toroidal-type electron energy analyzer [49], and these distributions are obtained as a two-dimensional image on a MCP/Phosphor detector coupled with a CCD camera. On the detector, an angular distribution of isoenergetic electrons forms an arcuate pattern as shown in Fig. 1.1. The signals of scattered electrons are discriminated from noise signals by counting the number of bright spots of electron signals appearing on CCD images within a time window of one second. Significant improvement in the count rate of the LAES signals is achieved by 5 kHz data acquisition with the high repetition-rate and high power Ti:sapphire laser system. The number of incident electrons per shot is made as small as possible in order to avoid energy broadening induced by the space charge effect, and a typical count rates of detection of electrons including those originating from the elastic scattering is around 10 cps. The energy resolution of the total detection system is around 0.7 eV, which is sufficiently smaller than the photon energy of laser light (1.56 eV).

1.3 Observation of LAES in Intense Laser Fields

The raw images of scattered electrons obtained from the LAES experiments with the light field conditions of $\Delta t = 200$ fs, $\lambda = 800$ nm, and $I = 1.8 \times 10^{12}$ W/cm^2 [45] are shown in Fig. 1.2. The net exposure time was around 83 hours for each image. Figure 1.2(a) shows electron scattering signals when laser pulses were introduced at the timing of the electron scattering by Xe atoms. The laser polarization was set to be "vertical", i.e., perpendicular to the electron beam axis. The intense signals forming an arcuate line seen at the central area in Fig. 1.2(a) is $n = 0$ scattering signals, and any other features could not be recognized in Fig. 1.2(a). Figure 1.2(b) is an amplified image of Fig. 1.2(a) obtained after adjusting the range of the signal intensity so that the weak LAES signals become visible. In Fig. 1.2(b), a weak arcuate lines indicated by the white arrows can be seen on both sides of the central arcuate line. On the other hand, such structures could not be seen in the background

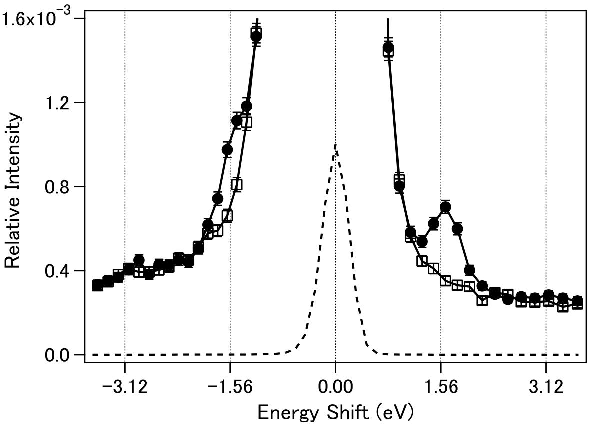

Fig. 1.3 The energy spectra of relative intensities of scattered electron signals [45]. The intensity is normalized with respect to the peak intensity of $n = 0$ scattering signal. Estimated statistical error bars are derived from square roots of signal counts. *Filled circles*: electron signals with vertically polarized laser fields; *Open squares*: background signals; *Broken line*: $n = 0$ scattering peak reduced by a factor of 1000

signals [Fig. 1.2(c)], which is obtained when the temporal delay of the electron pulse with respect to the laser pulse was set to be +100 ps.

The observed small difference between Figs. 1.2(b) and 1.2(c) becomes clear in the electron energy spectra, which are obtained through the integration of the signal of each pixel over the scattering angles along the arcuate isoenergetic coordinate. In the integration, signals in the region of $y > 105$ pixel in Fig. 1.2 were excluded from the analysis because the contributions of stray electrons are significantly large in this region. The filled circles and the open squares in Fig. 1.3 show the energy spectra obtained from Fig. 1.2(b) and (c), respectively. Unambiguous increases in the signal intensity appear at the kinetic energy shifts of $\pm\hbar\omega$, i.e., ±1.56 eV, in Fig. 1.3 (filled circles). This is a clear experimental evidence that the $n = \pm 1$ transitions in the LAES process are identified.

The filled circles in Fig. 1.4 represent the LAES signals obtained by subtracting the background signals from the scattering signals obtained with the laser field in Fig. 1.3. Both of the signals at the energies of $\pm\hbar\omega$ can be recognized as distinct peaks, and the intensities of these peaks are around 3×10^{-4} relative to the central $n = 0$ scattering peak.

In order to confirm our assignment, the relative intensities of the LAES signals were estimated by a numerical simulation based on (1.3). In the current experimental configuration with $\hat{\boldsymbol{\varepsilon}} \cdot \boldsymbol{p}_i = 0$, the $\tilde{\boldsymbol{p}}_i$ can be expressed as

$$\tilde{\boldsymbol{p}}_i = \boldsymbol{p}_i - \frac{n\hbar\omega|\boldsymbol{p}_f|}{2E_f \sin\theta}\hat{\boldsymbol{\varepsilon}}, \tag{1.6}$$

where $E_f \equiv |\boldsymbol{p}_f|^2/(2m)$ is the kinetic energy of a scattered electron. In the present high-energy scattering ($E_f \sim 1$ keV), $|\tilde{\boldsymbol{p}}_i| \simeq |\boldsymbol{p}_i|$ holds well because $\hbar\omega/(2E_f \sin\theta)$ is less than 0.03 in the detectable range of the scattering angle (1.5 deg. $< \theta <$ 14 deg.). Then, the $d\sigma_{\text{KWA}}^{(n)}/d\Omega$ can be approximated to be

$$\frac{d\sigma_{\text{KWA}}^{(n)}}{d\Omega} \simeq \frac{|\boldsymbol{p}_f|}{|\boldsymbol{p}_i|} J_n^2(\boldsymbol{\alpha}_0 \cdot \boldsymbol{s}) \frac{d\sigma(E_i; \boldsymbol{s})}{d\Omega}. \tag{1.7}$$

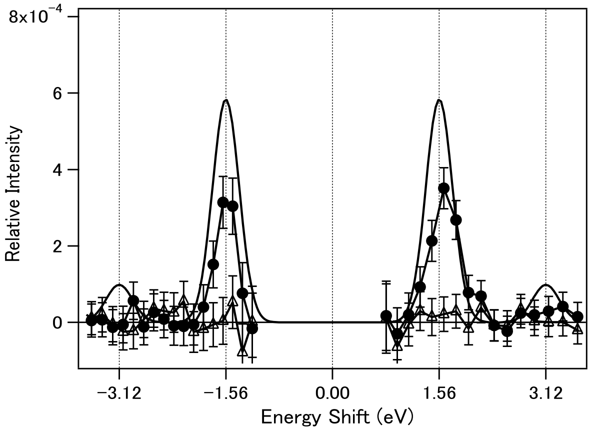

Fig. 1.4 The energy spectra of relative intensities of LAES signals [45]. Relative intensities are normalized with respect to the peak intensity of $n = 0$ scattering signal. Estimated statistical error bars are derived from square roots of signal counts. *Filled circles*: an energy spectrum obtained after the subtraction of the backgrounds from the signals recorded with vertically polarized laser fields; *Open triangles*: an energy spectrum obtained after the subtraction of the backgrounds from the signals recorded with horizontally polarized laser fields; *Solid line*: a calculated spectrum of the LAES signals when the laser fields are vertically polarized

In order to simulate the magnitudes of the observed LAES signals, denoted by $w^{(n)}(E_i; \boldsymbol{s})$, the differential cross section in (1.7) should be averaged over the spatiotemporal distribution of the three beams, i.e., the electron beam, the laser beam, and the atomic beam. Considering that the $d\sigma(E_i; \boldsymbol{s})/d\Omega$ is independent of the laser field, the $w^{(n)}(E_i; \boldsymbol{s})$ can be factorized into two parts,

$$w^{(n)}(E_i; \boldsymbol{s}) = F_n(E_i; \boldsymbol{s}) \frac{d\sigma(E_i; \boldsymbol{s})}{d\Omega}, \tag{1.8}$$

where

$$F_n(E_i; \boldsymbol{s}) \equiv \frac{|\boldsymbol{p}_f|}{|\boldsymbol{p}_i|} \int d\boldsymbol{r} \rho(\boldsymbol{r}) \int dt\, j(\boldsymbol{r}, t) J_n^2\big(\boldsymbol{\alpha}_0(\boldsymbol{r}, t) \cdot \boldsymbol{s}\big). \tag{1.9}$$

In (1.9), $\rho(\boldsymbol{r})$ is a density of the sample atom and $j(\boldsymbol{r}, t)$ is an electron flux density. The spatiotemporal distributions of the $\rho(\boldsymbol{r})$ and $j(\boldsymbol{r}, t)$ can be determined experimentally [46]. The vectorial quiver radius, $\boldsymbol{\alpha}_0(\boldsymbol{r}, t)$, becomes a function of $\boldsymbol{r}$ and t because of the spatiotemporal distribution of $\boldsymbol{\varepsilon}$, and can also be derived experimentally, as described in [46], using the laser field parameters, such as the pulse energy, the temporal shape of the pulse envelope, and the spatial profile at the scattering point. Therefore, $w^{(n)}(E_i; \boldsymbol{s})$ in (1.8) can be calculated using $F_n(E_i; \boldsymbol{s})$ obtained from (1.9) and the differential cross section $(d\sigma(E_i; \boldsymbol{s})/d\Omega)$ in the NIST database [6]. The results of the simulation are plotted with a solid line in Fig. 1.4. The calculated LAES signal intensities relative to $n = 0$ scattering signal intensities show good agreement with the experimental results.

When the laser polarization vector is set to be "horizontal", i.e., parallel to the direction of the incident electron beam, the factor of $\boldsymbol{\alpha}_0 \cdot \boldsymbol{s}$ in (1.3) becomes close to

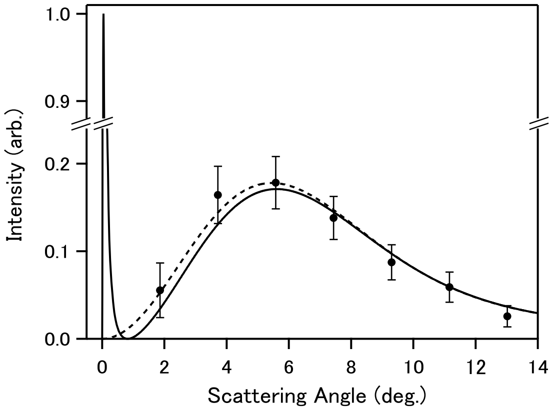

Fig. 1.5 The angular distributions of LAES for the $n = +1$ transitions with the vertically polarized laser field [45, 50]. *Filled circles*: observed LAES signals of $n = +1$; *Broken line*: the numerical calculation by KWA; *Solid line*: the numerical calculation by Zon's model. Estimated statistical error bars are derived from square roots of the signal counts

zero because the polarization vector is nearly perpendicular to the scattering vector, $\boldsymbol{s}$, for the forward scattering of the high-energy electrons. Consequently, the LAES signal intensities should be suppressed significantly except the signal intensity at $n = 0$. This polarization dependence should provide a further verification of our measurements of LAES signals of $n = \pm 1$. In Fig. 1.4, an energy spectrum with the horizontally polarized laser field is plotted with open triangles. In contrast to the corresponding spectrum obtained using the vertically polarized laser field, no distinguishable peaks are observed. This is consistent with the corresponding numerical calculation, showing that relative intensities for the $n = \pm 1$ transitions are nearly zero (7×10^{-6}).

The filled circles in Fig. 1.5 show the angular distribution of the background-subtracted LAES signals for the $n = +1$ transition recorded using the vertically polarized laser field. The broken line shows the results of numerical calculations with KWA. The calculated angular distribution is in good agreement with the experimental angular distribution. The angular distribution of the $n = -1$ transition is basically the same as that of the $n = +1$ transition, and also shows good agreement with the result of numerical calculations.

As discussed in Sect. 1.1.4, the characteristic peak structure is expected to appear at the zero angle in the angular distribution of LAES signals when target atoms are formed in the light-dressed states. This light-dressing effect [50] is examined by a simulation of the angular distribution of the $n = +1$ LAES signals using Zon's model [11] with the experimental laser field conditions ($\Delta t = 200$ fs, $\lambda = 800$ nm, $I = 1.8 \times 10^{12}$ W/cm^2). In this model, the laser-atom interaction is treated as a polarization of an electron cloud in a target atom, creating a laser-induced dipole moment expressed as

$$\boldsymbol{\mu}_{\text{ind}} = a(\omega)\boldsymbol{\varepsilon} \sin \omega t, \tag{1.10}$$

where $a(\omega)$ is the frequency-dependent polarizability of the target atom, which can be described by the Unsöld expression [51] as

$$a(\omega) = a(0)\frac{\omega_{\text{res}}^2}{\omega_{\text{res}}^2 - \omega^2}, \tag{1.11}$$

where ω_{res} is the resonance frequency of the target atom and $\omega_{\text{res}} \gg \omega$ is assumed. Because the scattering process is affected by the interaction potential between the charge of the incident electron and the laser-induced dipole of the polarized atoms, the Hamiltonian of the system is expressed as

$$\hat{H} = \frac{1}{2m}\left(\frac{\hbar}{i}\nabla + m\omega\boldsymbol{\alpha}_0 \cos\omega t\right)^2 + V(\boldsymbol{r}) - \frac{e\boldsymbol{\mu}_{\text{ind}} \cdot \boldsymbol{r}}{4\pi\varepsilon_0 r^3}. \tag{1.12}$$

Under the first Born approximation, the differential cross section of the LAES process can be derived analytically as

$$\frac{d\sigma_{\text{Zon}}^{(n)}}{d\Omega} = \frac{|\boldsymbol{p}_f|}{|\boldsymbol{p}_i|}\left| J_n(\xi) f_{\text{Born}}(\boldsymbol{s}) - \frac{m^2\omega^2 a(\omega)}{4\pi\varepsilon_0\hbar^2|\boldsymbol{s}|^2}\xi\left[J_{n-1}(\xi) - J_{n+1}(\xi)\right]\right|^2, \tag{1.13}$$

where $\xi \equiv \boldsymbol{\alpha}_0 \cdot \boldsymbol{s}$ and $f_{\text{Born}}(\boldsymbol{s})$ is the scattering amplitude without laser fields expressed as

$$f_{\text{Born}}(\boldsymbol{s}) = -\frac{m}{2\pi\hbar^2}\int V(\mathbf{r})e^{i\mathbf{s}\cdot\mathbf{r}}d\mathbf{r}, \tag{1.14}$$

in the first Born approximation. The first term in the squared modulus in (1.13) represents the scattering by the non-dressed potential, $V(\boldsymbol{r})$, and the second term in the squared modulus represents the laser-induced polarization of the target atom. If the second term in (1.13) is omitted, (1.13) becomes identical to (1.1).

The solid line in Fig. 1.5 shows the result of the numerical calculation obtained with Zon's model. In the calculation, the spatiotemporal overlaps of the three beams are taken into account in the same manner as in the calculation with KWA (broken line in Fig. 1.5), and $f_{\text{Born}}(\boldsymbol{s})$ is replaced by the numerical scattering amplitude given by the NIST database [6] in order to describe more accurately the scattering amplitude in the large scattering angle region. As shown with the solid curve, a sharp and intense peak profile can be seen around the zero angle region, exhibiting remarkable contrast to the calculated angular distribution shown in Fig. 1.5 with a broken line obtained by KWA. This peak profile appearing with Zon's model shows that the light dressing effect is sufficiently large in the present laser field conditions, so that the intensity of the sharp peak profile is in the detectable range. Unfortunately, the scattering signals in the small scattering-angle region could not be detected using our apparatus because the scattered electrons in the range of $\theta < 1.5$ degree are blocked by a Faraday cup placed in front of the entrance slit of the energy analyzer (Fig. 1.1).

Zon's model, in which the laser-atom interaction is considered as a perturbation, could not be used when the laser-atom interaction becomes substantially large associated with the increase in laser-field intensities. In such intense laser field conditions, Born-Floquet theory [15] and non-Hermite Born-Floquet theory [16] need to be introduced for describing LAES signals. When the laser field intensity increases more, for example, typically up to $\sim 10^{14}$ W/cm^2, even the Floquet-type theories are no longer practically feasible because the size of the Floquet Hamiltonian matrix becomes so large that a physical picture of the phenomena is difficult to be described by a Floquet-type basis set. In addition, these Floquet-type pictures hold well only

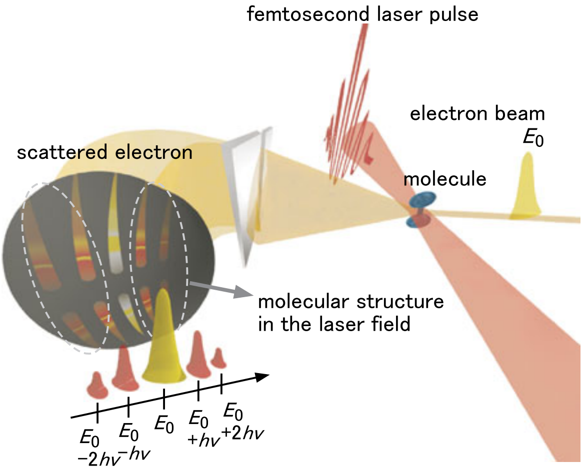

Fig. 1.6 The schematic of laser-assisted electron diffraction method

when the laser pulse duration is substantially longer than the period of the laser field, and will not hold when the laser field has only few-cycles. Therefore, another theoretical methods need to be developed to describe the LAES process induced by very intense laser pulses and/or few-cycle laser pulses.

1.4 Laser-Assisted Electron Diffraction

Gas electron diffraction has been a standard method to determine geometrical structures of molecules in the gas phase [52–54]. For probing temporal variation of geometrical structures of molecules, a pulsed gas electron diffraction method was developed, where electron diffraction patterns were obtained with ultrashort electron pulses [55]. However, the temporal resolution could not be improved beyond ∼1 ps so far [56], which is much longer than the typical timescale of nuclear motion of molecules, and, up to the present, femtosecond temporal resolution has not been achieved by the time-resolved pulsed gas electron diffraction method.

As proposed in our recent report [45], a new ultrafast gas electron diffraction method called laser-assisted electron diffraction (LAED) can be developed if the femtosecond LAES measurement is performed with a molecular target. The schematic of the LAED experiment is described in Fig. 1.6. The LAES process for molecular targets is basically the same as that for atomic targets, but interference diffraction patterns appear in the angular distribution of the LAES signals in the same manner as in conventional gas electron diffraction experiments. From the analyses of the diffraction patterns, geometrical structure of a molecule can be determined. Considering that LAES signals arise only when molecules are interacting with an ultrashort pulsed laser field, the determined geometrical structure can be regarded as “instantaneous structure” only during the femtosecond laser pulse duration. Therefore, if dynamical processes of molecules are induced by femtosecond

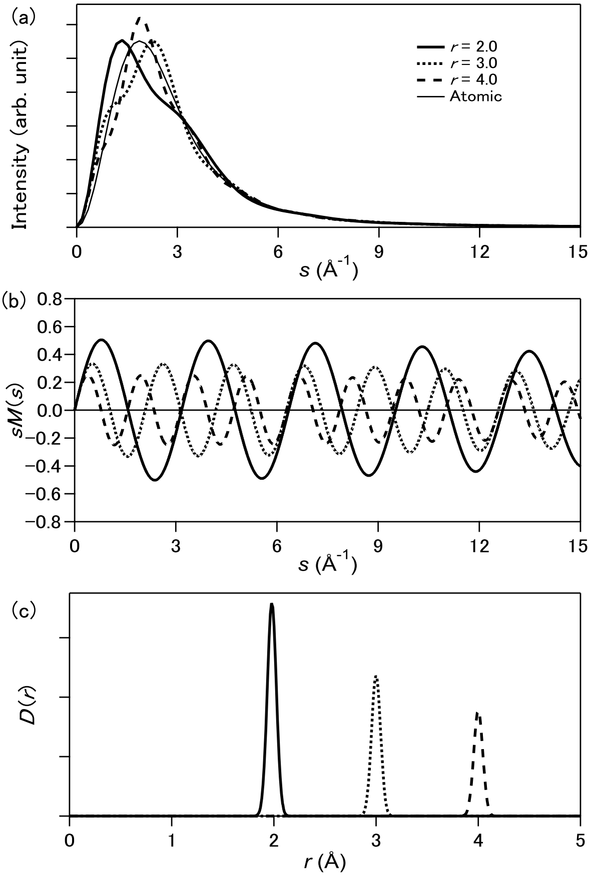

Fig. 1.7 The model calculations of (**a**) scattering intensities, (**b**) $sM(s)$, and (**c**) $D(r)$ of LAES by Cl_2 molecule with the different internuclear distances; $r = 2.0$ Å (*thick solid line*), 3.0 Å (*dotted line*), and 4.0 Å (*broken line*) for the $n = +1$ transition [45]. The mean amplitude is set to be $l_h = 0.044$ Å. Thin *solid line* in (**a**): the atomic scattering intensity of two Cl atoms

pump laser pulses and are probed by the femtosecond LAED method, the temporal resolution of the time-resolved gas electron diffraction will be of the order of femtoseconds, i.e., 10^2–10^3 times higher than ∼1 ps achieved by the previous pulsed gas electron diffraction methods [56].

The feasibility of the proposed LAED method is confirmed by the following numerical calculations. Figure 1.7(a) shows the results of numerical calculations of the scattering intensities of Cl_2 as a function of $s = |\boldsymbol{s}|$ for the $n = +1$ transition of LAES with the three different Cl-Cl internuclear distances; 2.0 Å, 3.0 Å, and 4.0 Å. In the numerical calculations, parameters describing the characteristics of the three beams and their spatiotemporal overlaps are assumed to be the same as in [45]. Through the same procedure as in the conventional gas electron diffraction method [52–54], a modified molecular scattering intensity, $sM(s)$, is obtained as shown in Fig. 1.7(b) from the observed angular distribution, and a radial distribution curve, $D(r)$, can be derived as shown in Fig. 1.7(c) through the Fourier transformation of $sM(s)$.

Fig. 1.8 The angular distributions of the $n = +1$ transition of LAES [57]. *Filled circles*: the observed LAES signals of Xe. *Broken line*: the calculated angular distribution of LAES signals of Xe by KWA. *Solid line*: the calculated angular distribution of LAES signals of CCl_4 by KWA

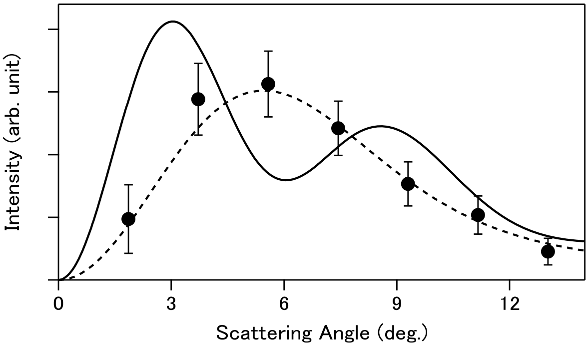

Only the additional approximation in the present procedure is KWA, which holds well for high-energy electron scattering in near-infrared laser fields as long as the dressing effect of targets is neglected. Because molecular structures are determined from the LAES signals in the relatively large scattering angle range, the light-dressing effect, that is expected to appear around the zero scattering angle ($|\boldsymbol{s}| < 0.3$ Å) as seen in Fig. 1.5, could have an only negligibly small effect in the geometrical structure of molecules to be determined. Therefore, correlation between the formation of light-dressed states and the variation of geometrical structure can be investigated by the analysis of the obtained LAED signals.

The solid line in Fig. 1.8 is a calculated angular distribution of the $n = +1$ transition of LAES by CCl_4, where the sample gas density and laser field conditions are assumed to be the same as those in the experiment of Xe [45]. The modulated interference pattern appears in the calculated angular distribution of LAES signals of CCl_4. The comparison between the modulation amplitude in the calculated LAED diffraction pattern of CCl_4 (solid line) and the observed LAES angular distribution of Xe (filled circles with the error bars) shows that the LAED method is applicable to determine geometrical structure of CCl_4. If pump-and-probe experiments are performed, the temporal evolution of the geometrical structure of CCl_4 can be probed by LAED. Therefore, the LAED method will be a promising approach for recording "molecular movies" with femtosecond temporal resolutions.

1.5 Concluding Remarks

In the present paper, recent studies of the LAES experiment in intense laser fields have been reviewed. As possible applications, "probing of light-dressed states in intense laser fields" and "laser-assisted electron diffraction with femtosecond temporal resolution" have been introduced. Considering the recent rapid advances in the technologies of high power and high repetition-rate femtosecond lasers [58–61], the count rate of LAES signals is expected to be raised by several orders of magnitude in the near future.

These experimental techniques of the femtosecond-LAES measurements can also be applied to investigations of other types of laser-assisted phenomena associated with electron inelastic scattering processes. For example, a variety of phenomena originating from electron impact processes occurring in intense laser fields will be used for the investigation of light-dressing effects in electronically-excited states of target atoms and molecules and for developing new time-resolved spectroscopy with femtosecond temporal resolution such as time-resolved electron energy-loss spectroscopy and time-resolved laser-assisted electron momentum spectroscopy [62]. This means that the present femtosecond LAES and femtosecond LAED experiments will guide us to a new class of research themes of electron-atom collision and electron-molecule collision processes in ultrashort intense laser fields.

Acknowledgements The research was supported by the Grant-in-Aid for Specially Promoted Research (Grant No. 19002006), the Grand-in-Aid for Scientific Research (A) (Grant No. 24245003), the Grant-in-Aid for Young Scientists (B) (Grant Nos. 19750003, 24750011), Global COE Program (Chemistry Innovation through Cooperation of Science and Engineering), and Special Coordination Funds for Promoting Science and Technology, from Ministry of Education, Culture, Sports, Science and Technology (MEXT), Japan.

References

1. N.J. Mason, Rep. Prog. Phys. **56**, 1275 (1993)
2. F.V. Bunkin, M.V. Fedorov, Sov. Phys. JETP **22**, 844 (1966)
3. W. Gordon, Z. Phys. **40**, 117 (1926)
4. D.M. Volkov, Z. Phys. **94**, 250 (1935)
5. N.M. Kroll, K.M. Watson, Phys. Rev. A **8**, 804 (1973)
6. A. Jablonski, F. Salvat, C.J. Powell, *NIST Electron Elastic-Scattering Cross-Section Database—Version 3.0* (National Institute of Standards and Technology, 2002)
7. J.I. Gersten, M.H. Mittleman, Phys. Rev. A **13**, 123 (1976)
8. M.H. Mittleman, Phys. Rev. A **14**, 1338 (1976)
9. M.H. Mittleman, Phys. Rev. A **16**, 1549 (1977)
10. M.H. Mittleman, Phys. Rev. A **18**, 685 (1978)
11. B.A. Zon, Sov. Phys. JETP **46**, 65 (1977)
12. E.L. Beilin, B.A. Zon, J. Phys. B **16**, L159 (1983)
13. F.W. Byron-Jr Jr., C.J. Joachain, J. Phys. B **17**, L295 (1984)
14. F.W. Byron-Jr, P. Francken, C.J. Joachain, J. Phys. B **20**, 5487 (1987)
15. F.H.M. Faisal, *Theory of Multiphoton Processes* (Plenum, New York, 1987). Chap. 12.3.4
16. M. Dörr, C.J. Joachain, R.M. Potvliege, S. Vučić, Phys. Rev. A **49**, 4852 (1994)
17. P.G. Burke, P. Francken, C.J. Joachain, J. Phys. B **24**, 761 (1991)
18. M. Terao-Dunseath, K.M. Dunseath, J. Phys. B **35**, 125 (2002)
19. A. Cionga, L. Dimou, F.H.M. Faisal, J. Phys. B **30**, L361 (1997)
20. F. Ehlotzky, A. Jaroń, J.Z. Kamiński, Phys. Rep. **297**, 63 (1998)
21. D. Andrick, L. Langhans, J. Phys. B **9**, L459 (1976)
22. A. Weingartshofer, J.K. Holmes, G. Caudle, E.M. Clarke, H. Krüger, Phys. Rev. Lett. **39**, 269 (1977)
23. A. Weingartshofer, C. Jung, in *Multiphoton Ionization of Atoms*, ed. by S.L. Chin, P. Lambropoulos (Academic Press, New York, 1984), p. 155
24. D. Andrick, L. Langhans, J. Phys. B **11**, 2355 (1978)
25. L. Langhans, J. Phys. B **11**, 2361 (1978)
26. D. Andrick, H. Bader, J. Phys. B **17**, 4549 (1984)
27. H. Bader, J. Phys. B **19**, 2177 (1986)
28. A. Weingartshofer, E.M. Clarke, J.K. Holmes, C. Jung, Phys. Rev. A **19**, 2371 (1979)

29. A. Weingartshofer, J.K. Holmes, J. Sabbagh, S.L. Chin, J. Phys. B **16**, 1805 (1983)
30. B. Wallbank, V.W. Connors, J.K. Holmes, A. Weingartshofer, J. Phys. B **20**, L833 (1987)
31. B. Wallbank, J.K. Holmes, A. Weingartshofer, J. Phys. B **20**, 6121 (1987)
32. B. Wallbank, J.K. Holmes, S.C. MacIsaac, A. Weingartshofer, J. Phys. B **25**, 1265 (1992)
33. B. Wallbank, J.K. Holmes, Phys. Rev. A **48**, R2515 (1993)
34. B. Wallbank, J.K. Holmes, J. Phys. B **27**, 1221 (1994)
35. B. Wallbank, J.K. Holmes, J. Phys. B **27**, 5405 (1994)
36. B. Wallbank, J.K. Holmes, J. Phys. B **29**, 5881 (1996)
37. B. Wallbank, J.K. Holmes, Can. J. Phys. **79**, 1237 (2001)
38. D. Nehari, J. Holmes, K.M. Dunseath, M. Terao-Dunseath, J. Phys. B **43**, 025203 (2010)
39. H. Bader, J. Phys. B **18**, 235 (1985)
40. I. Rabadán, L. Méndez, A.S. Dickinson, J. Phys. B **27**, L535 (1994)
41. S. Geltman, Phys. Rev. A **51**, R34 (1995)
42. S. Varró, F. Ehlotzky, Phys. Lett. A **203**, 203 (1995)
43. I.V. Hertel, W. Stoll, in *Proc. Int. Conf. Phys. Electron. At. Coll., 7th* (1973), p. 321
44. I.V. Hertel, W. Stoll, Adv. At. Mol. Phys. **13**, 113 (1978)
45. R. Kanya, Y. Morimoto, K. Yamanouchi, Phys. Rev. Lett. **105**, 123202 (2010)
46. R. Kanya, Y. Morimoto, K. Yamanouchi, Rev. Sci. Instrum. **82**, 123105 (2011)
47. B.A. deHarak, L. Ladino, K.B. MacAdam, N.L.S. Martin, Phys. Rev. A **83**, 022706 (2011)
48. J.C. Williamson, A.H. Zewail, Chem. Phys. Lett. **209**, 10 (1993)
49. F. Toffoletto, R.C.G. Leckey, J.D. Riley, Nucl. Instrum. Meth. Phys. Res. B **12**, 282 (1985)
50. R. Kanya, Y. Morimoto, K. Yamanouchi unpublished data
51. D.M. Bishop, Adv. Quantum Chem. **25**, 1 (1994)
52. K. Yamanouchi, M. Sugie, H. Takeo, C. Matsumura, K. Kuchitsu, J. Phys. Chem. **88**, 2315 (1984)
53. I. Hargittai, M. Hargittai (eds.), *Stereochemical Applications of Gas-Phase Electron Diffraction, Part A* (Wiley, New York, 1988)
54. K. Yamanouchi, *Quantum Mechanics of Molecular Structures* (Springer, Heidelberg, 2012)
55. R. Srinivasan, V.A. Lobastov, C. Ruan, A.H. Zewail, Helv. Chim. Acta **86**, 1761 (2003)
56. H. Ihee, V.A. Lobastov, U.M. Gomez, B.M. Goodson, R. Srinivasan, C.Y. Ruan, A.H. Zewail, Science **291**, 458 (2001)
57. R. Kanya, Y. Morimoto, K. Yamanouchi, Laser-assisted electron scattering and its application to laser-assisted electron diffraction of molecules in femtosecond intense laser fields, in *Multiphoton Processes and Attosecond Physics*, ed. by K. Yamanouchi, K. Midorikawa (Springer, Berlin, 2012), p. 351
58. F. Röser, D. Schimpf, O. Schmidt, B. Ortaç, K. Rademaker, J. Limpert, A. Tünnermann, Opt. Lett. **32**, 2230 (2007)
59. J. Limpert, F. Röser, T. Schreiber, A. Tünnermann, IEEE J. Sel. Top. Quantum Electron. **12**, 233 (2006)
60. J. Limpert, F. Röser, D.N. Schimpf, E. Seise, T. Eidam, S. Hädrich, J. Rothhardt, C.J. Misas, A. Tünnermann, IEEE J. Sel. Top. Quantum Electron. **15**, 159 (2009)
61. C.R.E. Baer, O.H. Heckl, C.J. Saraceno, C. Schriber, C. Kränkel, T. Südmeyer, U. Keller, Opt. Express **20**, 7054 (2012)
62. K.A. Kouzakov, Y.V. Popov, M. Takahashi, Phys. Rev. A **82**, 023410 (2010)

Chapter 2
Electron Localization in Hydrogen

Giuseppe Sansone, Francesca Calegari, and Mauro Nisoli

Abstract The control of the electronic motion inside a molecule by a light pulse is an ambitious goal with important implications for the steering in real time of the outcome of a chemical reaction. In femtochemistry, the unfolding of a reaction (for example the dissociation of a bound molecule) can be controlled by applying a femtosecond pulse whose envelope and frequency variations can be controlled and modified by using well established pulse shaping techniques. Technological breakthroughs over the last years have made available a new strategy for steering the dynamics of a bound electron wave packet based on the precise control of the electric field waveform rather than of its instantaneous frequency. In particular few-cycle pulses with a reproducible electric field have been demonstrated and applied to different strong field experiments and, in particular, to the generation of isolated attosecond pulses, which can trigger a reaction on a timescale shorter or comparable to the typical timescale of the electronic dynamics. The combination of field controlled few femtosecond pulses and attosecond XUV light bursts allows one to control with unprecedented temporal resolution the unfolding of ultrafast dynamics occurring in small molecules. As examples, we will review few experiments performed in hydrogen and deuterium based on single (intense IR few-cycle pulse) or two pulses (intense IR few-cycle pulses and isolated or train of attosecond pulses) in which the control of the electron localization during the dissociation of the molecular ion (H_2^+/D_2^+) was achieved. The experiments show that different mechanisms can be involved in the localization process unveiling the rich attosecond and femtosecond dynamics occurring in light molecules.

G. Sansone (✉) · M. Nisoli
Dipartimento di Fisica Politecnico, Piazza Leonardo da Vinci 32, 20133, Milan, Italy
e-mail: giuseppe.sansone@polimi.it

F. Calegari
CNR-IFN, Dipartimento di Fisica Politecnico, Piazza Leonardo da Vinci 32, 20133, Milan, Italy

K. Yamanouchi et al. (eds.), *Progress in Ultrafast Intense Laser Science X*,
Springer Series in Chemical Physics 106, DOI 10.1007/978-3-319-00521-8_2,

2.1 Introduction

A chemical reaction occurring in a molecule (for example dissociation, formation of a chemical bond, etc.) involves the motion of the nuclei in the landscape of the potential energy surfaces determined by the electronic configuration of the system. As such the typical timescale for a chemical reaction is in the femtosecond domain, even though the basic steps that govern the electronic dynamics occur in the attosecond regime. The application of femtosecond pulses has allowed the control of chemical reactions by controlling the coupling among different potential energy surfaces through a precise shaping of the pulse envelope $A(t)$ and the instantaneous frequency of the field $\omega(t) = \mathrm{d}\phi/\mathrm{d}t$, where $\phi(t)$ indicates the temporal phase of the pulse. In this strategy the combination of more pulses with a well defined phase relation (i.e. with a well defined delay) offers an additional tool for influencing the reaction during its unfolding. Recently, the development of few-cycle pulses with a well controlled electric field waveform [1] and the combination of few-cycle pulses in different spectral intervals [2] has opened the way to a new strategy for controlling the electronic motion based on the application of well defined and controllable electric fields. Such waveforms determine a control that relies on the temporal phase of the field $\phi(t)$ rather than on its time derivative $\omega(t)$ as usually performed in femtochemistry. The control of the electric field form corresponds to the control of the so called carrier-envelope phase (CEP), i.e. the temporal offset between the oscillations of the carrier wave (usually in the visible or infrared (IR) region) and the envelope of the pulse. At the same time the availability of CEP-controlled few-cycle pulses has pushed the frontier of ultrashort pulses down to the sub-femtosecond domain leading to the generation of bursts of light lasting only few tens of attoseconds, which can be used to trigger or monitor electronic dynamics on their typical timescale. The combination of attosecond pulses with field controlled few-femtosecond pulses offers an unprecedented temporal resolution in the control of the electronic motion which could play a key role for steering chemical reactions, that naturally evolve on a slower timescale.

2.2 Hydrogen Under Extreme Laser Fields

The investigation of molecular dynamics under extreme field conditions (ultrashort and intense pulses) has widely considered hydrogen as a benchmark for studying the fundamental processes at the basis of more complex mechanisms in larger molecules. Due to the presence of only two electrons, hydrogen represents the most simple system for studying the interplay between electronic correlation and nuclear motion. The dynamics of H_2 and H_2^+ was extensively investigated using femtosecond laser pulses [3, 4] and can be described in terms of laser dressed states, corresponding to single-photon or multi-photon couplings induced by the laser field among the different field-free potential energy curves of the molecule. Using this description several process such as laser induced dissociation (bond softening) [5]

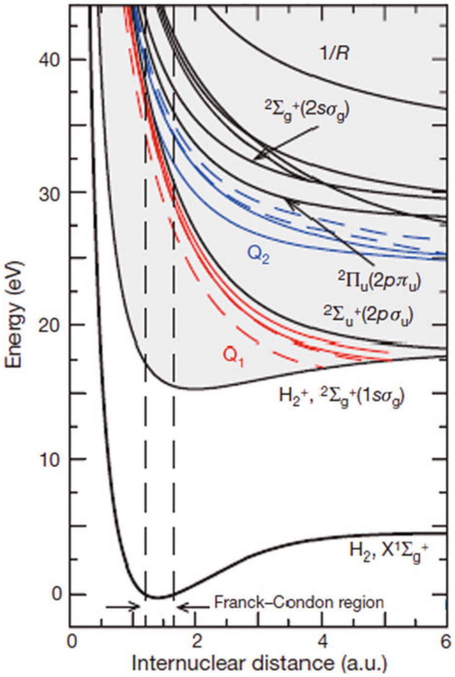

Fig. 2.1 Relevant energy levels of the neutral molecules H_2 (D_2) and of the molecular ion H_2^+ (D_2^+). The *vertical dashed lines* indicate the Franck-Condon region

and laser induced bond hardening [6] have been interpreted in terms of laser-induced coupling between the ground state $1s\sigma_g$ and the first excited state $2p\sigma_u$ of the molecular ion H_2^+ (see level scheme in Fig. 2.1).

The interaction of hydrogen with extreme ultraviolet (XUV) or X-ray photons can lead to dissociative ionization of the molecule and, eventually, to a complete break-up of the molecule as measured by Weber et al. [7], that reported a kinematically complete experiment on the photoionization and subsequent dissociation of hydrogen. The interaction of hydrogen with vacuum ultraviolet and soft X-ray radiation can also lead to the excitation of doubly excited resonances, that play a relevant role in the dissociation and ionization of the molecule. The investigation of the dynamics of these states allows one to obtain crucial information about electronic correlation. The dynamics associated to doubly excited states is on the order of few femtoseconds [8], making the time-resolved investigation of the corresponding motion one of the most ambitious aim of attosecond molecular dynamics.

In this contribution we will show how field-controlled few-cycle IR pulses and attosecond XUV pulses can be combined, or independently applied, to steer the electronic motion during the unfolding of a fundamental chemical reaction (dissociation of the molecular ion H_2^+). These experiments could be regarded as the first fundamental step of strategies aiming to steer chemical processes by controlling in real time the multi-electron wave-function of the molecule. In these pioneering experiments the control in time of the electronic motion is demonstrated by influencing the final emission direction of the ion released in the molecular dissociation, corresponding to the electron localization on the atom released in the opposite direction.

Different parameters such as the CEP, φ, of the few-cycle pulses and the pulse delay, τ, between the pump and probe pulses have been used as control tools. In Sect. 2.3 we will introduce the mathematical description underlying the localization process; the experiments (performed by various research groups) based on a single pulse or two-pulse scheme will be reviewed in Sects. 2.4 and 2.5, respectively.

2.3 Mathematical Description of the Electronic Localization

The localization of the bound electron in the molecular ions H_2^+ or D_2^+ corresponds to the creation of a coherent superposition of states characterized by different parity, ϕ_u and ϕ_g, where the subscripts u and g indicate the ungerade and gerade characters of the wave functions, respectively. The initial ionization of H_2 (D_2) can be performed using a few-cycle pulse with a well defined electric field evolution (i.e. CEP-stabilized) or attosecond pulses, in the form of a train of pulses, or of an isolated pulse 164. The wave function after the ionization step can be described as [9, 10]:

$$\begin{aligned}\Phi(1,2) = {} & c_1\big[\phi_g(1)\varepsilon l_g(2)\big]_g + c_2\big[\phi_g(1)\varepsilon l_u(2)\big]_u \\ & + c_3\big[\phi_u(1)\varepsilon l_u(2)\big]_g + c_4\big[\phi_u(1)\varepsilon l_g(2)\big]_u \qquad (2.1)\end{aligned}$$

where the variables 1 and 2 refer to the two electrons and the anti symmetrization operator has been omitted for the sake of clarity. The electron emitted in the continuum is described by a wave-function of energy ε and angular momentum $l_{g,u}$. The coefficients c_i characterize the amplitudes and phases of the four terms.

In general the interaction with the laser field can lead to the population of different states either of the molecular ions or of the neutral molecule. In particular, the ground and first excited states of the molecular ion, $1s\sigma_g$ and $2p\sigma_u$, can be populated by IR strong field photoionization and by the subsequent recollision of the ionized electronic wave packet with the parent ion. In the case of XUV radiation, the $1s\sigma_g$ state can be populated for photon energy $\hbar\omega > 18.1$ eV. For higher photon energies doubly excited state of the Q_1 series can be accessed up to the $2p\sigma_u$ state, which represent the limit of the Q_1 branch for highly excited states of the neutral molecule. For even higher energies doubly excited states of the Q_2 branch can also be populated. The relevant levels of the neutral and ionic molecule are shown in Fig. 2.1.

The position of the electron in the excited/ionized molecule can be controlled by a few-cycle pulse with stable CEP; this pulse can be represented by the trailing edge of the same pulse that ionized the molecule (single-pulse experiment), or by a second synchronized pulse with a variable temporal delay τ (two-pulse experiment). In the second case, the separation of the ionization step from the control one gives an additional degree of freedom for steering the electron position. In both approaches the control pulse induces a coupling between states of different symmetry, corresponding to a localization of the electron in the bound system:

$$\phi_{L,R} = \frac{1}{\sqrt{2}}(\phi_g \pm \phi_u) \qquad (2.2)$$

where the subscripts L and R indicate an electron localized on the left and right nuclei with respect to the polarization direction of the excitation pulse, respectively. The observation of the electron localization relies on the measurement of the emission direction of the ion resulting from the molecular dissociation, which freezes the motion of the electron wave packet when the distance between the two nuclei is too large. The ion-electron wave function of the molecular ion can be written as:

$$\Psi(R,t) = \psi_g(R,t)\phi_g(R) + \psi_u(R,t)\phi_u(R) \tag{2.3}$$

with R the internuclear distance and t the time. The electronic wave functions $\phi_{g,u}$ depend parametrically on R. $\psi_g(R,t)$ and $\psi_u(R,t)$ are functions describing the nuclear wave-packet on the two laser-coupled Born-Oppenheimer potential curves associated with the $1s\sigma_g$ and the $2p\sigma_u$ of $\mathrm{H}_2^+/\mathrm{D}_2^+$, respectively. We can therefore define the localized nuclear wave-functions ψ_L and ψ_R given by:

$$\psi_{L,R} = \frac{1}{\sqrt{2}}(\psi_g \pm \psi_u) \tag{2.4}$$

that represent states associated to the localized electron wave functions $\phi_{L,R}$.

From the experimental point of view, the asymmetry can be characterized by measuring the direction of the emitted ions and quantified through the asymmetry parameter:

$$A = \frac{N_L - N_R}{N_L + N_R} \tag{2.5}$$

where N_L and N_R indicate the number of ions emitted in the left and right directions, respectively. In general the asymmetry parameter could depend on the kinetic energy of the emitted ion (E_k) and on the CEP of the driving pulse (φ) for the single color experiment $A(E_k,\varphi)$, or on the CEP and on the temporal delay τ between the pump and probe pulses in the case of two-color experiments $A(E_k,\varphi,\tau)$. As the localization corresponds to the projection of the total wave function on localized states of the bound electron:

$$\begin{gathered} \langle \Phi_{L,i}(1,2) \mid \Phi(1,2)\rangle \\ \langle \Phi_{R,i}(1,2) \mid \Phi(1,2)\rangle \end{gathered} \tag{2.6}$$

(with $i = g, u$), the difference in the emission direction of the ions can be finally expressed as:

$$N_L - N_R = 4\mathrm{Re}\left[c_1 c_4^* + c_2 c_3^*\right] \tag{2.7}$$

2.4 Experiments in Hydrogen by CEP Stabilized Laser Pulses

The first experimental demonstration of electron localization was reported in 2006 using CEP stabilized IR few-cycle pulses that allowed one to expose the molecule to steep field gradients, which are reproduced from shot to shot [11]. In this pioneering experiment, Kling et al. reported on the control of the electron localization in a

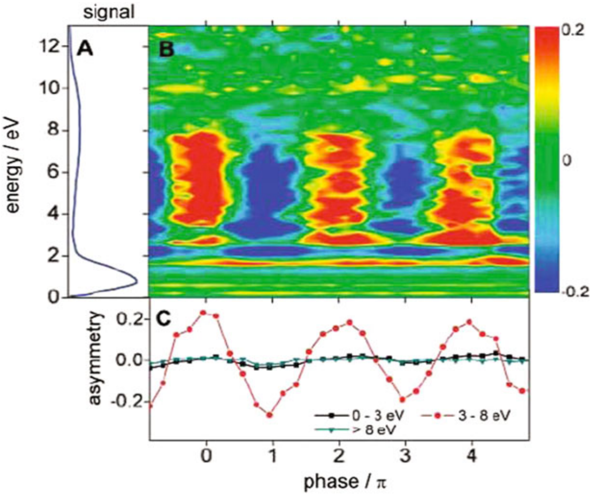

Fig. 2.2 Integrated ion yield as a function of the KER (**a**). Asymmetry evolution as a function of the CEP φ (**b**). Integrated asymmetry signal over the KER ranges 0–3 eV (*black line*), 3–8 eV (*red line*) and >8 eV (*green line*) (**c**). Reprinted with permission from Ref. [11]

D_2^+ molecular ion formed by strong field ionization. The steering of the electronic motion was demonstrated by characterizing the emission direction of the D^+ ion released in the molecular dissociation of the D_2^+ ion. The CEP was used to vary the asymmetry parameter for ion with kinetic energy in the range between 4 and 10 eV as shown in Fig. 2.2. The observation of an asymmetry implies that the few-cycle electric field couples the population of states with different symmetry localizing the electron on one of the two nuclei. In D_2^+ such states are given by the bound ground state of the molecular ion, $1s\sigma_g$ state, and by the dissociating excited state, $2p\sigma_u$.

In the experiment the photo-ionization step and the control of the electronic motion were linked as a single few-cycle pulse was used. In this scheme the intense few-cycle pulse ionizes the D_2 molecule thus producing a D_2^+ ion in the fundamental $1s\sigma_g$ state. As the pulse comprises only few oscillations of the optical field, strong field ionization is confined to the half-cycle corresponding to the peak of the pulse envelope. The released photoelectron wave-packet can be driven back to the parent molecule when the electric field changes sign and, upon recollision, can excite the remaining electron from the ground state to the excited state $2p\sigma_u$ thus triggering the molecular dissociation. The trailing edge of the IR pulse can couple the $2p\sigma_u$ and the $1s\sigma_g$ transferring population between these two states, corresponding to the creation of a coherent superposition of states. When the distance between the two nuclei increases, the electron wave-packet is trapped and the localization is frozen. Upon changing the CEP, the site and the degree of localization can be controlled.

Further experiments were performed by Kremer et al. [12] that reported on a kinematically complete experiment on H_2 using 6 fs CEP-controlled pulses. The authors measured in coincidence the photoionized electron and the emitted H^+ ion gaining access to the direction of the molecular orientation with respect to the laser polarization and to the emission direction of the electron with respect

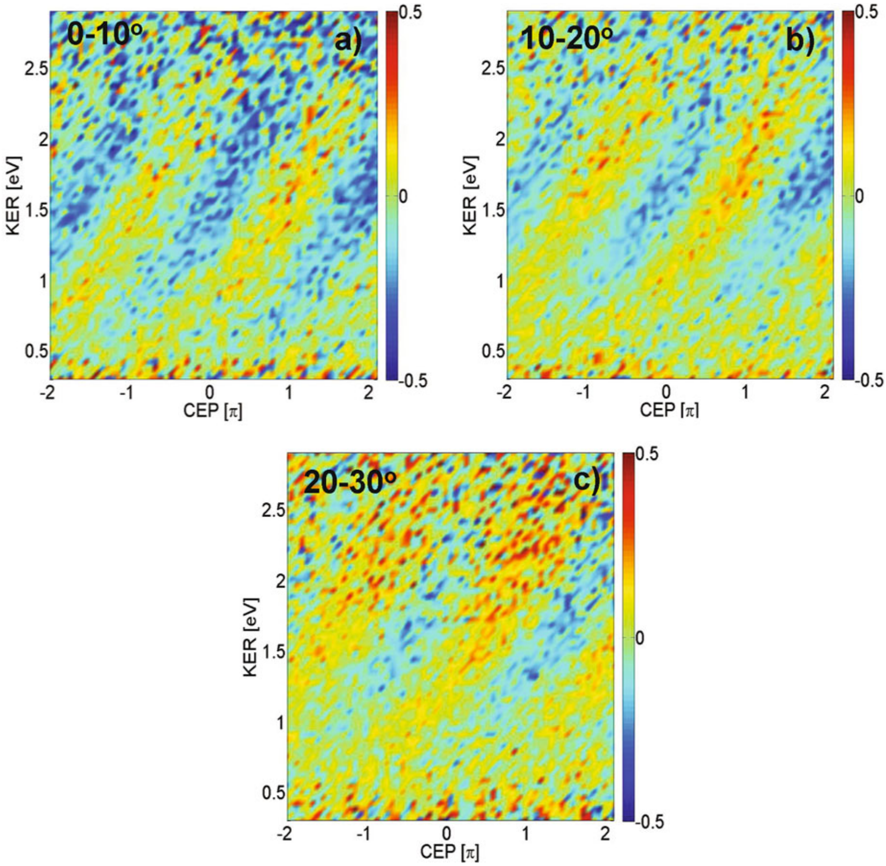

Fig. 2.3 Asymmetry map as a function of the CEP φ for different angle intervals α between the electric field and the molecular axis: $0° < \alpha < 10°$ (**a**), $10° < \alpha < 20°$ (**b**), $20° < \alpha < 30°$ (**c**). Courtesy of R. Moshammer

to the ion. An asymmetry oscillation in the range 0–3 eV characterized by a dependence on the energy and on the CEP was observed. These features were not observed in Ref. [11]. Moreover a shift of the asymmetry stripes as a function of the angle between the molecular axis and the laser polarization was reported as shown in Fig. 2.3. The physical mechanism inducing the electron localization is different from the one introduced in Ref. [11] as the low kinetic energy release (KER) of the fragments indicates that a bond softening mechanism is involved in the process. The laser pulse ionizes the molecule launching a bound nuclear wave-packet on the bound $1s\sigma_g$ state that moves outward reaching a distance where laser-induced coupling with the first excited state can occur. Simulations indicate that the coupling determines an asymmetry in the range between 0 and 2 eV, well matching the energy range observed in the measurements. The coincidence measurement of electron and ion originating from the same molecule allows one to investigate the interplay between the initial ionization step and the subsequent localization mechanism. In the experiment the asymmetry parameter for the photoionized electron was estimated for two different KER ranges (see Fig. 3c of Ref. [12]). No clear dependence of the asymmetry was visible indicating that the initial ionization step is not directly related to the subsequent dissociation of the molecule.

Znakovskaya et al. [13] extended the investigation of the control of electronic motion in D_2 to the mid-IR region. Using a CEP-stabilized pulse whose optical cycle is closer to the typical timescale of the molecular ion dynamics, a better control on the electron localization can be achieved and different mechanisms leading to the creation of the coherent superposition of states after the initial strong field photoionization can be evidenced. In this experiment both channels (IR-coupling of the initially populated $1s\sigma_g$ state with the $2p\sigma_u$ state and recollisional excitation from the $1s\sigma_g$ to the $2p\sigma_u$) responsible for the electronic localization were observed simultaneously. As the two mechanisms lead to the emission of ions with different kinetic energies a complex energy-CEP evolution of the asymmetry parameter was experimentally observed (as shown in Fig. 2.4).

2.5 Two-Pulse Experiment

2.5.1 CEP Controlled Pulses

Fischer et al. [14] performed a pump-probe experiment introducing a variable delay τ between the ionizing pulse (pump) and the controlling pulse (probe), thus separating the creation of the molecular ion from the steering of the electronic wave-packet. The first pulse ionizes the H_2 molecule launching a wave-packet on the ground state potential curve that oscillates with a period of about 18 fs. The probe pulse leads to molecular dissociation through a bond softening mechanism indicating an effective coupling between the $1s\sigma_g$ and $2p\sigma_u$.

The low KER of the ions presents oscillations corresponding to the periodic motion of the nuclear wave-packet in the potential well. The asymmetry parameter was estimated as a function of the CEP φ and of the delay τ; the results are presented in Fig. 2.5 and indicate a complex dependence on τ in the range 0.8–1.2 eV and an almost constant asymmetry in the range 1.6–2 eV. These observations suggest that different mechanisms are responsible for the electron localization in the two KER ranges. The coupling between the initially populated $1s\sigma_g$ and $2p\sigma_u$ can proceed through three different channels involving one photon (1ω channel), two photons (2ω channel) and three photons (3ω channel). In the 1ω channel case the coupling occurs at rather large internuclear distance R when the potential energy curves of the two states are spaced by the energy of a single IR photon. For the other channels, the coupling between the two states is produced by the absorption of three photons (3ω), that can be eventually followed by the emission of a photon, resulting

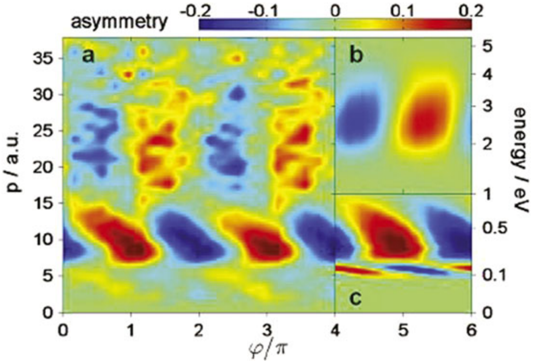

Fig. 2.4 (**a**) Asymmetry map as a function of the fragment momentum (corresponding kinetic energy scale on the right) and CEP s of the D^+ ion emission. (**b**) Asymmetry associated to the recollision excitation channel from the $1s\sigma_g$ to the $2p\sigma_u$ state. (**c**) Same as (**b**) for the bond softening channel. Reprinted with permission from Ref. [13]. Copyright (2012) by the American Physical Society

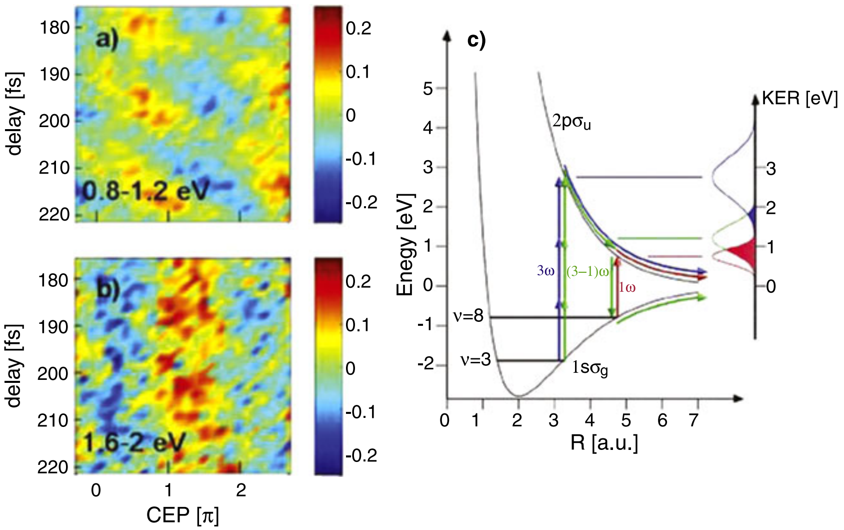

Fig. 2.5 Asymmetry map as a function of the delay and the CEP for the wave packet revival region for a KER between 0.8–1.2 eV (**a**) and between 1.6–2 (**b**). Adapted from Ref. [14]. Illustration of the three photons (3ω *blue arrows*), two photons ((3–1)ω *green arrows*) and one photon (1ω *red arrow*) dissociation channels involving the $\nu = 8$ and $\nu = 3$ vibrational states (**c**). KERs corresponding to the three channels are shown on the right; localization occurs for overlapping contributions of different symmetry (indicated by the *shaded areas*). Reprinted with permission from Ref. [14]. Copyright (2010) by the American Physical Society

in the net absorption of two photons (2ω). Due to the large bandwidth of the IR pulse, these three dissociation pathways can overlap leading to different qualitative behavior as a function of the delay τ. Whereas the contrast of the asymmetry is determined by the relative population of the $1s\sigma_g$ and $2p\sigma_u$ states, the shift of the asymmetry stripes depends on the relative phases of the two states:

$$\Delta\varphi = \varphi_g - \varphi_u \tag{2.8}$$

The phase can be expressed as a term depending on the time delay τ and a term depending on the CEP φ and the KER that can be different depending on the number of IR photons involved. These transitions will mainly select those vibrational states contributing to the bound wave packet oscillating on the $1s\sigma_g$ curve that are resonant with one or three IR photons transitions. These states are the $\nu = 8$ vibrational level for the 2ω and 3ω channels and the $\nu = 3$ for the 1ω channel. The three terms can be therefore expressed as:

$$\begin{aligned}
\varphi_u^{1\omega} &= \varphi_i^{\nu=8}(\tau) + \varphi_{ATD}^{1\omega}(\varphi, E_k) \\
\varphi_g^{2\omega} &= \varphi_i^{\nu=3}(\tau) + \varphi_{ATD}^{2\omega}(\varphi, E_k) \\
\varphi_u^{3\omega} &= \varphi_i^{\nu=3}(\tau) + \varphi_{ATD}^{3\omega}(\varphi, E_k)
\end{aligned} \tag{2.9}$$

where the terms $= \varphi_i^{\nu=3,8}(\tau)$ and $\varphi_A T D^{1,2,3\omega}$ indicate the delay-dependent and channels-dependent phase contributions, respectively. The interference between the 2ω and 3ω channels involves the same vibrational level and it is therefore independent from the time delay τ. On the other hand the interference at low KER involves the contributions of the 1ω and 2ω channels that start from different vibrational levels thus leading to a delay-dependence of the phase difference as observed in the experiment and in the simulation.

2.5.2 Experiments in Hydrogen by Isolated and Trains of Attosecond Pulses

The combination of trains or isolated attosecond pulses and a synchronized intense IR pulse allows one to disentangle the photoionization step from the control step offering a higher degree of control on the electronic dynamics. Moreover, differently from the case of strong-field photoionization, absorption of an XUV photon can lead to the excitation of doubly excited states, thus giving the possibility to investigate the influence of electronic correlation on the creation of the coherent superposition of states.

Attosecond pulse trains generated by an intense femtosecond pulse are spaced by half the optical cycle of the IR field. These pulses create electron and nuclear wave-packets that experience different phases of the IR field, as a π phase variation in the field oscillation occurs between ionization events triggered by consecutive attosecond pulses. As the localization mechanisms is based on the precise evolution of the electric field oscillations, it is questionable the possibility to use attosecond pulse trains in combination with IR pulses to control charge localization in H_2/D_2. This problem was overcome by Singh et al. by using a train of attosecond pulses composed by even and odd harmonics of the fundamental radiation synthesized by

Table 2.1 H^+ dissociation channels

	18.1–25 eV	25–30 eV	30–38 eV	38–45 eV
$1s\sigma_g$	<1 eV	<1 eV	<1 eV	<1 eV
$2p\sigma_u$	–	2–6 eV	4–10 eV	5–10 eV
$Q_1\ {}^1\Sigma_u^+(1) \rightarrow 1s\sigma_g$	–	2–6 eV	x	x
$Q_2\ {}^1\Sigma_u^+(1) \rightarrow 1s\sigma_g$	–	–	x	x
$Q_2\ {}^1\Sigma_u^+(1) \rightarrow 2p\sigma_u$	–	–	4–10 eV	x

⁻energetically not allowed

ˣnot identified or with vanishing contribution

First row: XUV photon energy

First column: ionic/neutral state; for the doubly excited stats, the decay channel is reported

the superposition of two $\omega - 2\omega$ fields [15, 16]. Due to the symmetry breaking, an attosecond pulse is generated each cycle of the fundamental field. Therefore the ionization events induced by the single attosecond pulse is followed by the same electric field evolution (at least in the limit case of long pulses). The signature of the electron localization was evidenced by measuring the emission direction of the D^+ ions released in the molecular dissociation after the ionization event that created the D_2^+ molecular ion. The harmonic field used in the experiment consisted of the superposition of the harmonics from the 11th up to the 17th. The photon energy of the harmonic field can ionize the D_2 molecule projecting the nuclear wave-packet on a vibrational level of the ground state $1s\sigma_g$ as shown in Fig. 2.1; the excess energy is carried by the emitted photoelectron. Photoionization to the $2p\sigma_u$ state requires an energy of $\hbar\omega = 25$ eV in the Franck Condon region (see Tables 2.1, 2.2) and this state can not be directly populated. A rather weak IR pulse ($I = 10^{13}$ W/cm^2) was used to control the electron localization in the D_2^+ molecular ion created by the attosecond pulse trains. The nuclear wavepacket on the $1s\sigma_g$ oscillates with a timescale of few femtoseconds (14 fs for H_2 and 22 fs for D_2). When the wavepacket reaches the outer turning point of the potential curve, the bond can be softened by the action of the IR and the molecule can dissociate leading to the emission of a neutral D and an ion D^+. The mechanism of bond softening can be described in terms of the undressed energy curves $1s\sigma_g$ and $2p\sigma_u$ that are coupled by the IR field transferring population from the initial populated $1s\sigma_g$ curve to the upper state, thus determining a localization mechanism similar to the single CEP-stabilized pulse experiment discussed in [14]. The dependence of the asymmetry parameter on the relative delay between the attosecond pulse trains and the IR field is shown in Fig. 2.6 and indicates a peak-to-peak contrast of 5 % It is important to point out that every cycle of the IR field a nuclear wave-packet is launched along the $1s\sigma_g$ curve. The overall asymmetry, therefore, is the result of the interference among successively launched wave packets. The good agreement between the experimental data and a simple two-level model including only a single ionization event by an isolated attosecond pulse suggests that such effects could be neglected.

Table 2.2 D^+ dissociation channels

	18.1–25 eV	25–30 eV	30–38 eV	38–45 eV
$1s\sigma_g$	$<$1 eV	$<$1 eV	$<$1 eV	$<$1 eV
$2p\sigma_u$	–	4–6 eV	4–10 eV	5–10 eV
$Q_1\ {}^1\Sigma_u^+(1) \rightarrow 1s\sigma_g$	–	2–5 eV	2–5 eV	x
$Q_2\ {}^1\Sigma_u^+(1) \rightarrow 1s\sigma_g$	–	–	x	x
$Q_2\ {}^1\Sigma_u^+(1) \rightarrow 2p\sigma_u$	–	–	4–10 eV	x

[–] energetically not allowed

[x] not identified or with vanishing contribution

First row: XUV photon energy

First column: ionic/neutral state; for the doubly excited stats, the decay channel is reported

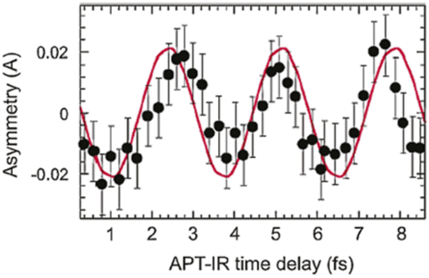

Fig. 2.6 Asymmetry parameter A as a function of the time delay between the attosecond pulse train and the IR field. The *black circles* indicate the experimental data with the corresponding experimental error. The *red solid line* represents the theoretical prediction obtained solving the two-level time-dependent Schrödinger equation. Reprinted with permission from Ref. [16]. Copyright (2010) by the American Physical Society

A more complex localization dynamics was investigated by Sansone et al. by using an isolated attosecond pulse and a CEP-stabilized IR pulse [17]. The isolated attosecond pulses were produced by the Polarization Gating (PG) method [18–20] focusing a CEP-stabilized few-cycle IR pulse in krypton in order to generate XUV photons that can directly photoionize the molecule to the ground state $1s\sigma_g$ and to the first excited state $2p\sigma_u$. The XUV spectrum can populate also the Q_1 and Q_2 series of doubly excited states; it is important to point out that the relevance of these states in single color experiment based on the initial strong-field photoionization of the molecule has not been reported. Higher lying molecular ion states, such as, the $2p\pi_u$ state can also be populated in the Franck-Condon region considering the extension of the XUV spectrum (up to 45 eV). Due to the large bandwidth of the isolated attosecond pulse, several mechanisms can lead to the formation of H^+/D^+ ion. All components above 18.1 eV can lead to the formation of a molecular ion either in the ground state ($\hbar\omega > 18.1$ eV) or in the first excited state $2p\sigma_u$ ($\hbar\omega > 25$ eV). For photon energy larger than 30 eV also the excited state $2p\pi_u$ can be

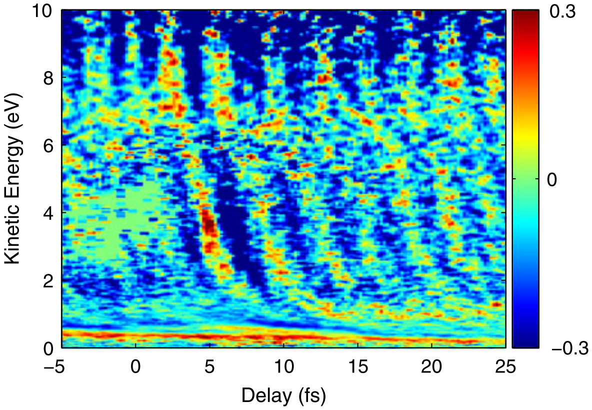

Fig. 2.7 Asymmetry map as a function of the delay τ between the isolated attosecond pulse and the synchronized CEP-stabilized pulse. Adapted from Ref. [17]

reached. Autoionizing states belonging to the Q_1 and Q_2 series can also contribute to the formation of ions. In this process the initial double excitation of the electronic wave-packet, triggers the dissociation of the nuclear wave-packet along the repulsive energy curves of the Q_1 and Q_2 series until autoionization occurs and the nuclear wave-packet is projected onto the $1s\sigma_g$ state (for the Q_1 and Q_2 states) or the $2p\sigma_u$ state (for the Q_2 state). These dissociation mechanisms lead to different KERs and are summarized in Table 2.1 for H_2 and Table 2.2 for D_2 that report the most relevant paths associated to parallel transitions.

The kinetic and angular distributions of the H^+ and D^+ ions were measured using a velocity map imaging spectrometer for different delays between the isolated attosecond pulse and the synchronized IR pulse. The asymmetry parameter was determined considering those ions emitted along the laser polarization direction in an angle of ±30°. The asymmetry map presented in Fig. 2.7 shows a complex pattern characterized by a dependence on the delay τ and the ion kinetic energy and oscillates with a period given by the optical field period T_0. The measurements clearly indicate that the use of a CEP-stabilized pulse allows one to control the direction in which the electron will be emitted when dissociation has completed. Due to the large bandwidth of the XUV pulses, different mechanisms can lead to the coupling of states of different parity. In particular two main processes were identified:

(1) The first one closely resembles the mechanism invoked to interpret the results of [11] and is based on the IR-induced coupling between the $2p\sigma_u$ and $1s\sigma_g$ states when molecular dissociation occurs. In this mechanism the initial wave-packet dissociates along the $2p\sigma_u$ state and the IR field arriving after the XUV pulse couples this state with the $1s\sigma_g$ giving origin to the electron localization. This mechanism characterizes the asymmetry evolution when the IR pulse arrives after the XUV.

(2) The second localization process characterizes the asymmetry around the delay $\tau = 0$ (i.e. for temporally overlapping pulses) and involves the autoionizing states of the Q_1 series. Without IR field the XUV pulse can ionize the molecule to the $2p\sigma_u$ leading to the emission of an electron characterized by an s-wave. At the same time the isolated attosecond pulse can excite one state of the Q_1 series triggering the dissociation of the neutral molecule. After few femtosecond the molecule

can autoionize projecting the nuclear wave packet on the $1s\sigma_g$ and ejecting an electron characterized mostly by a p-wave. The IR field redistributes the emitted photoelectron associated to the direct ionization among several angular momentum states (including a p-wave contribution); in this way the two paths lead to a coherent superposition of mixed-parity states for the same ion kinetic energy and for the same angular momentum of the outgoing electron. It is important to point out that this mechanism is particularly efficient when the isolated attosecond pulse and the IR pulses overlaps in time.

2.6 Future Experiments: Control of Charge Dynamics in Complex Molecules

The charge localization dynamics evidences that a sub-cycle control of the electronic motion can be induced in a simple molecular system and used to steer the outcome of a dissociation reaction. The experiment of Sansone et al. [17] has demonstrated the relevance of electronic correlation in the control of the electronic localization. Future experiments should be focused on those systems that show an attosecond dynamics as *natural* response to an initial ionization event. In this context Breidbach et al. have shown that an attosecond dynamics is ubiquitous after the sudden removal of an electron and can be as fast as few tens of attosecond [21]. In larger molecules electronic correlation can lead to charge oscillation on the few femtosecond timescale that will determine the subsequent nuclear dynamics. This effect has been shown to occur in different molecular systems and to be characteristics of ionization from inner valence and from outer valence electronic shells [22, 23]. This process of charge migration is driven by purely electronic correlation effects and could eventually couple to the nuclear motion when this will set in. It is important to point out that simulations cannot for the moment predict how this ultrafast charge migration will couple to the nuclear degrees of freedom. However indirect experimental evidences suggest that an initially localized absorption/ionization event at one end of a long polypeptide chain can lead in an ultrashort time to the breaking of a chemical bond at the opposite end of the molecule [24]. The charge migration could be a possible explanation for the ultrafast transport of energy of the entire molecular chain. Isolated attosecond pulses could be efficiently used to trigger the charge migration process; experimental demonstration of the charge oscillation could require the use of few-cycle CEP-controlled pulses to enhance or suppress the migration process depending on the relative phase of the IR field with respect to the one of the charge motion. Such a control will require a control over the molecular orientation that could be achieved by applying impulsive alignment techniques [25].

Acknowledgements Discussions with M. Vrakking, F. Martin and F. Kelkensberg are acknowledged. Financial support by the Alexander von Humboldt Foundation (Project "Tirinto"), the Ateneo italo-tedesco (Programma-Vigoni 2007–2009), the Italian Ministry of Research (Project FIRB No. RBID08CRXK), the European Research Council (ERC-Elyche, No. 227355) and the Marie Curie Research Training Network ATTOFEL is gratefully acknowledged.

References

1. A. Baltuska, T. Udem, M. Uiberacker, M. Hentschel, E. Goulielmakis, C. Gohle, R. Holzwarth, V.S. Yakoviev, A. Scrinzi, T.W. Hansch, F. Krausz, Attosecond control of electronic processes by intense light fields. Nature **421**(6923), 611–615 (2003)
2. A. Wirth, M.T. Hassan, I. Grguras, J. Gagnon, A. Moulet, T.T. Luu, S. Pabst, R. Santra, Z.A. Alahmed, A.M. Azzeer, V.S. Yakovlev, V. Pervak, F. Krausz, E. Goulielmakis, Synthesized light transients. Science **334**(6053), 195–200 (2011)
3. A. Giustisuzor, F.H. Mies, L.F. Dimauro, E. Charron, B. Yang, Dynamics of h^{+}_{-2} in intense laser fields. J. Phys. B, At. Mol. Opt. Phys. **28**(3), 309–339 (1995)
4. J.H. Posthumus, The dynamics of small molecules in intense laser fields. Rep. Prog. Phys. **67**(5), 623–665 (2004)
5. P.H. Bucksbaum, A. Zavriyev, H.G. Muller, D.W. Schumacher, Softening of the h_2^+ molecular-bond in intense laser fields. Phys. Rev. Lett. **64**(16), 1883–1886 (1990)
6. A. Zavriyev, P.H. Bucksbaum, J. Squier, F. Saline, Light-induced vibrational structure in h^{+}_{-2} and d_2^+ in intense laser fields. Phys. Rev. Lett. **70**(8), 1077–1080 (1993)
7. T. Weber, A.O. Czasch, O. Jagutzki, A.K. Muller, V. Mergel, A. Kheifets, E. Rotenberg, G. Meigs, M.H. Prior, S. Daveau, A. Landers, C.L. Cocke, T. Osipov, R.D. Muino, H. Schmidt-Bocking, R. Dorner, Complete photo-fragmentation of the deuterium molecule. Nature **431**(7007), 437–440 (2004)
8. J.L. Sanz-Vicario, H. Bachau, F. Martin, Time-dependent theoretical description of molecular autoionization produced by femtosecond xuv laser pulses. Phys. Rev. A **73**(3), 033410-1–033410-12 (2006)
9. F. Kelkensberg, G. Sansone, M.Y. Ivanov, M. Vrakking, A semi-classical model of attosecond electron localization in dissociative ionization of hydrogen. Phys. Chem. Chem. Phys. **13**(19), 8647–8652 (2011)
10. G. Sansone, F. Kelkensberg, F. Morales, J.F. Perez-Torres, F. Martin, M.J.J. Vrakking, Attosecond time-resolved electron dynamics in the hydrogen molecule. IEEE J. Sel. Top. Quantum Electron. **18**(1), 520–530 (2012)
11. M.F. Kling, C. Siedschlag, A.J. Verhoef, J.I. Khan, M. Schultze, T. Uphues, Y. Ni, M. Uiberacker, M. Drescher, F. Krausz, M.J.J. Vrakking, Control of electron localization in molecular dissociation. Science **312**(5771), 246–248 (2006)
12. M. Kremer, B. Fischer, B. Feuerstein, V.L.B. de Jesus, V. Sharma, C. Hofrichter, A. Rudenko, U. Thumm, C.D. Schroter, R. Moshammer, J. Ullrich, Electron localization in molecular fragmentation of h_{-2} by carrier-envelope phase stabilized laser pulses. Phys. Rev. Lett. **103**(21), 213003-1–213003-4 (2009)
13. I. Znakovskaya, P. von den Hoff, G. Marcus, S. Zherebtsov, B. Bergues, X. Gu, Y. Deng, M.J.J. Vrakking, R. Kienberger, F. Krausz, R. de Vivie-Riedle, M.F. Kling, Subcycle controlled charge-directed reactivity with few-cycle midinfrared pulses. Phys. Rev. Lett. **108**(6), 063002-1–063002-5 (2012)
14. B. Fischer, M. Kremer, T. Pfeifer, B. Feuerstein, V. Sharma, U. Thumm, C.D. Schroter, R. Moshammer, J. Ullrich, Steering the electron in h^{+}_{-2} by nuclear wave packet dynamics. Phys. Rev. Lett. **105**(22), 223001-1–223001-4 (2010)
15. J. Mauritsson, P. Johnsson, E. Gustafsson, A. L'Huillier, K.J. Schafer, M.B. Gaarde, Attosecond pulse trains generated using two color laser fields. Phys. Rev. Lett. **97**(1), 013001-1–013001-4 (2006)
16. K.P. Singh, F. He, P. Ranitovic, W. Cao, S. De, D. Ray, S. Chen, U. Thumm, A. Becker, M.M. Murnane, H.C. Kapteyn, I.V. Litvinyuk, C.L. Cocke, Control of electron localization in deuterium molecular ions using an attosecond pulse train and a many-cycle infrared pulse. Phys. Rev. Lett. **104**(2), 023001-1–023001-4 (2010)
17. G. Sansone, F. Kelkensberg, J.F. Perez-Torres, F. Morales, M.F. Kling, W. Siu, O. Ghafur, P. Johnsson, M. Swoboda, E. Benedetti, F. Ferrari, F. Lepine, J.L. Sanz-Vicario, S. Zherebtsov, I. Znakovskaya, A. L'Huillier, M.Y. Ivanov, M. Nisoli, F. Martin, M.J.J. Vrakking, Electron localization following attosecond molecular photoionization. Nature **465**(7299), 763 (2010)

18. I.J. Sola, E. Mevel, L. Elouga, E. Constant, V. Strelkov, L. Poletto, P. Villoresi, E. Benedetti, J.P. Caumes, S. Stagira, C. Vozzi, G. Sansone, M. Nisoli, Controlling attosecond electron dynamics by phase-stabilized polarization gating. Nat. Phys. **2**(5), 319–322 (2006)
19. G. Sansone, E. Benedetti, F. Calegari, C. Vozzi, L. Avaldi, R. Flammini, L. Poletto, P. Villoresi, C. Altucci, R. Velotta, S. Stagira, S. De Silvestri, M. Nisoli, Isolated single-cycle attosecond pulses. Science **314**(5798), 443–446 (2006)
20. G. Sansone, E. Benedetti, J.P. Caumes, S. Stagira, C. Vozzi, M. Nisoli, L. Poletto, P. Villoresi, V. Strelkov, I. Sola, L.B. Elouga, A. Zair, E. Mevel, E. Constant, Shaping of attosecond pulses by phase-stabilized polarization gating. Phys. Rev. A **80**(6), 063837-1–063837-8 (2009)
21. J. Breidbach, L.S. Cederbaum, Universal attosecond response to the removal of an electron. Phys. Rev. Lett. **94**(3), 033901-1–033901-4 (2005)
22. A.I. Kuleff, J. Breidbach, L.S. Cederbaum, Multielectron wave-packet propagation: general theory and application. J. Chem. Phys. **123**(4), 044111 (2005)
23. A.I. Kuleff, S. Lunnemann, L.S. Cederbaum, Ultrafast charge migration following valence ionization of 4-methylphenol: jumping over the aromatic ring. J. Phys. Chem. A **114**(33), 8676–8679 (2010)
24. R. Weinkauf, E.W. Schlag, T.J. Martinez, R.D. Levine, Nonstationary electronic states and site-selective reactivity. J. Phys. Chem. A **101**(42), 7702–7710 (1997)
25. H. Stapelfeldt, T. Seideman, Colloquium: aligning molecules with strong laser pulses. Rev. Mod. Phys. **75**(2), 543–557 (2003)

Chapter 3
Observation of Vibrational Wave-Packet Dynamics in D_2^+ Using High-Order Harmonic Pulses

Yusuke Furukawa, Yasuo Nabekawa, and Katsumi Midorikawa

Abstract High-order harmonic generation is a unique phenomenon to provide coherent ultrashort light source ranging to the extreme ultraviolet region. In recent years, ultrashort high-harmonic pulses have been used to study ultrafast dynamics in atoms and molecules. We present the pump-probe experimental results on the observation of the vibrational wave-packet dynamics in D_2^+ utilizing the high-order harmonic laser pulses of a sub-15 fs Ti:sapphire laser pulse. We launch the wave-packet of D_2^+ by using a sub-10 fs extreme ultraviolet high-harmonic pump pulse, and observe its evolution by using the split harmonic probe pulse, whose wavelength ranges from near infrared to vacuum ultraviolet. This pump-probe scheme can provide us with a powerful experimental tool for investigating a variety of wave packets evolving with a time scale of $\sim$20 fs.

3.1 Introduction

Ultrafast dynamics and reactions have been investigated in various molecular system, and in particular, the vibrational motion of a diatomic molecule [1, 2] is one of the prominent simple physical systems that can reveal the fundamental nature of the quantum dynamics of matter [3–6]. The generation, observation, and control of a vibrational wave packetare the key issues in utilizing the quantum nature of this system for applications such as quantum computation [7]. A singly charged hydrogen or deuterium molecule (H_2^+ or D_2^+), which is the simplest molecule containing only one electron, has strongly attracted our interest to demonstrate the developed technology and to examine the theoretical work by comparing with the experimental results.

Y. Furukawa · Y. Nabekawa · K. Midorikawa (✉)
Laser Technology Laboratory, RIKEN ASI, 2-1 Horisawa, Wako-shi, Saitama 351-0198, Japan
e-mail: kmidori@riken.jp

Y. Furukawa
e-mail: furukawa-y@riken.jp

Y. Nabekawa
e-mail: nabekawa@riken.jp

K. Yamanouchi et al. (eds.), *Progress in Ultrafast Intense Laser Science X*,
Springer Series in Chemical Physics 106, DOI 10.1007/978-3-319-00521-8_3,

The most significant issue in the real-time measurement of the vibrational wave-packet dynamics of D_2^+ (or H_2^+) [8–12] is the time resolution. The durations of both pump and probe pulses should be much shorter than the vibrational period, typically less than 10 fs. The hollow-core fiber compression technique combined with an near infrared (NIR) Ti:sapphire laser is now a feasible method for obtaining such a short pulse duration, and hence, an NIR Ti:sapphire laser pulse has been used as a probe in most related studies, except for those reported in Ref. [12]. In this probe scheme, the wave packet prepared on the adiabatic potential of the electronic ground state ($1s\sigma_g$) of D_2^+/H_2^+ is mapped onto the repulsive excited state ($2p\sigma_u$) or the Coulombic potential of $D^+ + D^+/H^+ + H^+$ via excitation/ionization by the strong-field interaction of a sub-10-fs NIR pulse. The variation of the kinetic energy release (KER) spectrum of D^+/H^+ with the scanning delay of the NIR probe pulse directly reflects the wave-packet motion. The analysis of this probe scheme requires the rigorous treatment of interactions between the adiabatic potential curves and the intense laser field of the NIR probe pulse, and the induced phenomena, such as bond softening and hardening [13].

In contrast, the lowest-order interaction, namely, the one-photon interaction, straightforwardly gives us the relation between the transition amplitude, delay time, and eigenstates to be probed. This probe scheme, however, exhibits a major drawback that not all the eigenstates contained in a wave packet can be detected owing to the limited bandwidth of the probe laser field, while the strong-field ionization can map the whole wave-packet motion onto the adiabatic repulsive potential. A wavelength range spanning from vacuum ultraviolet (VUV) to NIR is mandatory for investigating the dominant eigenstates in the wave packet of D_2^+. Thus, the key issue is the development of a probe light source with such a broad bandwidth and a short pulse duration in the sub-10-fs regime. The high-harmonic pulses with the pulse duration of sub-10 fs satisfy these requirements to the probe pulse.

In this chapter, we introduce our experimental observation of ultrafast wave-packet dynamics in D_2^+ using high-harmonic laser pulses. Nonlinear Fourier transform spectroscopy based on the interferometric autocorrelation measurement of the high-harmonic laser field, is described in Sect. 3.2, followed by the real-time measurement of the vibrational wave-packet motion of D_2^+, in Sect. 3.3.

3.2 Nonlinear Fourier Transform Spectroscopy Using High-Harmonic Radiation

In this section, we introduce the nonlinear Fourier transform spectroscopy (NFTS), which is useful for investigating the ionization and/or dissociation processes induced by two or more photon process with high-harmonic radiation. The unique feature of the NFTS is the use of the autocorrelation technique for measuring the pulse shape of the attosecond pulse train and relies on the broad harmonic spectra of the attosecond pulse train ranging from visible to extreme ultraviolet (XUV) wavelength region [14, 15]. The measured yields of the respective fragment ions of molecules

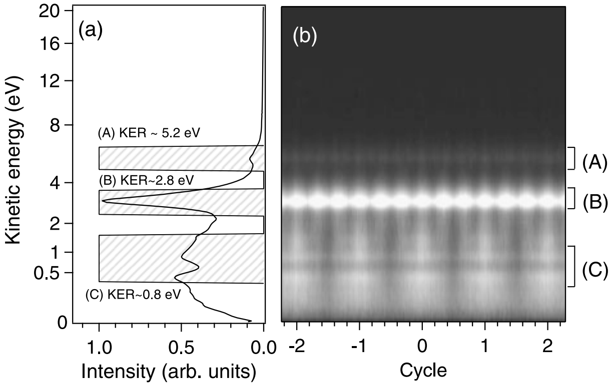

Fig. 3.1 (**a**) KER spectrum of D^+ produced by irradiation of the high-harmonic radiation. The KER spectrum exhibits three components: (A) a region around the peak at 5.2 eV, (B) a region around the peak at 2.8 eV, and (C) a region around the peak at 0.8 eV. (**b**) Variation of the KER distribution of D^+ as a function of the delay between a pair of harmonic fields. The *horizontal axis* of the delay is scaled by the periodic cycle of the fundamental frequency

through the two- or more photon process induced by the high-harmonic radiation are modulated in accordance with the temporal separation between two replicas of the high-harmonic radiation, and exhibit the interferometric autocorrelation signals. The ionization and dissociation pathways of molecules induced by the two-photon absorption of the high-harmonic radiation are identified by analyzing the frequency components of the interferometric fringes appearing in the interferometric autocorrelation traces [16, 17]. We describe the NFTS results for the dissociative ionization of D_2 [17] below.

The detail of the experimental setup of NFTS has been described in Refs. [14, 16–19]. And also refer to Sect. 3.3.1. The KER spectrum of D^+ fragment ions, which are produced by irradiation of the high-harmonic radiation, exhibits three components: (A) a region around the peak at 5.2 eV, (B) a region around the peak at 2.8 eV, and (C) a region with KER lower than 0.8 eV, as shown in Fig. 3.1(a). The intensities of the harmonic fields were sufficiently high to induce multi-photon processes under our experimental conditions [15, 16, 18, 20]. Thus, we expect that multi-photon absorption of the harmonic fields is responsible for the formation of D^+ in this experiment. To investigate how the harmonic fields interact with D_2, we performed NFTS on D_2 by scanning the delay between a pair of harmonic fields, as follows. By arranging the KER spectra in order of increasing temporal delay, the two-dimensional matrix map shown in Fig. 3.1(b) was constructed, which represents the temporal variation of the KER distribution. Periodic modulations of the D^+ signal as a function of the delay are clearly observed in this figure. The periods of the modulations at the three KER regions, (A), (B), and (C), are different from each other. Because the optically linear process could not give us the modulation after volume integration around the focal region, the observed periodic modulations in the ion yields can be regarded as evidence that the D^+ ions are generated from nonlinear optical processes [21], in which two or more photons are involved.

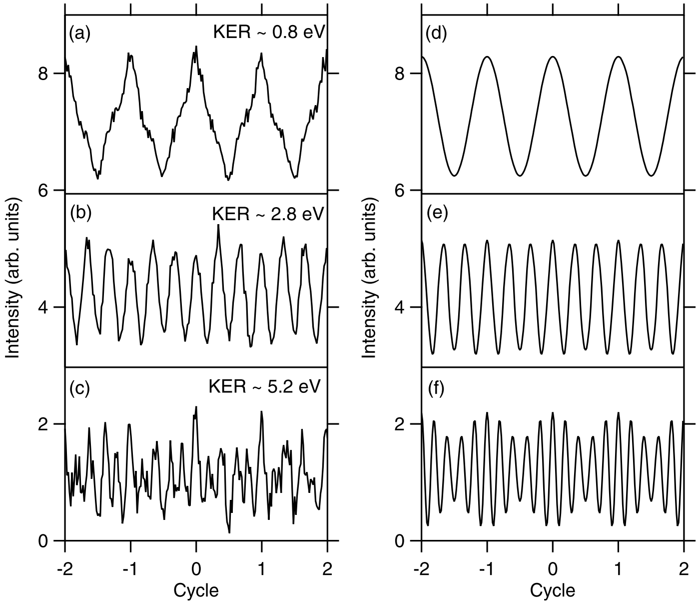

Fig. 3.2 Interferometric autocorrelation traces; (**a**), (**b**), and (**c**) appear in the KER regions around 0.8 eV (C), 2.8 eV (B), and 5.2 eV (A) in Fig. 3.1(b), respectively. The delay is scaled by the period of the fundamental laser field. Calculated interferometric autocorrelation traces (**d**), (**e**), and (**f**) by putting only the two frequency components of the fundamental and 11th-order harmonic fields, the third- and 11th-order harmonic fields, and the fifth- and 11th-order harmonic fields, respectively

To characterize the modulations, the ion yields in the narrow KER regions around 5.2 eV, 2.8 eV, and 0.8 eV in Fig. 3.1(b), were averaged at each time delay and plotted as a function of the delay, as shown in Figs. 3.2(a), (b), and (c). It is clear that the modulation period increases in the order of the KER values. By carrying out a Fourier transform of the traces in Figs. 3.2(a), (b), and (c), the squares of the modulus of the Fourier amplitude are obtained as shown in Figs. 3.3(a), (b), and (c), respectively. The frequency on the horizontal axis is scaled by the optical frequency of the fundamental laser field, ν_f; thus, the numbers on this axis represent the harmonic order. We find distinct features in these frequency spectra by comparing them with the frequency spectra obtained from the interferometric autocorrelation trace of N_2 and CO_2 reported in Refs. [14] and [16], respectively. First, the frequency components at $2\nu_f$ and $4\nu_f$ are negligibly small, although the interferometric autocorrelation trace in the case of N_2 exhibits these components, which originate from the pulse envelopes of the attosecond pulse train formed with the high-harmonic fields. Second, the optical frequencies in the XUV region that form the attosecond pulse train do not appear. Finally, the main contributions to the interference fringes in the traces in Figs. 3.3(a), (b), and (c) are the electric fields of $1\nu_f$, $3\nu_f$, and $5\nu_f$, respectively.

We attempted to reproduce the interferometric autocorrelation traces in Figs. 3.2(a), (b), and (c) by substituting only two frequency components, the

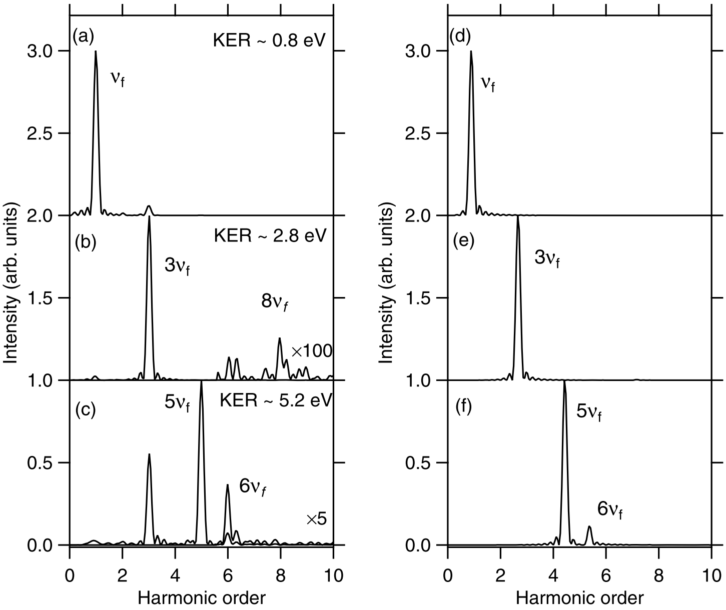

Fig. 3.3 Squared moduli, (**a**)–(**f**) of Fourier transforms of the interferometric autocorrelation traces in Figs. 3.2(a)–(f), respectively. The *horizontal axis* is scaled by the optical frequency of the fundamental laser field, ν_f

fundamental and 11th-order harmonic field, the third- and 11th-order harmonic fields, or the fifth- and 11th-order harmonic fields in the calculation code described in Ref. [15]. The calculated results are shown in Figs. 3.2(d), (e), and (f). We can observe the following similarities between Figs. 3.3(a)–(c) and 3.3(d)–(f): (i) the frequencies of $8\nu_f$ and $6\nu_f$ clearly appear, corresponding to the differences between the 11th- and third- and fifth-order harmonic fields, respectively, (ii) the peak height of the Fourier transform spectrum at even orders monotonically decreases with increasing frequency, such that the $10\nu_f$ spectrum could not be observed in Figs. 3.3(a) and 3.3(d). (iii) The other difference frequencies between the 13th-order or higher-order harmonic fields and the fundamental, third-, or fifth-order harmonic fields do not appear. By comparing these features of the calculated results with the experimental results, the observation of the frequencies of $8\nu_f$, and $6\nu_f$ in Figs. 3.3(b) and (c) and the absence of the difference frequencies originating from the 13th- or higher-order harmonic fields in Figs. 3.3(a), (b), and (c) is considered as evidence for the efficient D_2^+ yield resulting from one-photon absorption of the 11th-order harmonic field.

We conclude the ionization and dissociation pathway of D_2 with the high-harmonic radiation that D_2 molecules absorbing one photon of the 11th-order harmonic radiation ionized to D_2^+, followed by excitation to the first excited state by the one-photon absorption of the three low-order harmonic radiation, resulting in the dissociation into D^+, and D.

3.3 Real-Time Observation of the Vibrational Wave-Packet Motion of D_2^+ Using Multiple Harmonic Pulses

To observe the wave-packet dynamics in the real-time measurement, the durations of both pump and probe pulses should be much shorter than a vibrational period. In this section, we present the pump-probe experimental results for resolving the vibrational wave-packet dynamics of D_2^+ [22] utilizing the high-order harmonic laser pulses of a sub-15 fs Ti:sapphire laser pulse [23]. Thanks to the high-order harmonic generation using a sub-15-fs Ti:sapphire laser, we simultaneously provide both ultrafast XUV-pump and three-color probe pulses having suitable pulse durations with sufficient intensities for implementing the experiment. We could not achieve our time-resolved measurement using multi-color laser pulses without the intrinsic and accurate synchronization of the harmonic pulses.

We generate the wave-packet of D_2^+ by using a sub-10 fs XUV high-harmonic pump pulse, and observe its evolution through the one-photon transition into the electronic excited state by using the split harmonic probe pulse, whose wavelength ranges from NIR to VUV region. The vibrational period of 22 fs is clearly resolved as part of the wave packet owing to the short pulse duration ($\leq$10 fs) by observing the KER-resolved D^+ yield with a scanning delay. The analytical model of one-photon absorption of the probe pulse closely reproduces the experimental results. This pump-probe scheme can provide us with a powerful experimental tool for investigating a variety of wave packets evolving on a time scale of $\sim$20 fs. We describe our experimental setup for measuring the vibrational wave-packet dynamics of D_2^+, in Sect. 3.3.1, and then, introduce the experimental results, in Sect. 3.3.2.

3.3.1 Experimental Setup

The experimental setup is similar to that adopted in the nonlinear and linear autocorrelation measurement of an attosecond pulse train [14, 16–19] except for the specifications of the laser system. The chirped pulse amplification (CPA) system of a Ti:sapphire laser delivers driving laser pulses with a pulse duration of 15 fs to generate harmonic fields ranging from the third-order in the deep ultraviolet (DUV) region to 19th order in the XUV region. We put the compressor of the CPA system in a vacuum chamber to avoid the dispersion and nonlinear effects originating from the air and the window material of the vacuum chamber for harmonic generation. The repetition rate of the driving laser pulse was 100 Hz. The driving laser was loosely focused into a 10-cm static gas cell, which was filled with Xe gas as a nonlinear medium for harmonic generation. The focal length of the driving laser was 5 m. The loose-focusing geometry is appropriate for yielding intense high-harmonic pulses at the focal region [24].

The pulse energy of the driving laser and the pressure of Xe gas were adjusted typically to $\sim$15 mJ and $\sim$90 Pa, respectively, so as to optimize the spectral distribution and intensities of the high-harmonic fields, which were monitored using

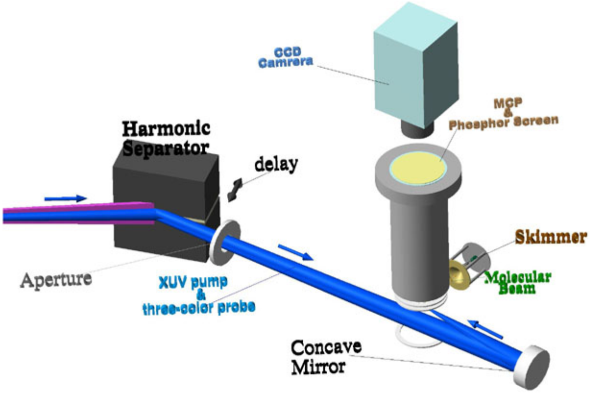

Fig. 3.4 Schematic figure of XUV autocorrelator and ion velocity map imaging spectrometer. The XUV autocorrelator is composed of a pair of Si harmonic separator mirrors and controls the delay between the two replicas of the reflected pulse. The pump and probe pulses are focused by an SiC concave mirror onto a molecular beam of D_2. The fragment ions of D^+ are detected by a velocity map imaging spectrometer, which is constructed from three electrodes, a flight tube, a stack of MCP plates attached to a phosphor screen, and a CCD camera

an XUV spectrometer. After the driving laser and harmonic pulses have propagated 6.4 m away from the gas cell, they are introduced into another vacuum chamber containing an ‘attocorrelator’, which is XUV autocorrelator composed of a pair of Si beam splitter mirrors that reflect XUV harmonic components. A schematic figure of the XUV autocorrelator and the following instruments is shown in Fig. 3.4.

The reflectivity of the Si beam splitter mirror for the harmonic components with photon energies exceeding $\sim$14 eV is approximately 50 % at an incident angle of 75 degrees, which is the Brewster angle for the fundamental laser field, while reflectivities for the fundamental, third harmonic, and fifth harmonic fields of the Ti:sapphire laser pulse are estimated to be less than 10^{-3}, $\sim$40 %, and $\sim$60 %, respectively, from the known refractive index of Si at the corresponding photon energies of 1.55 eV, 4.6 eV, and 7.7 eV, respectively. The 11th order harmonic field with a photon energy of $\sim$17 eV included in the XUV components mainly act as a pump pulse. We treat the synthesized light field composed of the strongly attenuated fundamental field and the suitably reflected third harmonic and fifth harmonic fields as a single probe pulse in principle, while we sometimes refer to a specific character of each frequency component such as the intensity and pulse duration. Note that the temporal profile of the probe pulse should exhibit modulation with a period of $\sim$1.33 fs due to the frequency difference among the three color fields. On the other hand, the smooth pulse envelope of each frequency component can be specified if we isolate one color field from the others.

The delay between the two replicas of the reflected pulse consisting of the superposition of the XUV components and three color probe pulse was changed by moving one of the beam splitter mirrors, which was set on a translation stage driven by a piezo-actuator.

All the reflected pulses from the XUV autocorrelator pass through an aperture with a diameter of 3 mm to eliminate the so-called long-trajectory high-order harmonic components, then they are introduced into an ion spectrometer chamber. We place a concave mirror made of SiC with a radius of curvature of 200 mm inside the ion spectrometer chamber to focus the incident pulses. The position of the focal point of the concave mirror is adjusted so as to maximize the ion yield from the molecular beam of D_2.

The pulse duration of each field, except for the fundamental laser field, is expected to be less than 10 fs owing to the fact that the measured spectra of the third harmonic and fifth harmonic fields are both sufficiently broad to form a sub-10 fs pulse with negligible dispersions at the reflections of the Si beam splitter mirror and SiC concave mirror, although we have not explicitly measured the durations. The peak intensity of the XUV (the 11th order harmonic) harmonic field is estimated to be order of 10^{13} W/cm^2, while those of the fifth harmonic, third harmonic, and fundamental fields are all less than 10^{12} W/cm^2.

A pulsed gas valve with a backing pressure of 2×10^5 Pa injects D_2 gas in the side chamber of the ion spectrometer for adiabatic cooling of the D_2 molecules, and the cooled molecules are prepared as a beam using a skimmer which separates the side chamber from the ion spectrometer.

The ions are accelerated by three electrodes and detected with a micro-channel plate (MCP) attached to a phosphor screen. The acceleration voltages applied to the electrode are fixed to image the initial velocity of ions onto the MCP plane. The time of flight (TOF) of ions depends on their mass-to-charge ratio; we can discriminate D^+ by applying a gate voltage to the MCP with a typical duration of 200 ns. The gate voltage is $\sim$30 % higher than the bias DC voltage. The MCP plane is set parallel to the polarization direction of the pump and probe pulses. The fluorescent image of the phosphor screen is recorded with a CCD camera.

We scanned the delay of the two replicas of the input pulse containing the XUV high-order harmonic, fifth harmonic, third harmonic, and fundamental fields by moving one of the beam splitter mirrors at intervals of 80 nm within the range from -0.8 μm to 88 μm. The scanning step and range corresponded to a temporal step of 0.14 fs and a delay of approximately 150 fs, respectively. We accumulated fluorescent images of the phosphor screen located behind the MCP for 2 s at every delay point, and repeated this measurement 25 times.

We show relevant potential energy curves against the nuclear distance of D_2 and D_2^+ in Fig. 3.5(a) to explain the photo absorption process in this experiment. The XUV high-order harmonic field of the 11th order with a photon energy of 17 eV and above can ionize D_2 molecules by one-photon absorption and create a vibrational wave packet on the $1s\sigma_g$ potential curve of D_2^+. Nevertheless, we have concluded from the NFTS of D_2 [17] that the 11th-order harmonic field mainly contributes the formation of this wave packet. Then, the probe pulse excites the D_2^+ in the $1s\sigma_g$ state to the $2p\sigma_u$ state by absorbing one photon of the fifth order harmonic component with a photon energy of $\sim$7.7 eV in the VUV region, the third harmonic component with a photon energy of $\sim$4.6 eV in the DUV region, or the fundamental component with a photon energy of $\sim$1.55 eV in the NIR region, after some delay from the

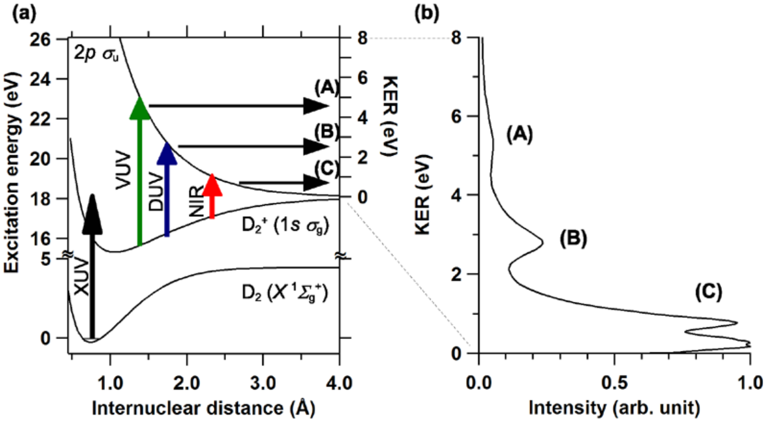

Fig. 3.5 Relevant energy diagram of D_2 and D_2^+ (**a**) and measured KER spectrum (**b**), in which KER means the dissociation energy of D_2^+ via $2p\sigma_u$ potential and is equally shared by two fragments, D^+ ion and D atom

ionization. The transition amplitude tends to be large at the nuclear distance where the energy difference between the $1s\sigma_g$ and $2p\sigma_u$ potentials is close to the photon energy. Hence, the several vibrational eigenstates whose eigenenergies are the same as the potential energy around this nuclear distance should be picked up and projected onto the repulsive potential of $2p\sigma_u$. We can find the partial wave-packet components in the whole generated wave packet by determining and analyzing the KER spectrum from the observed D^+ fragments.

We note that the harmonic components higher than the fifth order, which should be contained in both replica pulses, may induce the one-photon transitions from the $1s\sigma_g$ to $2p\sigma_u$ states. We could not, however, observe the KER spectrum resulting from these transitions due to the low magnitude of the dipole at a small nuclear distance where the transitions are most likely to occur by absorbing one photon of these harmonic components.

3.3.2 Results and Discussion

The measured KER spectrum of D^+ at a fixed delay ($\tau \simeq 0$ fs) is shown in Fig. 3.5(b). The spectrum exhibits three distinct parts labeled (A) around 5.2 eV, (B) around 2.8 eV, and (C) around 0.8 eV, which originate from the transition from the ground bound state of $1s\sigma_g$ to the upper repulsive excited state of $2p\sigma_u$ by absorbing one photon of the fifth order harmonic, third order harmonic, and fundamental components in the probe pulse, respectively. We have already shown how we assign the excitation process in Ref. [17]. We obtain a delay-KER spectrogram by arranging the KER spectra in ascending order of delay. Figure 3.6(a) shows the resultant delay-KER spectrogram after processing the raw data to correct the unimportant linear decrease of the spectral intensity relative to delay, the interference

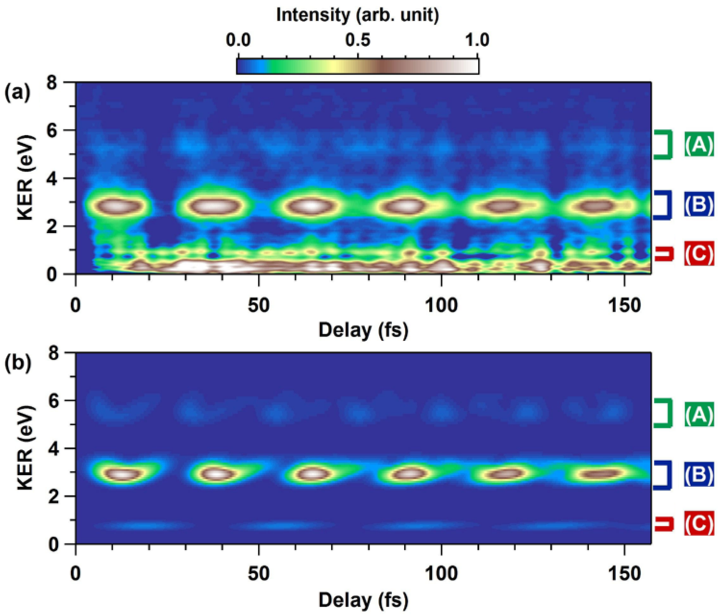

Fig. 3.6 Measured delay-KER spectrogram with constant background subtracted (**a**) and simulated delay-KER spectrogram (**b**). The three KER components labeled (A), (B), and (C) are assigned to the fragmentation processes induced by absorbing the VUV, DUV, and NIR components in the probe pulse, respectively

fringes of the probe pulse, and the constant background signal. We can notice the periodic modulation of the D^+ yield, the period of which is approximately 26 fs, in accordance with the delay in region (B). This is clear evidence of the vibrational motion of D_2^+.

In fact, the vibrational motion of D_2^+ also appears in regions (A) and (C). We show area profiles in regions (A), (B), and (C) as solid curves in Figs. 3.7(a), (b), and (c), respectively. These traces are obtained by integrating the delay-KER spectrogram with respect to the KER around the peaks within a range of ±0.5 eV, 0.5 eV, and 0.17 eV for regions (A), (B), and (C), respectively. We can recognize periodic modulation in the solid curves in of Figs. 3.7(a) and (c) similar to that appearing clearly in the middle panel of Fig. 3.7(b), while the modulation period is different in each case. This feature of the modulation period is more evident in Figs. 3.7(d), (e), and (f), which show the absolute squares of the magnitudes of the Fourier transforms of the solid curves in Figs. 3.7(a), (b), and (c), respectively. The primary peak of the frequency spectrum in Fig. 3.7(d) is located around 45 THz, and consequently the principal period of the modulation in Fig. 3.7(a) should be 22 fs. The monotonic decrease of the peak frequency following the decrease of the principal photon energy of the probe pulse component, shown in Figs. 3.7(a), (b), and (c) proves that the relevant vibrational eigenstates in the wave packet are extracted and resolved with the three-color probe pulse.

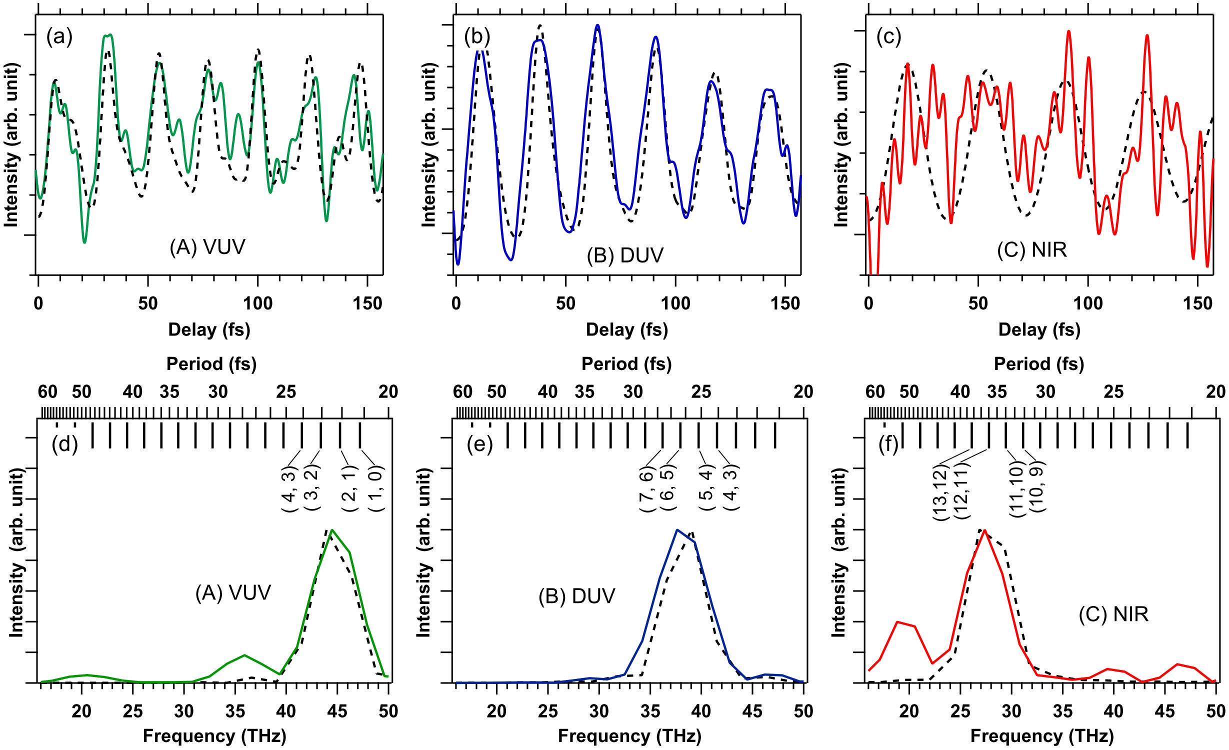

Fig. 3.7 Area profiles of the KER-delay spectrogram in region (A) (*solid curve*), region (B) (*solid curve*), and region (C) (*solid curve*), defined in Fig. 3.6(a), are shown in Fig. 3.7(**a**), (**b**), and (**c**), respectively. The absolute squares of the magnitude of the Fourier transforms of the *solid curves* in Fig. 3.7(**a**), (**b**), and (**c**), are plotted as *solid curves* in Fig. 3.7(**d**), (**e**), and (**f**), respectively. The *long marks* at the top axis of Fig. 3.7(**d**), (**e**), and (**f**) indicate the energy differences between the pairs of adjacent vibrational levels shown in *parentheses*. The *dotted curves* in all the figures are calculated results

We have assigned the quantum number of the vibrational states extracted with each photon-energy component in the probe pulse by comparing the frequency spectrum with the energy difference between adjacent vibrational states calculated from a known potential curve in Ref. [25]. The energy differences, which we converted to frequency differences, are depicted at the top axes in Figs. 3.7(d), (e), and (f) as long marks. The pairs of adjacent quantum numbers corresponding to the frequency differences contained in the frequency spectrum are explicitly shown in parentheses in each figure. Note that the resolution of the frequency spectrum is restricted by the limitation of the scanning range of the delay, which is estimated to be $\sim$7 THz $\simeq 1/(150\ \mathrm{fs})$, hence, we could not resolve the each difference-frequency corresponding to each long mark.

This experimental result for the probe process of the vibrational wave packet can be explained within a framework of the elementary time-dependent perturbation theory of interactions. By assuming the simple two-level system for the electronic state [8, 26–28], the probability of a transition from the ground state $(1s\sigma_g)$ to the excited state $(2p\sigma_u)$ induced by the probe pulse irradiated at time delay τ is approximately proportional to the absolute square of $T(\omega^u;\tau)$, defined as

$$T\big(\omega^u;\tau\big) \equiv \sum_{\nu} \mathscr{M}\big(\omega^u;\omega_\nu^g\big)\widetilde{E}^{+}\big(\omega^u-\omega_\nu^g\big)a'_\nu \mathrm{e}^{-i\omega_\nu^g\tau}, \tag{3.1}$$

where the discrete νth vibrational eigenenergy on the $1s\sigma_g$ state is denoted as $\hbar\omega_\nu^g$, the continuum eigenenergy on the $2p\sigma_u$ state is denoted as $\hbar\omega^u$, and $\hbar$ is the Planck constant, h, divided by 2π. The amplitude of the νth vibrational eigenstate is expressed as a', which may differ from the amplitude obtained from the Franck-Condon principle for the ionization process due to the finite pulse duration of the pump pulse. The matrix element with the transition dipole denoted as $\mathscr{M}(\omega^u;\omega_\nu^g)$ projects the νth vibrational state onto the continuum state whose eigenenergy is $\hbar\omega^u$. The Fourier amplitude of the positive-frequency part of the probe pulse electric field, $\widetilde{E}^{+}(\omega)$, should be finite around the three peaks at $\omega=\omega_0$, $3\omega_0$, and $5\omega_0$, and otherwise equal to 0, where we define ω to be the angular frequency variable of the probe pulse electric field and ω_0 to be the principal carrier angular frequency of the fundamental laser field. Therefore, the Fourier amplitude of $\widetilde{E}^{+}(\omega^u-\omega_\nu^g)$ acts as a bandpass filter for ω_ν^g satisfying $\omega^u-\omega_\nu^g \simeq \omega_0$, $3\omega_0$, and $5\omega_0$.

We can clearly see from (3.1) that the real-time evolution of the vibrational wave packet $(\sum_\nu \ldots a'_\nu \mathrm{e}^{-i\omega_\nu^g\tau})$ is partially extracted by the probe pulse $(\widetilde{E}^{+}(\omega^u-\omega_\nu^g))$ and projected onto the repulsive continuum state $(\mathscr{M}(\omega^u;\omega_\nu^g))$.

The delay-KER spectrogram calculated from (3.1) is shown in Fig. 3.6(b). In the actual calculation of the delay-KER spectrogram, we have adopted the numerical values of the adiabatic potential curves obtained in Ref. [25] to calculate the nuclear wave eigenfunctions $\chi_\nu^g(R)$ and $\varphi^u(\omega^u;R)$. The electronic transition dipole, $\mu(R)$, is assumed to be proportional to R [29, 30].

In order to obtain the amplitude of the νth eigenfunction, a_ν, we first calculated the Franck-Condon factor of $\chi_\nu^g(R)$, then multiplied it by $\int_{\omega_\nu^g+\omega_{Diss}}^{\infty} d\omega\, S_{11}(\omega)$, where $\hbar\omega_{Diss}$ is the dissociation energy and $S_{11}(\omega)$ is the spectrum of the 11th-order harmonic field, which is assumed to be Gaussian. We set the peak frequency of $S_{11}(\omega)$ to be 11 times the fundamental frequency and the spectral width so as to produce a 5.5 fs pulse at the Fourier limit. These conditions for $S_{11}(\omega)$ are approximately consistent with the measured spectrum of the 11th-order harmonic field, even though the measured spectrum does not have an exact Gaussian shape. The photon energy of the 11th-order harmonic field does not exceed the dissociation limit of the $1s\sigma_g$ potential of D_2^+. Thus, the amplitudes of the vibrational states, whose energy differences from the ground state of D_2 are larger than the photon energy of the 11th-order harmonic field, should be suppressed.

The calculated image in Fig. 3.6(b) agrees well with the experimental data shown in Fig. 3.6(a) except in the KER region lower than 0.4 eV. In this low-KER region, the photo ionization of D_2 via Rydberg states can significantly contribute to the D^+ yield. The process includes the one-photon electronic excitation of D_2 neutral molecules by XUV photo absorption and the one-photon ionization to the nuclear continuum state on the $1s\sigma_g$ potential of D_2^+ by NIR photo absorption. These interactions are not considered in our theoretical model.

The similarity of the calculated result can be seen more clearly in Figs. 3.7(a)–(f). The dotted curves in all these figures are obtained from the calculated spectrogram in Fig. 3.6(b) by data processing procedures similar to those adopted for the experimental data. We can see that the real-time traces of the oscillating behavior of the partial wave packet modeled with (3.1) reproduce the experimental traces in Figs. 3.7(a), (b), and (c). In particular, the measured trace probed with the third harmonic component (solid curve in Fig. 3.7(b)) very closely coincides with the calculated result. The intensity profiles of the Fourier transforms of the calculated traces in Figs. 3.7(d), (e), and (f) also support the experimental results. We note that multiplication by $\int_{\omega_v^g+\omega_{Diss}}^{\infty} d\omega\, S_{11}(\omega)$ with the significant reduction of the vibrational states higher than approximately the eighth order plays a crucial role in reproducing the oscillating period of the D^+ observed in the KER region (C), shown in Figs. 3.7(c) and (f).

3.4 Conclusion

We have demonstrated the experimental observation of the time evolution of the vibrational motion of the D_2^+ molecule in the measured KER spectrum of D^+ by using the harmonic fields of a sub-15 fs Ti:sapphire laser pulse as an XUV pump and three-color probe pulses. By comparing the experimental data with calculated results, we conclude that our theoretical model for the real-time observation of the vibrational wave packet with the three-color probe pulse correctly describes the experimental data, and we can state that we have directly and simultaneously measured the motion of three partial wave-packet components in the generated vibrational wave packet. Our demonstration of resolving the D_2^+ wave packet dynamics suggests that our experimental method may be useful for generation, observation, and control of various quantum systems that evolve in the time scale of $\sim$20 fs and require high-energy photons for the pump and/or probe pulses.

Acknowledgements We thank Professor K. Yamanouchi and Dr. T. Okino for valuable discussions. This work was carried out as part of the Advanced Photon Science Alliance (APSA) project commissioned by the Ministry of Education, Culture, Sports, Science and Technology (MEXT). Y.N. gratefully acknowledges financial support by a grant for Scientific Research (A) 21244066. K.M. directed this research with a grant for the Extreme Photonics Research Group in RIKEN.

References

1. M. Dantus, R.M. Bowman, A.H. Zewail, Femtosecond laser observations of molecular vibration and rotation. Nature **343**, 737–739 (1990)
2. T.S. Rose, M.J. Rosker, A.H. Zewail, Femtosecond real-time observation of wave packet oscillations (resonance) in dissociation reactions. J. Chem. Phys. **88**, 6672–6673 (1988)
3. N.F. Scherer, R.J. Carlson, A. Matro, M. Du, A.J. Ruggiero, V. Romero-Rochin, J.A. Cina, G.R. Fleming, S. Rice, Fluorescence-detected wave packet interferometry: time resolved molecular spectroscopy with sequence of femtosecond phase-locked pulse. J. Chem. Phys. **95**, 1487–1511 (1988)
4. E. Skovsen, M. Machholm, T. Ejdrup, J. Thøogersen, H. Stapelfeldt, Imaging and control of interfering wave packets in a dissociating molecule. Phys. Rev. Lett. **89**, 133004 (2002)
5. K. Ohmori, Y. Sato, E.E. Nikitin, S.A. Rice, High-precision molecular wave-packet interferometry with HgAr dimers. Phys. Rev. Lett. **91**, 243003 (2003)
6. H. Katsuki, H. Chiba, B. Girard, C. Meier, K. Ohmori, Visualizing picometric quantum ripples of ultrafast wave-packet interference. Science **311**, 1589–1592 (2006)
7. K. Hosaka, H. Shimada, H. Chiba, H. Katsuki, Y. Teranishi, Y. Ohtsuki, K. Ohmori, Ultrafast Fourier transform with a femtosecond-laser-driven molecule. Phys. Rev. Lett. **104**, 180501 (2010)
8. A.S. Alnaser, B. Ulrich, X.M. Tong, I.V. Litvinyuk, C.M. Maharjan, P. Ranitovic, T. Osipov, R. Ali, S. Ghimire, Z. Chang, C.D. Lin, C.L. Cocke, Simultaneous real-time tracking of wave packets evolving on two different potential curves in H_2^+ and D_2^+. Phys. Rev. A **72**, 030702(R) (2005)
9. T. Ergler, A. Rudenko, B. Feuerstein, K. Zrost, C.D. Schröter, R. Moshammer, J. Ullrich, Spatiotemporal imaging of ultrafast molecular motion: collapse and revival of the D_2^+ nuclear wave packet. Phys. Rev. Lett. **97**, 193001 (2006)
10. F. Kelkensberg, C. Lefebvre, W. Siu, O. Ghafur, T.T. Nguyen-Dang, O. Atabek, A. Keller, V. Serov, P. Johnsson, M. Swoboda, T. Remetter, A. L'fHuillier, S. Zherebtsov, G. Sansone, E. Benedetti, F. Ferrari, M. Nisoli, F. Lépine, M.F. Kling, M.J.J. Vrakking, Molecular dissociative ionization and wave-packet dynamics studied using two-color XUV and IR pump-probe spectroscopy. Phys. Rev. Lett. **103**, 123005 (2009)
11. C.R. Calvert, W.A. Bryan, W.R. Newell, I.D. Williams, Time-resolved studies of ultrafast wavepacket dynamics in hydrogen molecules. Phys. Rep. **491**, 1–28 (2010)
12. Y.H. Jiang, A. Rudenko, J.F. Pérez-Torres, O. Herrwerth, L. Foucar, M. Kurka, K.U. Kühnel, M. Toppin, E. Plésiat, F. Morales, F. Martín, M. Lezius, M.F. Kling, T. Jahnke, R. Dörner, J.L. Sanz-Vicario, J. van Tilborg, A. Belkacem, M. Schulz, K. Ueda, T.J.M. Zouros, S. Düsterer, R. Treusch, C.D. Schröter, R. Moshammer, J. Ullrich, Investigating two-photon double ionization of D_2 by XUV-pump-XUV-probe experiments. Phys. Rev. A **81**, 051402(R) (2010)
13. B. Feuerstein, T. Ergler, A. Rudenko, K. Zrost, C.D. Schröter, R. Moshammer, J. Ullrich, Complete characterization of molecular dynamics in ultrashort laser fields. Phys. Rev. Lett. **99**, 153002 (2007)
14. Y. Nabekawa, T. Shimizu, T. Okino, K. Furusawa, H. Hasegawa, K. Yamanouchi, K. Midorikawa, Interferometric autocorrelation of an attosecond pulse train in the single-cycle regime. Phys. Rev. Lett. **97**, 153904 (2006)

15. T. Shimizu, T. Okino, K. Furusawa, H. Hasegawa, Y. Nabekawa, K. Yamanouchi, K. Midorikawa, Observation and analysis of an interferometric autocorrelation trace of an attosecond pulse train. Phys. Rev. A **75**, 033817 (2007)
16. T. Okino, K. Yamanouchi, T. Shimizu, R. Ma, Y. Nabekawa, K. Midorikawa, Attosecond nonlinear Fourier transformation spectroscopy of CO_2 in extreme ultraviolet wavelength region. J. Chem. Phys. **129**, 161103 (2008)
17. Y. Furukawa, Y. Nabekawa, T. Okino, S. Saugout, K. Yamanouchi, K. Midorikawa, Nonlinear Fourier-transform spectroscopy of D_2 using high-order harmonic radiation. Phys. Rev. A **82**, 013421 (2010)
18. Y. Nabekawa, T. Shimizu, T. Okino, K. Furusawa, H. Hasegawa, K. Yamonouchi, K. Midorikawa, Conclusive evidence of an attosecond pulse train observed with the mode-resolved autocorrelation technique. Phys. Rev. Lett. **96**, 083901 (2006)
19. Y. Nabekawa, T. Shimizu, Y. Furukawa, E.J. Takahashi, K. Midorikawa, Interferometry of attosecond pulse trains in the extreme ultraviolet wavelength region. Phys. Rev. Lett. **102**, 213904 (2009)
20. T. Okino, K. Yamonouchi, T. Shimizu, K. Furusawa, H. Hasegawa, Y. Nabekawa, K. Midorikawa, Attosecond molecular coulomb explosion. Chem. Phys. Lett. **432**, 68–73 (2006)
21. Y. Nabekawa, K. Midorikawa, Interferometric autocorrelation of an attosecond pulse train calculated using feasible formulae. New J. Phys. **10**, 025034 (2008)
22. Y. Furukawa, Y. Nabekawa, T. Okino, A.A. Eilanlou, E.J. Takahashi, P. Lan, K.L. Ishikawa, T. Sato, K. Yamanouchi, K. Midorikawa, Resolving vibrational wave-packet dynamics of D_2^+ using multi-color probe pulses. Opt. Lett. **37**, 2922–2924 (2012). doi:10.1364/OL.37.002922
23. Y. Nabekawa, A.A. Eilanlou, Y. Furukawa, K.L. Ishikawa, H. Takahashi, K. Midorikawa, Multi-terawatt laser system generating 12-fs pulses at 100 Hz repetition rate. Appl. Phys. B **101**, 523–534 (2010)
24. E.J. Takahashi, Y. Nabekawa, K. Midorikawa, Generation of 10-μJ coherent extreme-ultraviolet light by use of high-order harmonics. Opt. Lett. **27**, 1920–1922 (2002)
25. K. Hoshina, A. Hishikawa, K. Kato, T. Sako, K. Yamanouchi, E.J. Takahashi, Y. Nabekawa, K. Midorikawa, Dissociative ATI of H_2 and D_2 in intense soft x-ray laser fields. J. Phys. B **39**, 1–17 (2006)
26. D.J. Tannor, R. Kosloff, S.A. Rice, Coherent pulse sequence induced control of selectivity of reactions: exact quantum mechanical calculations. J. Chem. Phys. **85**, 5805–5820 (1986)
27. U. Thumm, T. Niederhausen, B. Feuerstein, Time-series analysis of vibrational nuclear wave-packet dynamics in D_2^+. Phys. Rev. A **77**, 063401 (2008)
28. F. He, U. Thumm, Dissociative ionization of H_2 in an attosecond pulse train and delayed laser pulse. Phys. Rev. A **81**, 053413 (2010)
29. F.V. Bunkin, I.I. Tugov, Multiphoton processes in homopolar diatomic molecules. Phys. Rev. A **8**, 601–612 (1973)
30. K.C. Kulander, F.H. Mies, K.J. Schafer, Model for studies of laser-induced nonlinear processes in molecules. Phys. Rev. A **53**, 2562–2570 (1996)

Chapter 4
Frequency Tunable Attosecond Apparatus

Hiroki Mashiko, M. Justine Bell, Annelise R. Beck, Daniel M. Neumark, and Stephen R. Leone

Abstract The development of attosecond technology is one of the most significant recent achievements in the field of ultrafast optics; it opens up new frontiers in atomic and molecular spectroscopy and dynamics. A unique attosecond pump-probe apparatus using a compact Mach-Zehnder interferometer is developed. The interferometer system is compact ($\sim$290 cm^2) and completely located outside of the vacuum chamber. The location reduces the mechanical vibration from vacuum components such as turbopumps and roughing pumps. The stability of the interferometer is $\sim$50 as RMS over 24 hours, stabilized with an active feedback loop. The pump and probe fields can be easily altered to incorporate multiple colors. In the interferometer, double optical gating optics are arranged to generate isolated attosecond pulses with a supercontinuum spectrum. The frequencies of the attosecond pulses can be selected to be in the extreme ultraviolet (XUV) region (25–55 eV, 140 as) or the vacuum ultraviolet (VUV) region (15–24 eV, $\sim$400 as) by metal filters. Furthermore, the near infrared probe field (1.65 eV) can be upconverted to the ultraviolet (3.1 eV). The frequency tunability in the XUV and VUV is critical for selecting excited states of target atoms and molecules.

H. Mashiko (✉) · M.J. Bell · A.R. Beck · D.M. Neumark · S.R. Leone
Ultrafast X-ray Science Laboratory, Chemical Sciences Division, Lawrence Berkeley National Laboratory, CA, Berkeley, 94720, USA
e-mail: mashiko.hiroki@lab.ntt.co.jp

M.J. Bell · A.R. Beck · D.M. Neumark · S.R. Leone
Department of Chemistry, University of California, CA, Berkeley, 94720, USA

S.R. Leone
Department of Physics, University of California, CA, Berkeley, 94720, USA

H. Mashiko
Material Quantum Optical Physics Research Group, Optical Science Laboratory, NTT Basic Research Laboratory, 3-1, Morinosato Wakamiya, Atsugi-shi, Kanagawa 243-0198, Japan

K. Yamanouchi et al. (eds.), *Progress in Ultrafast Intense Laser Science X*,
Springer Series in Chemical Physics 106, DOI 10.1007/978-3-319-00521-8_4,

4.1 Introduction

The generation of attosecond pulses has had a profound impact on the study of dynamics of electrons in atoms [1–5], molecules [6] and solids [7]. Such pulses are produced by high-order harmonic generation (HHG) with intense field femtosecond laser pulses. Attosecond pulses offer high temporal [8] and spatial coherence [9]. Experimental schemes for measuring atomic and molecular dynamics by coupling an attosecond pulse and an optical laser pulse have been devised utilizing the detection of photons, ions, or photoelectrons [1–8]. Experimental systems in previous work each have individual advantages and disadvantages, but each system requires stabilization with attosecond time resolution and has various optical limitations in the extreme ultraviolet (XUV: 30–250 eV) and vacuum ultraviolet (VUV: 6–30 eV) regions [10]. In this review, we introduce several attosecond pump-probe systems from previous work and discuss their characteristics. Then, we discuss a system using a compact and robust Mach-Zehnder (MZ) type interferometer which can produce frequency tunable isolated attosecond pulses (IAP) and optical probe pulses of several colors. The tunability of the attosecond and optical pulses is important to initiate and probe specific chemical dynamics. Thus, the manipulation of the spectral distribution of the attosecond pulse is a key parameter. This system can generate IAP, using double optical gating (DOG) [11] and metal filters, in either the XUV (25–70 eV) or VUV (15–24 eV) frequency ranges. In addition, the IAP are temporally characterized with both 750 nm (1.6 eV) and 400 nm (3.1 eV) probe fields. The increased flexibility will pave the way for future chemical applications.

4.2 Attosecond Apparatus

4.2.1 Collinear Setup

In the past, a number of configurations have been developed to produce IAP or attosecond pulse trains with pump-probe capabilities, as shown in Fig. 4.1. In this figure, the dashed line indicates the boundary of the vacuum system. The systems have individual characteristics and are designed for specific applications based on photoelectron, photoion, and transient absorption methods. To date, the shortest IAP produced, with a duration of 80 as (bandwidth 55–110 eV), was generated using a collinear system as shown in Fig. 4.1(a) [8]. The advantage of this design is pump-probe stability, because the delay between the XUV beam and near-infrared (NIR) beam is produced by only one optic: a combined XUV multilayer coated mirror and Ag coated mirror [8, 12–14]. Furthermore, the delay can be stabilized with an active feedback loop (stability of 46 as over 33 hours) in order to counteract any slow drifts [15]. In addition, the multilayer mirror can be designed to select specific attosecond frequencies. The disadvantage of this system is that the probe pulse at the target is the residual NIR light from the HHG upconversion pulse, which collinearly propagates with the IAP. Thus, it is difficult to install extra optics to control this field.

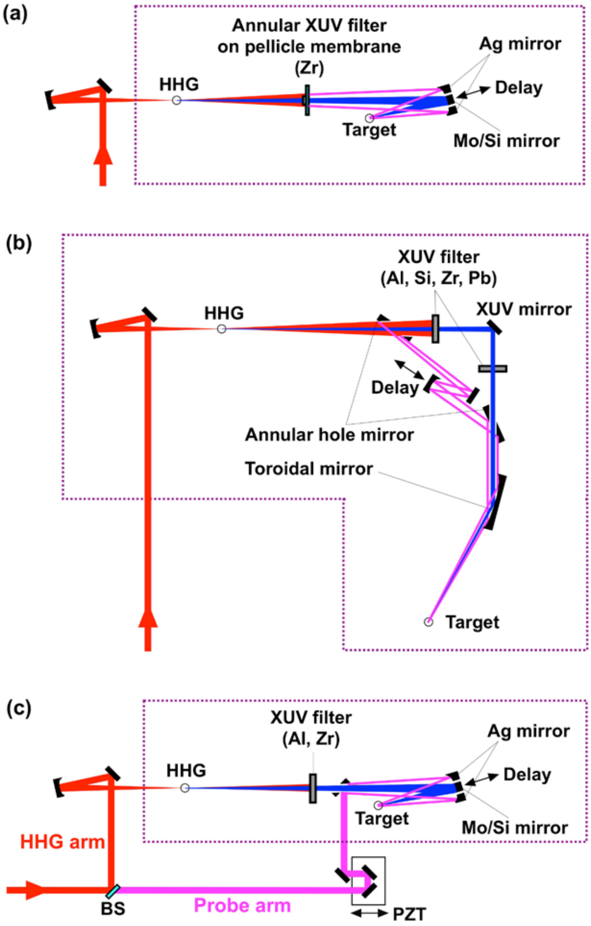

Fig. 4.1 Various configurations to produce attosecond pulses with merging XUV/VUV and NIR fields. FS: Fused silica plate, HHG: high harmonic generation, PZT: piezo-electronic transducer

4.2.2 *Large MZ Interferometer Setup*

With a MZ interferometer setup, it is easier to control the optical characteristics of the pump and probe pulses. Figure 4.1(b) shows an interferometer located after the high harmonics are generated [16]. The NIR field can be controlled with various optics such as a neutral density filter or a focusing mirror. However, the system is more complex and harder to operate compared to the collinear setup in Fig. 4.1(a). Also, the interferometer has a long propagation distance of several meters. Thus, an active stabilization loop was installed, which achieves 50 as stability over 1 hour with 2.5 ms (400 Hz) integration time (limited by the piezoelectric transducer response time). Although the stability is excellent, the feedback loop cannot compensate for the mechanical vibrations of 1 kHz frequency from vacuum turbopumps.

Fig. 4.1 (*Continued*)

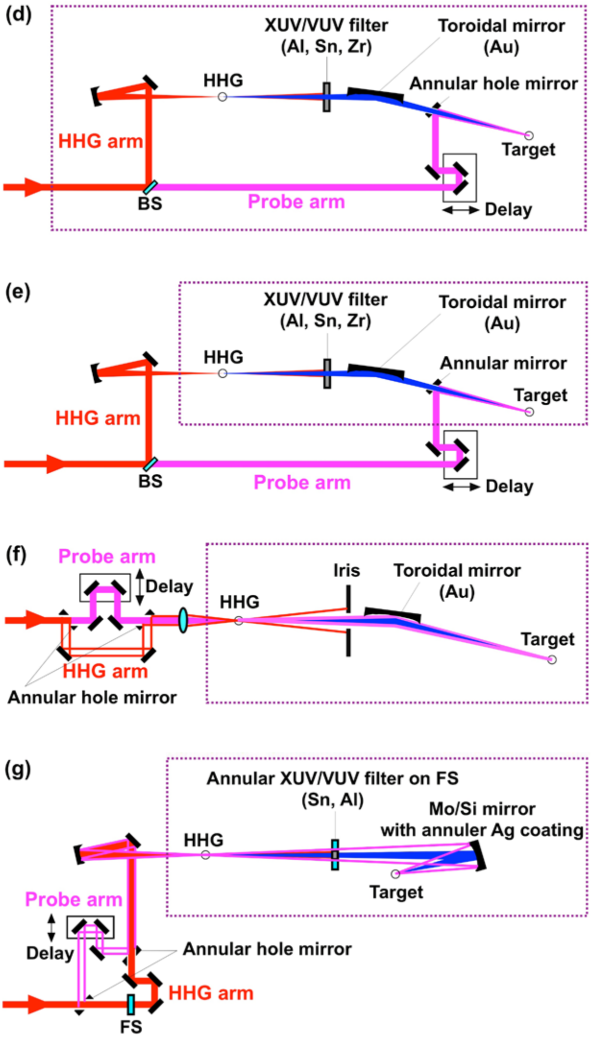

Figure 4.1(c) shows another type of MZ interferometer setup. One arm of the interferometer is located outside the vacuum chamber [17–19]. Thus, it is easy to access this arm to install optics. But, due to the extremely sensitive attosecond experiment, air fluctuations cannot be ignored. Thus, an active feedback loop was installed in the interferometer, which shows a stability of ∼8 as RMS (measured at 20 Hz) [19].

Another key technology is focusing optics for the XUV/VUV beam. In Fig. 4.1(d), the system is equipped with a Au coated toroidal mirror instead of a multilayer coated mirror [20–29]. The toroidal mirror allows broadband reflection and high reflectivity at grazing incidence [30], but it is difficult to machine and polish the mirror to the required surface figure and roughness. In this geometry, it is more difficult to focus the XUV beam than in the normal incidence case [31–34]. In addition, since many groups combine the XUV beam and the probe beam after HHG, the toroidal mirror configuration requires a longer propagation distance [20–29]. In order to improve the stability, some groups have built a robust interferometer inside the vacuum chamber [20, 28]. In another configuration, one arm is located outside of the chamber with an active feedback loop as shown in Fig. 4.1(e) [29]. Due to the large propagation distance, stabilization of the interferometer is critical and difficult to achieve.

4.2.3 Compact MZ Interferometer Setup

In order to solve the stabilization and complex manipulation issues, a compact MZ type interferometer was developed as shown in Fig. 4.1(f) [35]. The HHG driving laser (outer beam) is combined with the probe laser (inner beam) before the HHG cell. The interferometer is located completely outside of the vacuum chamber. After the HHG cell, the HHG driving beam is blocked by an iris and the probe NIR beam and harmonics collinearly propagate to the target. This arrangement is very stable owing to its compact size and the fact that it can be placed a significant distance from mechanical and turbo pumps. Another advantage is that it is easy to access both arms and to control the fields since the interferometer is outside the vacuum chamber. However, the system has three disadvantages. First, the two NIR pulses are overlapped in time and interfere at the HHG cell. Thus, even if the NIR probe pulse is much weaker than the HHG driving pulse, the generated harmonic spectrum is dramatically changed due to the highly nonlinear process of HHG. This effect is similar to the one encountered in two-color gating [36–43]. Second, since the harmonics and NIR probe beams are spatially overlapped and collinearly propagating, a metal filter cannot be installed. Then, the low order harmonic components (3rd, 5th, 7th, etc.) cannot be blocked. The gate width for the lower order harmonics is wider in time than the width for higher orders, so it is difficult to create the IAP with these low order harmonics, even if polarization gating [44] or DOG [11, 45] is used. Third, the HHG driving laser creates a dense plasma in the HHG cell [46, 47]. Thus, the NIR pulses are temporally stretched and spatially defocused due to the large material dispersion of the plasma [10].

In order to address these difficulties, we have developed a new compact MZ interferometer system as shown in Fig. 4.1(g) [48]. An inner beam (the HHG arm) passes through a fused silica plate (1 mm thick). In another arm, the outer beam (the probe arm) is reflected by an annular hole mirror. The stability of the interferometer with a 30 Hz active feedback loop (limited by CCD camera exposure time) is ∼50 as RMS over 24 hours. The fused silica produces a large group delay (∼5 ps) to the HHG driving pulse relative to the probe pulse. Thus, the two pulses do not temporally overlap in the HHG cell, nor do they interfere in the HHG process. Also, the fused silica plate in the interferometer produces a group delay dispersion in the pulse from the HHG arm relative to the pulse from the probe arm. As a result, the probe arm pulse is temporally stretched at the HHG cell; the HHG pulse is compressed while the dispersion in the probe pulse is overcompensated. Therefore, the probe arm pulse has a lower peak intensity ($<1 \times 10^{13}$ W/cm^2) so it cannot generate high harmonics. In addition, the NIR probe pulse passes through the HHG cell $\sim$5 ps earlier than the HHG driving pulse in the HHG cell. Thus, the probe pulse isn't temporarily stretched by a dense plasma created by the HHG driving pulse. The generated harmonic beam passes through a metal filter mounted in the center portion of an annular filter that blocks the co-propagating HHG driver beam and low order harmonic beams (3rd, 5th, 7th, etc.). The probe beam passes through the outer portion of the annular filter, a 1 mm thick fused silica plate. In order to reduce energy loss from diffraction, the filter is constructed so that it is the optical image of the last annular hole mirror in the interferometer. The thickness of the fused silica plate is chosen to match the plate in the HHG arm. Then, the probe pulse is compressed and the XUV and probe pulses are temporally overlapped in the target. A spherical mirror with the center part coated with Mo/Si and the outer ring coated with Ag focuses the beams to the target. As mentioned above, due to the MZ interferometer, the probe field can also be upconverted from 750 nm to 400 nm with an achromatic half-wave plate and a β-BaB$_2$O$_4$ (BBO) crystal. Further details of the 400 nm probe pulse generation and experimental conditions are described in Ref. [48]. Thus, with this simple system, it is possible to easily manipulate the power, polarization, and frequency of both pulses independently.

4.3 Frequency Tunable IAP with DOG

As mentioned above, the shortest IAP (80 as) were generated with linearly polarized 3.5 fs driving laser pulses [8]. This generation scheme extends the harmonic cutoff region up to 3.5 keV using 3 mJ, 12 fs pulses [49]. However, IAPs can only be produced near the cutoff region of the harmonics, which in practice is greater than 70 eV [50]. Double optical gating (DOG) [11, 51, 52] and polarization gating [20, 44] with elliptically polarized fields allow the generation of IAP in either the plateau region or the cutoff region of the harmonic spectrum because the HHG driving field is effectively gated to one half-cycle (1.3 fs). In particular, DOG has been used to generate an IAP with a 25–620 eV supercontinuum spectrum, which would support a 16 as pulse duration assuming flat phase [52].

In order to generate IAP in our system, a carrier-envelope (CE) phase stabilized Ti:Sapphire oscillator/chirped pulse amplifier followed by a hollow-core fiber compressor produces 7 fs, 1 mJ pulses centered at 750 nm wavelength with a 1 kHz repetition rate. In this laser system, the CE phase stability is $\sim$150 mrad RMS using a 30 Hz feedback loop. Figure 4.2(a) shows DOG optics. Two quartz plates (250 µm and 480 µm thickness) are inserted in the HHG arm in Fig. 4.1(g), and the BBO crystal (150 µm thickness) is located before the HHG cell inside the vacuum chamber. The BBO crystal can also be used to produce the second harmonic of the probe field. Figure 4.2(b) shows the typical harmonic spectrum (upper figure) with

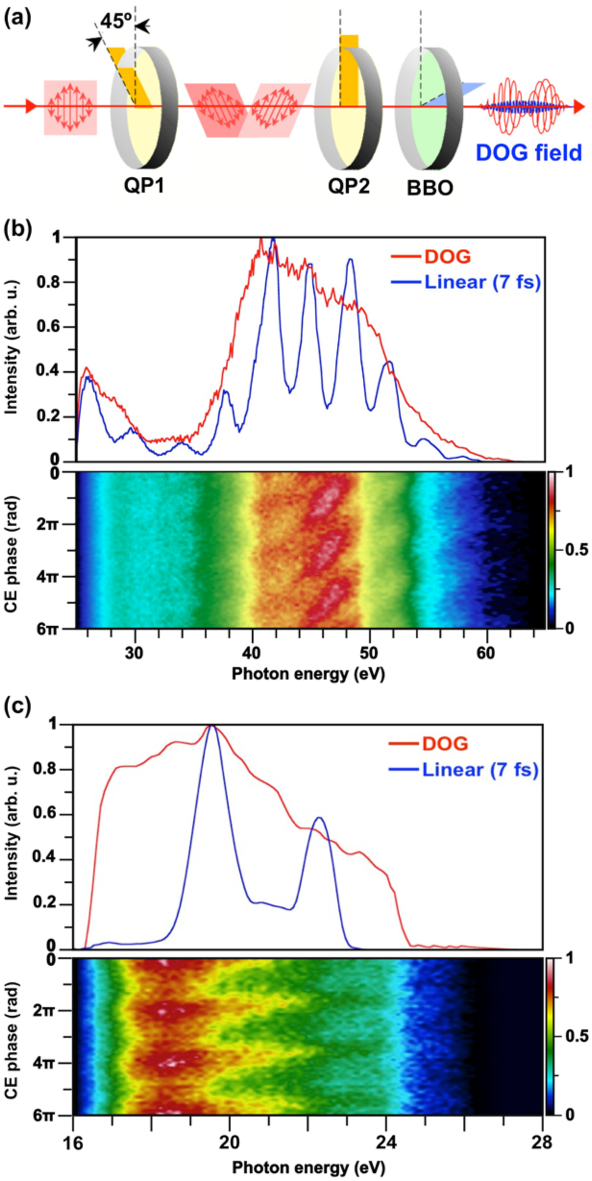

Fig. 4.2 DOG setup (**a**) and typical high-harmonic spectrum with linearly polarized pulse and DOG (*upper figure*) and CE phase dependence with DOG (*lower figure*) using (**b**) an Al filter for the XUV region and (**c**) a Sn filter for the VUV region. QP1: Quartz plate (250 μm), QP2: Quartz plate (480 μm), and BBO: β-BaB$_2$O$_4$ (150 μm)

a linearly polarized pulse and with DOG: the lower figure shows the CE phase dependence of the harmonic spectrum with DOG. Both panels were obtained using an Al filter. Analogous results using a Sn filter are shown in Fig. 4.2(c). Demonstrated here, the spectral bandwidth can be filtered by Al and Sn filters.

4.4 Temporal Characterization of IAP in XUV and VUV Regions

In order to characterize the pulses, the attosecond streak camera technique is used [53]. This technique is basically a cross-correlation of the XUV/VUV field and the probe field. Photoelectrons created by the IAP are given a momentum shift by the probe field. The photoelectron kinetic energy distribution is analyzed using a linear photoelectron time-of-flight spectrometer and measured as a function of delay time between the XUV/VUV and probe pulses [48]. The measured streak trace contains information about the temporal structure and the phase of the photoelectron wave packet. Figure 4.3(a) shows a measured streak trace with a 750 nm streak field using an Al filter and Ne as the target gas in the photoelectron spectrometer. The temporal profile and phase are reconstructed by the Principal Component Generalized Projections Algorithm method [54]. The temporal profile indicates a 140 as pulse as shown in Fig. 4.3(b). The satellite pulses are suppressed with less than a 1% contribution at 750 nm half (±1.25 fs) and full (±2.5 fs) cycles, indicating a well isolated pulse compared to Ref. [8] in which satellite pulses are measured with an 8 % contribution. In addition, the measured and the reconstructed harmonic spectra agree well as shown in Fig. 4.3(c).

Figure 4.4(a) shows the measured streak trace with a 750 nm field using a Sn filter and Ar as the target. The reconstructed temporal profile and phase indicate a 395 as pulse as shown in Fig. 4.4(b). Again, the pre- and post-pulses are suppressed to less than a 1 % contribution at the 750 nm half and full cycle regions. In addition, the measured and the reconstructed harmonic spectra agree well as shown in Fig. 4.4(c). These results indicate the flexibility of selecting the XUV or VUV frequency range. Of course, in future experiments, if other HHG gases (He, Ne, Kr, Xe, etc.), different filters (Zr, Si, Ti, Pb, etc.) [30], and/or various multilayer coated mirror (SiC/Mg, Sc/Si, Al/C, etc.) are used [55], IAPs with different central frequencies can be generated.

Finally, a streak trace is obtained with a 400 nm streak field using an Al filter and Ne as the target as shown in Fig. 4.5(a). The reconstructed temporal profile and phase indicate a 118 as pulse as shown in Fig. 4.5(b). The measured and the reconstructed spectra agree well as shown in Fig. 4.5(c). This result is important for chemical applications of attosecond pulses. For example, a plasmon resonance in a gold or silver nanoparticle can be excited with a pulse at 400 nm [56]. A streaking measurement can investigate the plasmon dephasing time by observing the enhancement of the photoelectron momentum shift due to the field of the plasmon resonance [5]. Frequency control of the excitation pulse allows nanoparticles of varying structures and plasmon resonance frequencies to be studied. The compact MZ interferometer design allows the probe field to be modified independently of the driving HHG field. In future work, the compact interferometer located outside of the vacuum chamber will easily allow the probe field to be modified using, for example, an optical parametric amplifier [57], an adaptive spatial light modulator [58], or THz oscillator [59].

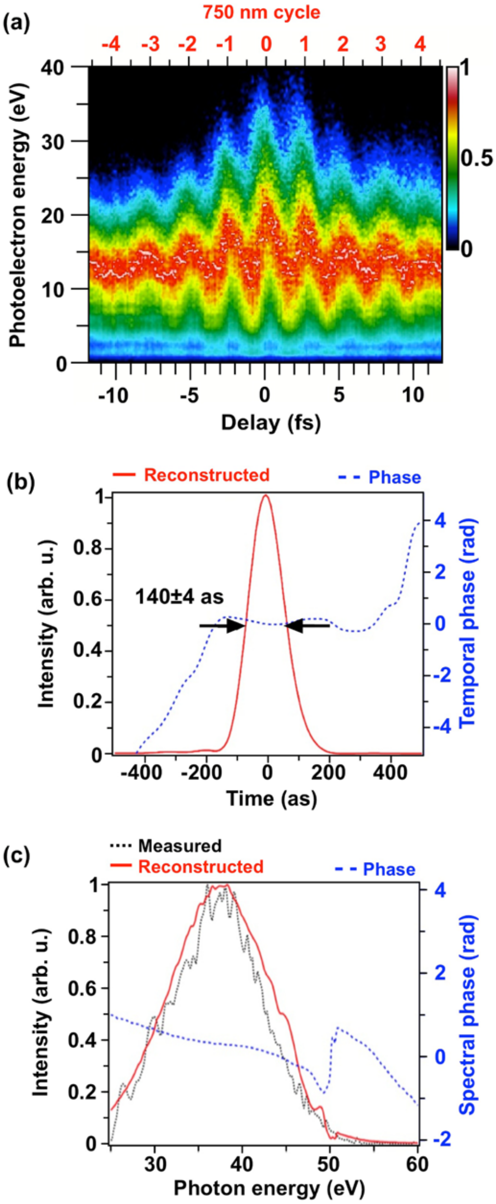

Fig. 4.3 Streak traces and XUV pulse characterization. (**a**) Measured streak trace with Al filter using 750 nm field. (**b**) The reconstructed pulse (*solid line*) and phase (*dotted line*). (**c**) The reconstructed spectrum (*solid line*) and phase (*dotted line*) and the measured spectrum (*dashed line*) without the streak field

4.5 Conclusions

The new setup with compact MZ interferometer realized robust, flexibility, and easy operation. An important step for future attosecond dynamics studies is made by generating IAP with variable center frequencies. XUV and VUV pulses with 140 as duration (26–55 eV) and 395 as duration (16–25 eV), respectively, are characterized.

Fig. 4.4 Streak traces and VUV pulse characterization. (**a**) Measured streak trace with Sn filter using 750 nm field. (**b**) The reconstructed pulse (*solid line*) and phase (*dotted line*). (**c**) The reconstructed spectrum (*solid line*) and phase (*dotted line*) and the measured spectrum (*dashed line*) without the streak field

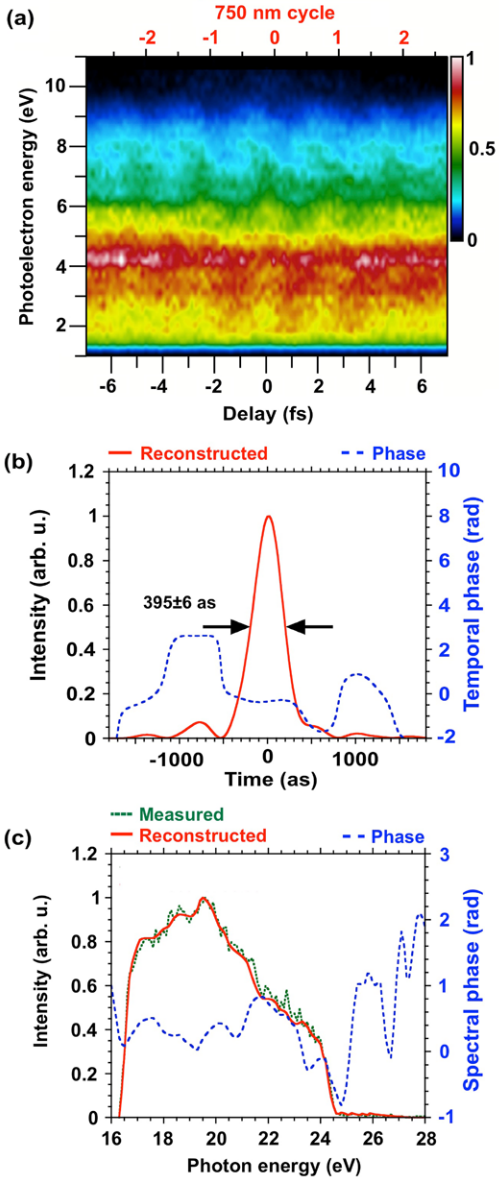

Tunable IAP will allow a greater variety of dynamics in atoms and molecules to be studied. In addition, the characterization of IAP (118 as duration, 26–67 eV) with a streaking measurement using a 400 nm streak field is demonstrated. Many atomic and molecular dynamics processes depend on which states are excited by the light pulses. Frequency control of pump and probe pulses will thus allow the temporal structures and the relative phases of a broader range of ultrafast electronic

Fig. 4.5 Streak traces and XUV pulse characterization. (**a**) Measured streak trace with Al filter using 400 nm field. (**b**) The reconstructed pulse (*solid line*) and phase (*dotted line*). (**c**) The reconstructed spectrum (*solid line*) and phase (*dotted line*) and the measured spectrum (*dashed line*) without the streak field

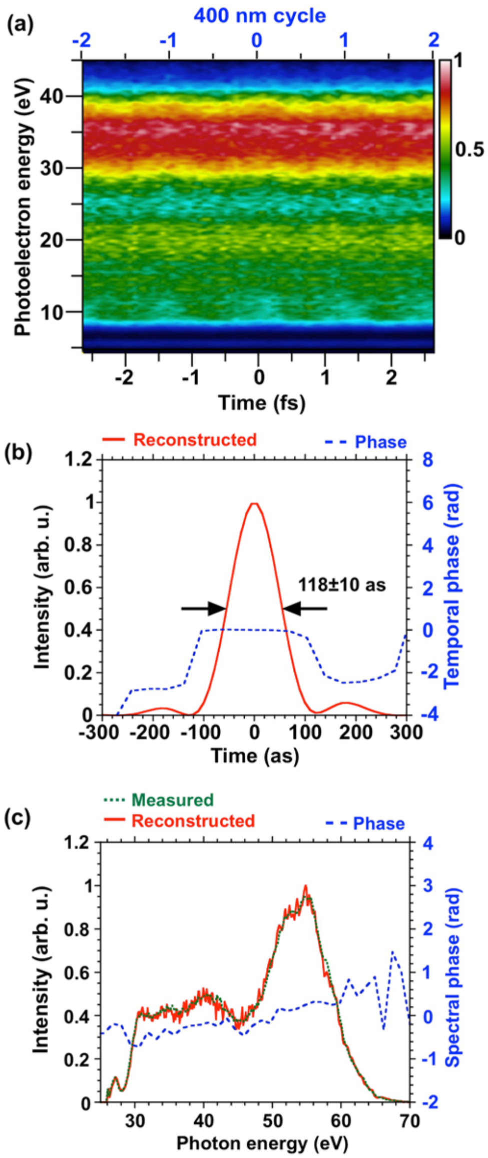

and molecular dynamics to be determined. This system and result increased flexibility will allow attosecond experimental techniques to be more widely applied to chemical systems.

Acknowledgements This work was supported by the Director, Office of Science, Office of Basic Energy Sciences, and the Division of Chemical Sciences, Geosciences, and Biosciences, of the U.S. Department of Energy at Lawrence Berkeley National Laboratory under Contract No. DE-AC02-05CH11231. M.J.B. and A.R.B. acknowledge support from National Science Foundation

Graduate Research Fellowships. S.R.L. acknowledges additional support from the National Science Foundation, Chemistry Division, a National Science Foundation, Extreme Ultraviolet Science Engineering Research Center, and a National Security Science and Engineering Faculty Fellowship. The authors thank the LBNL Center for X-Ray Optics (CXRO) for custom made XUV/VUV optics.

References

1. M. Drescher, M. Hentschel, R. Kienberger, M. Uiberacker, V. Yakovlev, A. Scrinzi, Th. Westerwalbesloh, U. Kleineberg, U. Heinzmann, F. Krausz, Time-resolved atomic inner-shell spectroscopy. Nature **419**, 803–807 (2002)
2. R. Kienberger, E. Goulielmakis, M. Uiberacker, A. Baltuška, V. Yakovlev, F. Bammer, A. Scrinzi, Th. Westerwalbesloh, U. Kleineberg, U. Heinzmann, M. Drescher, F. Krausz, Atomic transient recorder. Nature **427**, 817–821 (2004)
3. M. Uiberacker, Th. Uphues, M. Schultze, A.J. Verhoef, V. Yakovlev, M.F. Kling, J. Rauschenberger, N.M. Kabachnik, H. Schröder, M. Lezius, K.L. Kompa, H.G. Muller, M.J.J. Vrakking, S. Hendel, U. Kleineberg, U. Heinzmann, M. Drescher, F. Krausz, Attosecond real-time observation of electron tunnelling in atoms. Nature **446**, 627–632 (2007)
4. E. Goulielmakis, Z.-H. Loh, A. Wirth, R. Santra, N. Rohringer, V.S. Yakovlev, S. Zherebtsov, T. Pfeifer, A.M. Azzeer, M.F. Kling, S.R. Leone, F. Krausz, Real-time observation of valence electron motion. Nature **466**, 739–744 (2010)
5. T. Pfeifer, M.J. Abel, P.M. Nagel, A. Jullien, Z. Loh, M.J. Bell, D.M. Neumark, S.R. Leone, Time-resolved spectroscopy of attosecond quantum dynamics. Chem. Phys. Lett. **463**, 11–24 (2008)
6. G. Sansone, F. Kelkensberg, J.F. Pérez-Torres, F. Morales, M.F. Kling, W. Siu, O. Ghafur, P. Johnsson, M. Swoboda, E. Benedetti, F. Ferrari, F. Lépine, J.L. Sanz-Vicario, S. Zherebtsov, I. Znakovskaya, A. L'Huillier, M.Yu. Ivanov, M. Nisoli, F. Martín, M.J.J. Vrakking, Electron localization following attosecond molecular photoionization. Nature **465**, 763–767 (2010)
7. A.L. Cavalieri, N. Müller, T. Uphues, V.S. Yakovlev, A. Baltuška, B. Horvath, B. Schmidt, L. Blümel, R. Holzwarth, S. Hendel, M. Drescher, U. Kleineberg, P.M. Echenique, R. Kienberger, F. Krausz, U. Heinzmann, Attosecond spectroscopy in condensed matter. Nature **449**, 1029–1032 (2007)
8. E. Goulielmakis, M. Schultze, M. Hofstetter, V.S. Yakovlev, J. Gagnon, M. Uiberacker, A.L. Aquila, E.M. Gullikson, D.T. Attwood, R. Kienberger, F. Krausz, U. Kleineberg, Single-cycle nonlinear optics. Science **320**, 1614–1617 (2008)
9. H. Mashiko, A. Suda, K. Midorikawa, Focusing coherent soft-x-ray radiation to a micrometer spot size with an intensity of 10^{14} W/cm^2. Opt. Lett. **29**, 1927–1929 (2004)
10. D. Attwood, *Soft X-Rays and Extreme Ultraviolet Radiation* (Cambridge University Press, Cambridge, 1999)
11. H. Mashiko, S. Gilbertson, C. Li, S.D. Khan, M.M. Shakya, E. Moon, Z. Chang, Double optical gating of high-order harmonic generation with carrier-envelope phase stabilized lasers. Phys. Rev. Lett. **100**, 103906 (2008)
12. E. Goulielmakis, V.S. Yakovlev, A.L. Cavalieri, M. Uiberacker, V. Pervak, A. Apolonski, R. Kienberger, U. Kleineberg, F. Krausz, Attosecond control and measurement: lightwave electronics. Science **317**, 769–775 (2007)
13. T. Witting, F. Frank, W.A. Okell, C.A. Arrell, J.P. Marangos, J.W.G. Tisch, Sub-4-fs laser pulse characterization by spatially resolved spectral shearing interferometry and attosecond streaking. J. Phys. B, At. Mol. Opt. Phys. **45**, 074014 (2012)
14. I. Thomann, A. Bahabad, X. Liu, R. Trebino, M.M. Murnane, H.C. Kapteyn, Characterizing isolated attosecond pulses from hollow-core waveguides using multi-cycle driving pulses. Opt. Express **17**, 4611–4633 (2009)

15. F.M. Böttcher, B. Manschwetus, H. Rottke, N. Zhavoronkov, Z. Ansari, W. Sandner, Interferometric long-term stabilization of a delay line: a tool for pump–probe photoelectron–photoion-coincidence spectroscopy on the attosecond time scale. Appl. Phys. B, Lasers Opt. **91**, 287–293 (2008)
16. M. Fieß, M. Schultze, E. Goulielmakis, B. Dennhardt, J. Gagnon, M. Hofstetter, R. Kienberger, F. Krausz, Versatile apparatus for attosecond metrology and spectroscopy. Rev. Sci. Instrum. **81**, 093103 (2010)
17. O. Guyétand, M. Gisselbrecht, A. Huetz, P. Agostini, R. Taïeb, A. Maquet, B. Carré, P. Breger, O. Gobert, D. Garzella, J.-F. Hergott, O. Tcherbakoff, H. Merdji, M. Bougeard, H. Rottke, M. Böttcher, Z. Ansari, P. Antoine, Evolution of angular distributions in two-colour, few-photon ionization of helium. J. Phys. B, At. Mol. Opt. Phys. **41**, 051002 (2008)
18. K. Oguri, T. Nishikawa, T. Ozaki, H. Nakano, Sampling measurement of soft-x-ray-pulse shapes by femtosecond sequential ionization of Kr^+ in an intense laser field. Opt. Lett. **29**, 1279–1281 (2004)
19. S. Gilbertson, Y. Wu, S.D. Khan, M. Chini, K. Zhao, X. Feng, Z. Chang, Isolated attosecond pulse generation using multicycle pulses directly from a laser amplifier. Phys. Rev. A **81**, 043810 (2010)
20. G. Sansone, E. Benedetti, F. Calegari, C. Vozzi, L. Avaldi, R. Flammini, L. Poletto, P. Villoresi, C. Altucci, R. Velotta, S. Stagira, S. De Silvestri, M. Nisoli, Isolated single-cycle attosecond pulses. Science **314**, 443–446 (2006)
21. G. Gademann, F. Kelkensberg, W.K. Siu, P. Johnsson, M.B. Gaarde, K.J. Schafer, M.J.J. Vrakking, Attosecond control of electron–ion recollision in high harmonic generation. New J. Phys. **13**, 033002 (2011)
22. E. Mansten, J.M. Dahlström, P. Johnsson, M. Swoboda, A. L'Huillier, J. Mauritsson, Spectral shaping of attosecond pulses using two-colour laser fields. New J. Phys. **10**, 083041 (2008)
23. M. Holler, F. Schapper, L. Gallmann, U. Keller, Attosecond electron wave-packet interference observed by transient absorption. Phys. Rev. Lett. **106**, 123601 (2011)
24. O. Guyétand, M. Gisselbrecht, A. Huetz, P. Agostini, R. Taïeb, A. Maquet, B. Carré, P. Breger, O. Gobert, D. Garzella, J.-F. Hergott, O. Tcherbakoff, H. Merdji, M. Bougeard, H. Rottke, M. Böttcher, Z. Ansari, P. Antoine, Evolution of angular distributions in two-colour, few-photon ionization of helium. J. Phys. B, At. Mol. Opt. Phys. **41**, 051002 (2008)
25. Q. Li, K. Hoogeboom-Pot, D. Nardi, M.M. Murnane, H.C. Kapteyn, M.E. Siemens, E.H. Anderson, O. Hellwig, E. Dobisz, B. Gurney, R. Yang, K.A. Nelson, Generation and control of ultrashort-wavelength two-dimensional surface acoustic waves at nanoscale interfaces. Phys. Rev. B **85**, 195431 (2012)
26. D.H. Ko, K.T. Kim, J. Park, J.-h. Lee, C.H. Nam, Attosecond chirp compensation over broadband high-order harmonics to generate near transform-limited 63 as pulses. New J. Phys. **12**, 063008 (2010)
27. W. Cao, G. Laurent, C. Jin, H. Li, Z. Wang, C.D. Lin, I. Ben-Itzhak, C.L. Cocke, Spectral splitting and quantum path study of high-harmonic generation from a semi-infinite gas cell. J. Phys. B, At. Mol. Opt. Phys. **45**, 074013 (2012)
28. http://www.physics.ohio-state.edu/~dimauro/lab.html
29. M. Chini, H. Mashiko, H. Wang, S. Chen, C. Yun, S. Scott, S. Gilbertson, Z. Chang, Delay control in attosecond pump-probe experiments. Opt. Express **17**, 21459–21464 (2009)
30. B.L. Henke, E.M. Gullikson, J.C. Davis, X-ray interactions: photoabsorption, scattering, transmission, and reflection at E = 50–30000 eV, Z = 1–92. At. Data Nucl. Data Tables **54**, 181–342 (1993)
31. D. Yoshitomi, T. Shimizu, T. Sekikawa, S. Watanabe, Generation and focusing of submilliwatt-average-power 50-nm pulses by the fifth harmonic of a KrF laser. Opt. Lett. **27**, 2170–2172 (2002)
32. C. Valentin, D. Douillet, S. Kazamias, Th. Lefrou, G. Grillon, F. Augé, G. Mullot, Ph. Balcou, P. Mercére, Ph. Zeitoun, Imaging and quality assessment of high-harmonic focal spots. Opt. Lett. **28**, 1049–1051 (2003)

33. E.J. Takahashi, Y. Nabekawa, H. Mashiko, H. Hasegawa, A. Suda, K. Midorikawa, Generation of strong optical field in soft x-ray region by using high-order harmonics. IEEE J. Sel. Top. Quantum Electron. **10**, 1315–1328 (2004)
34. H. Mashiko, A. Suda, K. Midorikawa, Focusing multiple high-order harmonics in the extreme-ultraviolet and soft-x-ray regions by a platinum-coated ellipsoidal mirror. Appl. Opt. **45**, 573–577 (2006)
35. Y. Mairesse, A. de Bohan, L.J. Frasinski, H. Merdji, L.C. Dinu, P. Monchicourt, P. Breger, M. Kovaćev, R. Taïeb, B. Carré, H.G. Muller, P. Agostini, P. Saliéres, Attosecond synchronization of high-harmonic soft x-rays. Science **302**, 1540–1543 (2003)
36. M.D. Perry, J.K. Crane, High-order harmonic emission from mixed fields. Phys. Rev. A **48**, R4051 (1993)
37. H. Eichmann, A. Egbert, S. Nolte, C. Momma, B. Wellege-hausen, W. Becker, S. Long, J.K. McIver, Polarization-dependent high-order two-color mixing. Phys. Rev. A **51**, R3414 (1995)
38. U. Andiel, G.D. Tsakiris, E. Cormier, K. Witte, High-order harmonic amplitude modulation in two-colour phase-controlled frequency mixing. Europhys. Lett. **47**, 42 (1999)
39. T.T. Liu, T. Kanai, T. Sekikawa, S. Watanabe, Significant enhancement of high-order harmonics below 10 nm in a two-color laser field. Phys. Rev. A **73**, 063823 (2006)
40. I.J. Kim, G.H. Lee, S.B. Park, Y.S. Lee, T.K. Kim, C.H. Nam, T. Mocek, K. Jakubczak, Generation of submicrojoule high harmonics using a long gas jet in a two-color laser field. Appl. Phys. Lett. **92**, 021125 (2008)
41. N. Dudovich, O. Smirnova, J. Levesque, Y. Mairesse, M.Yu. Ivanov, D.M. Villeneuve, P.B. Corkum, Measuring and controlling the birth of attosecond XUV pulses. Nat. Phys. **2**, 781–786 (2006)
42. J. Mauritsson, P. Johnsson, E. Gustafsson, A. L'Huillier, K.J. Schafer, M.B. Gaarde, Attosecond pulse trains generated using two color laser fields. Phys. Rev. Lett. **97**, 013001 (2006)
43. Y. Oishi, M. Kaku, A. Suda, F. Kannari, K. Midorikawa, Generation of extreme ultraviolet continuum radiation driven by a sub-10-fs two-color field. Opt. Express **14**, 7230 (2006)
44. I.J. Sola, E. Mével, L. Elouga, E. Constant, V. Strelkov, L. Poletto, P. Villoresi, E. Benedetti, J.-P. Caumes, S. Stagira, C. Vozzi, G. Sansone, M. Nisoli, Controlling attosecond electron dynamics by phase-stabilized polarization gating. Nat. Phys. **2**, 319 (2006)
45. Z. Chang, Controlling attosecond pulse generation with a double optical gating. Phys. Rev. A **76**, 051403R (2007)
46. M.J. Abel, T. Pfeifer, P.M. Nagel, W. Boutu, M.J. Bell, C.P. Steiner, D.M. Neumark, S.R. Leone, Isolated attosecond pulses from ionization gating of high-harmonic emission. Chem. Phys. **366**, 9–14 (2009)
47. A. Jullien, T. Pfeifer, M.J. Abel, P.M. Nagel, M.J. Bell, D.M. Neumark, S.R. Leone, Ionization phase-match gating for wavelength-tunable isolated attosecond pulse generation. Appl. Phys. B **93**, 433–442 (2008)
48. H. Mashiko, M.J. Bell, A.R. Beck, M.J. Abel, P.M. Nagel, C.P. Steiner, J. Robinson, D.M. Neumark, S.R. Leone, Tunable frequency-controlled isolated attosecond pulses characterized by either 750 nm or 400 nm wavelength streak fields. Opt. Express **18**, 25887–25895 (2010)
49. E. Seres, J. Seres, Ch. Spielmann, X-ray absorption spectroscopy in the keV range with laser generated high harmonic radiation. Appl. Phys. Lett. **89**, 181919 (2006)
50. P.B. Corkum, F. Krausz, Attosecond science. Nat. Phys. **3**, 381–387 (2007)
51. X. Feng, S. Gilbertson, H. Mashiko, H. Wang, S.D. Khan, M. Chini, Y. Wu, K. Zhao, Z. Chang, Generation of isolated attosecond pulses with 20 to 28 femtosecond lasers. Phys. Rev. Lett. **103**, 183901 (2009)
52. H. Mashiko, S. Gilbertson, M. Chini, X. Feng, C. Yun, H. Wang, S.D. Khan, S. Chen, Z. Chang, Extreme ultraviolet supercontinua supporting pulse durations of less than one atomic unit of time. Opt. Lett. **34**, 3337–3339 (2009)
53. J. Itatani, F. Quéré, G.L. Yudin, M.Yu. Ivanov, F. Krausz, P.B. Corkum, Attosecond streak camera. Phys. Rev. Lett. **88**, 173903 (2002)
54. D.J. Kane, Principal components generalized projections: a review. J. Opt. Soc. Am. B **25**, A120–A132 (2008)

55. M. Yamamoto, M. Yanagihara, H. Kimura, M. Watanabe, Soft x-ray multilayer optics for use with synchrotron radiation. J. Jpn. Soc. Sync. Rad. Res. **9**, 16–39 (1996) (in Japanese)
56. P.K. Jain, M.A. El-Sayed, Plasmonic coupling in noble metal nanostructures. Chem. Phys. Lett. **487**, 153–164 (2010)
57. A. Shirakawa, I. Sakane, T. Kobayashi, Pulse-front-matched optical parametric amplification for sub-10 fs pulse generation tunable in the visible and near infrared. Opt. Lett. **23**, 1292–1294 (1998)
58. E. Matsubara, K. Yamane, T. Sekikawa, M. Yamashita, Generation of 2.6 fs optical pulses using induced-phase modulation in a gas-filled hollow fiber. J. Opt. Soc. Am. B **24**, 985–989 (2007)
59. K. Tanaka, H. Hirori, M. Nagai, THz nonlinear spectroscopy of solids. IEEE Trans. Terahertz Sci. Technol. **1**, 301–312 (2011)

Chapter 5
Strong-Field Atomic Physics in the X-ray Regime

Louis F. DiMauro and Christoph A. Roedig

Abstract In 1999 the DOE Basic Energy Sciences Advisory Committee defined an innovative scientific direction for the new millennium. In the report the panel recognized the scientific opportunity posed by accelerator-based and tabletop sources of short wavelength radiation. The report emphasized that revolutionary science would be enabled by source parameters that include "high degree of coherence, pulse brevity and high pulsed energy" while pushing the frontiers towards the hard x-ray regime. The panel recommended strategic investment in a new light source, which marked the genesis of the world's first x-ray free-electron laser project. This chapter reports on some of the initial atomic physics experiments conducted at the Linac Coherent Light Source (LCLS) at SLAC and addresses the question as to limits of validity of perturbation theory in describing an intense x-ray pulse interacting with matter.

5.1 Introduction

The last decade has seen the emergence of a new class of sources, dubbed fourth-generation, that provide light with unprecedented pulse duration and/or energy at high photon frequency. Various approaches have been pursued that produce different attributes for investigating new regimes of light-matter interactions. For example, high harmonic generation [1, 2] has enabled the attosecond frontier [3]. However, free-electron lasers operating in the soft and hard x-ray regime are defining unique capabilities and applications that are unrivaled by previous electron-based sources. In the context of this review, x-ray free-electron lasers (XFEL) are allowing the first experimental realization aimed at addressing intense x-ray-matter interactions, thus we will limit our discussion to only this aspect. The reader is referred to a number of recent reviews that provide a more comprehensive treatment of these devices and their application.

The first step towards a user-based facility was initiated in Hamburg, Germany with the commissioning of the **F**ree electron **LAS**er in **H**amburg (FLASH) in 2005

L.F. DiMauro (✉) · C.A. Roedig
Department of Physics, The Ohio State University, Columbus, OH 43210, USA
e-mail: dimauro@mps.ohio-state.edu

K. Yamanouchi et al. (eds.), *Progress in Ultrafast Intense Laser Science X*,
Springer Series in Chemical Physics 106, DOI 10.1007/978-3-319-00521-8_5,

at DESY. Initially the FLASH FEL produced ~100 μJ, 50–10 fs pulses at fundamental photon energies of 25–95 eV while an upgraded, FLASH II, in 2007 pushed operation to 200 eV. The reader is referred to some recent review on the machine capabilities [4] and science program [5]. A parallel project at Stanford Linear Accelerator Center (SLAC) in Menlo Park, California pursued the development of a millijoule, hard x-ray (0.8–8 keV fundamental operation) FEL. In the summer of 2009, the **L**inac **C**oherent **L**ight **S**ource (LCLS) was commissioned and rapidly achieved full output specifications [6] while a user scientific program began that Autumn [7].

5.2 Initial LCLS Ionization Studies in Neon Atoms

In sharp contrast with optical ionization where valence shell excitation dominates, x-rays preferentially ionize inner shell electrons. Examination of the absorption spectrum of neon shows that less than ten percent of the total cross-section (0.35 Mb) at the K-edge (870.1 eV) is attributable to valence shell excitation. Consequently, photoionization creates an inner shell vacancy that is an excited state which spontaneously relaxes by emitting a photon or Auger decay. For neon, and other low-Z atoms, the ultra-fast (2.6 fs) Auger process dominates (one valence electron fills the $1s$-hole and one is freed [~820–850 eV energy]) leaving a doubly-charged neon ion. Ionization with unity probability by linear absorption of a 10 fs, 870.1 eV pulse requires a flux of 3×10^{32} photons/cm^2 s or a peak intensity of 4×10^{16} W/cm^2. This intensity is order of magnitudes larger than that needed to drive near-threshold 1-photon ionization of a $2p$-valence electron (21.6 eV binding energy) with unit probability, in fact it even exceeds that required to tunnel ionize helium at optical frequencies. However, as we will see in Sect. 5.3, this extraordinary soft x-ray intensity produces little quiver of the continuum electron due to the λ^2 scaling of the ponderomotive energy.

5.2.1 Sequential Ionization of Neon with High Fluence X-rays

The first LCLS experiment studied the photoionization of neon atoms using the AMO end-station, the reader is referred to a review paper [8] for a detailed description. In summary, the LCLS could deliver 100–200 fs, millijoule pulses over a 0.8–2 keV photon energy into the Atomic, Molecular and Optical Science (AMOS) end-station. The high-field chamber of the AMO end-station is equipped with a Wiley-McLaren time-of-flight (TOF) ion spectrometer and five TOF electron spectrometers with retarding electrostatic lenses [9], oriented at different angles with respect to the x-ray polarization axis. The focusing optics, a Kirkpatrick-Baez (KB) mirror pair, has been characterized to yield a focal spot of ~2 μm^2.

In the experiment [10], neon ion m/q-distributions were investigated at different intensities, pulse durations and photon energies. Figure 5.1 shows the (a) measured ion yields and (b) a comparison between theory and experiment at three different photon energies. Clearly, the large fluence of x-rays is sufficient not only to saturate the neutral neon ionization, as estimated above, but essentially strip off all

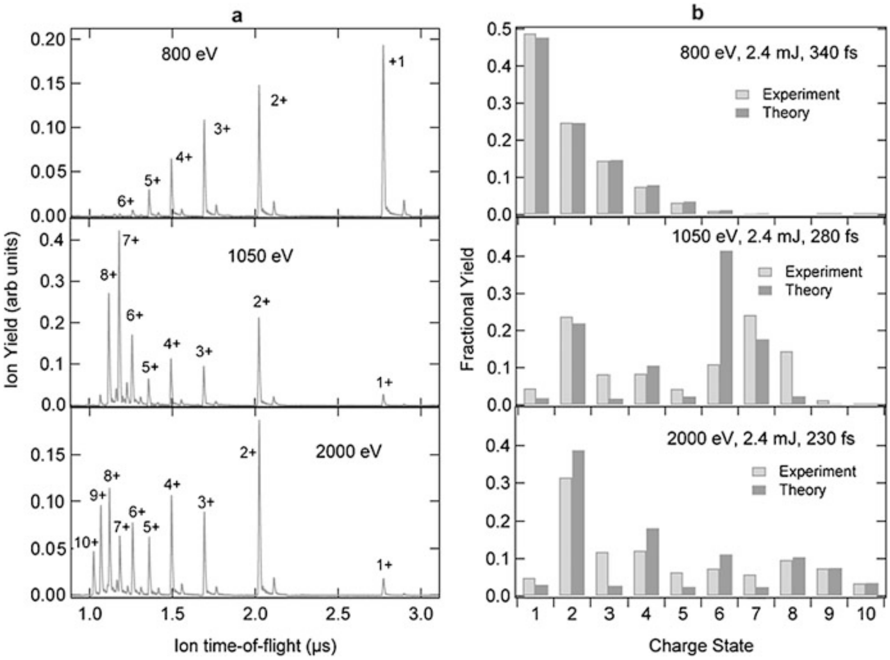

Fig. 5.1 Neon charge-state yields for x-ray energies below, above and far above the 1*s*-shell binding energy, 0.87 keV. (**a**) Experimental charge-state distribution for 0.8 keV (*top*), 1.05 keV (*middle*) and 2.0 keV (*bottom*). (**b**) Comparison of experimental charge-state yields, corrected for detection efficiency, with rate equation simulations. The cross-sections in the model are based on perturbation theory. The weaker peaks to the right of each charge state is the less abundant ^{22}Ne isotope. The figure is reproduced, with permission, from [10]

the electrons. The three different wavelengths provide a window into the ionization sequence. At the low photon energy (800 eV), K-shell ionization cannot occur via 1-photon ionization, thus charge state production proceeds through a sequence of valence shell excitation terminating at Ne^{8+} since only the 8, $n = 2$ electrons can be ionized. At 2 keV photon energy all 10-electrons are removed through a sequence of 1*s*-photoionization followed by Auger decay resulting in a propensity in even-charge state production (see bottom graphs in Fig. 5.1). This measurement is the first observation of sequential atomic ionization from the inside out, as opposed to sequential valence ionization (outside-in) by strong optical fields. At intermediate photon energy (1.05 keV) ionization of the low-charge states proceeds via photoionization/Auger decay until the K-shell binding energy (1096 eV for Ne^{6+}) exceeds 1.05 keV. At this point, valence photoionization proceeds removing the $2s^2$-electrons, terminating with the production of Ne^{8+}. The theoretical calculations, shown in Fig. 5.1(b), are based on a rate equation model that includes only sequential single-photon absorption and Auger decay processes, which produces reasonable agreement with the measurement. The agreement is best at 800 eV since valence shell ionization dominates and becomes less satisfactory and therefore interesting as inner-shell processes contribute. This investigation provided a preview of the richness of new phenomena that can arise from matter interacting with an intense x-ray pulse but equally important, it showed that the primary ionization mechanisms were well within the framework of perturbation theory, even at intensities of $10^{17}\ \mathrm{W/cm^2}$.

5.2.2 Nonlinear Two-Photon Ionization of Neon

The potential to study laser-matter interaction involving x-ray intensities near $10^{17}\ \mathrm{W/cm^2}$ led naturally to the objective of observing for the first time nonlinear, multiphoton x-ray absorption. The study and application of nonlinear processes from the microwave to the ultra-violet frequencies is extensive and well documented. Recently, those studies have been extended to the extreme ultraviolet (XUV) photon energy range, first with high harmonics sources [11, 12], and then with FLASH XUV free-electron lasers [5]. One reason for the absence of experiments is the rapid decrease of nonlinear susceptibility with increasing frequency ν. This can be seen by considering a perturbative 2-photon transition whose cross-section, $\sigma^{(2)}$ can be approximated as $\sigma^{(1)}\tau\sigma^{(1')}$, where $\sigma^{(1)}$ and $\sigma^{(1')}$ are 1-photon cross-sections and τ is the reciprocal of the detuning [13]. For the non-resonant case, $\sigma^{(1)}$ and $\sigma^{(1')}$ can be assumed equal and $\tau \propto \nu^{-1}$ or equivalently, the virtual state lifetime is the optical period. Consequently, passing from the visible frequencies to kilovolt x-rays results in at least a thousand-fold decrease in $\sigma^{(2)}$, thus requiring higher intensity.

Initial efforts focused on the interaction with simple atomic targets, specifically helium and neon. Helium was chosen because of its simple valence structure. On the other hand, neon offers the possibility of inner-shell excitation and larger cross-sections in the photon energy range available from the LCLS during these first experimental runs (0.2–2 keV). For helium, the small (860 barns at 0.8 keV) cross-section limited measurement to photon energies near 0.8 keV (minimum LCLS photon energy). Total ion yield and photoelectron energy spectrum were studied as a function of intensity at 0.8 keV while additional ion yields were recorded at shorter wavelengths ($\sim$ 1 keV). The measurements produced no evidence of an ATI electron peak (2-photon one-electron ionization) near 1.6 keV. However, the helium measurement provided valuable information on the LCLS performance. For example, the dependence of the ratio of $\mathrm{He}^{2+}/\mathrm{He}^{+}$ ionization on x-ray pulse energy revealed a maximum intensity of $5 \times 10^{16}\ \mathrm{W/cm^2}$, approximately an order of magnitude less than expected performance.

For neon, ion and electron measurements were performed to study the ionization of a K-shell electron by simultaneous absorption of two x-ray photons [14]. An estimate based on the expected x-ray fluxes and a value of two-photon ionization cross-section [15, 16] given by perturbation theory suggested that the effect would be weak, but observable. One caveat stems from the fact that the x-ray radiation can be accompanied by harmonics of the fundamental frequency, including a small (<1 %) amount of 2nd harmonic that was verified by ionization measurements using

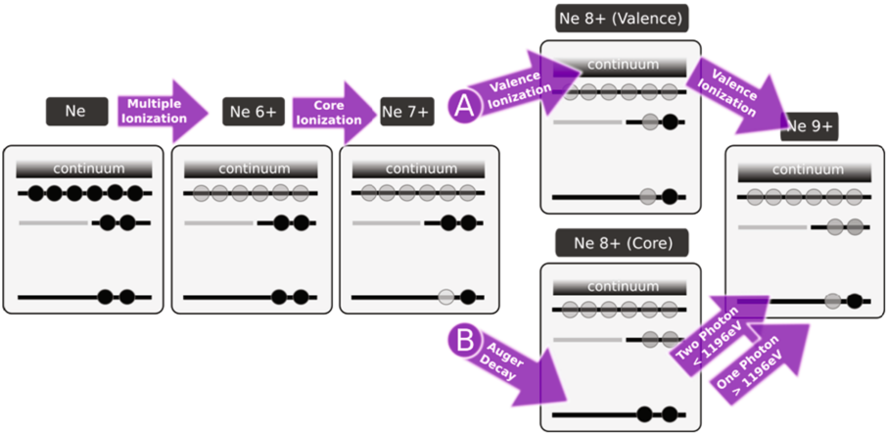

Fig. 5.2 Schematic of ionization pathway that includes a possible 2-photon ionization process. Neutral neon undergoes multiple ionization and relaxation to Ne^{6+}. K-Shell ionization produces a single core hole state in Ne^{7+}. (A) Valence ionization produces Ne^{8+} in an excited state. (B) Auger decay produces Ne^{8+} in helium-like configuration. Path (A) reaches Ne^{9+} via valence ionization. In path (B), the Ne^{8+} ground state (1.196 keV binding energy) can only be ionized by a two-photon process when the photon energy is tuned below threshold

the helium atoms discussed above. At the photon energies required to avoid direct K-shell ionization of neon (<870 eV), the 2nd harmonic falls in a region where the LCLS transport mirrors reflectivity is high, so the contamination on target is too large to be able to isolate the nonlinear contribution. The LCLS AMO end-station mirror reflectivity was specifically designed to provide a sharp cutoff above 2.0 keV. Thus, working at photon energies >1.1 keV insured good discrimination against harmonic content. Furthermore, the neon investigations discussed above showed that at 1.05 keV photon energy that the atom sequentially absorbs a large number of photons, leaving the ion stripped of all valence electrons [10]. However, the experiment did observe a small production of Ne^{9+} that was not accountable with the linear absorption model calculations. Based on this evidence, the experiment focused on production of Ne^{9+} at two photon energies (1.11 keV and 1.225 keV).

At the lower photon energy (1.11 keV), the last ground state ion that can be ionized by a single-photon/Auger sequence is Ne^{6+} resulting in the creation of Ne^{8+} which cannot be ionized by 1-photon absorption. This is illustrated by path (B) in Fig. 5.2 and produces a helium-like ground state neon ion. In this scenario, the lowest-order channel resulting in Ne^{9+} production is a two-photon, one-electron process. In contrast, Ne^{8+} ionization is possible with 1.225 keV photons, resulting in the direct production of Ne^{9+}. Alternately, another “below-threshold” route that could form Ne^{9+} is depicted as path (A) in Fig. 5.2. In this case, the $1s2s$ helium-like excited neon ion (formed by valence ionization of Ne^{7+} in a time short compared to Auger decay) can be ionized by a 1.11 keV photon but is not a two-photon, one-electron process. Thus, investigating the production of Ne^{9+} at these two photon energies as a function of pulse energy (intensity) should then reveal

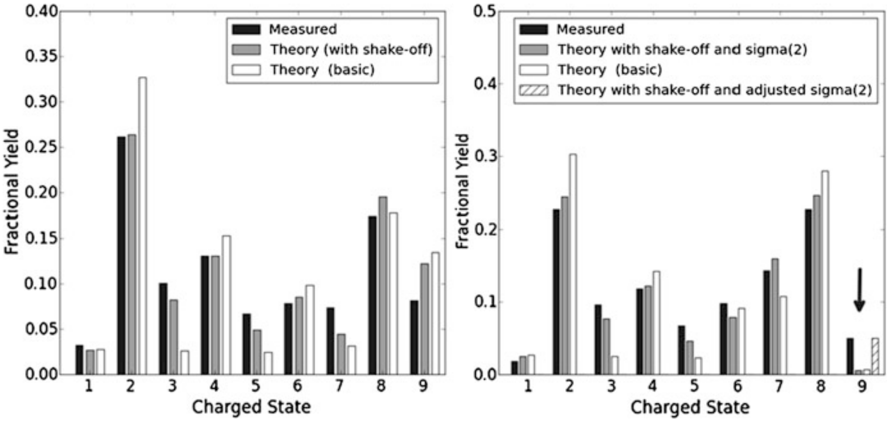

Fig. 5.3 Neon experimental (*black bars*) and simulated (*white* and *gray bars*) charge state distributions produced by (**a**) 1.225 keV and (**b**) 1.11 keV x-ray beams. The *white bars* are based on the basic model used in [10] while the *gray bars* result from an improved model that accounts for shake-off processes. The striped bar in (**b**) incorporates the adjusted two-photon cross-section needed to reproduce the Ne^{9+} production below threshold. The figure is reproduced, with permission, from [14]. Copyright (2011) by the American Physical Society

the linearity/non-linearity of the process. Figure 5.3 shows a typical histogram ion time-of-flight spectra obtained at both wavelengths. The first thing to note is that the LCLS easily ionizes 8-electrons from neon at both photon energies. The presence of Ne^{9+} is small but obvious at 1.11 keV, while at 1.225 keV Ne^{9+} the larger production proceeds by allowed single-photon ionization.

Figure 5.4 shows the evolution of the ratio of Ne^{9+}/Ne^{8+} production as a function of the measured x-ray pulse energy. In order to facilitate the comparison, each ratio has been normalized at 0.8 mJ pulse energy. The ratios vary from 0.5–2.5 % at 1.11 keV, and 15–60 % at 1.225 keV. The analysis clearly shows that the intensity-dependence is very different in both cases: linear at 1.225 keV and quadratic at 1.11 keV, a signature of second order nonlinearity.

Interpretation of the experimental results was aided by theoretical calculations performed by the group of Dr. Robin Santra at the Center for Free Electron Laser Science in Hamburg, Germany. The model's final charge-state distribution were derived using a rate equation approach, cross-sections derived by perturbation theory, and spatial and temporal averaging to mimic the experiment. The predictions of the model using different ingredients are plotted in Fig. 5.3 along with the measured charge state distribution for wavelengths below and above the Ne^{8+} K-edge threshold. The white bars contain (labeled basic) only the elements of sequential single-photon absorption and Auger decay processes, in a manner consistent with Ref. [10]. The gray bars shows the charge-state distribution resulting from an improved model that includes contributions from shake-off and nonlinear absorption processes.

As was noted by Young et al. [10], the basic model underestimates the odd charge state production while over emphasizing the even states but the improved shake-off model results in better agreement on both accounts and our analysis shows that

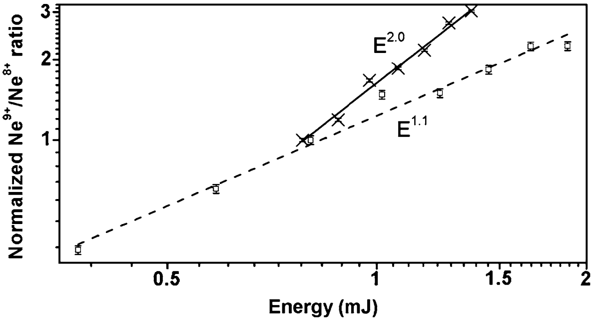

Fig. 5.4 Normalized Ne^{9+}/Ne^{8+} ratio as a function of pulse energy for 1.11 keV (*filled circles*) and 1.225 keV (*open squares*). Fits yield a quadratic response at 1.11 keV (*solid line*) and linear behavior at 1.225 keV (*dashed line*). The figure is reproduced, with permission, from [14]. Copyright (2011) by the American Physical Society

shake-off is the major factor. As discussed earlier (see Fig. 5.2), there are two paths for which Ne^{9+} can be formed by exposure to photons below the 1.196 keV threshold. The branching between the two-photon path [(B) in Fig. 5.2] and the valence ionization path [(A) in Fig. 5.2] is determined by whether the fluence-dependent valence ionization to Ne^{8+} can occur before the $1s2s^2 \rightarrow 1s^2$ Auger decay. The improve model includes this path and the two-photon cross-section for the ionization of Ne^{8+}. The two-photon cross-section was calculated using second order perturbation theory to be 10^{-56} cm^4 s [15, 16]. However, the improved model still fails in predicting the Ne^{9+} production below threshold. In order to reproduce the observed Ne^{9+} yield the value for $\sigma^{(2)}$ had to be increased by a factor of seven (see hashed bar in Fig. 5.2(b)) compared to the calculated value of Refs. [15, 16].

Note, a recent theoretical study by Sytcheva et al. [17] has shown that the $\sigma^{(2)}$ cross-section is indeed enhanced by the presence of the $1s4p$ state. The resonantly enhanced two-photon ionization, neglected in Ref. [15], is a consequence of the LCLS's wavelength and bandwidth (10 eV). The new model confirms our observation of a *direct* 2-photon, 1-electron ionization and points to the importance of near resonant behavior in nonlinear inner-shell ionization.

In conclusion, neon atoms subjected to ultra-intense, 1 keV x-rays undergo a complex sequence of excitation, ionization and relaxation processes. Experiments combined with theoretical analysis have begun to establish a clearer picture of the linear and nonlinear response of atoms to a high-flux x-ray pulse.

5.3 In Search of the Strong-Field Limit at X-ray Frequencies

At the time of this writing, all the X-ray observations at the LCLS are well described, *as expected*, by a perturbative framework. This leads to the obvious query: where is the strong-field non-perturbative limit for x-ray frequencies. The purpose of the following section is to develop the basic principles of wavelength scaling and the metrics that guide strong-field physics. This scaling has provided a consistent picture of the atomic response at low-frequency, so there is some merit in extrapolating into the unfamiliar realm of intense x-rays. Thus, we will try to comprehend the x-ray response by virtue of contrast with the optical regime.

A simple metric of an intense laser-atom interaction is the *atomic unit* (*au*) of field[1] (50 V/Å). As already mentioned the LCLS can easily exceed 1 *au* field, in fact so can focused amplified ultrafast laser systems. However, central to studying light-matter interactions is determined by the maximum intensity experience by an atom and this will be determined by the depletion (saturation) of the initial state. For low-frequency ionization ($\hbar\omega < \mathrm{I}_p$, where I_p is the ionization potential) the saturation intensity (I_{sat}) can be estimated by classical over-the-barrier ionization [18] given as $\mathrm{I}_{OTB} = cI_p/128\pi Z^2$ ($Z \equiv$ effective charge) or ADK tunneling [19]. In this scenario, all ground state neutral atoms experience intensities less than an atomic unit, e.g. for helium ($\mathrm{I}_p = 24$ eV), $\mathrm{I}_{sat} \sim 1$ PW/cm^2. However, the situation is different for x-rays ionizing core electrons since the higher binding energy and smaller absorptions cross-sections pushes depletion beyond 1 *au* field. For example, the neon charge states shown in Fig. 5.1 ionize at 10^{17} W/cm^2 or higher which is also consistent with perturbative calculations [20].

The ponderomotive or quiver energy, U_p, is an important quantity in strong-field physics particularly at optical frequencies since the external field dominates the continuum electron dynamics. U_p in atomic units is given as $I/4\omega^2$, where ω and I are the laser frequency and intensity, respectively. At an intensity of 1 PW/cm^2 (helium saturation intensity) a typical titanium sapphire femtosecond 0.8 μm optical field yields $\mathrm{U}_p \sim 60$ eV. In stark contrast, a 1 PW/cm^2, 1 keV x-ray pulse only produces 0.1 meV energy, thus x-rays are ineffective for quivering electrons. Although U_p appears as an irrelevant concept for x-ray-atom physics, it does prove useful in the design of 2-color x-ray/IR streaking metrology [21] for x-ray characterization.

In 1965 Keldysh [22] established an important strong-field metric by extending the dc-tunnel formalism to include ac-fields. He defined an adiabaticity parameter, γ, as the ratio of the tunnel time to the optical period. In the limit $\gamma \ll 1$ electrons dominantly ionize by tunneling through the barrier of the Stark potential, a prerequisite for strong-field non-perturbative interaction. For $\gamma \gg 1$, for which the field changes rapidly compared with the tunneling time, ionization is multiphoton and perturbative. Using the width of the barrier and the electron velocity Keldysh derived an expression for γ in terms of I_p, and U_p, as $\gamma = (I_p/2U_p)^{1/2}$. Using the expression for U_p, γ is found to be proportional to $\lambda^{-1}(2I_p/I)^{1/2}$. Thus in the optical regime where $\gamma \leq 1$ is a typical condition, at the same intensity for the x-rays, $\gamma \gg 1$.

It has been pointed out that $\gamma < 1$ is a necessary but not sufficient condition for tunneling and a non-perturbative interaction [23, 24]. A more complete set of metrics are defined by the bound-state and continuum-state intensity parameters [23].

---

[1] The Coulomb field in the hydrogen atom ground state equates to an equivalent light intensity of 35 PW/cm^2.

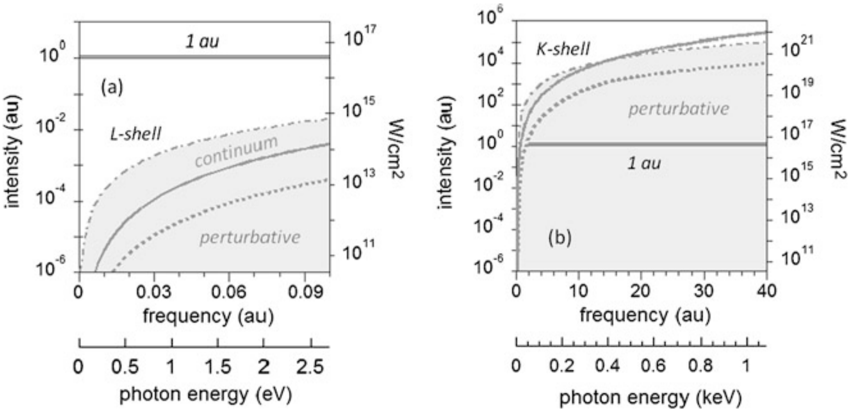

Fig. 5.5 A plot of the z (continua-state: *solid line*) and z_1 (bound-state: *dash-dotted line*) scaling parameter in the (**a**) optical and (**b**) x-ray regimes as a function of intensity. The bound state is assumed to be the neon (**a**) L-shell (~20 eV) and (**b**) K-shell (~870 eV). The lines are defined for the z-parameters equal to unity and the axis are plotted in atomic units (au) and standard units. The *dotted line* is the perturbative limit defined as 10 % of the (**a**) continuum z-parameter and (**b**) combined z and z_1 parameters. The *double line* designates 1 *a.u.* field. At optical frequencies, it is the large amplitude quiver motion of the continuum states that define the perturbative breakdown, conversely in the x-ray regime it is the tunneling of the bound state. Also noticed that the intensity required to see non-perturbative behavior is 7-orders of magnitude higher for x-rays than visible radiation

The former parameter describes the distortion of the atomic structure by relating the energy characterizing the electromagnetic field to an energy associated with a bound state. One implication is that in the non-perturbative regime the bound-state power broadening $|\mathbf{E} \bullet \mathbf{r}| \approx E a_o$ (a_o is the Bohr radius) becomes comparable to the single photon energy. This parameter can be expressed as $z_1 = (E/\omega)^2/I_p = 2/\gamma^2$. The intensity dependence of the continuum-state, z, can be defined as the ratio of the quiver energy to the photon energy, $U_p/\omega = I/4\omega^3$. A perturbative treatment of the atom-field interaction requires that $\gamma > 1$, and z and $z_1 < 1$.

Using these parameters let us examine the consequence of frequency on the strong-field condition. Figure 5.5 is a plot of intensity versus frequency for $z = 1$ (solid line: continua), $z_1 = 1$ (dash-dotted line: bound) and the perturbative limit (dotted line), below which perturbation theory is valid. Figure 5.5(a) plots the parameters in the optical regime (0.35–1.6 eV) and the bound state is assumed to be the neon valence L-shell ($I_p \sim 20$ eV). These wavelengths are typical of those used in our laboratory for strong-field studies and attosecond generation. From this plot a picture emerges that is a consistent picture with the quasi-classical model of rescattering [25, 26]. As the intensity increases, perturbation theory breaks down due to the distortion of the continua (z-parameter, e.g. $U_p \geq \hbar\omega$) and this occurs for intensities between $10^{-3} < I < 1$ PW/cm^2. However, the strong-field condition (z_1, $z > 1$ and $\gamma > 1$) is not satisfied until the intensity is further increased, at this point the atom tunnel ionizes and the classical ansatz fulfilled.

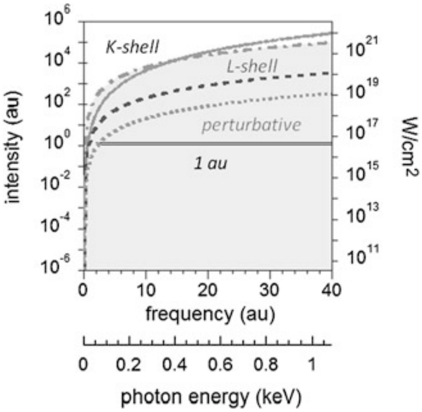

Fig. 5.6 A plot of the z (continua-state: *solid line*) and z_1 (neon K-shell: *dash-dotted line* and L-shell: *dashed line*) intensity scaling parameter in the x-ray regime as a function of intensity. The lines are for the z-parameters equal to unity and the axis are plotted in atomic units (*au*) and standard units. The *dotted line* is the perturbative limit that is now defined as 10 % of the L-shell z_1-parameter. The L-shell strong-field limit is at a lower intensity than the K-shell but still beyond the intensity used in the initial LCLS experiments

Figure 5.5(b) scales these parameters into x-ray frequencies. In this plot, the bound-state intensity parameter is calculated for the K-shell core ($I_p \sim 870$ eV) of neon (dash-dotted line-bound). For this case a very different picture emerges, as expected the intensity needed to reach the strong-field limit is significantly higher in the x-ray regime, $\sim 10^{20}$ W/cm^2 at 1 keV. This is corroborated by the LCLS neon experiments described above that are performed at a maximum intensity of $\sim 10^{17}$ W/cm^2 and here perturbation theory appears appropriate in describing the observables. In addition, as the intensity increases the strong-field condition and the breakdown of perturbation occur together. Thus the K-shell distortion dominates above 500 eV photon energy, the atom starts tunneling but the electron does not quiver, a stark contrast to the optical regime.

It must be kept in mind that the validity of this extrapolations to high frequency is highly dubious. Figure 5.6 suggests one weakness and perhaps a behavior in the x-ray regime that is significantly different. In the strong-field optical regime, a description based on an independent electron approximation for valence excitation has been highly successful in describing the dominant interactions observed in experiments. However in the x-ray regime the field can couple to several shells, for instance for neon above 1 keV both K- and L-shell electrons are ionized. Figure 5.6 also plots the z_1-parameter for the neon's valence L-shell. Now entrance into the strong-field regime is lower in intensity ($\sim 10^{17}$ W/cm^2) by almost 2-orders of magnitude. Furthermore, the bound-state contributions (K- plus L-shell) present a dichotomy in the perturbative limit and clearly at odds. Thus, the physics involved in the perturbative breakdown will be unique to the x-ray regime since it may involve many-body interactions, not seen in the optical regime.

5.4 Outlook

The combination of ultrafast duration, high pulse energy and excellent spatial mode has allowed the LCLS to generate intensities that surpass all known laboratory x-ray sources by seven-orders of magnitude in intensity. In fact in this regard LCLS is equivalent to state-of-the-art amplified optical lasers, easily achieving electric field strengths in excess of an atomic unit.

The LCLS XFEL is allowing the first experimental realization aimed at addressing intense x-ray-matter interactions. The initial experiments are unrivaled in scientific discovery but equally important, they also provide a preview of transformational science whose objectives can be met by future XFEL project, such as the LCLS II. One obvious frontier is defined by intensity, this paper argues that the strong-field limit is within reach of current XFEL parameters and provides an opportunity to explore a new frontier in laser-matter interactions.

Future experiments will benefit from improvements in the control of the XFELs pulse characteristics, while the multiplication of such devices in the world will make the access easier and provide new opportunities to explore and develop x-ray nonlinear optics.

Acknowledgements We wish to thank the post-doctoral researchers and graduate students, past and present, who have contributed to these early experiments: Cosmin Blaga, Anthony DiChiara, Gilles Doumy, Anne Marie March, Emily Sistrunk and Kaikai Zhang. The authors acknowledge support from the U.S. Department of Energy and supported by its Division of Chemical Science, Office of Basic Energy Sciences and the National Science Foundation. LFD gratefully acknowledges the continued support of Dr. Edward and Sylvia Hagenlocker.

References

1. P. Salières, A. L'Huillier, P. Antoine, M. Lewenstein, in *Adv. At. Mol. Opt. Phys*, vol. 41, ed. by B. Bederson, H. Walther (Academic Press, San Diego, 1999)
2. T. Brabec, F. Krausz, Intense few-cycle laser fields: frontiers of nonlinear optics. Rev. Mod. Phys. **72**, 545–591 (2000)
3. P. Agostini, L.F. DiMauro, The physics of attosecond pulses. Rep. Prog. Phys. **67**, 813–855 (2004)
4. K. Tiedtke, A. Azima, N. von Bargen, L. Bittner, S. Bonfigt, S. Dusterer et al., The soft x-ray free-electron laser FLASH at DESY: beamlines, diagnostics and end-stations. New J. Phys. **11**, 023029 (2009)
5. M. Meyer, J.T. Costello, S. Dusterer, W.B. Li, P. Radcliffe, Two-colour experiments in the gas phase. J. Phys. B **43**(19), 194006 (2010)
6. P. Emma, R. Akre, J. Arthur, R. Bionta, C. Bostedt, J. Bozek et al., First lasing and operation of an angstrom-wavelength free-electron laser. Nat. Photonics **4**, 641–644 (2010)
7. P.H. Bucksbaum, R. Coffee, N. Berrah, in *Adv. At. Mol. Opt. Phys*, vol. 60, ed. by E. Arimondo, P. Berman, C.C. Lin (Academic Press, San Diego, 2011)
8. J. Bozek, AMO instrumentation for the LCLS X-ray FEL. Euro. Phys. J. **169**, 129–132 (2009)
9. O. Hemmers, S.B. Whitfield, P. Glans, H. Wang, D.W. Lindle, R. Wehlitz, I.A. Sellin, High-resolution electron time-of-flight apparatus for the soft x-ray region. Rev. Sci. Instrum. **69**, 3809–3817 (1998)

10. L. Young, E.P. Kanter, B. Krassig, Y. Li, A.M. March, S.T. Pratt et al., Femtosecond electronic response of atoms to ultraintense x-rays. Nature **466**, 56–61 (2010)
11. Y. Kobayashi, T. Sekikawa, Y. Nabekawa, S. Watanabe, 27-fs extreme ultraviolet pulse generation by high-order harmonics. Opt. Lett. **23**, 64–66 (1998)
12. N.A. Papadogiannis, L.A.A. Nikolopoulos, D. Charalambidis, G.D. Tsakiris, P. Tzallas, K. Witte, Two-photon ionization of He through a superposition of higher harmonics. Phys. Rev. Lett. **90**, 133902 (2003)
13. P. Lambropoulos, X. Tang, Multiple excitation and ionization of atoms by strong lasers. J. Opt. Soc. Am. B **4**, 821–832 (1987)
14. G. Doumy, C. Roedig, S.K. Son, C.I. Blaga, A.D. DiChiara, R. Santra et al., Nonlinear atomic response to intense ultrashort x-rays. Phys. Rev. Lett. **106**, 083002 (2011)
15. S.A. Novikov, A.N. Hopersky, Two-photon excitation-ionization of the 1s shell of highly charged positive atomic ions. J. Phys. B **34**, 4857–4863 (2001)
16. S.A. Novikov, A.N. Hopersky, Two-photon knocking-out of two electrons of the $1s^2$-shell of the neon atom. J. Phys. B **35**, L339–L343 (2002)
17. A. Sytcheva, S. Pabst, S.-K. Son, R. Santra, Enhanced nonlinear response of Ne^{8+} to intense ultrafast x-rays. Phys. Rev. A **85**, 023414 (2012)
18. S. Augst, D. Strickland, D.D. Meyerhofer, S.L. Chin, J.H. Eberly, Tunneling ionization of noble gases in a high-intensity laser field. Phys. Rev. Lett. **63**, 2212–2215 (1989)
19. M.V. Amosov, N.B. Delone, V.P. Krainov, Tunnel ionization of complex atoms and of atomic ions in an alternating electromagnetic field. Sov. Phys. JETP **64**, 1191–1194 (1986)
20. N. Rohringer, R. Santra, X-ray nonlinear optical processes using a self-amplified spontaneous emission free-electron laser. Phys. Rev. A **76**, 033416 (2007)
21. S. Düsterer, P. Radcliffe, C. Bostedt, J. Bozek, A.L. Cavalieri, R. Coffee et al., Femtosecond x-ray pulse length characterization at the Linac Coherent Light Source free-electron laser. New J. Phys. **13**, 093024 (2011)
22. V.S. Keldysh, Ionization in the field of a strong electromagnetic wave. Sov. Phys. JETP **20**, 1307–1314 (1965)
23. V.P. Krainov, H.H. Reiss, B.M. Smirnov, *Radiative Processes in Atomic Physics* (Wiley, New York, 1997)
24. H.R. Reiss, Limits on tunneling theories of strong-field ionization. Phys. Rev. Lett. **101**, 043002 (2008)
25. K.J. Schafer, B. Yang, L.F. DiMauro, K.C. Kulander, Above threshold ionization beyond the high harmonic cutoff. Phys. Rev. Lett. **70**, 1599–1602 (1993)
26. P.B. Corkum, Plasma perspective on strong-field multiphoton ionization. Phys. Rev. Lett. **71**, 1994–1997 (1993)

Chapter 6
Third Harmonic Generation from Perturbed Femtosecond Filaments in Air

Yi Liu, Magali Durand, Yohann Brelet, Amélie Jarnac, Benjamin Forestier, Aurélien Houard, Arnaud Couairon, and André Mysyrowicz

Abstract We investigate third harmonic generation from femtosecond laser filaments. A two-order-of-magnitude enhancement of third harmonic light is observed when the (signal) filament is perturbed by a second laser (pump) filament. This enhancement is studied as function of laser polarization, time delay between the pump and signal filaments, the pump filament energy, etc. Based on these systematic results, we attribute the enhancement to a quenching of the interference effects of the third harmonic generated in the first and second half of the signal filament. Numerical simulations based on a two-color propagation model reproduce well the experimental observations and confirms our explanation.

6.1 Introduction

Intense femtosecond pulses launched in ambient air undergo nonlinear propagation. With laser peak power exceed a critical power $P_{cr} = 3.72\lambda_0^2/8\pi n_0 n_2$, the optical Kerr effect leads to a catastrophic collapse of the pulses in the spatial domain [1, 2]. In ambient air, this critical power corresponds to 5 GW for 800 nm pulses. With the catastrophic focusing of the laser pulse, the corresponding laser intensity becomes sufficient to ionize air molecules. The dynamic competition between the defocussing effect due to the created underdense plasma and the Kerr focusing effect results in a spectacular nonlinear propagation phenomenon, called filamentation, where the laser pulse keeps a high intensity ($\sim 10^{13}$–10^{14} W/cm^2) much long than the Rayleigh length and a weak ionized plasma channel (10^{16} W/cm^3) is left in the wake of the propagating pulse.

Following its discovery in 1995 [3], femtosecond laser filamentation has attracted much attention due in particular to many potential applications. These applications

---

Y. Liu · M. Durand · Y. Brelet · A. Jarnac · B. Forestier · A. Houard · A. Mysyrowicz (✉)
Laboratoire d'Optique Appliquée, ENSTA Paristech/CNRS/Ecole Polytechnique, Boulevard des Maréchaux, 91762, Palaiseau, France
e-mail: andre.mysyrowicz@ensta-paristech.fr

A. Couairon
Centre de Physique Théorique, CNRS, Ecole Polytechnique, 91128 Palaiseau, France

K. Yamanouchi et al. (eds.), *Progress in Ultrafast Intense Laser Science X*,
Springer Series in Chemical Physics 106, DOI 10.1007/978-3-319-00521-8_6,

range from guiding and triggering of high voltage discharge [1, 4, 5], optical frequency conversion to UV and infrared regime [1, 6], generation of few-cycle pulses [7], generation of intense Terahertz pulse [8, 9], far-off detection of pollutants [10], virtual antenna emitting at radiofrequency [11], backwards N_2 laser emission [12], to quote a few. Among these applications, the conversion from the fundamental laser frequency to its third harmonic (TH) in filaments has become an attractive topic because it provides an extremely simple and robust method for UV pulse generation. The subject has been pioneered by Aközbek et al. [13]. Subsequent papers reported conversion efficiency to TH in air ranging from $\sim 10^{-5}$ to 0.2 % [14–18].

Very recently, this subject has been revived by reports that the third harmonic from a filament (hereafter the signal filament) is enhanced by 2 orders of magnitude in the presence of a second filament (hereafter pump filament), which intersects the signal filament in its middle [19–21]. However, the results reported by several groups differ in several aspects. First, Yang et al. found that the TH is enhanced only during the temporal overlap of the pump and signal filaments [20]. However, Suntsov et al. reported that the enhancement is observed for pump/signal delays up to 40 ps [19, 21]. The second discrepancy concerns the influence of the laser pulses polarizations. In the experiment of Yang et al., significant TH enhancement is observed for same polarization states of the pump and signal filaments, while no enhancement is found when they are orthogonal to each other [20]. However, Suntsov and coworkers found that the laser polarization does not have any observable influence on the enhanced TH [19, 21]. These discrepancies in experimental observations naturally led to different explanations. In Ref. [20], the authors suggested that the signal filament is elongated in the presence of the pump filament and hence the TH yield is correspondingly enhanced. The authors of Refs. [19] and [21] proposed that the enhanced TH originated from an increased third order susceptibility of the plasma created at the crossing point of the two filaments.

Aside the above experiments where the signal filament is perturbed by another filament, other groups reported that the TH can be also enhanced when the filament is partially blocked by objects like thin copper wire, fused silica plate, and gas pressure gradient [22–26]. Zhang and coworkers blocked the filament with a thin copper wire (diameter $\sim$40 μm) and observed that the TH is enhanced by one order of magnitude [23]. Later, Yao et al. reported similar enhancement when the filament is terminated by a pair of fused silica wedge [25]. Therefore, a natural question is whether the TH enhancement obtained with these different methods have their origin in the same physical mechanism?

In this work, we investigate the enhanced TH as a function of the pump laser pulse energy, polarization of the pump pulse, and pump/signal time delay τ_d. To interpret our results, we explicitly consider the π phase shift which exists between the harmonic wave generated in the front and tail of the filament [27]. This Gouy phase shift leads to a large cancellation of third harmonic at the end of an unperturbed filament. By limiting the filament length to its first half distance with a pinhole formed by the filament itself on an aluminum foil, we observe a two orders of magnitude enhancement of TH because the destructive interference is canceled. At the same time, numerical simulations based on the two color propagation model reproduces well our observations, which further confirms our phenomenological interpretation. We also point out that the results of Refs. [22–26] can be interpreted consistently along the same lines, namely the suppression of destructive interference which prevents back-conversion from the TH to the fundamental pulse.

6.2 Experimental Results

In our experiment, we employed a chirped pulse amplification laser system (Thales, Alpha 100). This system delivers 50 fs laser pulses at 800 nm with a maximum pulse energy of 15 mJ. The laser pulse is first split into two replicas with a 50/50 beam splitter. The polarization and energy of the two pulses can be individually varied by a combination of a half wave plate and a Glan polarizor mounted on each beam path. The two pulses, the filament forming signal pulse and the pump pulse, are focused by two convex lens f_1 and f_2 and cross each other with an angle φ. The time delay between the two pulses can be continuously varied by a delay line. The focus of the pump pulse is adjusted to intersect the signal filament at its middle distance, as see in Fig. 6.1(a). In a second experiment, an aluminum foil of 150 μm thickness is mounted around the filament area (Fig. 6.1(b)). With successive laser shots, the intense filament core starts to drill a hole through the Al foil. This Al pinhole blocks largely the surrounding energy reservoir and hence terminates the further propagation of the filament. On the other hand, the TH generated before the pinhole largely pass through it because the TH is mainly confined in the intense filament core due to its nonlinear generation mechanism.

In order to measure the TH beyond the filaments crossing point or after the Al pinhole, two detection systems are used. In the first detection scheme, several low-pass color filters (UG11) are used to filter out the TH signal while attenuating the fundamental pulse heavily. Then, the pulses are projected on a white paper screen situated 70 cm after the filament area, where a charge-coupled detector camera captures its far field pattern (Fig. 6.1(c)). To measure the spectrum and intensity of the TH, the total TH radiation is collected with a convex lens of fused silica with diameter $d = 2$ cm and focal distance $f = 15$ cm positioned 50 cm after the end of the filament and sent to a spectrometer or a calibrated photodiode after blocking the fundamental frequency with color filters (Fig. 6.1(d)).

In Fig. 6.2(a)–(e), we present photographs of the luminescence track left by the filament plasma string for different pump pulse energies. The two pulses are crossed with an angle of 50°. The corresponding far field patterns of the TH generated by the signal filament are shown in Fig. 6.2(a′)–(e′). The filament length is about 4 cm for an incident laser pulse energy of 520 μJ which corresponds to $2P_{\mathrm{cr}}$. In Fig. 6.2(a) and (a’), the pump pulse is turned off. In the far field we observe weak residual 800 nm light and broadband continuum but almost no third harmonic. From (b) to (e), the energy of the pump pulse is 100, 210, 380, 520 μJ respectively. With the increase of the pump energy, a bright plasma spot appears at the overlapping region and above $E_{\mathrm{p}} \sim 210$ μJ the pump beam starts forming its own filament. At the same time, a significant enhancement of third harmonic from the signal filament is observed in the

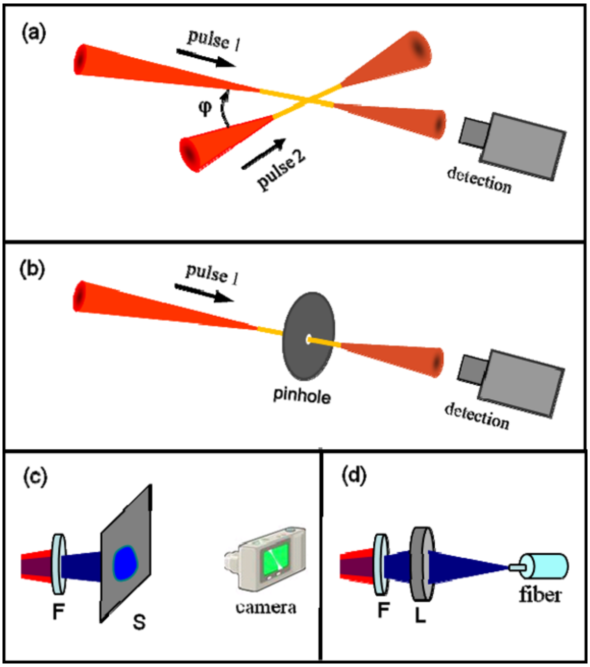

Fig. 6.1 Schematic experimental setup. (**a**) Two femtosecond pulses form filaments in air, which cross with angle φ. (**b**) An aluminum foil is mounted on the filament. The intense filament core drills a hole on the foil, which largely terminates the further propagation of filament by blocking the surrounding energy reservoir while leaves the third harmonic generated before the pinhole pass through. The detection is detailed in (**c**) and (**d**). (**c**) The signal pulse (pulse 1) after interaction is filtered by color filters (F) and projected on a paper screen S. The fluorescence induced by the third harmonic on the screen is observed by a camera. (**d**) The third harmonic after the filters is focused by a fused silica lens (L) and detected by a fiber spectrometer or a calibrated photodiode

far field. At low pump pulse energy, below $E_\mathrm{p} = 100$ µJ, a centro-symmetric circular emission pattern of the TH centered on the filament axis is observed. At higher pump pulse energy ($E_\mathrm{p} > 210$ µJ), part of the TH emission appears at a larger angle, preferentially in the direction orthogonal to the plane formed by the two crossing filaments. Figure 6.3 shows the spectrum of the third harmonic with and without the pump pulse, corresponding to Fig. 6.2(a) and (d). An enhancement of the third harmonic energy by a factor 100 is observed for a pump energy of 380 µJ.

We performed systematic measurements to address the role of the pump pulse polarization and the time delay τ_d between the two pulses in the enhancement of the third harmonic. Figure 6.4 shows the enhanced TH signal as a function of the time delay τ_d for different energies and polarizations of the pump pulse. For $E_\mathrm{p} = 120$ µJ, an enhanced TH signal is observed in the case of parallel polarization within a delay of a few hundred femtoseconds (Fig. 6.4(a)). These observations are similar to those in Ref. [20]. At high pump pulse energy of 520 µJ (Fig. 6.4(d)), almost no difference is found between the two laser polarizations, in agreement with Refs. [19] and [21].

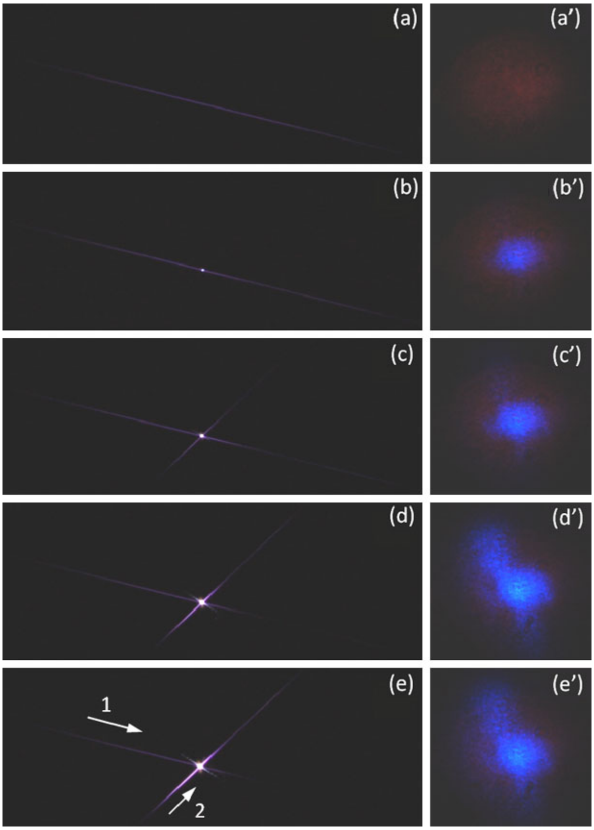

Fig. 6.2 Photos of the characteristic plasma luminescence of a free propagating filament (**a**) and filaments intercepted by a pump pulse (**b**)–(**e**). The signal pulse (1) and pump pulse (2) are focused by convex lenses of focal length $f_1 = 100$ cm and $f_2 = 50$ cm. The *arrows* in (**e**) represent their propagation directions. The pump pulse energies are 100, 210, 380, and 520 μJ for (**b**), (**c**), (**d**), and (**e**), respectively. (**a**′)–(**e**′) show the corresponding images of the third harmonic generated by the signal filament and the residual IR component

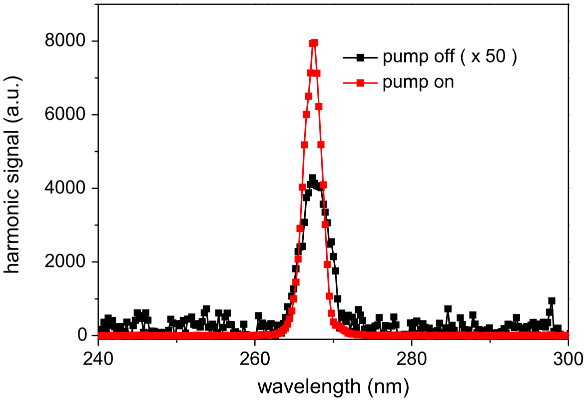

Fig. 6.3 Spectrum of the third harmonic with and without the pump pulse, corresponding to the case of Fig. 6.2(a) and (d)

For pump energy between 120 μJ and 520 μJ, an intermediate behavior is observed, in which the two polarizations produce different third harmonic signals during the ∼200 fs time overlap, while later no difference is observed (Fig. 6.4(b) and (c)). We further measured the maximum enhanced third harmonic as a function of the pump

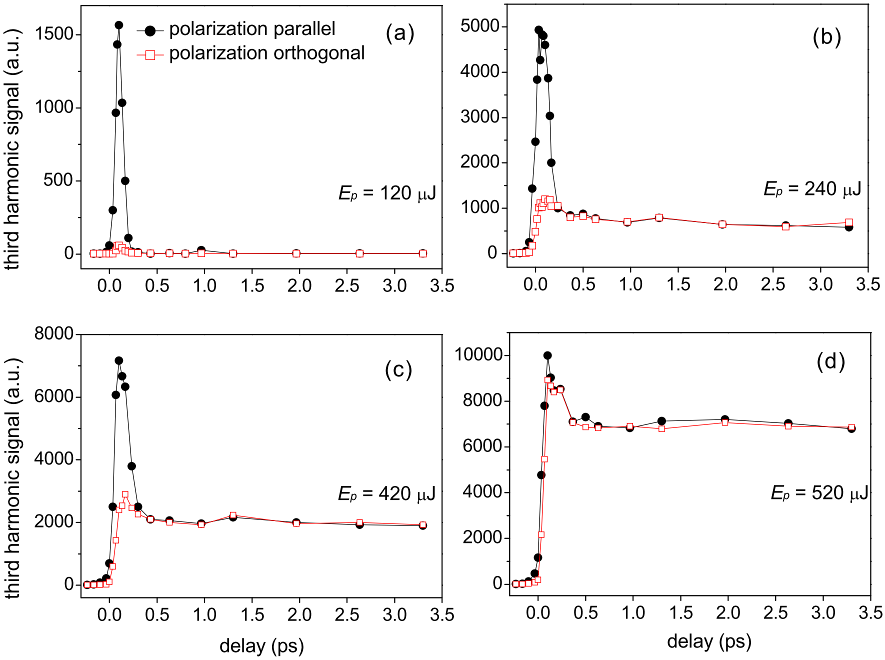

Fig. 6.4 Third harmonic signal as a function of delay τ_d for different pump polarizations and pump pulse energies. The lenses used to focus the signal and pump pulses are $f_1 = 100$ cm and $f_2 = 15$ cm. The cross angle φ of the two filaments is 90°. The energy of the signal pulse is 320 μJ

Fig. 6.5 Enhanced TH signal as a function of the pump pulse energy, while the signal filament pulse energy is fixed to 330 μJ. The experiment conditions are the same as in Fig. 6.4

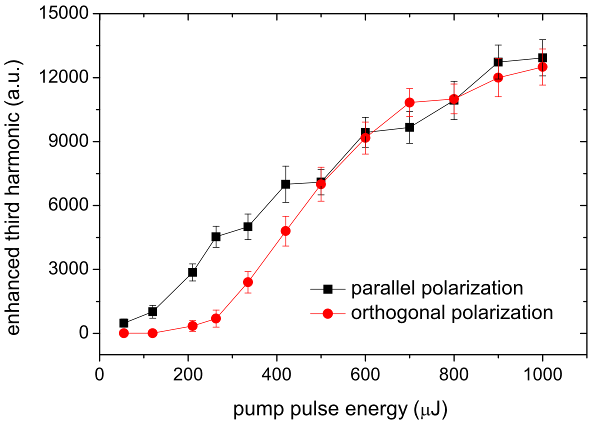

pulse energy systematically for the two orthogonal pump polarizations. The results are presented in Fig. 6.5. Consistent with the above results, for pump pulse energy relatively low (<500 μJ) the two polarizations exhibit significant difference while a similar enhancement is observed for higher energy pump pulse.

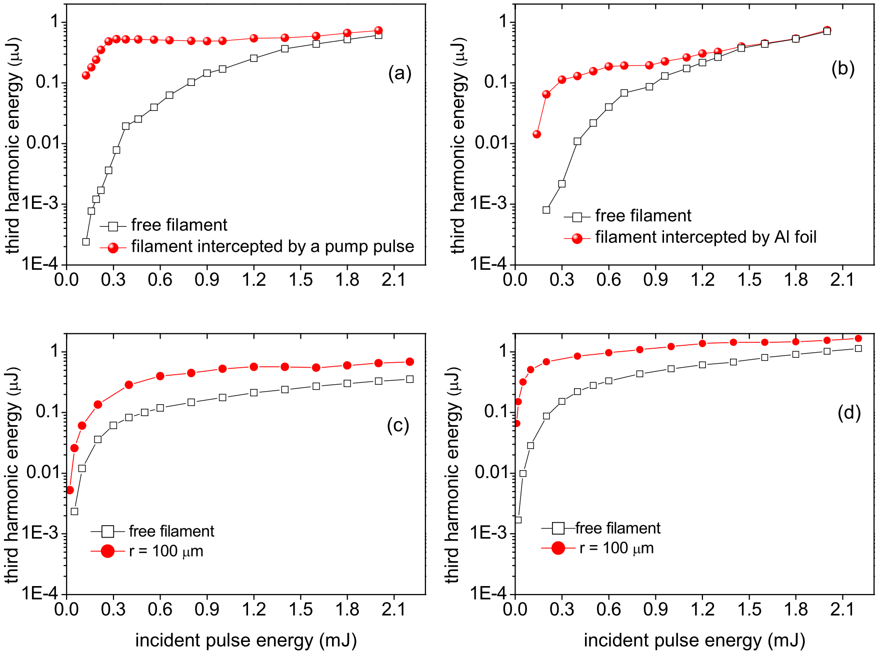

Fig. 6.6 (**a**) Measured TH signal from a free propagating filament as a function of the signal pulse energy, and maximum TH signal from filament intercepted by a 300 μJ pump pulse. (**b**) Same as in (**a**) but the filament is intercepted by an Al foil. (**c**) Calculated TH energy from a free filament (10 cm after the focus) and maximum TH energy contained in a 100 μm aperture as a function of the input energy of the fundamental pulse. The nonlinear index coefficient is $n_2 = 3.2 \times 10^{-19}$ cm^2/W. (**d**) Same as in (**c**) but the nonlinear index coefficient is $n_2 = 1.8 \times 10^{-19}$ cm^2/W

We further compared the TH signal from a free propagating filament with the maximum enhanced TH signal in the presence of a pump filament with $E_p = 300$ μJ. Results are presented in Fig. 6.6(a). For low signal pulse energy (<400 μJ) an enhancement by a factor of 100 is observed, while this improvement effect weakens gradually with the increment of the incident pulse energy.

Concerning the underlying mechanism for the TH enhancement, we find some clues in Fig. 6.2. In this figure it is seen that the filament luminescence track is gradually shortened in the presence of the pump pulse. Yet the maximum TH radiation is obtained when the filament is the shortest. This observation suggests that the TH generated in the first part of the filament is largely canceled by the second half of the filament in the far field.

To check this hypothesis, we employed another method to reduce the length of the filament, leaving its first part unperturbed. We inserted a 150 μm thick aluminum foil in the middle of a 4 cm long filament formed by a 600 μJ laser pulse focused with a lens of $f = 1$ m. After about 2 seconds, the intense filament core starts to drill a hole on the metallic foil and partially penetrates through it. As a result, a small diaphragm with a diameter corresponding to the intense filament core is realized. We monitored the TH signal in the far field during this process and present the results

Fig. 6.7 Third harmonic signal measured after the insert of a 150 μm thickness Al foil around the center of a 4 cm long filament. The *insets* present the photos of the filament drilled pinholes, with the numbers indicating the exposition time in seconds

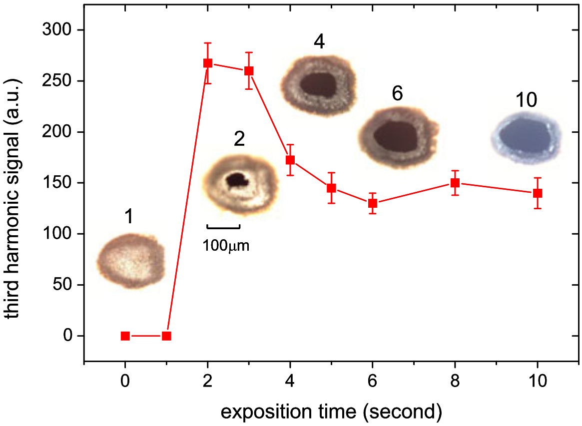

in Fig. 6.7 as a function of the exposition time. The evolution of the diaphragm is also presented as an inset. It is not surprising to find that the diaphragm enlarges gradually, followed by a rather stable state of constant diameter with the subsequent accumulation of laser shots. However, the TH energy presents a maximum around $t = 2$–3 s and decreases substantially after 4 seconds when a larger opening is achieved. We argue that with a smaller pinhole of around 60 μm, corresponding to the exposition time from 2 s to 4 s, the laser energy reservoir surrounding the filament core is largely blocked, preventing further filamentation after the pinhole [28, 29]. Meanwhile, the third harmonic wave generated inside the intense core of the filament before the diaphragm is transmitted through the pinhole. With the further enlargement of the pinhole opening, the transmitted laser power becomes larger than P_{cr}. As a result, an underdeveloped filament continues after the pinhole [28, 29] and serves as additional TH source to the total TH yield in the far field. Therefore, the observed decreasing of the TH after $t = 3$ s in Fig. 6.7 leads to the conclusion that the TH generated after the pinhole contributes destructively to the total TH yield.

To monitor the amount of TH generated in different sections of the filament, we displaced the Al foil along the filament axis and recorded the corresponding maximum TH yield. The results are presented in Fig. 6.8. The TH signal increases in the first section of the filament, reaches a maximum and then decreases in the second half section. This observation supports the hypothesis that the TH radiation generated in the filament tail interferes destructively with the TH generated in the first section. It is further confirmed by the following measurement. The filament is first intercepted at mid distance by the pump pulse. A pre-formed 100 μm diaphragm is then placed beyond the crossing point and the TH is measured again by displacing the diaphragm along increasing z. The result is also shown in Fig. 6.8. As can be seen, the TH signal remains almost constant after the crossing point, instead of decreasing rapidly as it is the case with a fully developed filament. This observation suggests that the dense plasma at the crossing point actually acts as a blocker that partially stops the filament formation and hence arrests the back

Fig. 6.8 Third harmonic energy after the pinhole created by the filament core on the aluminum foil. For crossed filaments, a pre-formed 100 μm pinhole is scanned after the filament cross at $z = 0$ cm. The energies of the signal and pump pulse are 320 μJ and 300 μJ

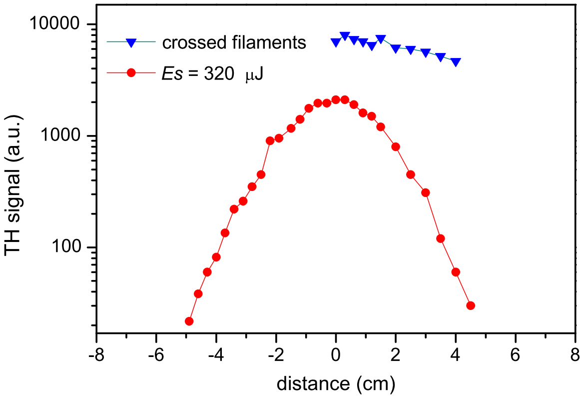

conversion of the TH generated in the upstream half filament into the fundamental frequency.

We therefore conclude that the TH produced on the leading and trailing parts of the filament possess opposite carrier phase, which is at the origin of the large cancellation of TH at the end of a fully developed filament. In the presence of an intercepting pump filament or other objects (small size pinhole, thin copper wire, water droplet, etc.), the development of the filament is suppressed after the obstacle, breaking the large cancellation of the TH at the end of the filament. As a result, an enhancement of the total TH yield is generally observed. We note that the same conclusion is implicit in Ref. [30]: passing through the regime of filamentation the TH will first increase and then after the focus energy will return back to the pump.

Finally, we compared the maximum enhanced TH as a function of the input energy in the presence of the Al diaphragm with that of an unperturbed filament, as shown in Fig. 6.6(b). A basically similar scenario is found comparing to Fig. 6.6(a), confirming the same physical mechanism underlying the two methods for TH enhancement.

6.3 Numerical Simulations and Discussion

Modeling the generation of third harmonic generation and two-color pulse propagation in the experiments was performed by means of numerical simulations based on an extension of the two-color propagation model initially developed by Aközbek et al. [13].

The electric field is written in terms of the fundamental $E_{\omega_0}(\vec{r}, t, z)$ and third harmonic $E_{3\omega_0}(\vec{r}, t, z)$ envelopes:

$$E = E_{\omega_0} \exp\big[i(k_{\omega_0} z - \omega_0 t)\big] + E_{3\omega_0} \exp\big[i(k_{3\omega_0} z + \Delta k z - 3\omega_0 t)\big] \tag{6.1}$$

with $k_{\omega_0} \equiv k(\omega_0)$, $k_{3\omega_0} \equiv k(3\omega_0)$, and $\Delta k = 3k(\omega_0) - k(3\omega_0) = -5\ \text{cm}^{-1}$ (air at 800 nm) where $k(\omega)$ denotes the dispersion relation in air [31].

As discussed by Kolesik et al. [15], this decomposition is valid as long as the spectrum of the TH component remains well separated from the spectrum of the fundamental pulse, i.e., when it does not overlap with the supercontinuum generated by nonlinear propagation of the fundamental pulse. This assumption was well satisfied in our calculations.

The propagation equations for the fundamental and third harmonic pulse envelopes are written in the Fourier domain for $\hat{E}_{\omega_0}(k_\perp, \omega, z)$ and $\hat{E}_{3\omega_0}(k_\perp, \omega, z)$ and take the form of two coupled canonical propagation equations [32]:

$$\frac{\partial \hat{E}_{\omega_0}}{\partial z} = i K_{\omega_0}(\omega, k_\perp)\hat{E}_{\omega_0} + i Q_{\omega_0}(\omega)\left(\frac{\hat{P}_{\omega_0}}{\varepsilon_0} + \frac{i}{\omega}\frac{\hat{J}_{\omega_0}}{\varepsilon_0}\right) \tag{6.2}$$

$$\frac{\partial \hat{E}_{3\omega_0}}{\partial z} = i K_{3\omega_0}(\omega, k_\perp)\hat{E}_{3\omega_0} + i Q_{3\omega_0}(\omega)\left(\frac{\hat{P}_{3\omega_0}}{\varepsilon_0} + \frac{i}{\omega}\frac{\hat{J}_{3\omega_0}}{\varepsilon_0}\right) \tag{6.3}$$

Here the linear terms representing diffraction, dispersion and space-time coupling read $K_{\omega_0}(\omega, k_\perp) \equiv \frac{1}{2}(k_{\omega_0} + k'_{\omega_0}(\omega - \omega_0))^{-1}[k^2(\omega) - (k_{\omega_0} + k'_{\omega_0}(\omega - \omega_0))^2 - k_\perp^2]$, and $K_{3\omega_0}(\omega, k_\perp) = \Delta k + \frac{1}{2}(k_{3\omega_0} + k'_{\omega_0}(\omega - 3\omega_0))^{-1}[k^2(\omega) - (k_{3\omega_0} + k'_{\omega_0} \times (\omega - 3\omega_0))^2 - k_\perp^2]$, where the dispersive properties of the medium are described by a Sellmeier-like relation $k(\omega)$, and $k_{\omega_0} \equiv k(\omega_0), k'_{\omega_0} \equiv dk/d\omega|_{\omega_0}, k_{3\omega_0} \equiv k(3\omega_0)$. The nonlinear dispersive terms for each component read $Q_{\omega_0}(\omega) \equiv \frac{1}{2}(k_{\omega_0} + k'_{\omega_0}(\omega - \omega_0))^{-1}(\omega^2/c^2)$ and $Q_{3\omega_0}(\omega) \equiv \frac{1}{2}(k_{3\omega_0} + k'_{\omega_0}(\omega - 3\omega_0))^{-1}(\omega^2/c^2)$. In comparison with the standard modeling of pulse propagation with nonlinear envelope equations of the nonlinear Schrödinger type, these frequency dependent operators in (6.2) and (6.3) extend the model validity to pulses with broad spectra, as short as a single cycle. The derivation is explained in details in Refs. [30, 32]. Note that group velocity mismatch is included in the propagation constant for the third harmonic pulse, as can be readily seen by an expansion of $K_{3\omega_0}(\omega, k_\perp)$ around $\omega = 3\omega_0$.

In the temporal domain, both the fundamental and the third harmonic pulses are propagated in the frame of the fundamental pulse $\tau = t - k'_0 z$, where t denotes time in the laboratory frame. The nonlinear terms in (6.2) and (6.3) are all included in the nonlinear polarization envelopes $\hat{P}_{\omega_0}(k_\perp, \omega, z)$, $\hat{P}_{3\omega_0}(k_\perp, \omega, z)$ and current envelopes $\hat{J}_{\omega_0}(k_\perp, \omega, z)$, $\hat{J}_{3\omega_0}(k_\perp, \omega, z)$, acting as source terms for the propagation of the fundamental and TH pulses. The nonlinear polarization describes the optical Kerr effect with self- and cross-phase modulation, third-harmonic generation and back-conversion:

$$\frac{P_{\omega_0}}{\varepsilon_0} = 2n_{\omega_0}n_2\big[\big(|E_{\omega_0}|^2 + 2|E_{3\omega_0}|^2\big)E_{\omega_0} + E^{*2}_{\omega_0}E_{3\omega_0}\big] \tag{6.4a}$$

$$\frac{P_{3\omega_0}}{\varepsilon_0} = 2n_{3\omega_0}n_2\left[\big(|E_{3\omega_0}|^2 + 2|E_{\omega_0}|^2\big)E_{3\omega_0} + \frac{E^3_{\omega_0}}{3}\right] \tag{6.4b}$$

The currents describe plasma absorption and plasma defocussing in the framework of the Drude model, with collision time τ_c, for the fundamental and the third harmonic pulses:

$$\frac{J_{\omega 0}}{\varepsilon_0} = c\sigma_{\omega 0}(1 + i\omega_0\tau_c)\rho E_{\omega 0} + cn_{\omega 0}\beta_{K_{\omega_0}}|E_{\omega 0}|^{2K_{\omega 0}-2}E_{\omega 0} \tag{6.5a}$$

$$\frac{J_{3\omega 0}}{\varepsilon_0} = c\sigma_{3\omega_0}(1 + i3\omega_0\tau_c)\rho E_{3\omega_0} + cn_{3\omega_0}\beta_{K_{3\omega_0}}|E_{3\omega_0}|^{2K_{3\omega_0}-2}E_{3\omega_0} \tag{6.5b}$$

The various parameters in (6.4a), (6.4b), (6.5a), (6.5b), are: the linear refractive index n_{ω_0} and $n_{3\omega_0}$, the cross sections for inverse Bremsstrahlung $\sigma_{\omega_0} = 5.5 \times 10^{-20}$ cm^2 and $\sigma_{3\omega_0} = 6.1 \times 10^{-21}$ cm^2, the cross sections for multiphoton absorption $\beta_{K_{\omega_0}} = 1.8 \times 10^{-94}$ cm^{13} W^{-7} and $\beta_{K_{3\omega_0}} = 1.4 \times 10^{-26}$ cm^3 W^{-2}, the numbers of photons $K_{\omega_0} = 8$ and $K_{3\omega_0} = 3$ involved in the process at the fundamental and third harmonic frequencies, respectively; the collision time $\tau_c = 350$ fs in air and the nonlinear index coefficient n_2 [33, 34]. We performed simulations for 2 values of the nonlinear index coefficient: $n_2 = 3.2 \times 10^{-19}$ cm^2/W and $n_2 = 1.8 \times 10^{-19}$ cm^2/W. The first value is more appropriate for pulse durations of 50 fs or more while the second value corresponds to pulse durations for which the role of the retarded Kerr effect is negligible [35, 36].

Ionization of air is described by a single rate equation for the generation of free electrons with density ρ. Consistently with the two-color propagation model, each source term corresponding to multiphoton ionization or avalanche processes comprises a contribution for each color:

$$\begin{aligned}\frac{\partial\rho}{\partial t} &= \left(\sigma_{K_{\omega_0}}|E_{\omega 0}|^{2K_{\omega_0}} + \sigma_{K_{3\omega_0}}|E_{3\omega 0}|^{2K_{3\omega 0}}\right)(\rho_{nt} - \rho)\\ &\quad + \left(\sigma_{\omega 0}|E_{\omega_0}|^2 + \sigma_{3\omega_0}|E_{3\omega_0}|^2\right)\frac{\rho}{U_i}\end{aligned} \tag{6.6}$$

where $\sigma_{K_{\omega_0}} = 3.7 \times 10^{-96}$ cm^{16} W^{-8} s^{-1} and $\sigma_{K_{3\omega_0}} = 2.5 \times 10^{-28}$ cm^6 W^{-3} s^{-1} denote the cross sections for multiphoton ionization at the fundamental and third harmonic frequencies, ρ_{nt} denotes the density of neutral oxygen molecules which is the main ionized species at intensities of a few 10^{13} W/cm^2 and U_i denotes its ionization potential.

Figure 6.9 shows the beam characteristics for the fundamental and TH pulses during the propagation of an incident pulse of low energy (1 pJ). The maximum intensity of the fundamental and third harmonic pulses, their Full Width at Half Maximum (FWHM) and the energy contained in a cylinder of radius 100 microns are shown as functions of the propagation distance. At low energy, the propagation of the fundamental pulse is governed by the laws of Gaussian optics. Energy of the TH pulse increases progressively before the focus and decreases again after the focus. The clearly visible oscillation period of the TH pulse corresponds to the expected value determined by the phase mismatch. The amplitude of this oscillation decreases when the focusing geometry is tighter as in our experiments. In the far-field, all the TH energy returned to the pump. This behavior has been attributed to the Gouy phase shift between the fundamental and third harmonic [13, 27], which leads to destructive interference between the third harmonic waves generated before and after the focus.

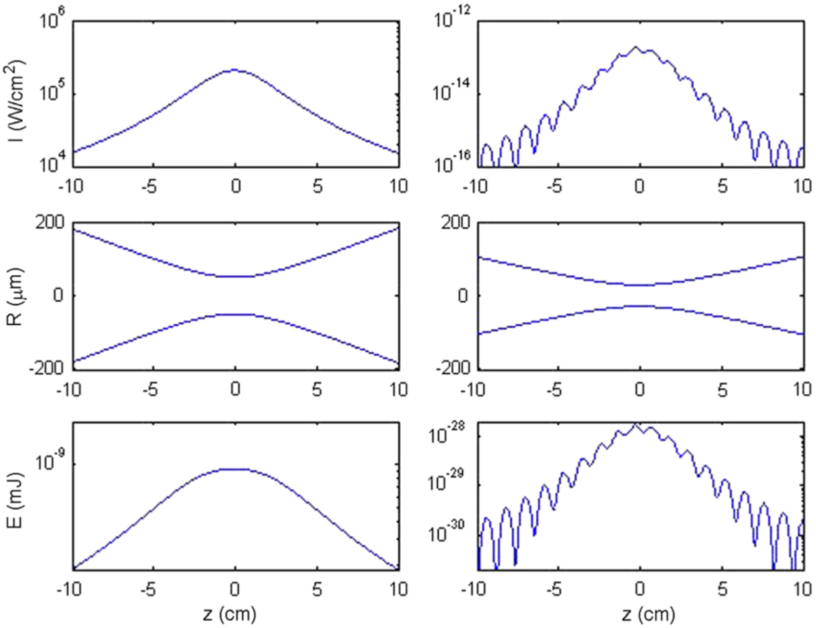

Fig. 6.9 Propagation dynamics of the fundamental (*first column*) and the TH (*second column*) pulses at low energy. *First line*: Maximum intensity as a function of the propagation distance z. *Second line*: Beam FWHM vs z, calculated from the fluence distributions of the fundamental and third harmonic, respectively. *Third line*: Energy contained within a cylinder of radius 100 microns. The energy of the fundamental pulse is 1 pJ and its waist at focus $z = 0$ cm is 100 microns

Figure 6.10 shows the same quantities for parameters corresponding to our experiments (waist at the focus of 30 μm and pulse energies of 100 and 500 μJ). The fundamental pulse forms a short filament with increasing length when the input energy increases. The propagation of the TH pulse exhibits attenuated contrast in the oscillations. For both pulses with input energy of 100 μJ and 500 μJ, the TH energy decreases slightly after its maximum but its energy is not entirely given back to the fundamental pulse. Although the energy of the TH pulse at the end of filamentation may be several decades below the maximum energy reached in the filament, it retains an energy of several nanojoules for an input pulse of 500 μJ. The discontinuity of the beam width of the third harmonic in the nonlinear regime is due to the fact that the TH beam exhibits an axial and a conical component as will be illustrated below. Only the axial component gives its energy back to the pump whereas the conical component stores most of the energy retrieved at the end of the filamentation stage. The beam width plotted in Fig. 6.10 therefore jumps from the radius of the axial component to the radius of the ring-like conical component.

In Fig. 6.6(c), (d), we presented the TH yield from a fully developed filament for fundamental pulse energies up to 2.2 mJ. To mimic the function of the Al diaphragm, we simulate it with a numerical aperture with a diameter of 100 μm and monitor the maximum TH contained in this area during filamentation. The results are shown in

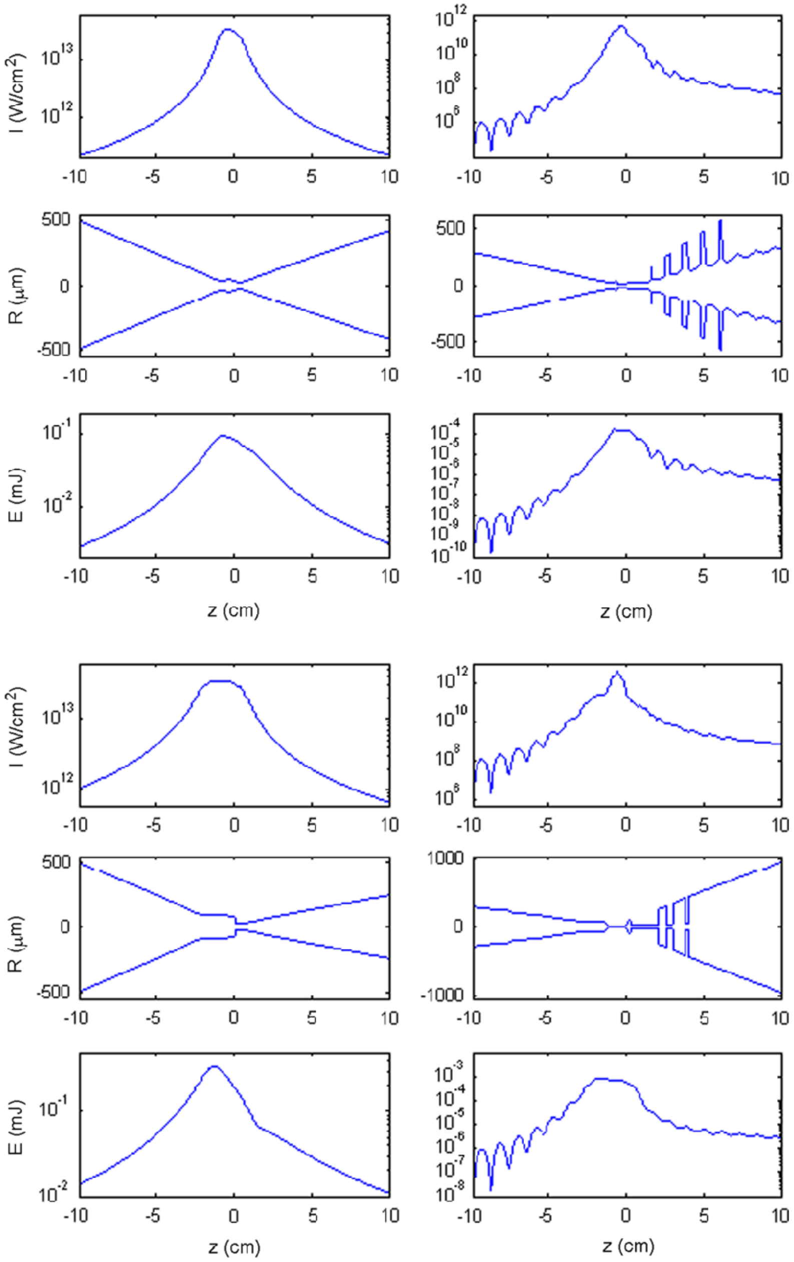

Fig. 6.10 Propagation dynamics of the fundamental (*first column*) and the TH (*second column*) pulses in the conditions of the experiment. The energy of the fundamental pulse is 100 μJ (*top figure*) and 500 μJ (*bottom figure*) and in both cases, its waist at focus $z = 0$ cm would be 30 microns if the propagation was linear. The same quantities as in Fig. 6.9 are presented but the log scale was used in the *first* and *third line* to stress that the energy in the third harmonic pulse does not entirely return to the pump

Fig. 6.6(c) for a nonlinear index coefficient $n_2 = 3.2 \times 10^{-19}$ cm^2/W corresponding to the critical power of 3 GW, and in Fig. 6.6(d) for $n_2 = 1.8 \times 10^{-19}$ cm^2/W corresponding to the critical power of 5 GW. The qualitative agreement between the experiment and simulation confirms our above phenomenological explanation. The energy of the TH pulse increases rapidly for increasing but low energies of the fundamental pulse. Above 500 µJ, the TH energy still increases but at a slower rate. We note that the difference between the TH energy passing through the aperture of 100 µm and the total TH energy calculated at the end of the filament decreases at large fundamental pulse energies. This is due to the fact that increasing nonlinearity due to the longer filamentation length quenches the destructive interference responsible for the back conversion of the energy in the axial component of the TH pulse. Consequently, the fraction of TH energy that remains in the axial component is closer to the maximum TH energy for large fundamental pulse energies.

The space-time dynamics of the fundamental and TH pulses are shown in Fig. 6.11 as functions of the propagation distance around the linear focus for an incident energy of 500 µJ. The fundamental pulse follows a standard filamentation dynamics with well-defined stages: self-focusing, plasma generation, defocussing of the trailing part (positive times) of the pulse and formation of a ring-shaped beam surrounding the intense central part. A refocusing process finally brings part of the energy of this ring back to the center but the fluence profile at the end of the filament still exhibits an intense axial beam surrounded by a conical beam. The dynamics of the TH pulse is slave to that of the fundamental. This comes from the third harmonic generation term (last term in (6.4b)) which plays the most important role among nonlinearities affecting the TH pulse. Therefore, we observe the formation of a ring in the TH pulse which is also clear from the time integrated (fluence) profiles plotted as white curves on each figure. As previously shown [13, 16, 18], this TH ring is not only the result of third harmonic generation by the ring-shaped fundamental pulse but also the result of a phase matching process involving the axial part of the fundamental pulse and a preferential angle for the TH pulse. The structures which are not visible in the fundamental pulse but appear in the TH pulse profile indicate the latter phase matching process leading to conical TH generation. The conical part of the TH pulse does obviously not spatiotemporally overlap with the conical part of the fundamental pulse. This confirms that the energy corresponding to the conical emission of the TH pulse cannot go back to the pump as four wave mixing governed by the last term in (6.4a), which should induce this back conversion, is prevented in the absence of spatial and temporal overlap. In contrast the axial part of the fundamental and TH pulses do overlap over a significant propagation distance within the filament, thereby allowing for back conversion from the TH pulse to the fundamental.

As a final comment, we would like to come back to the discrepancies concerning the TH enhancement with a pump filament and the comparison of all these methods. In our opinion, previous experiments reporting strong TH enhancement with short perturbed filaments can be interpreted consistently along the same lines. The apparent contradictory results concerning the delay can be reconciled by considering the type of perturbation introduced in the filament. For low power pump pulse, like the

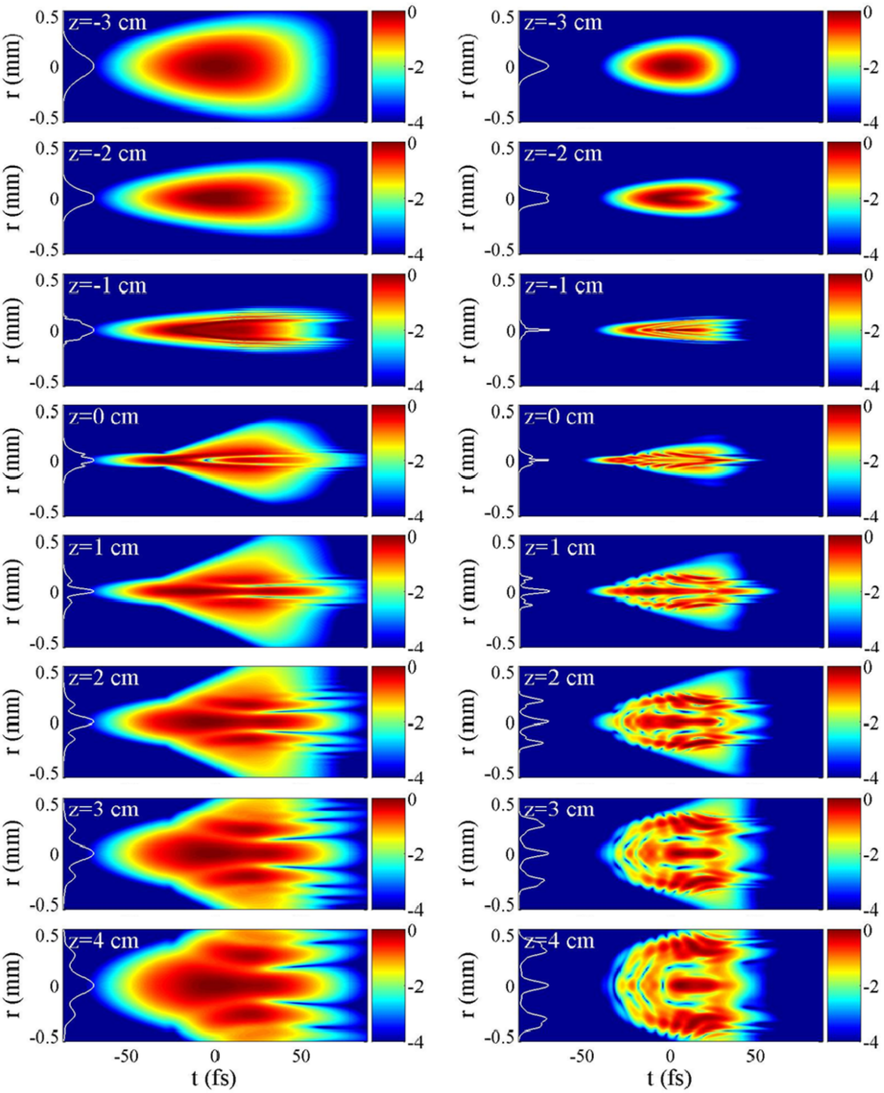

Fig. 6.11 Spatiotemporal dynamics of the fundamental (*left column*) and the TH (*right*) pulses as a function of the propagation distance. The energy of the fundamental pulse is 500 μJ and its waist at focus $z = 0$ cm would be 30 microns if the propagation was linear. The white curves on the left of each subfigure represent the fluence profiles for the fundamental and the TH pulses

results in Ref. [20] and ours in Fig. 6.4(a), an enhanced TH signal is observed in the case of parallel polarization and within a delay of a few hundred femtoseconds. This can be attributed to the fact that a plasma blocker is formed by the interference pattern between the pump and signal laser fields, acting as an efficient interference grating. This requires that the signal and pump pulses have the same polarization and similar intensities. At higher pump pulse energies, almost no difference is found between the two laser polarizations [19, 21]. This is similar to the results presented in Fig. 6.4(d). This phenomenon is due to the fact that the pump intensity is now much higher than that of the signal pulse and the plasma formed by the pump pulse acts now as a filament blocker. The polarization of the pump pulse is no longer crucial for the TH enhancement since the contribution of the relatively weaker signal pulse to the formation of the plasma blocker is negligible. Concerning the other methods for TH enhancement, blocking partially the filament with thin metallic fiber or fused silica wedge, we argue that the roles of these obstacles are also to perturb the filament develop and lead to break of the large cancellation of TH generated inside, like it was pointed out by the authors [22–26].

6.4 Conclusion

We studied the enhanced third harmonic generation from a femtosecond laser filament intercepted by a pump femtosecond pulse. Systematic measurement of the enhanced TH as function of the pulse polarization, time delay and pulse energies, have been performed. Based on these results, we concluded that the enhancement of the TH originates from the breaking of the large cancellation of the TH in a filament perturbed by a pump pulse. Numerical simulations have been performed to examine the dynamics of the TH generation in a filament. It is revealed that for pulse with relatively low energy pulse, it is the geometrical Gouy phase shift that is responsible for the TH cancellation inside the filament. Meanwhile, for more energetic pulses, the nonlinear propagation effects overcome largely the effect of the Gouy phase shift so that substantial TH survives at the end of a free propagating filament, as confirmed by the experiments.

References

1. A. Couairon, A. Mysyrowicz, Phys. Rep. **441**, 47 (2007)
2. S.L. Chin et al., Can. J. Phys. **83**, 863 (2005)
3. A. Braun et al., Opt. Lett. **20**, 73 (1995)
4. B. Forestier et al., AIP Adv. **2**, 012151 (2012)
5. A. Houard et al., Appl. Phys. Lett. **90**, 171501 (2007)
6. J. Kasparian et al., Opt. Lett. **25**, 1397 (2000)
7. C.P. Hauri et al., Appl. Phys. B **79**, 673 (2004)
8. C. D'Amico et al., New J. Phys. **10**, 013015 (2008)
9. Y. Liu et al., Phys. Rev. Lett. **99**, 135002 (2007)
10. J. Kasparian et al., Science **301**, 61 (2003)
11. B. Forestier et al., Appl. Phys. Lett. **14**, 141111 (2011)
12. J. Yao et al., Phys. Rev. A **84**, 051802(R) (2011)
13. N. Aközbek et al., Phys. Rev. Lett. **89**, 143901 (2002)
14. H. Yang et al., Phys. Rev. E **67**, 015401(R) (2003)
15. M. Kolesik, E.M. Wright, A. Becker, J.V. Moloney, Appl. Phys. B **85**, 531 (2006)

16. F. Théberge, N. Aközbek, W. Liu, J.F. Gravel, S.L. Chin, Opt. Commun. **245**, 399 (2005)
17. N. Kortsalioudakis et al., Appl. Phys. B **80**, 211 (2005)
18. F. Théberge, N. Aközbek, W. Liu, J. Filion, S.L. Chin, Opt. Commun. **276**, 298 (2007)
19. S. Suntsov, D. Abdollahpour, D.G. Papazoglou, S. Tzortzakis, Opt. Express **17**, 3190 (2009)
20. X. Yang et al., Appl. Phys. Lett. **95**, 111103 (2009)
21. S. Suntsov, D. Abdollahpour, D.G. Papazoglou, S. Tzortzakis, Phys. Rev. A **81**, 033817 (2010)
22. T.T. Xi, X. Lu, J. Zhang, Opt. Commun. **282**, 3140 (2009)
23. Z. Zhang et al., Opt. Lett. **35**, 974 (2010)
24. E. Schulz et al., Opt. Lett. **36**, 4389 (2011)
25. J.P. Yao, B. Zeng, W. Chu, J.L. Ni, Y. Cheng, J. Mod. Opt. **59**, 245 (2012)
26. Z. Liu et al., Opt. Express **20**, 8837 (2012)
27. R.W. Boyd, *Nonlinear Optics*, 3rd edn. (Academic Press, San Diego, 2008)
28. W. Liu, J.F. Gravel, F. Théberge, A. Becker, S.L. Chin, Appl. Phys. B **80**, 857 (2005)
29. W. Liu et al., Opt. Lett. **30**, 2602 (2005)
30. M. Kolesik, E.M. Wright, J.V. Moloney, Opt. Lett. **32**, 2816 (2007)
31. E.R. Peck, K. Reeder, J. Opt. Soc. Am. **62**, 958 (1972)
32. A. Couairon et al., Eur. Phys. J. Spec. Top. **199**, 5 (2011)
33. M. Mlejnek et al., Opt. Lett. **23**, 382 (1998)
34. M.D. Feit, J.A. Fleck, Appl. Phys. Lett. **24**, 169 (1974)
35. E.T.J. Nibbering, G. Grillon, M.A. Franco, B.S. Prade, A. Mysyrowicz, J. Opt. Soc. Am. B **14**, 650 (1997)
36. W. Liu, S.L. Chin, Opt. Express **13**, 5750 (2005)

Chapter 7
Strong and Coherent Forward Emissions from Molecules Driven by Femtosecond Infrared Laser Pulses

Huailiang Xu, Jinping Yao, Wei Chu, Bin Zeng, Jielei Ni, Guihua Li, Ya Cheng, Zhizhan Xu, Daniil Kartashov, Skirmantas Alisauskas, Audrius Pugzlys, Andrius Baltuska, Kaoru Yamanouchi, and See-Leang Chin

Abstract Strong narrow-band coherent emission lines of the $B^2\Sigma_u^+$–$X^2\Sigma_g^+$ transition of N_2^+ in air and the $A^2\Pi_u$–$X^2\Pi_g$ transition of CO_2^+ in CO_2 gas are observed from filaments generated by intense infrared femtosecond laser pulses (1150–2000 nm, <200 fs) in air. The coherent emission stimulated by self-generated third and/or fifth harmonics of the infrared femtosecond laser pulses is found to propagate in the forward direction along the infrared laser beam and has the same polarization direction as the third and fifth harmonics serving as the seed light. The intensity of the strong forward emissions of N_2^+ and CO_2^+, exhibiting excellent temporal and spatial coherence properties, is two orders of magnitude stronger than that of the fluorescence of molecules, and is strongly dependent on the pump laser intensity, the intensity of the seed harmonic radiation, and the filament length. The possible mechanisms responsible for the generation of the strong coherence emissions are discussed.

H. Xu (✉)
State Key Laboratory on Integrated Optoelectronics, College of Electronic Science and Engineering, Jilin University, Changchun 130012, China
e-mail: huailiang@jlu.edu.cn

J. Yao · W. Chu · B. Zeng · J. Ni · G. Li · Y. Cheng (✉) · Z. Xu
State Key Laboratory of High Field Laser Physics, SIOM, CAS, Shanghai 201800, China
e-mail: Ya.Cheng@siom.ac.cn

D. Kartashov · S. Alisauskas · A. Pugzlys · A. Baltuska
Photonics Institute, Vienna University of Technology, 1040 Vienna, Austria

K. Yamanouchi
Department of Chemistry, School of Science, The University of Tokyo, 7-3-1 Hongo, Bunkyo-ku, Tokyo 113-0033, Japan

S.-L. Chin
Department of Physics & Center for Optics, Photonics and Laser, Laval University, Québec City, G1V 0A6 Canada

K. Yamanouchi et al. (eds.), *Progress in Ultrafast Intense Laser Science X*,
Springer Series in Chemical Physics 106, DOI 10.1007/978-3-319-00521-8_7,

7.1 Introduction

When femtosecond laser pulse with the power beyond a threshold value (critical power) propagates in air, it self-focuses by the optical Kerr effect, and leads to multi-photon and/or tunnel ionization of atoms and molecules in air. Then, plasma produced by the ionization defocuses the laser beam. A dynamic balance between the Kerr self-focusing and the plasma defocussing is finally achieved so that intensity clamping occurs at around the laser intensity of about $5 \times 10^{13}\ \mathrm{W/cm^2}$ in the focal spot in air when 800 nm laser pulses are employed, and leaves a long weak plasma column, a so-called filament, in the laser propagation path [1–4]. This high clamped intensity induces fluorescence emission of atoms and molecules inside the filaments, which could be further amplified along the path of the filaments if population inversion conditions are fulfilled in the state populations in atomic and molecular species formed in the filaments [4–6].

Recently, remote lasing actions occurring as amplified spontaneous emissions (ASE) have been observed, which are induced by the filamentation of intense femtosecond laser pulses propagating in air [7–9]. It was found that the ASE-based lasers in air were operated either with N_2 or O_2 as gain medium. For N_2, it was shown from the detection of the backward scattered fluorescence that the fluorescence intensity of N_2 at 357 nm increases exponentially with a gain coefficient of $0.3\ \mathrm{cm^{-1}}$ as the filament length increases. In this circumstance, laser pulses (800 nm, 42 fs) were focused directly into air to generate a single filament with a length of a few centimeters that varies as a function of the input laser energy of the femtosecond laser pulses. Besides the 357 nm laser emission, several other fluorescence lines such as 337 nm from the second positive band of N_2 were found to be amplified to generate ASE with a similar gain [7, 8]. The population inversion for the nitrogen ASE lasers was ascribed to the recombination of free electrons with ions in the plasma. For O_2, the ASE lasing line resulting from O atoms with the $3p^3P$–$3s^3S$ transition at 845 nm was observed when a 226-nm, 100-ps laser pulse was used to induce two-photon dissociation of O_2 and the subsequent two-photon resonant excitation of the ground state O atom fragments, which produce the emission at 845 nm. Well-collimated coherent light beams with a gain coefficient of $62\ \mathrm{cm^{-1}}$ were observed in both backward and forward propagation directions as reported previously in Ref. [9].

The observations of remote lasing actions mentioned above are very promising since femtosecond filamentation enables us to reach a remote distance as far as a few kilometers [10]. However, because the lifetimes of the excited states of N_2 and O_2 in air are in the picosecond and nanosecond range, only a small portion of the long filament induced by ASE lasers is used for the lasing with one laser pulse [11, 12]. To overcome this limit, a multiple-pulse scheme was proposed, which relies upon a pulse train to boost the plasma density in the seed channel to satisfy the transient population inversion for amplification [13]. Theoretical simulations on the possible mechanisms for the remote atmospheric ASE lasing were also reported recently [14–16].

More recently, we demonstrated experimentally that multi-wavelength narrowband coherence emissions of molecules are induced by intense femtosecond infrared laser pulses in air as well as in CO_2 gases [17, 18]. It was found that these strong narrow-band emissions result from the electronic bands of molecular ions of N_2^+ and CO_2^+, and could only be produced along the propagation direction of the fundamental laser light. In addition, these forward coherence emissions were shown to occur within an unexpectedly short time scale comparable to the pump laser pulse duration (∼200 fs), which were tentatively attributed to seed-laser amplification of the self-generated harmonics of the pump infrared lasers [17]. The abovementioned observations are fundamentally different from the previously reported ASE lasers, which are based either on electron recombination of ionized N_2 or on resonant two-photon excitation of O fragments produced through the resonant two-photon dissociation of O_2.

In this chapter, we will first present in Sect. 7.2 a typical experimental apparatus for generating the strong multi-wavelength coherence emissions, which is followed by our results on N_2 in air (Sect. 7.3) and N_2 mixed with Ar, Xe and Ne (Sect. 7.4). In Sect. 7.5, we will introduce the coherence narrow-band emissions produced in CO_2. We will then discuss in Sect. 7.6 regarding the mechanisms responsible for this coherence emission of molecular ions induced by intense laser fields. Finally, the summary and conclusions are presented in Sect. 7.7.

7.2 Experimental Setup

The experiments of remote narrow-band coherence emission of molecular ions were conducted using an optical parametric amplifier (OPA, HE-TOPAS, Light Conversion, Inc.), which was pumped by a commercial Ti:Sapphire laser system (Legend Elite-Duo, Coherent, Inc.) with a repetition rate of 1 kHz and a central wavelength of ∼800 nm [17, 18]. The central wavelength of the infrared pulses from the OPA can be continuously tuned in the spectral range from ∼1200 nm to 2500 nm. In the spectral range of 1600–2500 nm that corresponds to the idler output of OPA, the maximum pulse energy of the OPA reached to ∼700 μJ, and the pulse duration at around 1900 nm was ∼200 fs. In the spectral range of 1200–1600 nm that corresponds to the signal output of OPA, the pulse energy of the OPA reached ∼1.2 mJ, and the pulse duration at around 1284 nm was ∼80 fs. The pump infrared laser pulses were focused into a vacuum chamber filled with different gases or directly into air by using lenses of different focal lengths ranging from 36 mm to 300 mm, so that the third or fifth harmonics of the fundamental laser pulse as well as the amplified emissions are generated. A grating spectrometer (Shamrock 303i, Andor) with a 1200 grooves/mm grating was used to record the spectra of the plasma of different gases. For measuring the fluorescence spectra of the emissions, the light emitting to the backward direction and side direction from the filament was guided into the grating spectrometer through a focal lens to couple the fluorescence light into a fiber.

Fig. 7.1 Forward direction spectra obtained with three different input energies of 1960 nm pump pulse excitation

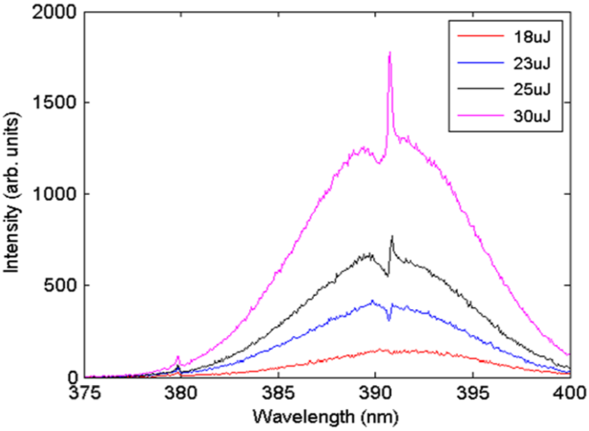

7.3 Switchable Multi-wavelength Coherence Emissions in Air

Figure 7.1 shows the 5th harmonic spectra in the 375–400 nm range obtained with 1960 nm pump pulses at three different input energies. The focal length of the lens was 36 mm. It can be seen that as the input energy increases a strong, narrow-bandwidth emission at 391 nm appears on the top of the spectrum of the 5th harmonic. The 391 nm band corresponds to the $B^2\Sigma_u^+$–$X^2\Sigma_g^+$ (0, 0) transition of N_2^+. The strong 391-nm narrow-band emission on the top of the fifth harmonic spectrum does not appear when the input energy of the laser pulse is lower (18 and 23 μJ) even if the 5th harmonic has already been produced, but when the laser energy reached 30 μJ, the strong narrow-band emission at 391 nm takes place. This implies that the emission has a strong dependence on the laser intensity. It should be noted that the calculated intensity of 3.4×10^{13} W/cm^2 for the value of 30 μJ has not reached yet the clamped intensity for the filamentation if we assume that the pulse is focused into vacuum.

The strong narrow-bandwidth emission at 391 nm was found to have an excellent polarization property. In Fig. 7.2, the strong narrow-band emission at 391 nm produced by the laser pulse with the energy of 150 μJ and the central wavelength of 1920 nm is illustrated. Its polarization property was measured using a Glan-Taylor polarizer, which was placed just before the spectrometer. It was found that the strong emission at 391 nm is linearly polarized with the direction parallel to the polarization direction of the pump infrared laser pulses. This perfectly linearly polarized strong narrow-band emission at 391 nm shows a totally different feature from the ASE laser whose polarization is isotropic.

The strong 391-nm emission propagated in the same direction as the laser propagation direction, that is, the forward direction. We measured the fluorescence spectra of the filament both from the side and the backward direction. It was found that the spectra recorded from the backward and side directions did not show any strong emission at 391 nm, and their spectra were similar to each other with comparable fluorescence line intensities for both N_2 and N_2^+ [11], which were two orders of

Fig. 7.2 The fifth harmonic spectrum and the 391 nm laser emission obtained with 1920 nm pump pulse excitation at 150 μJ. The data were averaged over 500 laser shots. The *inset* shows the polarization property of the 391 nm line emission

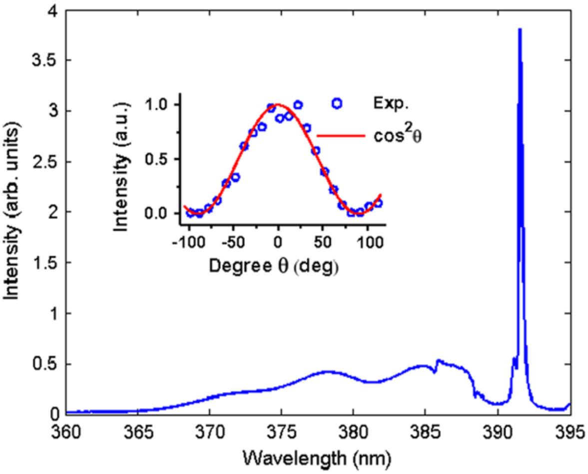

Fig. 7.3 The 391 nm line intensity versus the plasma channel length in air. The *solid line* is the fitted exponential curve of the coherence line emission

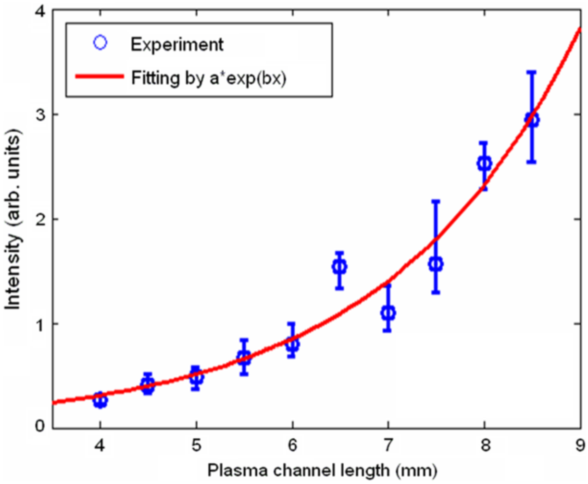

magnitude lower than the 391-nm emission propagating towards the forward direction.

The dependence of the forward 391-nm emission on the filament length was measured, as shown in Fig. 7.3, by truncating the length of the plasma channel of the filament using a pair of uncoated fused silica plates [19] and by recording the signal intensity of the 391 nm emission at the respected truncated filament lengths. In this measurement, a pair of uncoated fused silica plates was intersected with the plasma channel induced by the infrared pump laser. Thus, the intense femtosecond laser beam was reflected by the front and back surfaces of these two fused silica plate, and the loss of the laser energy by the transmission through the plate pair reduces largely the peak intensity of the reflected femtosecond laser beam, and consequently, the plasma channel is truncated. The filament length was determined by moving the

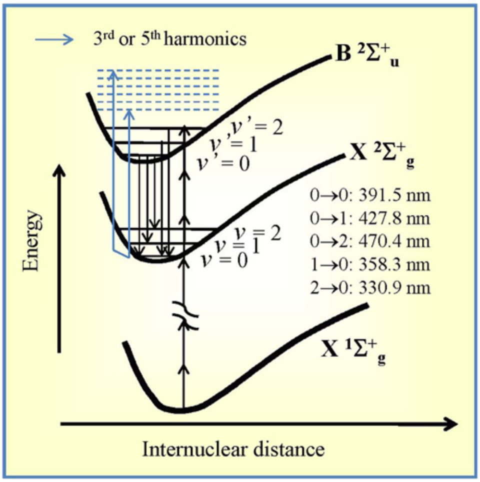

Fig. 7.4 A simplified energy-level diagram of ionized and neutral nitrogen molecules and the transitions corresponding to the narrow-band line emissions

focal lens along the propagation direction of the femtosecond laser beam. The signal intensity of the 391 nm emission recorded by the spectrometer was estimated by integrating the spectral flux over a narrow spectral window peaked at 391.4 nm with a spectral width of ~0.3 nm (full width at half maximum, FWHM). In order to remove the fluorescence signal from the spectrum, a polarizer was placed just before the spectrometer so that only the light with the polarization direction parallel to that of the pump laser passes through. The recorded intensity of the 391 nm emission shows a clear exponential dependence on the plasma length with a coefficient of ~5.02 cm^{-1}, which is more than one order of magnitude higher than that ($\sim 0.3\ \mathrm{cm}^{-1}$) of the ASE as reported in Ref. [7].

It should be pointed out that, when the pump wavelengths are respectively tuned to 1682, 1760, 2050 and 1415 nm [17], the coherent narrow-band emissions in air were also observed at 331, 358, 428 and 471 nm, which correspond respectively to the $\mathrm{B}^2\Sigma_\mathrm{u}^+$–$\mathrm{X}^2\Sigma_\mathrm{g}^+$ $(2,0)$, $(1,0)$, $(0,1)$, and $(0,2)$ emission transitions of N_2^+ (see Fig. 7.4). Because the pump pulse energy of our OPA source drops significantly when the wavelength is longer than 2200 nm, the forward coherence emission at 471 nm was seeded by the 3rd harmonic of the pump laser pulse with the wavelength at 1415 nm.

7.4 Strong Forward Nitrogen Coherence Emissions in Different Gas Mixtures

In order to investigate the mechanisms of the generation of the narrow-band strong forward emissions, the emission at 391 nm was measured using the mixtures of N_2 with three different rare gas species, i.e., N_2-Xe, N_2-Ar, and N_2-Ne, where the pump laser wavelength and energy were set to be 1184 nm and 0.96 mJ, respectively, and the N_2 pressure was fixed at 0.1 bars. The 391 nm emission in the forward

Fig. 7.5 Forward direction spectra obtained with the excitation of 1184 nm infrared laser pulses in N_2, N_2-Xe, N_2-Ar and N_2-Ne

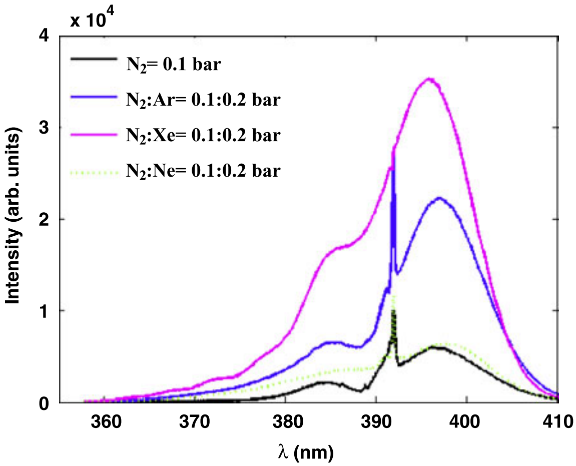

direction was attenuated to 1 % by a neutral density filter, and then, accumulated by the spectrometer over 100 laser shots, while the fluorescence signal from the side of the filament was accumulated over 1000 laser shots. In Table 1, the ionization potentials I_p and second-order Kerr refractive index coefficients n_2 (at 800 nm, 1 atm) of Xe, N_2, Ar, and Ne are listed for further discussion [20–22].

In Fig. 7.5, we demonstrate the spectra of the 3rd harmonic as well as the strong 391 nm emissions in the forward direction in the N_2-Xe, N_2-Ar, and N_2-Ne mixtures. The three rare gas pressures were kept to be at 0.2 bars. It can be seen that the introduction of Xe, Ar and Ne leads to different effects on the 391 nm laser emission, which disappears in N_2-Xe, slightly increases in N_2-Ne, but is significantly enhanced in N_2-Ar.

As discussed above, the forward coherence emissions are dependent on the intensity of the fundamental laser pulses. The clamped intensity in the filament plasma is determined by the balance between Kerr self-focusing and plasma defocussing, $n_2 I = N_e(I)/(2N_{\text{crit}})$ [1–4], where $N_{\text{crit}} = \varepsilon_0 m\omega^2/e^2$ is the critical plasma density with m, e and ω being the electron mass, elementary charge, and the central frequency of the laser field, respectively, $N_e(I)$ is the electron density induced by multiphoton and tunnel ionization, and therefore, is dependent on the ionization potential I_p of the atoms or molecules in the filament. According to this formula, the clamped intensity in N_2 is higher than that in Xe, lower than that in Ne, and comparable with that in Ar.

In the N_2-Xe mixture, it is expected that the clamped intensity decreases with the increase of the Xe pressure and gradually becomes close to the value obtained in pure Xe with the high Xe pressure. In order to confirm this, we measure fluorescence intensity at 391 nm from the side of the filament (Fig. 7.6), which can be used to estimate the clamped intensity because the 391 nm fluorescence emission is a radiative decay of the excited state $B^2\Sigma_u^+$ of N_2^+ [23], and thus, depends on the ionization rate of N_2, and correspondingly, the clamped intensity inside the filament. In Fig. 7.6, the 391 nm fluorescence first decays with the increase of Xe pressure,

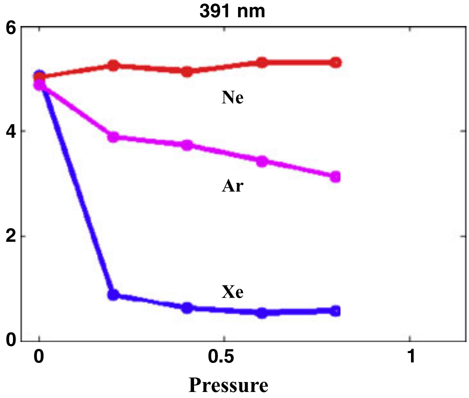

Fig. 7.6 Experimentally measured fluorescence intensities at 391 nm from the side of the plasma in three different gas mixtures. The nitrogen pressure was fixed at 0.1 bar

and then, and is stabilized at the higher Xe pressure, which reflects the fact that the clamped intensity inside the filament first decreases as the Xe pressure increases, and then, becomes constant. When the clamped intensity decreases, the population in the $B^2\Sigma_u^+$ state decreases sharply, and consequently, the 391 nm emission is quenched.

On the other hand, in the N_2-Ne mixture, it is expected that the clamped intensity increases with the increase of the Ne pressure, and gradually becomes close to the value obtained in pure Ne. However, as shown in Fig. 7.6, as the Ne pressure increases, the 391 nm fluorescence intensity tends to be slightly enhanced, suggesting that the clamped intensity in the N_2-Ne mixture slightly increases as the Ne pressure increases. This is because the ionization potential of Ne is so high that N_2 is mainly ionized in the plasma. The slightly increased clamped intensity may increase the ionization rate of N_2. Moreover, since the third harmonic in a filament can be scaled as $I_{3w} \propto (\chi_{\mathrm{Ne}}^{(3)} N_{\mathrm{Ne}} + \chi_{\mathrm{N2}}^{(3)} \mathrm{N}_{\mathrm{N2}})^2 I_w^3$ with $\chi^{(3)} = 4\varepsilon_0 c n_0^2 n_2/3$ [24], the third harmonic in the spectrum is produced mainly by N_2 and the intensity of the third harmonic grows as the clamped intensity increases because the second-order Kerr refractive index coefficient n_2 of Ne is at least one order of magnitude smaller than that of N_2 under the same pressure. Finally, because n_2 depends both on gas species and pressure, and because the pressure of Ne is nearly one order of magnitude higher than that of N_2, the change in the position of the Kerr self-focusing point, and accordingly the change in the filament length can be neglected. The intensity of the 391 nm emission in Fig. 7.5 becomes slightly stronger when the Ne pressure increases, revealing the role of both the slightly enhanced 3rd harmonic intensity and the increased population in the $B^2\Sigma_u^+$ state.

In the N_2-Ar mixture, the clamped intensity should remain nearly the same value even when the Ar pressure varies because, as listed in Table 7.1, n_2 and I_p values of Ar and N_2 are almost the same. Therefore, the population lying on the $B^2\Sigma_u^+$ state is expected to maintain nearly the same. In this case, the growth of the Ar pressure promotes significantly the 3rd harmonic intensity as can be seen in Fig. 7.5. In addition, because n_2 increases with the pressure, the position of the collapse of the self-focusing is shifted away from the focusing point of the lens at the high

Table 7.1 Ionization potentials and second-order Kerr refractive index coefficients (800 nm at 1 atm) of Xe, N_2, Ar, and Ne [20–22]

Material	Xe	N_2	Ar	Ne
I_p (eV)	12.13	15.58	15.76	21.56
n_2 (10^{-20} cm^2/W)	93	11	10	0.74

pressure of Ar according to Marburger's law, resulting in the formation of a longer filament. Because, in the case of the N_2-Ar mixture, the harmonic signals are much stronger and the length of the filament becomes longer compared with the N_2-Ne mixture, and the clamped laser intensity is almost independent of the pressure, the final output of 391 nm emission is expected to be enhanced more significantly than in the N_2-Ne mixture. This is indeed the case as observed in our experiment as seen in Fig. 7.5.

It can be seen from the measurement of the 391 nm emission in the three different gas mixtures that the forward coherence emission at 391 nm is mainly determined by the three factors i.e., the pump laser intensity, the intensity of the harmonic radiation, and the filament length. This seems to follow the well-known small signal gain equation of $I_{laser} = I_{seed}e^{gL}$ [25], where L is the length of the gain medium, which corresponds to the filament length in our experiment and can be estimated based on the Marburger's law and geometric optics [26, 27], I_{seed} the seed intensity corresponding to the 3rd harmonic intensity in our experiment, and $g = \Delta n \times \delta_{21}$ the gain coefficient of the medium with Δn being the population inversion, and δ_{21} the stimulated emission cross section, which is strongly dependent on the ionization rate of N_2, and accordingly, the clamped intensity in the filament.

7.5 Simultaneous Multi-wavelength Remote Line Emissions in CO_2

Strong multi-wavelength coherence emissions were observed also in CO_2. In Fig. 7.7a, we show the measured spectrum of the emission propagating in the forward direction, that is, the propagating direction of an infrared pump laser pulse that was characterized with the energy of ~1.1 mJ, the pulse duration of $\Delta t \sim 80$ fs, and the central wavelength at $\lambda \sim 1322$ nm. The focal length of the lens was 50 mm, and the CO_2 gas pressure inside the chamber was fixed at ~800 mbar. As shown in Fig. 7.7(a), intense narrow-bandwidth emissions peaked at 326 nm, 337 nm and 351 nm appear in the spectrum. These emission lines correspond to the $\mathrm{A}^2\Pi_\mathrm{u}$–$\mathrm{X}^2\Pi_\mathrm{g}$ transitions of CO_2^+. It can be seen in this spectrum that all of these three narrow-bandwidth emission lines exhibit a typical double-peak structure, which are ascribable to the Renner-Teller effect of CO_2^+ [28, 29]. These strong narrow-band emission lines shown in Fig. 7.7(a) are different from the broad fluorescence spectral bands of CO_2 [18]. It can also be observed in Fig. 7.7(a) that the line intensities at 326 nm, 337 nm and 351 nm of CO_2^+ decrease dramatically as the angle between

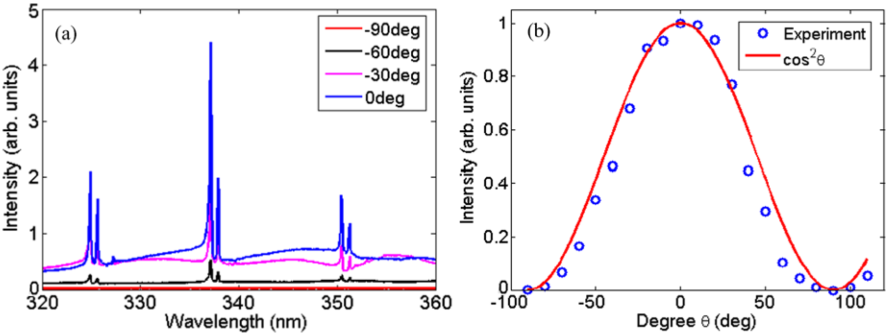

Fig. 7.7 (**a**) Forward direction spectra obtained with the excitation of 1322 nm infrared laser pulses with different polarization conditions in CO_2. (**b**) Polarization property of the 337 nm laser emission

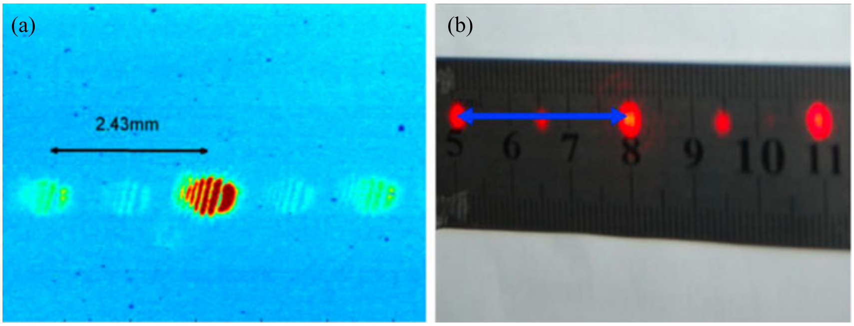

Fig. 7.8 Spatial coherence properties of (**a**) the CO_2 narrow-band emission at 337 nm and (**b**) the He-Ne laser line at 632 nm

the polarizer axis and the pump laser polarization direction is varied from the 0° to ±90°, showing that the narrow band emission lines are linearly polarized. The polarization property of the narrow-band emission at 337 nm in the spectral range of 336–339 nm shown in Fig. 7.7b is similar to the case of the strong coherent emission lines of N_2^+ as described in the preceding sections above.

The spatial coherence property of the strong CO_2^+ line emissions was examined by recording the diffraction pattern of the forward 337 nm emission. For this measurement, the laser beam at 337 nm was filtered out using an interference filter with the central wavelength of 335 nm and the bandwidth of 10 nm. After the laser beam was dispersed by a home-made 1000 grooves/mm diffraction grating engraved on fused silica glass by being irradiated with femtosecond laser pulses, the diffraction pattern was measured by a CCD camera placed 7.1 cm behind the grating. As shown in Fig. 7.8(a), the distance between the zero-th order and the first order diffraction peaks is 2.43 mm, which is consistent with the theoretical calculation. The weak spots between the zero-th order and the first order diffraction peaks in Fig. 7.8(a) are ascribed to the imperfection of the grating. In order to verify the distance between the zero-th order and the first order diffraction for the 337 nm emission, the spatial diffraction pattern of a He-Ne laser was also recorded as shown in Fig. 7.8(b), in which the distance between the zero-th order and the first order diffraction peaks is 3.0 mm, which is in good agreement with the calculated value of 2.97 mm. The interference fringes appearing in each diffracted beam pattern of Fig. 7.8(a) are ascribable to the interference between the beam reflected from the front and back surfaces of the narrow-band interference filter. This was confirmed by the fact that the interference fringes moved when the angle between the narrow-band filter and the laser beam was varied.

The dependence of the emission intensity at 337 nm on the filament length was also measured by truncating the plasma channel induced by the pump infrared laser using a pair of uncoated fused silica plates in the same procedure as that described in Sect. 7.3. The emission intensity at 337 nm was estimated by integrating the spectral flux over a narrow window from 336 nm to 337.5 nm. The recorded emission spectrum is peaked at 337 nm with the spectral width of $\sim$0.5 nm (FWHM). The measured intensity of the emission at 337 nm varying as a function of the filament length gives an exponential coefficient of $\sim$4.43 cm^{-1} [18].

7.6 Mechanism of Strong Forward Coherence Emissions

In order to interpret the mechanisms responsible for the strong forward coherence emission of N_2^+ and CO_2^+ induced by intense infrared laser pulses, an external-seeding experiment was carried out. In this experiment, the second harmonic of an 800 nm Ti:Sappire laser pulse was generated, whose polarization direction was arranged to be perpendicular to that of the 1920 nm pump pulses. The 400 nm probe and the 1920 nm pump beams were first overlapped spatially, and then focused into air by a plano-convex lens to produce a plasma channel. The temporal synchronization between the second harmonic and the pump pulses was achieved using a time-delay line. A Glan-Taylor polarizer was placed just before the spectrometer to allow the light with the polarization direction parallel to the second harmonic of the 800 nm laser pulses to be recorded by the spectrometer. Figure 7.9 shows the spectra measured without (blue dashed curve) and with (red solid curve) the 1920 nm pump laser. Similar to the coherent emissions appearing on the top of the 5th harmonic of the 1920 nm pump laser shown in Fig. 7.2, the 391 nm line emission appears on the second harmonic spectrum of the 800 nm laser pulses when the pump laser is introduced and the spatiotemporal overlap between the second harmonic of the 800 nm laser pulses and the 1920 nm pump laser was achieved. In addition, when the second harmonic of the 800 nm laser pulses was blocked while the infrared 1920 nm pump laser was still on, only a typical fluorescence spectrum of ionized and neutral nitrogen molecules were observed, as shown by the green dotted curve in Fig. 7.9, showing that the injection of a seed pulse is necessary for achieving the strong forward coherence emission.

Fig. 7.9 Spectra of externally injected second harmonic of an 800-nm Ti:sapphire laser measured before (*blue dashed*) and after (*red solid*) switching on the 1920-nm pump laser, and the spectrum obtained with only 1920-nm pump pulses (*green dotted*)

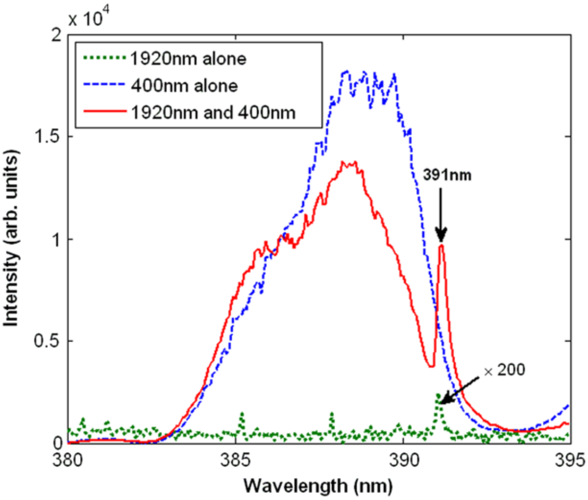

Based on the above observations, the seed amplification scheme that may be responsible for the forward coherence emission of N_2 was examined first. In this scheme, the population inversion needs to be established within an ultrashort time period for initiating the amplification of the UV harmonics, which are resonant with the transitions of electronic states in N_2^+, generated during the propagation of the infrared pump laser pulses in gases. However, it is known that the ejection of an inner-valence electron (HOMO-2) of N_2 leaves the ion N_2^+ in the excited $B^2\Sigma_u^+$ state, whereas the ionization of an outer-valence electron (HOMO) leads to N_2^+ lying on the ground $X^2\Sigma_g^+$ state [28], and it is considered from previous calculations [30] that the ionization probability of HOMO-2 is about one to two orders of magnitude smaller than that of HOMO in an intense laser field. Thus, as discussed below, there must be some other mechanisms which may exist for achieving the population inversion between the upper and lower levels if the seed-amplification scheme works.

The first consideration for the building-up of the population inversion is a linear pump scheme induced by the harmonic radiations as described below. The population of N_2^+ in the ground state resulting from the HOMO electron ionization could be reduced by absorption of the harmonic photons. As shown in Fig. 7.4, because of the broad band of the harmonic radiations of the infrared pump pulses, the harmonic photons resonant with the transitions from the low vibrational levels of the electronic ground to some vibrational levels of the $B^2\Sigma_u^+$ state of N_2^+ will be absorbed, leading to an efficient reduction of the population of N_2^+ in the ground state, and thus to the population inversion for the transitions indicated in Fig. 7.4. In this scenario, the harmonics of the infrared pump pulses play the following two kinds of roles for achieving the amplification. The first is to serve as a seed source, i.e., the spectral portion of the harmonic of the infrared pump pulses that matches the resonant transition wavelength of N_2^+ shown in Fig. 7.4 is to be amplified. The second is to reduce the ground state population, as described above. It should be emphasized that this is a multiple-level system to build up the population inversion

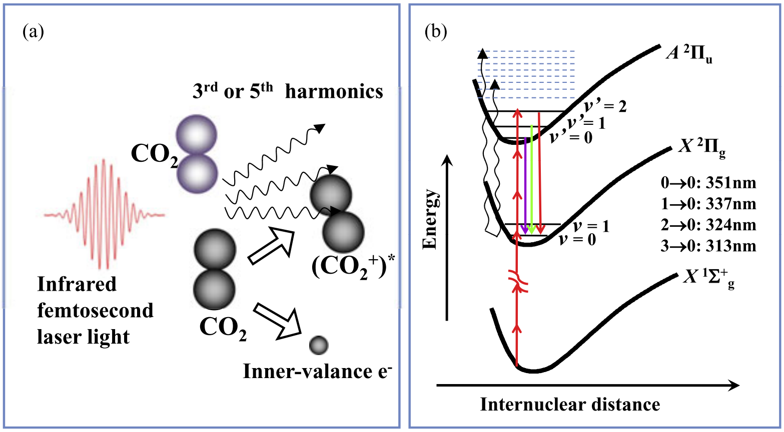

Fig. 7.10 (**a**) Interaction of CO_2 molecules simultaneously with mid-IR laser field and its third or fifth harmonics resulting in the formation of molecular CO_2 ions at an excited state by ionization of inner-valance electrons, giving rise to a strong forward line emissions. (**b**) A simplified energy-level diagram of ionized and neutral CO_2 molecules with corresponding laser transitions

for lasing. Interestingly, with this harmonic-seeding mechanism, it would be impossible to achieve the seeded laser action at 337 nm, which is associated with the $C^3\Pi_u$–$B^3\Pi_g$ transition of N_2, even though there is a population inversion. This is because the $C^3\Pi_u$ state of N_2 is formed through the dissociative recombination occurring in a picosecond time scale through the following processes: $N_2^+ + N_2 \Rightarrow N_4^+$; $N_4^+ + e \Rightarrow N_2(C^3\Pi_u) + N_2$ in air [11], in which the population inversion can only be achieved in a ps time scale, which is much longer than the time scale of the harmonics generated during the filamentation with a pulse duration comparable to infrared pump laser pulses. This is indeed the case in our experiment that no lasing at 337 nm was observed.

Similarly, in CO_2^+, the population inversion between the vibrational levels of the $A^2\Pi_u$ and $X^2\Pi_g$ states, as shown in Fig. 7.10, may result from a "cooperative" process of the fundamental infrared pump pulse, and its third and fifth harmonics on the ionization and excitations of CO_2. The populations of the $X^2\Pi_g$ and $A^2\Pi_u$ states come from two distinct channels of the ionization, i.e., the HOMO ($1\pi_g$) electron ionization resulting in the formation of the ground $X^2\Pi_g$ state of CO_2^+, whereas the HOMO-1 ($1\pi_u$) electron ionization resulting in the formation of excited $A^2\Pi_u$ ionic state. On the other hand, the fifth harmonic spectrum peaked at around 275 nm also overlaps with the transitions between the $X^2\Pi_g$ and $A^2\Pi_u$, and thus, the absorption of the fifth harmonic photons by CO_2^+ reduce its population in the lowest vibrational level of the ground $X^2\Pi_g$ state. Because the nonradiative decays between the vibrational levels in molecules would occur in a time scale of ps-ns, the efficient reduction of the population of CO_2^+ in the lowest vibrational level of the electronic ground state leads to the population inversion for the transitions as those indicated in Fig. 7.10. Furthermore, the third harmonic of the infrared 1322 nm pump pulse, the tail of whose spectrum extends to about 320 nm, plays a role as the seed for promoting the strong forward coherence emission.

Besides the linear absorption of the harmonic photons that are resonant with the transitions in N_2^+ and CO_2^+ to deplete the population in the ground state, the other mechanism proposed to be responsible for the instantaneous population inversion is a nonlinear (multiple-photon) absorption process in which the infrared pump laser photons and also its harmonic photons may participate. Because of the high laser intensity inside the filament, the nonlinear absorption process could induce the absorption of a few photons to deplete the population in the lower vibrational levels of the ground state of N_2^+ and CO_2^+, thus achieving the population inversion.

Another possible scheme for the forward coherence emission is four-wave mixing, in which the population inversion is not required. In this scheme, two laser photons with different frequencies in the broad spectrum of the fundamental infrared pump laser pulses and one harmonic pulses resonant with the B–X transition of N_2^+ or the A–X transition of CO_2^+ stimulate the emission of the fourth frequency photon that is resonant with the lasing transition of N_2^+ and CO_2^+. However, at this stage, only based on our experimental results reported in the present study, it is difficult to specify definitely the responsible mechanisms for the coherent and strong forward emissions.

7.7 Summary

In this chapter, we have introduced our recent measurements of the coherent and strong forward emissions of $B^2\Sigma_u^+$–$X^2\Sigma_g^+$ transitions of N_2^+ and the $A^2\Pi_u$–$X^2\Pi_g$ transitions of CO_2^+ driven by strong femtosecond infrared laser pulses. It was found from the measurements of the 391 nm emissions in N_2^+ in the three kinds of gas mixtures of N_2-Xr, N_2-Ar, and N_2-Ne that the coherence emissions are dependent sensitively on the pump laser intensity, the intensity of the seed harmonic radiation, and the filament length. It was also shown from the external-seed experiment that the mechanisms responsible for the forward emissions may be the seed amplification with the instantaneous population inversion built up in an ultrashort time scale comparable to the pulse duration of the femtosecond infrared pump pulses.

Because the forward emissions have been observed in both N_2 and CO_2, it is expected that this type of strong and coherent forward emissions induced by intense femtosecond laser pulses are general phenomena that could also be observed with other molecules. The observed coherence emissions of N_2^+ and CO_2^+ in the forward direction are two orders of magnitude stronger than the fluorescence, which may be used in the remote sensing, because this strong and coherent emission can be scattered by particles in air and the scattered light can be stronger than the backward fluorescence.

Acknowledgements This work was partially supported by National Natural Science Foundation of China (Grant Nos. 11074098, 10974213, 60825406, 61235003), National Basic Research Program of China (Grant 2011CB808102), New Century Excellent Talent of China (NCET-09-0429), Basic Research Program of Jilin University, Canada Research Chairs, NSERC, DRDC Valcartier, CIPI, CFI, Femtotech and FQRNT.

References

1. S.L. Chin, S.A. Hosseini, W. Liu, Q. Luo, F. Théberge, N. Aközbek, A. Becker, V.P. Kandidov, O.G. Kosareva, H. Schroeder, Can. J. Phys. **83**, 863 (2005)
2. A. Couairon, A. Mysyrowicz, Phys. Rep. **441**, 47 (2007)
3. L. Berge, S. Skupin, R. Nuter, J. Kasparian, J.P. Wolf, Rep. Prog. Phys. **70**, 1633 (2007)
4. S.L. Chin, *Femtosecond Laser Filamentation* (Springer, New York, 2010)
5. S.L. Chin, H.L. Xu, Q. Luo, F. Théberge, W. Liu, J.F. Daigle, Y. Kamali, P.T. Simard, J. Bernhardt, S.A. Hosseini, M. Sharifi, G. Méjean, A. Azarm, C. Marceau, O. Kosareva, V.P. Kandidov, N. Aközbek, A. Becker, G. Roy, P. Mathieu, J.R. Simard, M. Châteauneuf, J. Dubois, Appl. Phys. B **95**, 1 (2009)
6. H.L. Xu, S.L. Chin, Sensors **11**, 32 (2011)
7. Q. Luo, W. Liu, S.L. Chin, Appl. Phys. B **76**, 337 (2003)
8. Q. Luo, A. Hosseini, W. Liu, S.L. Chin, Opt. Photonics News **15**, 44 (2004)
9. A. Dogariu, J.B. Michael, M.O. Scully, R.B. Miles, Science **331**, 442 (2011)
10. M. Rodriguez, R. Bourayou, G. Méjean, J. Kasparian, J. Yu, E. Salmon, A. Scholz, B. Stecklum, J. Eislöffel, U. Laux, P. Hatzes, R. Sauerbrey, L. Wöste, J.-P. Wolf, Phys. Rev. E **69**, 036607 (2004)
11. H.L. Xu, A. Azarm, J. Bernhardt, Y. Kamali, S.L. Chin, Chem. Phys. **360**, 171 (2009)
12. J. Bernhardt, W. Liu, F. Théberge, H.L. Xu, J.F. Daigle, M. Châteauneuf, J. Dubois, S.L. Chin, Opt. Commun. **281**, 1268 (2008)
13. P.R. Hemmer, P. Polynkin, T. Siebert, A.V. Sokolov, P. Sprangle, M.O. Scully, Proc. Natl. Acad. Sci. USA **108**, 3130 (2011)
14. P. Sprangle, J. Peñano, B. Hafizi, D. Gordon, M. Scully, Appl. Phys. Lett. **98**, 211102 (2011)
15. M.N. Shneider, A. Baltuška, A.M. Zheltikov, J. Appl. Phys. **110**, 083112 (2011)
16. J. Peñano, P. Sprangle, B. Hafizi, D. Gordon, R. Fernsler, J. Appl. Phys. **111**, 033105 (2012)
17. J.P. Yao, B. Zeng, H.L. Xu, G.H. Li, W. Chu, J.L. Ni, H.S. Zhang, S.L. Chin, Y. Cheng, Z.Z. Xu, Phys. Rev. A **84**, 051802(R) (2011)
18. W. Chu, B. Zeng, J. Yao, H.L. Xu, J. Ni, G. Li, H. Zhang, F. He, C. Jing, Y. Cheng, Z.Z. Xu, Europhys. Lett. **97**, 64004 (2012)
19. Y. Fu, H. Xiong, H. Xu, J.P. Yao, B. Zeng, W. Chu, Y. Cheng, Z.Z. Xu, W. Liu, S.L. Chin, Opt. Lett. **34**, 3752 (2009)
20. C. Brée, A. Demircan, G. Steinmeyer, IEEE J. Quantum Electron. **46**, 433 (2010)
21. H.J. Lehmeier, W. Leupacher, A. Penzkofer, Opt. Commun. **56**, 67 (1985)
22. V. Loriot, E. Hertz, Q. Faucher, B. Lavorel, Opt. Express **17**, 13429 (2009). Opt. Express, **18**, 3011 (2010)
23. A. Becker, A.D. Bandrauk, S.L. Chin, Chem. Phys. Lett. **343**, 345 (2001)
24. R.W. Boyd, *Nonlinear Optics*, 3rd edn. (Academic Press, London, 2008)
25. T.S. William, *Laser Fundamentals*, 2nd edn. (Cambridge University Press, Cambridge, 2004)
26. J.H. Marburger, Prog. Quantum Electron. **4**, 35 (1975)
27. A. Brodeur, S.L. Chin, J. Opt. Soc. Am. B **16**, 637 (1999)
28. G. Chambaud, W. Gabriel, P. Rosmus, J. Rostas, J. Phys. Chem. **96**, 3285 (1992)
29. M.A. Gharaibeh, D.J. Clouthier, J. Chem. Phys. **132**, 114307 (2010)
30. S.F. Zhao, C. Jin, A.T. Le, T.F. Jiang, C.D. Lin, Phys. Rev. A **81**, 033423 (2010)

Chapter 8
Tests of Classical and Quantum Electrodynamics with Intense Laser Fields

Sebastian Meuren, Omri Har-Shemesh, and Antonino Di Piazza

Abstract In this chapter classical and quantum electrodynamics in intense laser fields are discussed. We focus on the interaction of relativistic electrons with strong laser pulses. In particular, by analyzing the dynamics of this interaction, we show how the peak intensity of a strong laser pulse can be related to the spectrum of the radiation emitted by the electron during the interaction itself. The discussed method could be used to accurately measure high peak laser intensities exceeding 10^{20} W/cm^2 up to about 10^{23} W/cm^2 with theoretical envisaged accuracies of the order of 10 %. Furthermore, we investigate non-linear quantum effects originating from the interaction of an electron with its own electromagnetic field in the presence of an intense plane wave. These "radiative corrections" modify the electron wave-function in the plane wave. The self-interaction changes, amongst others, the dynamics of the electron's spin in comparison with the prediction of the Dirac equation. We show that this effect can be measured, in principle, already at intensities of the order of 10^{22} W/cm^2.

8.1 Introduction

Electrodynamics is nowadays considered as well understood, since both the classical and the quantum description of how electric charges interact have been verified to an outstanding precision in many experiments. However, there are still phenomena both in the classical and in the quantum regime of the theory, which have not been investigated yet. Generally speaking, in order to explore these effects one needs very strong electromagnetic fields. A possible source of strong electric fields, which has

---

S. Meuren · O. Har-Shemesh · A. Di Piazza (✉)
Max Planck Institute for Nuclear Physics (MPIK), Saupfercheckweg 1, 69117 Heidelberg, Germany
e-mail: dipiazza@mpi-hd.mpg.de

S. Meuren
e-mail: s.meuren@mpi-hd.mpg.de

O. Har-Shemesh
e-mail: omrihar@gmail.com

K. Yamanouchi et al. (eds.), *Progress in Ultrafast Intense Laser Science X*,
Springer Series in Chemical Physics 106, DOI 10.1007/978-3-319-00521-8_8,

been investigated since a long time, are highly-charged ions with charge number Z of the order of $1/\alpha \approx 137$, where α is the fine-structure constant. The field of a highly-charged ion has to be taken into account exactly in the calculations if the parameter $Z\alpha$ is of the order of unity (like, e.g., for U^{91+}). For example, the processes of bremsstrahlung and of electron-positron photoproduction in a highly-charged ion have been widely investigated [1–4]. For an overview on high-order QED effects in highly-charged ions the reader is referred to the literature [5–8].

In this chapter, however, we will mainly focus on strong-field effects arising in the interaction of a relativistic electron with a strong laser pulse. Coulomb and laser fields have a very different structure and they can be employed for complementary tests of QED. Since the first experimental realization of a laser in 1960 [9], the available intensities steadily increased due to a continuous flow of innovations like the chirped pulse amplification technique [10, 11]. Nowadays various optical petawatt laser systems are operating, capable of producing intensities in the range of 10^{20}–10^{22} W/cm^2 [12–19] (2×10^{22} W/cm^2 is the current intensity record [20]). Furthermore, multi-petawatt systems are under construction, which could reach intensities up to $\sim 10^{23}$ W/cm^2 if focused down to the diffraction limit [21–23]. At the Extreme Light Infrastructure (ELI) [24], the High Power laser Energy Research facility (HiPER) [25] and the Exawatt Center for Extreme Light Studies (XCELS) [26] even intensities of the order of 10^{24}–10^{25} W/cm^2 are envisaged (see also the review [27]). To effectively reach even higher field strengths one often collides laser pulses with ultra-relativistic particles, as in their rest frame the field strength is boosted by the relativistic Lorentz factor. In the near future also all-optical setups of this kind will be feasible by using laser wakefield accelerators, which have already allowed for electron energies of the order of 1 GeV [28, 29] (see also the reviews [30, 31]). We are therefore at the dawn of a new exciting era of strong-field experiments using intense laser fields [32].

Classically, charged particles interact via the electromagnetic field **E**, **B** which obeys Maxwell's equations[1] [33]. In a manifestly relativistic covariant formulation the electric and the magnetic field form the components of the anti-symmetric field tensor $F^{\mu\nu}$ ($\mathbf{E}^i = F^{i0}$, $F^{ij} = \varepsilon^{jik}\mathbf{B}^k$). While the homogeneous Maxwell equations are fulfilled by introducing the four-potential A^μ ($F^{\mu\nu} = \partial^\mu A^\nu - \partial^\nu A^\mu$), the inhomogeneous Maxwell equations become $\partial_\mu F^{\mu\nu} = 4\pi j^\nu$, where $j^\mu = (\varrho, \mathbf{j})$ is the four current vector (ϱ is the electric charge distribution and $\mathbf{j}$ the electric current density). The intensity I of an electromagnetic field is defined by the magnitude of

---

[1] In this chapter natural units $\hbar = c = 1$ are used (in some formulas $\hbar$ and c are restored for clarity). The magnetic field is rescaled with c and the charge is measured in Gaussian units ($4\pi\varepsilon_0 = 1$). The electron mass and charge are denoted by m and $e < 0$, respectively and this implies that $\alpha = e^2$. In covariant expressions the space-time metric $\eta_{\mu\nu}$ with signature $(1, -1, -1, -1)$ is used and $\partial_\mu = (\partial/\partial t, \boldsymbol{\nabla})$ is the four-derivative. Greek and Latin indices take the values $(0, 1, 2, 3)$ and $(1, 2, 3)$, respectively. Contractions of four-vectors are denoted by $a^\mu b_\mu = ab$, scalar products of three-vectors by $\mathbf{a}^i\mathbf{b}^i = \mathbf{ab}$ and summation over repeated indices is understood. The symbol ε^{ijk} denotes the totally anti-symmetric tensor in three dimensions with $\varepsilon^{123} = 1$. Dirac gamma matrices are denoted by γ^μ and $\not{a} = a_\mu\gamma^\mu$. For a spinor u it is $\bar{u} = u^\dagger\gamma^0$ and for a matrix M in spinor space it is $\bar{M} = \gamma^0 M^\dagger \gamma^0$.

the Poynting vector and for a plane wave ($\mathbf{E} \perp \mathbf{B}$) it is given by $I = \frac{1}{4\pi}|\mathbf{E}||\mathbf{B}|$. As a consequence of the inhomogeneous Maxwell equations electric charges produce electromagnetic fields. On the other hand electromagnetic fields also exert forces on electric charges according to the Lorentz force (LF) law $\frac{\mathrm{d}}{\mathrm{d}\tau} p^\mu = eF^{\mu\nu}u_\nu$, written down for an electron, $p^\mu = mu^\mu = (\varepsilon, \mathbf{p})$ denoting its (on-shell) four-momentum (u^μ is the four-velocity, $\varepsilon = \gamma m = \sqrt{\mathbf{p}^2 + m^2}$ the energy, γ the relativistic Lorentz factor and τ the proper time). Often one can neglect one of these two effects and considers only how electric charges produce electromagnetic fields for a given charge trajectory or how given electromagnetic fields act on electric charges. However, in principle, one has to solve Lorentz and Maxwell equations self-consistently in the most general case. This allows for a back-reaction of the electromagnetic field produced by a charge on the charge itself, which is called radiation reaction (RR). If one is interested only in the trajectory of a charge, one can eliminate the degrees of freedom of the radiation field by replacing the LF law by the Lorentz-Abraham-Dirac (LAD) equation. This equation was originally derived by Lorentz in the non-relativistic limit and then generalized to the relativistic case by Abraham [34, 35] and Dirac [36]. In relativistic covariant form the LAD equation for an electron is given by [33]

$$\frac{\mathrm{d}p^\mu}{\mathrm{d}\tau} = eF^{\mu\nu}u_\nu + \frac{2}{3}\alpha\left(\frac{\mathrm{d}^2u^\mu}{\mathrm{d}\tau^2} + \frac{\mathrm{d}u^\nu}{\mathrm{d}\tau}\frac{\mathrm{d}u_\nu}{\mathrm{d}\tau}u^\mu\right), \tag{8.1}$$

where $F^{\mu\nu}$ is the field tensor of the external field. Beside the Lorentz-force, (8.1) contains also terms proportional to the fine-structure constant α which represent the electron's self-force due to RR. The LAD equation has the deficiency that it allows for run-away solutions (see [32] and references therein). In [33] the authors perform a perturbative reduction of order of the LAD equation. They argue that this is possible since only terms which go beyond the validity of classical electrodynamics are neglected. The result is the so-called Landau-Lifshitz (LL) equation

$$\begin{aligned}\frac{\mathrm{d}p^\mu}{\mathrm{d}\tau} = eF^{\mu\nu}u_\nu + \frac{2}{3}\alpha\bigg[&\frac{e}{m}\big(\partial_\alpha F^{\mu\nu}\big)u^\alpha u_\nu \\ &- \frac{e^2}{m^2}F^{\mu\nu}F_{\alpha\nu}u^\alpha + \frac{e^2}{m^2}\big(F^{\alpha\nu}u_\nu\big)\big(F_{\alpha\lambda}u^\lambda\big)u^\mu\bigg].\end{aligned} \tag{8.2}$$

To be more specific, the reduction of order is allowed if in the instantaneous rest frame of the electron the typical amplitude of the external field is much smaller than E_{cr}/α and its typical wavelength is larger than $\alpha\lambda\!\!\!^{-}_c$, where $E_{\mathrm{cr}} = m^2c^3/\hbar|e| = 1.3 \times 10^{16}$ V/cm is the so-called "critical" electric field of QED (analogously the critical magnetic field is given by $B_{\mathrm{cr}} = m^2c^3/\hbar|e| = 4.4 \times 10^{13}$ G) and $\lambda\!\!\!^{-}_c \equiv \hbar/mc \approx 3.9 \times 10^{-11}$ cm is the (reduced) Compton wavelength. The critical field corresponds to a peak laser intensity of $I_{\mathrm{cr}} = E_{\mathrm{cr}}^2/4\pi = 4.6 \times 10^{29}$ W/cm^2. Note that the above conditions on the validity of the reduction of order are beyond the validity of classical electrodynamics. In fact, quantum effects become already important if the typical amplitude and wavelength of the external field are of the order of E_{cr} and $\lambda\!\!\!^{-}_c$, respectively (in the instantaneous rest frame of the electron). In the case of a Coulomb field, for example, the conditions on the reduction of order are of course not always fulfilled due to the field divergence at small distances from the Coulomb center. The interested reader can find a solution of the LL equation for a non-relativistic charge in a Coulomb field in [37].

Contrary to the LAD equation, the LL equation does not allow for run-away solutions. The LAD and the LL equations have been discussed extensively in the literature (see [32] and the referenced therein). However, up to now, no experimental investigations were carried out to test the LL equation as one needs quite strong fields. Since, as outlined at the beginning, existing and planned laser facilities will provide very strong electromagnetic fields, intense laser pulses could be employed to test RR as described by the LL equation. For example, in [38] a setup has been put forward, where RR effects, as predicted by the LL equation, could in principle be measured already with available laser technology. The laser and electron parameters in this setup are chosen in such a way that the longitudinal momentum of the electron inside the field is almost compensated by the momentum exerted by the laser, resulting in a regime very sensitive to RR effects.

If spatial-focusing effects are negligible, a laser pulse can be described using the plane-wave approximation. In this case the four-vector potential $A^\mu = A^\mu(\varphi)$ (in Lorentz gauge) can be chosen such that it depends only on the laser phase $\varphi = kx$ where $k^\mu = n^\mu \omega_0$ ($k^2 = kA = 0$) is the wave four-vector and ω_0 the central angular frequency of the pulse. In the case of a linearly polarized laser the four-potential can be written as $A^\mu(\varphi) = a_0^\mu \psi(\varphi)$, where a_0^μ is a constant four-vector ($a_0^2 = -E_0^2/\omega_0^2$, $a_0 k = 0$, E_0 characterizes the peak electric field strength) and $\psi(\varphi)$ is the laser shape function such that $\psi(\pm\infty) = 0$ and $|\psi(\varphi)|, |\psi'(\varphi)| \lesssim 1$, otherwise being arbitrary (the prime denotes a derivative with respect to the argument). The field tensor of the plane wave is then given by $F^{\mu\nu}(\varphi) = f_0^{\mu\nu}\psi'(\varphi)$ with $f_0^{\mu\nu} = k^\mu a_0^\nu - k^\nu a_0^\mu$. The special case $\psi'(\varphi) = 1$ corresponds to a constant-crossed field ($\mathbf{E}^2 = \mathbf{B}^2$, $\mathbf{EB} = 0$) with an electric field amplitude $|\mathbf{E}| = E_0$. In general, due to the properties of the shape function $\psi(\varphi)$, E_0 corresponds roughly also to the peak field amplitude of the plane-wave field. For such an external electromagnetic field described by $F^{\mu\nu}(\varphi)$ the LL equation can be solved analytically, as shown in [39]. This solution is further discussed in Sect. 8.2. There, we present a relatively simple method to determine the peak intensities of ultra-relativistic laser pulses [40]. It is well known that accelerated ultra-relativistic charged particles emit radiation mostly into a cone around the particle's instantaneous velocity with aperture of the order of $\gamma^{-1}(t)$ (here $\gamma(t)$ is the instantaneous Lorentz factor of the particle) [33]. Our method takes advantage of this high directionality and relates the angular aperture of the emitted spectrum to the peak intensity of the laser pulse. By comparing the analytical solutions obtained for a plane-wave field with numerical calculations done for Gaussian laser profiles we show that the analytical predictions give accurate results also for tightly focused beams. To the best of our knowledge, the peak intensity of ultra-relativistic pulses is currently determined by methods which are prone to very large errors. As the total energy in the laser pulse is normally known, the determination of the laser's spot-size and pulse duration is the standard technique to estimate its intensity. Since this is done at a lower intensity, one cannot measure these parameters very precisely as they are affected by increasing the intensity of the pulse [20, 41, 42]. With our method intensities in the range between 10^{20} W/cm^2 up to about 10^{23} W/cm^2 can be measured, in principle, with theoretical accuracies of the order of 10 %.

The classical description of electrodynamics we have discussed so far fails at both very low and very high field intensities. At very low intensities the quantized nature of the fields becomes apparent and has to be taken into account. Whereas, at very high intensities quantum effects like spontaneous electron-positron pair production become in general sizable. The first consistent treatment of QED was given by Feynman, Schwinger, Tomonaga and Dyson at the end of the 1940s. In QED one obtains a completely different picture of the interaction process taking place between charged particles. The electromagnetic force is mediated via the exchange of photons, the quanta of the electromagnetic field [43]. The enormous success of QED is based on the smallness of the fine-structure constant α, which allows for a perturbative expansion of the S-matrix at low field intensities. We will indicate this regime as vacuum QED. However, at very high field intensities this perturbative approach is not valid any more.

In order to characterize the field strength of a plane-wave laser field interacting with an electron having the initial four-momentum p_0^μ, the following two Lorentz invariant parameters are used

$$\begin{aligned} \xi_0 &\equiv \frac{|e|\sqrt{-a_0^2}}{mc} = \frac{|e|E_0}{mc\,\omega_0}, \\ \chi_0 &\equiv \frac{|e|\hbar}{m^3c^4}\sqrt{p_0^\mu f_{0\mu\nu}^2 p_0^\nu} = \gamma_0(1+\beta_0)\frac{E_0}{E_{\text{cr}}} \end{aligned} \tag{8.3}$$

(the last expression in the second equation holds in the case of a head-on collision between the plane-wave laser field and the electron). Here γ_0 is the (initial) relativistic Lorentz factor, $\beta_0 = (1-1/\gamma_0^2)^{\frac{1}{2}} = v_0/c$, v_0 the magnitude of the initial velocity. We call the invariants in (8.3) the classical intensity and the quantum non-linearity parameter, respectively.

If ξ_0 is of the order of unity (which happens already at intensities of the order of 10^{18} W/cm^2 at $\omega_0 \approx 1$ eV), the strong laser field must be treated in a non-perturbative way. This can be understood qualitatively by a comparison of two Feynman diagrams which differ only by one external field interaction as shown in Fig. 8.1. The additional external field vertex adds a factor ea_0^μ to the transition amplitude and the additional propagator (evaluated heuristically at $p^\mu = 0$) a factor $\sim m^{-1}$. Thus, we expect that the relative strength of the contribution to the probability amplitude is of the order of ξ_0, which is indeed observed in actual calculations [44]. Therefore, the exchange of multiple laser photons starts to play an important role if $\xi_0 \gtrsim 1$. This regime, where the external field has to be treated non-perturbatively, is referred to as the strong-field regime. The external field can be taken into account exactly by using the Furry picture, where only the radiation field is quantized and treated as a perturbation [45].

Since ξ_0 does not contain $\hbar$, it can also be interpreted classically. In a constant electric field with amplitude E_0, ξ_0 measures the energy which can be transferred to

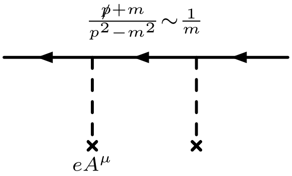

Fig. 8.1 Feynman diagram showing a perturbative expansion in the four-potential A^μ of the external field. For each additional coupling with the external field we obtain another vertex and a free electron propagator. Since the momentum p^μ of the virtual electron is integrated out, we heuristically evaluate the propagator at $p^\mu = 0$ and obtain an additional factor of ξ_0 for each interaction with the external field

an electron over the distance c/ω_0 (corresponding to one reduced laser wavelength) in units of the electron rest energy mc^2. This implies that at $\xi_0 \approx 1$ an electron may become relativistic within one laser cycle even if it was initially at rest. Therefore, the regime $\xi_0 \geq 1$ is also called the relativistic regime [11].

However, the condition $\xi_0 \geq 1$ does not necessarily imply that quantum effects are important. On the contrary, the importance of multiple photon exchanges "hides" in a certain sense the quantized nature of the external field. An electron in such a field behaves in many respects like a classical particle. Therefore, we indicate the regime $\xi_0 \gg 1$ as the quasi-classical regime. As an example we discuss the occurrence of an intensity-dependent electron "quasi-momentum" inside a monochromatic plane-wave external field (with laser photon four-momentum k^μ), one of the most appealing predictions of strong-field QED. The electron's quasi-(four-)momentum is defined classically as its average (four-)momentum in the plane wave over one laser period. For an electron with initial four-momentum p_0^μ inside a linearly-polarized laser field the quasi-momentum q_0^μ is given by [32]

$$q_0^\mu = p_0^\mu + \frac{m^2\xi_0^2}{4(kp_0)}k^\mu. \tag{8.4}$$

Unlike the momentum p_0^μ the quasi-momentum q_0^μ is conserved during interactions like photon emission in the strong-field regime [46–50]. We can therefore introduce an effective "dressed" mass $\sqrt{q_0^2} = m^* = m\sqrt{1+\xi_0^2/2}$ of the electron in the plane wave. The results of the only experiment performed so far on strong-field QED in a background laser field, the E-144 SLAC experiment, are in agreement with the electron behaving as having this dressed mass [51–54]. The origin of this quasi-momentum can be understood completely classically from the trajectory of a classical electron [33]: due to the "quiver" motion of the electron inside the laser field its inertia is effectively increased.

On the other hand non-linear quantum effects become important if the parameter χ_0—which contains $\hbar$—is of order one. It measures the magnitude of the electric field in the initial rest frame of the electron in units of E_{cr}. Already in 1931 Sauter [55] pointed out that at field strengths of the order of E_{cr} qualitative new quantum effects start to play an important role. In a heuristic (pictorial) description one can understand this as follows. Owing to the equivalence of mass and energy, an electron-positron pair (with rest energy of the order of $\varepsilon = mc^2$) can be created for a short time τ, restricted by the Heisenberg uncertainty relation to $\varepsilon\tau \sim \hbar$. After this time the pair has to annihilate again. Thus, the vacuum is by no means empty, but contains many such "virtual pairs", which are called quantum fluctuations. The typical length scale of these fluctuations is given by the (reduced) Compton wavelength $\lambda\!\!\!^{-}_c \equiv \hbar/mc$. Along a path of this length a constant electric field of the order of $E_{\text{cr}} \equiv m^2c^3/|e|\hbar$ can transfer energy of the order of mc^2 to a particle with charge $\pm e$. Thus, an electron-positron pair which is "born" as a vacuum fluctuation can become real due to an external field of the order of E_{cr}. This process is called spontaneous or Schwinger pair-creation from the vacuum [56–62]. We can also imagine the pair creation process as a tunneling through the tilted energy barrier of the Dirac sea. In [63] it has been shown that the tunneling length can be considerably shortened and even controlled by superimposing a weak, high-frequency field, implying a substantial increase of the pair-production probability.

Since the lifetime of a real electron-positron pair is no longer restricted by the Heisenberg uncertainty principle, photon-photon coupling via vacuum fluctuations is greatly enhanced at the scale E_{cr}. For fields with a typical angular frequency ω, which vary slowly with respect to the Compton length of the electron ($\hbar\omega \ll mc^2$) we can include this effect by modifying the Maxwell equations. The dynamics of the free electromagnetic field is now determined by the Euler-Heisenberg Lagrangian density which for the case $E \ll E_{\text{cr}}$ and $B \ll B_{\text{cr}}$ is given by [56, 64]

$$\mathscr{L} = \frac{1}{8\pi}\left(\mathbf{E}^2 - \mathbf{B}^2\right) + \frac{\alpha}{360\pi^2 E_{\text{cr}}^2}\left[\left(\mathbf{E}^2 - \mathbf{B}^2\right)^2 + 7(\mathbf{EB})^2\right] + \cdots. \tag{8.5}$$

It adds non-linear terms to Maxwell's theory which violate the superposition principle for electromagnetic waves also in vacuum and thus the vacuum is predicted to exhibit birefringence and dichroism. As a consequence photons can split [65] and scatter [66, 67] in the presence of a background electromagnetic field. In [68, 69] this is used to realize a "matterless double slit". In [68], in particular, a physical scenario is put forward, where two strong laser beams collide head-on with a weak probe pulse, whose photons may interact with either one or the other strong beam, giving rise to a which-way condition typical for double-slit experiments. For a more detailed overview of these vacuum-polarization effects the reader is referred to the reviews [32, 70].

Since at $\chi_0 \sim 1$ the effective electric field of the laser becomes of the order of E_{cr} in the electron's rest frame, we expect new "quantum" features in the dynamics of the electron at this scale. In Sect. 8.3 we present one particular strong-field QED effect inside a laser pulse, originating from the electron's interaction with its own electromagnetic field [71]. At lowest order in the radiation field an electron inside a plane-wave field is described by so-called Volkov states, exact solutions of the Dirac equation [43, 72]. However, the interaction of the electron with its own radiation field introduces finite radiative corrections even for on-shell electrons. They can be taken into account by solving the Dirac-Schwinger equation [43, 58]

$$(\mathrm{i}\partial\!\!\!/ - eA\!\!\!/ - m)\psi = M\psi, \tag{8.6}$$

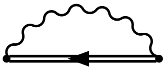

Fig. 8.2 Leading-order Feynman diagram for the mass operator in an external plane-wave field. The "dressed" electron propagator in the plane wave (Volkov propagator) is indicated by the *double solid line* and the *wiggly line* represents a non-laser photon belonging to the quantized radiation field. Using the unitarity of the S-matrix this contribution to the mass operator can be linked to the leading-order non-linear Compton scattering diagram

which contains the mass operator M in the external field shown (to leading order in α) in Fig. 8.2. Therefore, the exact electron wave-function inside a plane-wave field is not given by the Volkov states but by the solution of (8.6). By solving it in the quasi-classical limit $\xi_0 \gg 1$, we obtained the leading-order modifications to the Volkov states (for a linearly-polarized laser field) in [71]. One observes that due to the electron's self-interaction its quasi-momentum q_0^μ undergoes a pure quantum contribution which depends only on χ_0 and not, like the classical one, on ξ_0. Interestingly, this quantum-contribution is in general different for two different spin states of the electron. This implies that one can, in principle, observe radiative corrections by analyzing the spin dynamics of electrons in strong laser-fields—a qualitatively new feature not predicted by the Dirac equation. This situation is analogous to the Lamb-shift for bound electrons, where QED effects also remove the degeneracy with respect to an angular momentum quantum number [73].

On this respect, we conclude here by shortly elaborating on the relation between the classical and the quantum approach to the electron self-interaction. As we have already mentioned, in classical electrodynamics all self-field effects are taken into account in the LAD equation of motion (8.1). Since this equation is in principle equivalent to the coupled system of Maxwell and Lorentz equations, its solution would correspond quantum-mechanically to the complete determination of the S-matrix. This task is, of course, impossible to be performed exactly because it would require the calculation of all possible processes arising in the collision of a single electron with the external field (the plane wave in our specific case). Classical RR effects include, in particular, the fact that the electron looses energy and momentum as it is accelerated because of the resulting emission of electromagnetic radiation. In QED this energy-momentum loss is already taken into account in the basic single-photon emission process, i.e. in multiphoton Compton scattering. However, in [74] it has been shown that at $\chi_0 \sim 1$ and at $\alpha\xi_0 \gtrsim 1$, the incoherent emission of many photons substantially modifies the multiphoton Compton spectrum, which arises from single-photon emission. In that paper the quantum RR at moderate values of χ_0 is identified with multiple photon recoils experienced by the laser-driven electron due to consecutive incoherent photon emissions.

8.2 Peak Intensity Measurement of Strong Laser Pulses Using Non-linear Thomson Scattering

In this section we describe a recently proposed method [40] for the measurement of the peak intensity of strong laser pulses. The method exploits the highly directional nature of the emission of radiation by an ultra-relativistic, accelerated charged particle. As was mentioned in the introduction, the measurement of the peak intensity of a very strong laser pulse is a difficult task, and it is usually inferred rather than directly measured. Several other methods have been proposed to perform in situ measurements of the peak intensity, most of these suggest placing a certain species of atoms in the laser focus (chosen according to the expected peak intensity) and then either by measuring the ionization fraction [41, 75] or by measuring the photo-ion momentum distribution [76] one can infer the peak intensity. Another proposal suggests using Thomson radiation of electrons "born" through ionization inside the laser pulse [77].

As will be explained later in this section, the method proposed in [40] could be used, at least in principle, to measure peak intensities in the range between $10^{20}\ \mathrm{W/cm^2}$ and $10^{23}\ \mathrm{W/cm^2}$. The lower limit is set by the requirement that the electrons involved in the measurement process must be ultra-relativistic and the higher limit is set by the requirement that we stay in the classical regime (since angular-resolved, quantum many-photon-emission spectra have not yet been successfully computed) and incidentally this is also the regime where RR effects are small.

Our strategy for the development of the method will be as follows: first, we calculate the trajectory of an ultra-relativistic electron, colliding head-on with a linearly-polarized plane-wave pulse by solving the LF equation. Then, by assuming that in the ultra-relativistic limit the electron emits electromagnetic radiation entirely along its instantaneous velocity, we will relate the aperture of the electron's radiation pattern to the peak intensity of the laser pulse. We will then discuss error estimates of this method and use the generalization to the LL equation (8.2) in order to take RR into account and to estimate the regime where this is necessary.

Newton's second law for the electromagnetic interaction between the electron and the plane-wave field is given by the LF equation:

$$\frac{\mathrm{d}p^\mu}{\mathrm{d}\tau} = eF^{\mu\nu}u_\nu = e\big(k^\mu A'^\nu - A'^\mu k^\nu\big)u_\nu. \tag{8.7}$$

The solution of (8.7) in terms of the plane-wave phase φ for the initial conditions $A^\mu(\varphi = 0) = 0$ is given by:

$$u^\mu(\varphi) = u_0^\mu - \frac{e}{m}A^\mu(\varphi) + \frac{e}{m}\frac{k^\mu}{ku_0}\left[u_0 A(\varphi) - \frac{e}{2m}A^2(\varphi)\right], \tag{8.8}$$

where $u_0^\mu \equiv u^\mu(\varphi = 0)$.

We restrict our attention to a plane wave, linearly polarized in the $\hat{\mathbf{x}}$ direction, propagating in the positive $\hat{\mathbf{z}}$ direction, and an electron counter-propagating in the $-\hat{\mathbf{z}}$ direction, with an initial gamma factor $\gamma_0 \gg 1$. The initial four-velocity satisfying these initial conditions is $u_0 = \gamma_0(1, 0, 0, -\beta_0)$, where $ku_0 = \omega_0\gamma_0(1 + \beta_0)$.

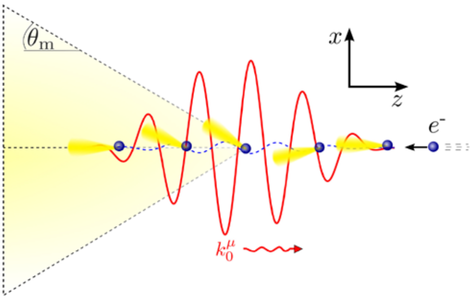

Fig. 8.3 A sketch of the proposed method to measure the peak intensity of ultra-relativistic lasers. θ_m is the maximal angle to which radiation arrives and k_0^μ is the central wave four-vector of the pulse

Writing the solution in terms of these initial conditions, and using the definition of the shape function $\psi(\varphi)$ from the introduction, we obtain [33]:

$$u^\mu(\varphi) = \begin{pmatrix} \gamma_0 + \frac{1}{2\gamma_0(1+\beta_0)}\xi_0^2\psi^2(\varphi) \\ -\xi_0\psi(\varphi) \\ 0 \\ -\gamma_0\beta_0 + \frac{1}{2\gamma_0(1+\beta_0)}\xi_0^2\psi^2(\varphi) \end{pmatrix}, \tag{8.9}$$

where we introduced the classical intensity parameter ξ_0 (8.3).

From the solution (8.9) we learn that the electron stays relativistic throughout its motion within the laser pulse (since $\gamma(\varphi) = u^0(\varphi) \geq \gamma_0 \gg 1$) and that the motion is confined to the $x - z$ plane. The angle between the velocity vector and the $-\hat{\mathbf{z}}$ axis (and in the ultra-relativistic limit, the angle to which radiation is being emitted) is:

$$\tan\theta(\varphi) = -\frac{u^x}{u^z} \approx \frac{\xi_0}{\gamma_0}\frac{\psi(\varphi)}{\xi_0^2\psi^2(\varphi)/4\gamma_0^2 - 1}. \tag{8.10}$$

In order to find the maximal angle to which radiation arrives, we need to maximize this expression with respect to φ. By assuming that $\max|\psi(\varphi)| = 1$ it is easy to see that the maximal angle θ_m is reached when $|\psi(\varphi)| = 1$. This allows us to invert the relation and find ξ_0 as a function θ_m:

$$\xi_0 = 2\gamma_0\frac{\sin\theta_\mathrm{m}}{1+\cos\theta_\mathrm{m}}. \tag{8.11}$$

In order to obtain the peak intensity, we use the relation $I_\mathrm{p} = E_0^2/4\pi$ to obtain:

$$I_\mathrm{p}\left[10^{18}\ \mathrm{W/cm^2}\right] \approx 1.8\omega_0^2[\mathrm{eV}]\xi_0^2 = 28\left[\frac{\omega_0[\mathrm{eV}]\varepsilon_0[\mathrm{MeV}]\sin\theta_\mathrm{m}}{1+\cos\theta_\mathrm{m}}\right]^2, \tag{8.12}$$

where $\varepsilon_0 = m\gamma_0$ is the electron's initial energy in MeV. In Fig. 8.3 a sketch of the proposed method is shown, defining both θ_m and the axes as described in the text.

Several remarks about this solution are in order:

1. The solution does not depend on the shape function $\psi(\varphi)$. This is an attractive feature since the method does not require us to make any assumptions about the exact shape of the laser pulse.

2. We can repeat the same analysis for a circularly polarized plane wave, by choosing an appropriate four-potential. The resulting relation between θ_m and I_p is exactly the same as in (8.12). The definition of θ_m in this case will be different since now the electron's radiation will not be confined to a line but rather to a cone whose opening angle is θ_m.
3. By integrating the four-velocity (8.9) with respect to φ, we obtain the trajectory of the electron as a function of the plane-wave phase (using $\mathrm{d}\tau = \mathrm{d}\varphi/ku_0$):

$$x^\mu(\varphi) = x_0^\mu + \frac{1}{\omega_0}\left(\frac{1}{2}\varphi + \delta_0^2 f_2(\varphi), -\delta_0 f_1(\varphi), 0, -\frac{1}{2}\varphi + \delta_0^2 f_2(\varphi)\right), \quad (8.13)$$

where we set $\beta_0 = 1$ (since $\gamma_0 \gg 1$), and defined $f_n(\varphi) \equiv \int_0^\varphi \psi^n(\varphi')\,\mathrm{d}\varphi'$ and $\delta_0 \equiv \xi_0/2\gamma_0$. It is interesting to note that the trajectory depends on the initial electron energy and on the laser intensity only through the parameter δ_0, which can therefore be used to characterize different parameter regimes.

The uncertainty in the intensity measurement can be estimated using standard error propagation theory. If we indicate by ΔF the uncertainty in the generic quantity F, the relative theoretical uncertainty in the peak intensity (in the case of a plane-wave field) is given by:

$$\frac{\Delta I_\mathrm{p}}{I_\mathrm{p}} = 2\sqrt{\left(\frac{\Delta\omega_0}{\omega_0}\right)^2 + \left(\frac{\Delta\varepsilon_0}{\varepsilon_0}\right)^2 + \left(\frac{\Delta\theta_\mathrm{m}}{\sin\theta_\mathrm{m}}\right)^2}. \quad (8.14)$$

The relative uncertainty in ω_0 is usually small and can safely be neglected. The uncertainty in the initial electron energy ε_0 depends on the quality of the electron beam used in the experiment. Current laser-plasma accelerators can provide a beam with $\Delta\varepsilon_0/\varepsilon_0 \approx 5\ \%$ [30], and electron guns can provide beams with a much lower uncertainty. The third term depends to a large extent on the value of θ_m. It diverges for $\theta_\mathrm{m} = 0, \pi$ and is minimal for $\sin\theta_\mathrm{m} = 1$. These divergences have a simple physical interpretation: $\theta_\mathrm{m} \approx 0$ indicates that the initial energy of the electron was so high ($\delta_0 \ll 1$) that the electron was almost not deflected at all by the laser pulse. $\theta_\mathrm{m} \approx \pi$ indicates that the initial electron energy was too low ($\delta_0 \gg 1$) and as a result the electron was almost completely reflected by the laser pulse. Both cases are insensitive to the exact value of the peak intensity, and can only indicate that the intensity is less than or more than a certain threshold value, respectively. If we want to achieve a high level of accuracy, we have to select the initial energy of the electron such that it will be deflected to $\theta_\mathrm{m} \sim \pi/2$. In order to achieve that, we estimate the expected laser intensity, and then select the initial energy of the electron accordingly. As can be seen from (8.10) this can be achieved by selecting $\delta_0 \approx 1$. We call this the "optimal regime". In terms of the initial electron energy and laser intensity, the condition is:

$$\varepsilon_{0,\mathrm{optimal}}\ [\mathrm{MeV}] = \frac{0.19\sqrt{I_\mathrm{p}[10^{18}\ \mathrm{W/cm^2}]}}{\omega_0\ [\mathrm{eV}]}, \quad (8.15)$$

where I_p is the expected peak laser intensity.

By estimating $\Delta\theta_{\mathrm{m}} \approx 1^\circ$ (corresponding to the ratio between dimension of a typical high-energy photon detector $\sim$1 cm and the distance of $\sim$1 m of the detector from the interaction region), $\sin\theta_{\mathrm{m}} = 1$ and $\Delta\varepsilon_0/\varepsilon_0 \approx 5\ \%$ we obtain $\Delta I_{\mathrm{p}}/I_{\mathrm{p}} \approx 10\ \%$. In comparison with other methods employed nowadays, whose accuracies are often even larger than 50 %, this theoretical accuracy is a major improvement.

The assumption that the electrons are relativistic is critical for our method. As we have seen from the error analysis, however, if an electron has an initial energy which is too high relative to the laser intensity, the maximal angle θ_{m} will tend to zero and we could not use our method to determine the laser intensity. This sets a lower limit on the domain of validity of the method since it indicates that we cannot measure very low laser intensities. In order to find a rough estimate of this lower bound, let us assume that we would like to have electrons with at least $\gamma_0 = 10$, and that the minimal angle we can measure is 45° (for example, because of the experimental setup). Plugging this into (8.12) we obtain that the minimal intensity we can measure is $I_{\mathrm{p,min}} \approx 1.25 \times 10^{20}\ \mathrm{W/cm^2} \times (\omega_0[\mathrm{eV}])^2$ which for an optical laser with $\omega_0 = 1.55$ eV means $I_{\mathrm{p,min}} \approx 3.0 \times 10^{20}\ \mathrm{W/cm^2}$.

As was discussed in the introduction, the LF equation (8.7) does not take RR effects into account. In order to do so we should use the LL equation (8.2) instead. The LL equation has been solved analytically for a general plane wave [39]. This general solution can be used both to obtain corrections to the previous result (8.12) and to derive its limits of validity.

Employing the same initial conditions leading to (8.9), the general solution has the form:

$$u^\mu(\varphi) = \frac{1}{h(\varphi)} \begin{pmatrix} \gamma_0 + \frac{1}{2\gamma_0(1+\beta_0)}[h^2(\varphi) - 1 + \xi_0^2 \mathscr{I}^2(\varphi)] \\ -\xi_0 \mathscr{I}(\varphi) \\ 0 \\ -\beta_0\gamma_0 + \frac{1}{2\gamma_0(1+\beta_0)}[h^2(\varphi) - 1 + \xi_0^2 \mathscr{I}^2(\varphi)] \end{pmatrix}, \tag{8.16}$$

with

$$h(\varphi) = 1 + \frac{2}{3}\alpha\frac{\omega_0}{m}\gamma_0(1+\beta_0)\xi_0^2 \int_0^\varphi \mathrm{d}\zeta\, \left[\psi'(\zeta)\right]^2, \tag{8.17}$$

$$\mathscr{I}(\varphi) = \int_0^\varphi \mathrm{d}\zeta \left[h(\zeta)\psi'(\zeta) + \frac{2}{3}\alpha\frac{\omega_0}{m}\gamma_0(1+\beta_0)\psi''(\zeta)\right]. \tag{8.18}$$

This solution goes over to the LF solution (8.8) when we take the formal limit $\alpha \to 0$, which is to be expected since the corrections to the LF equation are proportional to α. The largest correction to the LF solution comes from the second term in $h(\varphi)$ and is proportional to $\frac{2}{3}\alpha\frac{\omega_0}{m}\gamma_0(1+\beta_0)\xi_0^2 N \approx 2 \times 10^{-8}\omega_0[\mathrm{eV}]\gamma_0\xi_0^2 N$, where N is the number of cycles in the pulse. So wee see that in the ultra-relativistic limit one can neglect RR effects as long as $\omega_0[\mathrm{eV}]\gamma_0\xi_0^2 N \ll 5 \times 10^7$, or in terms of initial electron energy, peak laser intensity and central laser frequency:

$$\frac{\varepsilon_0[\mathrm{MeV}]I_{\mathrm{p}}[10^{18}\,\mathrm{W/cm^2}]N}{\omega_0[\mathrm{eV}]} \ll 4.8 \times 10^7. \tag{8.19}$$

This means, for example, that for an optical laser pulse with $\omega_0 = 1.55$ eV, $N = 10$ cycles and an intensity of 10^{22} W/cm^2, the initial energy of the electron must be much smaller than 744 MeV, which is quite reasonable. However, already at the intensity of 10^{23} W/cm^2, the initial energy must obey $\varepsilon_0 \ll 74$ MeV. Since the optimal initial energy for this scenario would be $\varepsilon_0 \approx 39$ MeV we can infer that it is no longer possible to neglect RR effects.

RR incorporates into the equations of motion the loss of energy and momentum due to the radiation of electromagnetic waves by the particle. We can expect that taking this dissipative effect into account will have an effect similar to friction. We should therefore not be surprised that now θ_m will depend on the shape function we choose for the laser pulse, since it influences the electron's trajectory and thus the energy loss. We can also expect that by the time the electron reaches the peak of the laser pulse, it will have less energy than what is predicted by the LF equation. This means that it will be more deflected by the pulse, and will therefore reach larger angles than our previous result would suggest, meaning that in general we expect $\theta_{\mathrm{m,with\,RR}} \geq \theta_{\mathrm{m,no\,RR}}$.

In order to incorporate RR corrections effects in our method, we repeat the procedure described above by calculating the angle $\tan\theta(\varphi)$ using (8.16) and maximizing it (numerically) with respect to φ. After this maximization, we obtain a sixth degree polynomial in ξ_0 which we have to solve in order to find the intensity as a function of the maximal angle θ_m. This is numerically a straightforward procedure which requires, however, a model for the shape function $\psi(\varphi)$. One can chose, for example, $\psi'(\varphi) = \sin^2(\varphi/2N)\sin(\varphi + \varphi_0)$ where N is the number of cycles of the laser pulse (and for our initial conditions $\varphi_0 = 0$).

In the preceding analysis, we modeled the laser pulse as a plane-wave field. While this model allowed us to obtain analytical results, it is obviously not a very realistic model for a focused laser pulse. It represents a wave that is infinite in the perpendicular directions and the shape of the laser pulse does not change in time or, equivalently, as the pulse advances along the z direction. Real laser beams are spatially confined in the perpendicular directions and change their shape as they propagate. Since we would like to use our method to measure very high intensities which are only attainable by ultra-short, spatially compressed laser pulses, it is important to check the validity of the plane-wave result by employing simulations of a more realistic laser beam.

Gaussian beams are often used to model laser beams, at least to a first approximation [78]. A Gaussian beam is a cylindrically symmetric beam characterized by a waist size w_0, which has a Gaussian intensity profile in the perpendicular direction (at maximum focus, w_0 is the perpendicular distance where the intensity profile decreases by 1/e) and a magnitude that varies along the propagation direction.

In order to evaluate the proposed method, we performed a number of numerical simulations employing a Gaussian beam with a waist size $w_0 = 5$ µm and wavelength of 800 nm. For these parameters the Rayleigh length is $z_r = \pi w_0^2/\lambda_0 \approx 98$ µm and the divergence angle $\theta_0 = 0.05$. Expressions for **E** and **B** fields to first order in θ_0 were calculated and an envelope function $g(\varphi) = \sin^2(2\varphi/N)$ with $N = 10$ cycles (see [79] for the expressions and notation). The trajectory of the electron was

Fig. 8.4 Radiation spectrum of an electron with initial energy $\varepsilon_0 = 72$ MeV colliding head-on with a laser pulse with peak intensity $I_\mathrm{p} = 10^{22}$ W/cm^2. *Vertical dashed* (*solid*) *lines* represent theoretical expectations neglecting (taking into account) RR effects

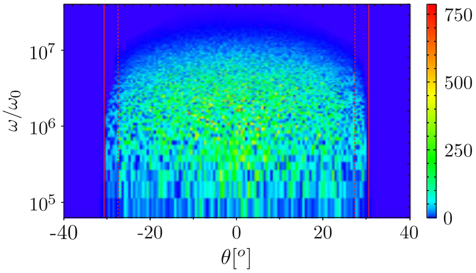

obtained by numerically integrating the LL equation (8.2) using a variable step-size Runge-Kutta method (numerical recipes in Fortran, “odeint” routine [80]). From the trajectory, the frequency spectrum has been computed according to [81]:

$$\frac{\mathrm{d}^2 I}{\mathrm{d}\omega\,\mathrm{d}\Omega} = \frac{e^2}{4\pi^2}\left|\int_{-\infty}^{\infty} \frac{\mathbf{n} \times [(\mathbf{n} - \boldsymbol{\beta}) \times \dot{\boldsymbol{\beta}}]}{(1 - \boldsymbol{\beta} \cdot \mathbf{n})^2} \mathrm{e}^{\mathrm{i}\omega(t - \mathbf{n}\cdot\mathbf{r}(t))}\,\mathrm{d}t\right|^2, \tag{8.20}$$

for different values of the vector $\mathbf{n}$ corresponding to varying the polar angle θ at $\phi = 0$ and $\phi = \pi$ (the x–z plane).

For each simulated laser intensity, several initial energies of the electron have been used. The initial position of the electron has been varied as well, in order to simulate an (incoherently emitting) electron beam. This is a good approximation since typically at the edge of the spectrum high-frequency radiation is emitted, and at the typical electron densities we are interested in (e.g., electron bunches produced at laser-plasma accelerators), the emission of these frequencies is incoherent. All simulations were performed for $\chi_0 \ll 1$, so that quantum effects can safely be neglected. In Fig. 8.4 we show the spectrum from one such simulation. The vertical lines represent our theoretical expectation according to the plane-wave approximation. The dashed (solid) lines were calculated using the solution of the LF (LL) equation, thus neglecting (taking into account) RR effects. The simulation was performed for a peak intensity of $I_\mathrm{p} = 10^{22}$ W/cm^2 and an initial electron energy of $\varepsilon_0 = 72$ MeV. From the figure we see that the estimate for θ_m, which included taking RR effects into account, was very good. This example has been chosen, however, to show a case where RR effects are noticeable. In fact, by choosing an initial energy according to (8.15) ($\varepsilon_0 = 23$ MeV) we could have reduced the difference between the two calculations to about 2.2°.

In general, the obtained radiation spectra had an angular aperture which fit very well the theoretically calculated one, and, in the regime where it is expected that RR effects are important, the angular aperture fit the theoretical expectations of the modified method. When the initial position of the electron was far off-axis, the angular aperture of its radiation was smaller than the theoretically expected one since it sampled a region of the beam with a reduced intensity. This means that, in general, these electrons will not interfere with our method, since they will not radiate to large angles.

8.3 Quantum Electron Self-interaction in a Strong Laser Field

In this section we will discuss non-linear QED effects originating from radiative corrections more in depth. As already mentioned in the introduction, if $\xi_0 \geq 1$ we have to take the external field into account exactly by using the Furry picture [45]. Starting from the ordinary QED-Lagrangian density, one splits the total four-potential A^μ_{tot} into the background field A^μ and the radiation field A^μ_{rad} [82]

$$\mathscr{L}_{\text{QED}} = \bar{\psi}(\mathrm{i}\partial\!\!\!/ - m)\psi - \frac{1}{16\pi} F^{\text{tot}}_{\mu\nu} F^{\mu\nu}_{\text{tot}} - e\bar{\psi}\gamma_\mu \psi A^\mu_{\text{tot}}, \quad A^\mu_{\text{tot}} = A^\mu_{\text{rad}} + A^\mu \tag{8.21}$$

where $F^{\mu\nu}_{\text{tot}} = \partial^\mu A^\nu_{\text{tot}} - \partial^\nu A^\mu_{\text{tot}}$. If the background field is relativistically intense, one can neglect quantization effects and treat A^μ as a classical field. Thus, we quantize only the radiation field (and take it into account perturbatively) while the background field is kept exactly in all expressions. In order to quantize the fermion field in the presence of the background field, one has to solve the interacting Dirac equation. For a plane-wave external field $A^\mu = A^\mu(\varphi)$, $A^\mu(\pm\infty) = 0$ (which we will consider exclusively in the following) this was first carried out by Volkov [72]. For electrons the solution can be written as [43, 44] $\psi^V_{\mathbf{p},\zeta}(x) = \mathscr{E}(p,x)u_{\mathbf{p},\zeta}/\sqrt{2\varepsilon}$, where the quantization volume has been set to unity, the so-called Ritus matrices

$$\begin{aligned}\mathscr{E}&(p,x)\\ &= \left[\mathbf{1} + \frac{e k\!\!\!/ A\!\!\!/(kx)}{2pk}\right] \exp\left\{-\mathrm{i}px - \mathrm{i}\int_{-\infty}^{kx} \left[\frac{eA(\varphi')p}{pk} - \frac{e^2A^2(\varphi')}{2pk}\right] \mathrm{d}\varphi'\right\},\end{aligned} \tag{8.22}$$

have been introduced and where $u_{\mathbf{p},\zeta}$ is a free spinor which corresponds to the density matrix [43, 83]

$$u_{\mathbf{p},\zeta}\bar{u}_{\mathbf{p},\zeta} = \mathbf{1}\frac{m}{2} + \gamma^\mu \frac{p_\mu}{2} + \frac{m}{2}\gamma^\mu\gamma^5\zeta_\mu + \frac{\mathrm{i}}{4}\gamma^\mu\gamma^\nu\varepsilon_{\mu\nu\rho\sigma}\zeta^\rho p^\sigma. \tag{8.23}$$

Here $p^\mu = (\varepsilon, \mathbf{p})$ is the on-shell ($p^2 = m^2$) four-momentum describing the electron in the absence of the field and ζ^μ is the spin four-vector defined by $2m\zeta^\mu \equiv \bar{u}_{\mathbf{p},\zeta}\gamma^5\gamma^\mu u_{\mathbf{p},\zeta}$, which describes the electron's spin degree of freedom. Using the standard representation of the gamma matrices from [43], the free spinor and the spin four-vector can be written as

$$\begin{aligned} u_{\mathbf{p},\zeta} &= \begin{pmatrix} \sqrt{\varepsilon+m}\,\omega \\ \sqrt{\varepsilon-m}\,(\mathbf{p}\boldsymbol{\sigma}/|\mathbf{p}|)\,\omega \end{pmatrix}, \qquad \zeta^\mu = \left(\frac{\mathbf{p}\boldsymbol{\zeta}}{m}, \boldsymbol{\zeta} + \frac{\mathbf{p}(\mathbf{p}\boldsymbol{\zeta})}{m(\varepsilon+m)}\right), \\ \boldsymbol{\zeta} &\equiv \omega^\dagger \boldsymbol{\sigma}\omega, \end{aligned} \tag{8.24}$$

where $\boldsymbol{\sigma}^i$ are the Pauli-matrices. Thus, the free spinor $u_{\mathbf{p},\zeta}$ is described completely by its momentum $\mathbf{p}$ and the rest frame spin polarization $\boldsymbol{\zeta}$.

Before we will discuss non-linear quantum effects we analyze the properties of the Volkov states and their spin dynamics a bit more in detail. Despite the fact that the Volkov states are exact solutions of the interacting Dirac equation, both their phase and spinor structure can be understood essentially quasi-classically. This can be seen from the classical trajectory of an electron inside a plane-wave field. By solving the LF equation (8.8) we find that the four-momentum $p^\mu(\varphi)$ of a classical electron is given by [84, 85]

$$p^\mu(\varphi) = p^\mu + \frac{e\mathscr{F}^{\mu\nu}p_\nu}{pk} + \frac{e^2\mathscr{F}^{\mu\nu}\mathscr{F}_{\nu\rho}p^\rho}{2(pk)^2}, \tag{8.25}$$

where p^μ is the initial four-momentum at $\varphi \to -\infty$, $kp(\varphi) = kp$ is a constant of motion and

$$\mathscr{F}^{\mu\nu}(\varphi) \equiv \int_{-\infty}^{\varphi} \mathrm{d}\varphi'\, F^{\mu\nu}(\varphi') = k^\mu A^\nu(\varphi) - k^\nu A^\mu(\varphi). \tag{8.26}$$

If we insert the solution given in (8.25) into the classical action for an electron interacting with an external electromagnetic field [33]

$$S = \int_{-\infty}^{t} \mathrm{d}t' \left[-\frac{mc^2}{\gamma} - \frac{e}{c}A^\mu \frac{\mathrm{d}x_\mu}{\mathrm{d}t} \right], \tag{8.27}$$

we obtain (up to the imaginary unit) the exponent of the Volkov solution.

To analyze the spin dynamics of the Volkov solution we consider the expectation value of the spin four-vector

$$\zeta'^\mu(\varphi) = \frac{\bar\psi^V_{\mathbf{p},\zeta}\gamma^5\gamma^\mu\psi^V_{\mathbf{p},\zeta}}{\bar\psi^V_{\mathbf{p},\zeta}\psi^V_{\mathbf{p},\zeta}} = \zeta^\mu + \frac{e\mathscr{F}^{\mu\alpha}\zeta_\alpha}{pk} + \frac{e^2\mathscr{F}^{\mu\alpha}\mathscr{F}_{\alpha\beta}\zeta^\beta}{2(pk)^2}, \tag{8.28}$$

which is an exact solution of the semi-classical Bargmann-Michel-Telegdi (BMT) equation [43, 86]

$$\frac{\mathrm{d}\zeta^\mu}{\mathrm{d}\tau} = \frac{e}{m}F^{\mu\nu}\zeta_\nu \tag{8.29}$$

for an electron as having an intrinsic magnetic moment $e\hbar\boldsymbol{\zeta}/2mc$. Thus, also the precession of the spin inside the plane-wave field can be understood semi-classically.

We point out that even the spin continuously changes its orientation while the electron propagates through a plane-wave field, according to the Volkov solution it recovers its initial configuration after the electron has left the plane-wave field again. This is due to the fact that the phase in (8.22) does not depend on the spin polarization. This changes, however, if non-linear quantum corrections are taken into account.

Since the laser field depends only on the phase $\varphi = kx$, it is useful to introduce light-cone coordinates in strong-field QED calculations [49, 87–90]. To this end we define the following four basis four-vectors

$$n^\mu = (1, \mathbf{n}), \qquad \bar n^\mu = \frac{1}{2}(1, -\mathbf{n}), \qquad e^\mu_i = (0, \mathbf{e}_i), \tag{8.30}$$

where $i \in (1, 2)$, $\mathbf{n}^2 = 1$ and $\mathbf{e}_i\mathbf{e}_j = \delta_{ij}$, $\mathbf{e}_1 \times \mathbf{e}_2 = \mathbf{n}$. These four-vectors obey generalized orthonormality relations

$$n^2 = \bar n^2 = 0, \qquad \bar n^\mu n_\mu = 1, \qquad e^\mu_i e_{j\,\mu} = -\delta_{ij}, \qquad e^\mu_i n_\mu = e^\mu_i \bar n_\mu = 0, \tag{8.31}$$

meaning that the four-vectors e^μ_i represent the two possible polarization directions of the laser field. Light-cone coordinates (primed indices) are now obtained by using the following transformation

$$a^{\mu'} = \Lambda^{\mu'}{}_{\nu} a^{\nu}, \qquad b_{\mu'} = b_{\nu} \Lambda^{-1\nu}{}_{\mu'}, \qquad \Lambda^{-1\rho}{}_{\mu'} \Lambda^{\mu'}{}_{\sigma} = \delta^{\rho}_{\sigma} \tag{8.32}$$

for arbitrary four-vectors a^{μ} and b^{μ}, and corresponding generalizations for higher tensors, where δ^{μ}_{ν} is the unit tensor and

$$\Lambda^{\mu'}{}_{\nu} = \delta^{\mu'}_{-} n_{\nu} + \delta^{\mu'}_{I} e_{1\nu} + \delta^{\mu'}_{II} e_{2\nu} + \delta^{\mu'}_{+} \bar{n}_{\nu} \tag{8.33}$$

(we use the indices $-$, I, II, $+$ for light-cone components). Even if the transformation is symmetric with respect to the components $(-,+)$, we take $(-)$ as the generalized time-component since the laser phase is now given by $\varphi = kx = \omega_0 x^- \equiv \omega_0 \phi$. The price for this nice relation is a non-diagonal metric

$$\eta_{\mu'\nu'} = \delta^{-}_{\mu'} \delta^{+}_{\nu'} - \delta^{I}_{\mu'} \delta^{I}_{\nu'} - \delta^{II}_{\mu'} \delta^{II}_{\nu'} + \delta^{+}_{\mu'} \delta^{-}_{\nu'} \tag{8.34}$$

which implies

$$a^{\mu} b_{\mu} = a^{\mu'} b_{\mu'} = a^{-} b^{+} + a^{+} b^{-} - a^{I} b^{I} - a^{II} b^{II}. \tag{8.35}$$

We point out that the four-potential for a plane-wave field can always be chosen such that it obeys $A^+ = A^- = 0$. Since the determinant of the transformation in (8.33) is unity we obtain $\mathrm{d}^4 x = \mathrm{d}x^- \mathrm{d}x^+ \mathrm{d}^2 x^{\perp}$, where $\perp = (I, II)$. In the following we will always use a coordinate system where $-\mathbf{e}_1 = \mathbf{e}_x = (1,0,0)$, $-\mathbf{e}_2 = \mathbf{e}_y = (0,1,0)$ and $\mathbf{n} = \mathbf{e}_z = (0,0,1)$, which implies that the light-cone components of a four-vector v^{μ} are given by $v^- = v^0 - v^3$, $v^+ = \frac{1}{2}(v^0 + v^3)$, $v^I = v^1$ and $v^{II} = v^2$. In light-cone coordinates the Ritus matrices can be written as

$$\mathscr{E}(p,x) = \left(\mathbf{1} + \frac{e\not{n}\not{A}}{2p^-}\right) \exp\left[-\mathrm{i}px - \mathrm{i}\int_{-\infty}^{x^-} \mathrm{d}\phi' \left(\frac{eAp}{p^-} - \frac{e^2 A^2}{2p^-}\right)\right]. \tag{8.36}$$

They obey the following four-dimensional completeness and orthogonality relations

$$\begin{aligned} &\int \frac{\mathrm{d}^4 p}{(2\pi)^4} \mathscr{E}(p,x) \bar{\mathscr{E}}(p,x') = \delta^4(x - x'), \\ &\int \frac{\mathrm{d}^4 x}{(2\pi)^4} \bar{\mathscr{E}}(p',x) \mathscr{E}(p,x) = \delta^4(p' - p). \end{aligned} \tag{8.37}$$

To prove the first equation one performs the p^+ integration first and uses the obtained delta-function $\delta(x^- - x'^-)$ to simplify the integrand. The second relation can be shown similarly by first integrating over $x^+, x^{\perp}$. Equations (8.37) allow us to expand the fermionic field operator in terms of Volkov states rather than plane-waves as done in vacuum QED [43, 91]

$$\hat{\psi}(\mathbf{x},t) = \sum_{\mathbf{p},\zeta} \hat{a}_{\mathbf{p},\zeta} \mathscr{E}(p,x) \frac{u_{\mathbf{p},\zeta}}{\sqrt{2\varepsilon}} + \hat{b}^{\dagger}_{\mathbf{p},\zeta} \mathscr{E}(-p,x) \frac{u_{-\mathbf{p},-\zeta}}{\sqrt{2\varepsilon}}. \tag{8.38}$$

The operators $\hat{a}^{\dagger}_{\mathbf{p},\zeta}$ and $\hat{b}^{\dagger}_{\mathbf{p},\zeta}$ create now "laser-dressed" (Volkov) electrons and positrons, respectively, which take the interaction with the external field into account exactly ($u_{-\mathbf{p},-\zeta}$ are the negative-energy free spinors). Correspondingly, the laser-dressed or Volkov propagator reads [44, 47]

$$G(x,y) = \lim_{\mathscr{O} \to 0} \int \frac{\mathrm{d}^4 p}{(2\pi)^4} \mathscr{E}(p,x) \frac{\not{p} + m}{p^2 - m^2 + \mathrm{i}\mathscr{O}} \bar{\mathscr{E}}(p,y), \tag{8.39}$$

which is depicted by a double line in Feynman diagrams.

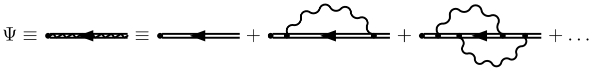

Fig. 8.5 The exact electron wave-function inside an external (classical) plane-wave field. Here the *double line* represent Volkov states which take the background field into account exactly. The *wiggly line* depicts photons of the quantized radiation field which represent the interaction of the electron with its own electromagnetic field. The exact electron wave-function obeys the Schwinger-Dirac equation (8.6)

As already mentioned in the introduction, the Volkov states describe an electron only at tree level and they are modified by radiative corrections (see Fig. 8.5). To obtain the exact electron wave-function inside an external field, one has to solve the Schwinger-Dirac equation (8.6) which includes the mass operator. For a plane-wave field the leading-order contribution in α to the mass operator M was first derived in [92]. Starting from this expression for a linearly polarized plane-wave field, we considered the experimentally interesting limit $\xi_0 \gg 1$ and solved the Schwinger-Dirac equation to leading order in α [71]. This perturbative approach is valid as long as $\alpha\chi_0^{2/3} \ll 1$ [44]. We worked in a mixture between position and momentum space by transforming only the three coordinates x^+, $x^\perp$ to p^-, $p^\perp$ and keeping the dependence on the laser phase x^-. For spin polarizations $\boldsymbol{\zeta}$ along the direction of the magnetic field $\mathbf{B}^*$ (corresponding to $f_0^{\mu\nu}$) in the electron's rest frame, the solution can be written as

$$\Psi^R_{\mathbf{p},\boldsymbol{\zeta}}(x) = \mathscr{E}_{R,\sigma}(p,x)\frac{u_{\mathbf{p},\boldsymbol{\zeta}}}{\sqrt{2\varepsilon}}, \quad \boldsymbol{\zeta} = \sigma\frac{\mathbf{B}^*}{|\mathbf{B}^*|}, \quad \sigma = \pm 1, \tag{8.40}$$

where we have defined the radiatively-corrected Ritus matrices

$$\mathscr{E}_{R,\sigma}(p,x) = \left\{1 + \frac{m\not{n}}{2p^-}\left[\frac{e\not{A}}{m} + R_{0,\sigma}\left(p,x^-\right)\right]\right\}\mathrm{e}^{\mathrm{i}S_{R,\sigma}(p,x)}, \tag{8.41}$$

with the radiatively-corrected electron "action"

$$S_{R,\sigma}(p,x) = -px - \int_{-\infty}^{x^-} \mathrm{d}\phi' \left[\frac{epA}{p^-} - \frac{e^2A^2}{2p^-} + \frac{m^2}{p^-}\sum_{i=1}^{2} R_{i,\sigma}\left(p,\phi'\right)\right]. \tag{8.42}$$

Here $R_{j,\sigma}(p,\phi) = C_j(p,\phi) + D_j(p,\phi)\sigma$ and the functions C_j and D_j are defined in [71]. We point out that these functions are proportional to the fine-structure constant α and vanish in the formal limit $\alpha \to 0$. They depend on the laser phase φ only via the "instantaneous" value of the quantum non-linear parameter $\chi(\varphi) = \chi_0|\psi'(\varphi)|$. Thus, for $\chi_0 \gtrsim 1$ non-linear quantum correction start to play a role and the degeneracy of the quasi-energy for the two spin states is removed since $S_{R,\sigma}$ depends on σ [93]. However, for quasi-monochromatic laser pulses the spin-dependence of the quasi-energy averages out and one obtains the following modified quasi-momentum

$$Q^\mu = q^\mu + \frac{m^2}{p^-}\left[\langle C_0\rangle(p) + \langle C_1\rangle(p)\right]n^\mu, \tag{8.43}$$

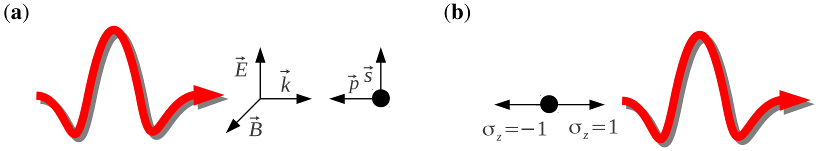

Fig. 8.6 (**a**) An electron collides head-on with a linearly polarized laser pulse propagating in z-direction. The electron's spin is initially polarized along the polarization direction of the laser (x-direction). (**b**) After the interaction the spin polarization is measured along the z-direction

where q^μ is the classical quasi-momentum (8.4). Correspondingly, also the electron's dressed mass is shifted by non-linear quantum effects inside the field

$$\delta m_*^2 \equiv Q^2 - q^2 = 2m^2\big[\langle C_0\rangle(p) + \langle C_1\rangle(p)\big]. \tag{8.44}$$

The influence of the electron self-interaction on the spin dynamics can be revealed using short laser pulses for which $\langle D_i\rangle(p) \neq 0$. In [71] we suggested the experimental setup sketched in Fig. 8.6 to measure this effect. An on-shell electron with initial four-momentum $p^\mu = (\varepsilon, 0, 0, -p)$ collides head-on with a laser beam linearly polarized along the x-direction, with electric field amplitude E_0 and central angular frequency ω_0 (wavelength $\lambda_0 = 2\pi/\omega_0$). In the electron's rest frame, its spin is initially polarized along the direction of the electric field of the laser ($\boldsymbol{\zeta} = \mathbf{e}_x$). Thus, the initial electron state in the laser field is described by $\Psi^R_{\mathbf{p},\mathbf{e}_x}$. Since the radiatively corrected Volkov states only have the simple structure (8.40) if the spin is polarized along the direction of the magnetic field (the y-direction), we expand the state $\Psi^R_{\mathbf{p},\mathbf{e}_x}$ into the eigenstates $\Psi^R_{\mathbf{p},\sigma\mathbf{e}_y}$ ($\sigma = \pm 1$). From (8.42) we conclude that the component with a given quantum number σ acquires a phase factor of the form $\exp(-\mathrm{i}\Phi_\sigma)$, where $\Phi_\sigma = \Phi_0 + \sigma\Phi_s$. Thus, the probabilities $P_{\uparrow/\downarrow}$ that the electron spin points along the positive/negative z-direction after the interaction with the laser pulse are given by

$$P_{\uparrow/\downarrow} = \frac{\mathrm{e}^{2\Im(\Phi_0)}}{2}\big[\cosh\big(2\Im(\Phi_s)\big) \mp \sin\big(2\Re(\Phi_s)\big)\big]. \tag{8.45}$$

These probabilities are exponentially suppressed since an electron inside a laser field is unstable with respect to photon emission (the imaginary part $\Im(\Phi_0)$ is proportional to the total probability for non-linear Compton scattering by the unitarity of the S-matrix). It is therefore also from this point of view favorable to employ rather short laser pulses in order to observe enough electrons which did not radiate during the interaction with the pulse. Having selected these electrons by appropriate methods, the following observable is convenient

$$\mathscr{A} \equiv \frac{P_\uparrow - P_\downarrow}{P_\uparrow + P_\downarrow} = -\frac{\sin(2\Re(\Phi_s))}{\cosh(2\Im(\Phi_s))}, \tag{8.46}$$

which describes the asymmetry of the measured spin populations. As aforementioned, the Volkov states predict no relative phase between two different spin states and thus $\mathscr{A} = 0$. Measuring a non-zero asymmetry would therefore be a clear signature for non-linear QED contributions to the electron's spin dynamics. In Fig. 8.7

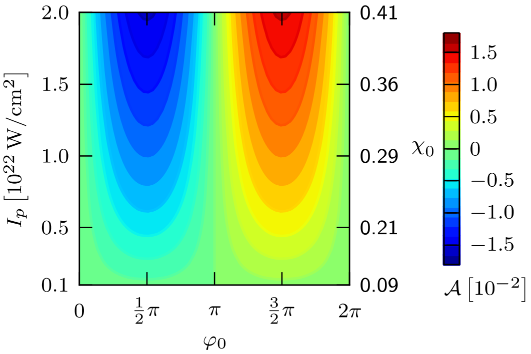

Fig. 8.7 Expected spin asymmetry $\mathscr{A}$ given in (8.46) as a function of the laser peak intensity I_p and the laser carrier-envelope phase (CEP) φ_0 for a laser pulse described by $\psi'(\varphi) = \sin^2(\varphi/2N)\sin(\varphi + \varphi_0)$ if $\varphi \in [0, 2\pi N]$ and zero otherwise with the parameters $\omega_0 = 1.55$ eV, $N = 2$ (corresponding to a pulse duration $\tau = 2\pi N/\omega_0 \approx 5$ fs) colliding head-on with electrons of $\varepsilon = 500$ MeV (corresponding to $\gamma \approx 1000$). The peak intensity I_p and the peak value for χ_0 are related by $\chi_0 = \gamma_0(1 + \beta_0)\sqrt{I_p/I_{\text{cr}}}$ ($I_{\text{cr}} = 4.6 \times 10^{29}$ W/cm^2)

we have plotted the asymmetry $\mathscr{A}$ given in (8.46) for 500 MeV electrons colliding head-on with an optical laser pulse ($\omega_0 = 1.55$ eV) with a duration of ≈ 5 fs. We point out that CEP-stabilized pulses with $\tau \sim 5$ fs and $I_p \gtrsim 10^{22}$ W/cm^2 are experimentally envisaged [94] and spin asymmetries of one percent have already bean measured even at electron energies ~ 1 GeV [95]. Furthermore, polarized ultra-relativistic electron beams with $\mathscr{N} \approx 10^{10}$ electrons, a spot area $\approx 1.7\ \mu\text{m} \times 0.75\ \mu\text{m}$ and a length l_e of about 0.5 mm can be produced [96, 97]. Assuming that one would combine a Gaussian laser beam focused to one wavelength (spot radius $w_0 = \lambda_0$ and Rayleigh length $l_r = \pi w_0^2/\lambda_0 = \pi\lambda_0$) [98] with such an electron beam, about $\mathscr{N}^* \sim \mathscr{N} \times \exp[2\Im(\Phi_0)] \times 2l_r/l_e \sim 10^7$ electrons pass through the strong-field region without radiating (at a peak intensity of $I_p = 1.5 \times 10^{22}$ W/cm^2, we obtain a suppression factor due to the finite lifetime of $\exp[2\Im(\Phi_0)] \approx 0.1$). Thus, the absolute difference of the expected electrons with opposite spin is $\sim \mathscr{A}_0 \times \mathscr{N}^* \sim 10^5$. Note also that in the above example the transverse excursion of an electron in the field is (for our parameters) approximately $\lambda_0 m\xi_0/\varepsilon \approx 0.06\lambda_0$, i.e. much smaller than w_0 and therefore the plane-wave approximation of the laser field should be adequate [33]. Thus, we conclude that a spin asymmetry due to the electron's self-interaction should be, in principle, measurable with presently available technology.

8.4 Conclusions and Outlook

In this chapter we have discussed some effects in the realm of classical and quantum electrodynamics occurring in the presence of intense laser fields. In particular, we have discussed a relatively simple method proposed in [40] to determine the peak intensity of ultra-relativistic laser pulses in an all-optical setup. By exploiting the high directionality of the radiation emitted by ultra-relativistic electrons, we could show that this methods allows for single-shot measurements with accuracies better than those presently available. Furthermore, we investigated radiative corrections to the Volkov states which were calculated in [71]. We have shown that inside a laser field the effective momentum of the electron is affected by the interaction of the electron with its own electromagnetic field and becomes dependent on the quantum parameter χ_0. Finally, we discussed a possible experimental setup which allows to measure the effect of non-linear quantum corrections to the electron spin dynamics with available laser and electron accelerator technology.

We conclude by discussing some of the challenges in strong-field QED, that still need to be investigated. According to the results in [44], radiative corrections in a strong plane-wave field at $\xi_0, \chi_0 \gg 1$ scale as $\alpha\chi_0^{2/3}$, unlike in vacuum QED where they scale as α (apart from an inessential logarithm of the typical energy of the process in units of the electron mass). This implies that at $\chi_0 \gtrsim 10^3$, QED becomes a strongly-coupled theory as QCD and the interaction between the photon and the electron-positron fields cannot be accounted for perturbatively. The main challenge would be to develop an approach to investigate strong-field QED processes beyond perturbation theory with respect to the photon field. Another challenge is also the capability of performing strong-field calculations with realistic background fields, i.e., going beyond the plane-wave approximation in the case of a laser field. In such cases, in fact, the Dirac equation in the presence of the background field cannot be solved exactly and approximated methods have to be applied. Recently, a quasiclassical approach has been developed in [99] in order to investigate processes in the presence of an atomic field and of a plane-wave field but at energies much larger than the electron mass. The Dirac equation for this field configuration cannot be solved exactly either, and one can hope to extend this method also to treat spatially focused laser beams. Finally, we mention the possibility of describing strong-field processes in configuration rather than in momentum space. This goal has not yet been achieved in strong-field QED, although there are already calculations [100] going in this direction for one-dimensional model-systems as one scalar and one fermion field coupled via a Yukawa potential.

References

1. W. Nakel, The elementary process of bremsstrahlung. Phys. Rep. **243**, 317–353 (1994)
2. V.N. Baier, V.M. Katkov, Concept of formation length in radiation theory. Phys. Rep. **409**, 261–359 (2005)
3. U.I. Uggerhøj, The interaction of relativistic particles with strong crystalline fields. Rev. Mod. Phys. **77**, 1131–1171 (2005)
4. R. Ruffini, G. Vereshchagin, S. Xue, Electron–positron pairs in physics and astrophysics: from heavy nuclei to black holes. Phys. Rep. **487**, 1–140 (2010)
5. W. Greiner, B. Müller, J. Rafelski, *Quantum Electrodynamics of Strong Fields* (Springer, Berlin, 1985)

6. P.J. Mohr, G. Plunien, G. Soff, QED corrections in heavy atoms. Phys. Rep. **293**, 227–369 (1998)
7. S.G. Karshenboim, Precision physics of simple atoms: QED tests, nuclear structure and fundamental constants. Phys. Rep. **422**, 1–63 (2005)
8. G. Baur, K. Hencken, D. Trautmann, Electron–positron pair production in ultrarelativistic heavy ion collisions. Phys. Rep. **453**, 1–27 (2007)
9. T.H. Maiman, Stimulated optical radiation in ruby. Nature **187**, 493–494 (1960)
10. D. Strickland, G. Mourou, Compression of amplified chirped optical pulses. Opt. Commun. **56**, 219–221 (1985)
11. G.A. Mourou, T. Tajima, S.V. Bulanov, Optics in the relativistic regime. Rev. Mod. Phys. **78**, 309 (2006)
12. Z. Wang, et al., High-contrast 1.16 PW Ti:sapphire laser system combined with a doubled chirped-pulse amplification scheme and a femtosecond optical-parametric amplifier. Opt. Lett. **36**, 3194–3196 (2011)
13. J.H. Sung, S.K. Lee, T.J. Yu, T.M. Jeong, J. Lee, 0.1 Hz 1.0 PW Ti:sapphire laser. Opt. Lett. **35**, 3021–3023 (2010)
14. E.W. Gaul, et al., Demonstration of a 1.1 petawatt laser based on a hybrid optical parametric chirped pulse amplification/mixed nd:glass amplifier. Appl. Opt. **49**, 1676–1681 (2010)
15. V.V. Lozhkarev, et al., Compact 0.56 petawatt laser system based on optical parametric chirped pulse amplification in KD*P crystals. Laser Phys. Lett. **4**, 421–427 (2007)
16. C.N. Danson, et al., Vulcan petawatt: design, operation and interactions at $5 \times 10^{20}\ \mathrm{W\,cm^{-2}}$. Laser Part. Beams **23**, 87–93 (2005)
17. Y. Kitagawa, et al., Prepulse-free petawatt laser for a fast ignitor. IEEE J. Quantum Electron. **40**, 281–293 (2004)
18. M. Aoyama, et al., 0.85-PW, 33-fs ti:sapphire laser. Opt. Lett. **28**, 1594–1596 (2003)
19. M.D. Perry, et al., Petawatt laser pulses. Opt. Lett. **24**, 160–162 (1999)
20. V. Yanovsky, et al., Ultra-high intensity- 300-TW laser at 0.1 Hz repetition rate. Opt. Express **16**, 2109–2114 (2008)
21. A. Lyachev, et al., The 10PW OPCPA Vulcan Laser Upgrade, in *High Intensity Lasers and High Field Phenomena* (Optical Society of America, 2011). OSA Technical Digest (CD), p. HThE2
22. J.P. Chambaret, et al., The Extreme Light Infrastructure project ELI and its prototype APOLLON/ILE: "The Associated Laser Bottlenecks", in *Frontiers in Optics* (Optical Society of America, 2009). OSA Technical Digest (CD), p. FMI2
23. D. Habs, T. Tajima, V. Zamfir, Extreme light infrastructure–nuclear physics (ELI–NP): new horizons for photon physics in Europe. Nucl. Phys. News **21**, 23–29 (2011)
24. F. Amiranoff, et al., ELI—Proposal for a European extreme light infrastructure, http://www.extreme-light-infrastructure.eu/pictures/ELI-scientific-case-id17.pdf
25. http://www.hiperlaser.org
26. Exawatt Center for Extreme Light Studies (XCELS), http://www.xcels.iapras.ru/img/XCELS-Project-english-version.pdf
27. A.V. Korzhimanov, A.A. Gonoskov, E.A. Khazanov, A.M. Sergeev, Horizons of petawatt laser technology. Phys. Usp. **54**, 9–28 (2011)
28. W.P. Leemans, et al., GeV electron beams from a centimetre-scale accelerator. Nat. Phys. **2**, 696–699 (2006)
29. J. Osterhoff, et al., Generation of stable, low-divergence electron beams by laser-wakefield acceleration in a steady-state-flow gas cell. Phys. Rev. Lett. **101**, 085002 (2008)
30. E. Esarey, C.B. Schroeder, W.P. Leemans, Physics of laser-driven plasma-based electron accelerators. Rev. Mod. Phys. **81**, 1229 (2009)
31. T. Tajima, Laser acceleration and its future. Proc. Jpn. Acad. Ser. B, Phys. Biol. Sci. **86**, 147–157 (2010)
32. A. Di Piazza, C. Müller, K.Z. Hatsagortsyan, C.H. Keitel, Extremely high-intensity laser interactions with fundamental quantum systems. Rev. Mod. Phys. **84**, 1177–1228 (2012)

33. L.D. Landau, E.M. Lifshitz, *The Classical Theory of Fields*, 4th edn. (Butterworth, Stoneham, 1987)
34. M. Abraham, Prinzipien der Dynamik des Elektrons. Ann. Phys. **315**, 105–179 (1902)
35. M. Abraham, Zur Theorie der Strahlung und des Strahlungsdruckes. Ann. Phys. **319**, 236–287 (1904)
36. P.A.M. Dirac, Classical theory of radiating electrons. Proc. R. Soc. Lond. Ser. A, Math. Phys. Sci. **167**, 148–169 (1938)
37. S.G. Rajeev, Exact solution of the Landau-Lifshitz equations for a radiating charged particle in the Coulomb potential. Ann. Phys. **323**, 2654 (2008)
38. A. Di Piazza, K.Z. Hatsagortsyan, C.H. Keitel, Strong signatures of radiation reaction below the radiation-dominated regime. Phys. Rev. Lett. **102**, 254802 (2009)
39. A. Di Piazza, Exact solution of the Landau-Lifshitz equation in a plane wave. Lett. Math. Phys. **83**, 305–313 (2008)
40. O. Har-Shemesh, A. Di Piazza, Peak intensity measurement of relativistic lasers via nonlinear Thomson scattering. Opt. Lett. **37**, 1352–1354 (2012)
41. A. Link, et al., Development of an in situ peak intensity measurement method for ultraintense single shot laser-plasma experiments at the Sandia Z petawatt facility. Rev. Sci. Instrum. **77**, 10E723 (2006)
42. S. Bahk, et al., Generation and characterization of the highest laser intensities (10^{22} $\mathrm{W/cm^2}$). Opt. Lett. **29**, 2837–2839 (2004)
43. L.D. Landau, E.M. Lifshitz, *Quantum Electrodynamics*, 2nd edn. (Butterworth, Stoneham, 1982)
44. V.I. Ritus, Quantum effects of the interaction of elementary particles with an intense electromagnetic field. J. Russ. Laser Res. **6**, 497–617 (1985)
45. W.H. Furry, On bound states and scattering in positron theory. Phys. Rev. **81**, 115–124 (1951)
46. A.I. Nikishov, V.I. Ritus, Quantum Processes in the field of a plane electromagnetic wave and in a constant field. I. Sov. Phys. JETP **19**, 529–541 (1964)
47. L.S. Brown, T.W.B. Kibble, Interaction of intense laser beams with electrons. Phys. Rev. **133**, 705–719 (1964)
48. F. Mackenroth, A. Di Piazza, C.H. Keitel, Determining the carrier-envelope phase of intense few-cycle laser pulses. Phys. Rev. Lett. **105**, 063903 (2010)
49. D. Seipt, B. Kämpfer, Nonlinear Compton scattering of ultrashort intense laser pulses. Phys. Rev. A **83**, 022101 (2011)
50. F. Hebenstreit, A. Ilderton, M. Marklund, J. Zamanian, Strong field effects in laser pulses: the Wigner formalism. Phys. Rev. D **83**, 065007 (2011)
51. C. Bula, et al., Observation of nonlinear effects in Compton scattering. Phys. Rev. Lett. **76**, 3116 (1996)
52. D.L. Burke, et al., Positron production in multiphoton light-by-light scattering. Phys. Rev. Lett. **79**, 1626 (1997)
53. H. Hu, C. Müller, C.H. Keitel, Complete QED theory of multiphoton trident pair production in strong laser fields. Phys. Rev. Lett. **105**, 080401 (2010)
54. A. Ilderton, Trident pair production in strong laser pulses. Phys. Rev. Lett. **106**, 020404 (2011)
55. F. Sauter, Über das Verhalten eines Elektrons im homogenen elektrischen Feld nach der relativistischen Theorie Diracs. Z. Phys. **69**, 742–764 (1931)
56. W. Heisenberg, H. Euler, Folgerungen aus der Diracschen Theorie des Positrons. Z. Phys. **98**, 714–732 (1936)
57. V. Weisskopf, Über die Elektrodynamik des Vakuums auf Grund der Quantentheorie des Elektrons. K. Dan. Vidensk. Selsk. Mat. Fys. Medd. **XIV** (1936)
58. J. Schwinger, On gauge invariance and vacuum polarization. Phys. Rev. **82**, 664–679 (1951)
59. E. Brezin, C. Itzykson, Pair production in vacuum by an alternating field. Phys. Rev. D **2**, 1191–1199 (1970)

60. N.B. Narozhnyi, A.I. Nikishov, Pair production by a periodic electric field. Sov. Phys. JETP **38**, 427 (1974)
61. S.S. Bulanov, N.B. Narozhny, V.D. Mur, V.S. Popov, Electron-positron pair production by electromagnetic pulses. J. Exp. Theor. Phys. **102**, 9–23 (2006)
62. M. Ruf, G.R. Mocken, C. Müller, K.Z. Hatsagortsyan, C.H. Keitel, Pair production in laser fields oscillating in space and time. Phys. Rev. Lett. **102**, 080402 (2009)
63. A. Di Piazza, E. Lötstedt, A.I. Milstein, C.H. Keitel, Barrier control in tunneling $e^+ - e^-$ photoproduction. Phys. Rev. Lett. **103**, 170403 (2009)
64. W. Dittrich, H. Gies, *Probing the Quantum Vacuum* (Springer, Berlin, 2000)
65. A. Di Piazza, A.I. Milstein, C.H. Keitel, Photon splitting in a laser field. Phys. Rev. A **76**, 032103 (2007)
66. E. Lundström, et al., Using high-power lasers for detection of elastic photon-photon scattering. Phys. Rev. Lett. **96**, 083602 (2006)
67. A. Di Piazza, K.Z. Hatsagortsyan, C.H. Keitel, Light diffraction by a strong standing electromagnetic wave. Phys. Rev. Lett. **97**, 083603 (2006)
68. B. King, A. Di Piazza, C.H. Keitel, A matterless double slit. Nat. Photonics **4**, 92–94 (2010)
69. B. King, A. Di Piazza, C.H. Keitel, Double-slit vacuum polarization effects in ultraintense laser fields. Phys. Rev. A **82**, 032114 (2010)
70. M. Marklund, P.K. Shukla, Nonlinear collective effects in photon-photon and photon-plasma interactions. Rev. Mod. Phys. **78**, 591 (2006)
71. S. Meuren, A. Di Piazza, Quantum electron self-interaction in a strong laser field. Phys. Rev. Lett. **107**, 260401 (2011)
72. D.M. Volkov, Über eine Klasse von Lösungen der Diracschen Gleichung. Z. Phys. **94**, 250–260 (1935)
73. W.E. Lamb, R.C. Retherford, Fine structure of the hydrogen atom by a microwave method. Phys. Rev. **72**, 241–243 (1947)
74. A. Di Piazza, K.Z. Hatsagortsyan, C.H. Keitel, Quantum radiation reaction effects in multiphoton Compton scattering. Phys. Rev. Lett. **105**, 220403 (2010)
75. H.G. Hetzheim, C.H. Keitel, Ionization dynamics versus laser intensity in laser-driven multiply charged ions. Phys. Rev. Lett. **102**, 083003 (2009)
76. C. Smeenk, et al., Precise in-situ measurement of laser pulse intensity using strong field ionization. Opt. Express **19**, 9336–9344 (2011)
77. J. Gao, Laser intensity measurement by Thomson scattering. Appl. Phys. Lett. **88**, 091105 (2006)
78. J. Alda, Laser and Gaussian beam propagation and transformation, in *Encyclopedia of Optical Engineering: Paraxial Optics* (Dekker, New York, 2003)
79. Y.I. Salamin, G.R. Mocken, C.H. Keitel, Electron scattering and acceleration by a tightly focused laser beam. Phys. Rev. Spec. Top., Accel. Beams **5**, 101301 (2002)
80. W.H. Press, S.A. Teukolsky, W.T. Vetterling, B.P. Flannery, *Numerical Recipes in FORTRAN: The Art of Scientific Computing*, 2nd edn. (Cambridge University Press, New York, 1992)
81. J.D. Jackson, *Classical Electrodynamics*, 3rd edn. (Wiley, Hoboken, 1998)
82. C. Itzykson, J.B. Zuber, *Quantum Field Theory* (McGraw-Hill, New York, 1980)
83. L. Michel, A.S. Wightman, Covariant formalism describing the polarization of spin one-half particles. Phys. Rev. **98**, 1190 (1955)
84. J.W. Meyer, Covariant classical motion of electron in a laser beam. Phys. Rev. D **3**, 621–622 (1971)
85. E.S. Sarachik, G.T. Schappert, Classical theory of the scattering of intense laser radiation by free electrons. Phys. Rev. D **1**, 2738–2753 (1970)
86. V. Bargmann, L. Michel, V.L. Telegdi, Precession of the polarization of particles moving in a homogeneous electromagnetic field. Phys. Rev. Lett. **2**, 435–436 (1959)
87. P.A.M. Dirac, Forms of relativistic dynamics. Rev. Mod. Phys. **21**, 392–399 (1949)
88. R.A. Neville, F. Rohrlich, Quantum electrodynamics on null planes and applications to lasers. Phys. Rev. D **3**, 1692–1707 (1971)

89. F. Hebenstreit, A. Ilderton, M. Marklund, Pair production: the view from the lightfront. Phys. Rev. D **84**, 125022 (2011)
90. A. Ilderton, Lightfront DHW functions and strong field QED. Few-Body Syst. **52**, 431–436 (2012)
91. E.S. Fradkin, D.M. Gitman, S.M. Shvartsman, *Quantum Electrodynamics with Unstable Vacuum* (Springer, Berlin, 1991)
92. V.N. Baier, V.M. Katkov, V.M. Strakhovenko, Operator approach to quantum electrodynamics in an external field: the mass operator. Sov. Phys. JETP **40**, 225–232 (1975)
93. V.N. Baier, A.I. Milstein, Radiation effects in the field of an electromagnetic wave. Sov. Phys. Dokl. **21**, 734 (1977)
94. S. Karsch, et al., The petawatt field synthesizer: a new approach to ultrahigh field generation. ASSP, WF1 (2008)
95. S. Escoffier, et al., Accurate measurement of the electron beam polarization in JLab Hall A using Compton polarimetry. Nucl. Instrum. Methods A **551**, 563–574 (2005)
96. SLAC-376, Final Focus Test Beam Project Design Report (Stanford Linear Accelerator Center, 1991)
97. V.A. Alexandrof, et al., Results of final focus test beam. SLAC-PUB-9961 (1995)
98. B.E.A. Saleh, M.C. Teich, *Fundamentals of Photonics*, 2nd edn. (Wiley, New York, 2007)
99. A. Di Piazza, A.I. Milstein, Quasiclassical approach to high-energy QED processes in strong laser and atomic fields. Phys. Lett. B **717**, 224 (2012)
100. R.E. Wagner, Q. Su, R. Grobe, Time resolved Compton scattering for a model fermion-boson system. Phys. Rev. A **82**, 022719 (2010)

Chapter 9
Quantum Vacuum Polarization Searches with High Power Lasers Below the Pair Production Regime

Daniele Tommasini, David Novoa, and Luis Roso

Abstract For high enough electromagnetic fields, such as those that can be achieved by ultra-intense laser pulses, light is expected to interact with light through the interchange of virtual particles. A rich phenomenology is then predicted to occur, such as the possible production of real electron-positron pairs for electromagnetic fields close enough to the Schwinger limit, or the polarization of the vacuum itself. These effects may be amplified by new physics, so that their search can also be used to test non-standard models involving axions or mini-charged particles. A recent work suggests that the diffraction of light by light in vacuum, in the absence of any material slit or obstacle, is most probably the first signature of the polarization of the vacuum that will be reachable in the near future. Surprisingly enough, this result could be achieved very soon in principle, either at a high repetition rate Petawatt facility such as VEGA, that is expected to be operative at the beginning of 2014 in Salamanca, Spain, or at other Multi-PW facilities, such as ELI-10 PW or PETAL. Calculations for a prospective 100-PW system are also included.

9.1 Introduction

Besides their multiple technological applications, extreme lasers are becoming part of a conceptually new experimental set-up to explore fundamental properties of the quantum world. Quantum Electrodynamics (QED) has been the most successful

---

D. Tommasini
Department of Applied Physics, University of Vigo, 32004 Ourense, Spain
e-mail: daniele@uvigo.es

D. Novoa · L. Roso (✉)
Centro de Láseres Pulsados, CLPU, Edificio M3—Parque Científico, Calle del Adaja, 37185 Villamayor, Spain
e-mail: roso@usal.es

L. Roso (✉)
e-mail: roso@clpu.es

D. Novoa
e-mail: david.novoa@mpl.mpg.de

K. Yamanouchi et al. (eds.), *Progress in Ultrafast Intense Laser Science X*,
Springer Series in Chemical Physics 106, DOI 10.1007/978-3-319-00521-8_9,

theory ever proposed, predicting properties at the atomic scale with an astonishing precision. Due to its triumphs, it has been used in Particle Physics as a guide for the construction of the theories of the strong and weak interactions as well.

However, QED effects implying the exchange of a very high number of particles are still controversial. In Classical Electrodynamics, Maxwell's equations in vacuum are linear in the fields and so do not allow for any interaction of light with light. In QED, however, two photons can couple each other by the exchange of a virtual particle-antiparticle pair (most likely an electron-positron virtual pair) [29]. Quantum vacuum can thus be polarized by electromagnetic fields. For many years this idea has been considered a gedanken experiment [33], but we hope that in the near future some features of the exchange of such virtual pair of particles may become observable [35].

Todays femtosecond lasers can achieve the Petawatt level and beyond. When such lasers have a good quality wavefront—not easy at all at such extreme powers—the laser pulse can be focused at intensities of the order of 10^{23} W/cm^2 or beyond, and probably in less than a decade the 10^{25} W/cm^2 intensity will be reached in the lab frame, and much more if we consider a Lorentz boosted frame. In such cases, the photon concentration is so extreme that many photons can interact with a single electron almost instantaneously. Photons are bosons and so they can be packed in a large number at the same quantum state at the same point. If they did not interact with each other, in principle their density could be arbitrarily high. In other words, there should be no limit for the maximum intensity of a laser pulse. However, QED predicts that photons interact, and it has been argued since Schwinger times that there is a theoretical limit for the field, beyond which vacuum would become unstable and spontaneous pair production would take place. This limit is now referred as the Schwinger limit [49], and corresponds to the critical value 1.3×10^{16} V/cm for the electric field. For a laser pulse, this corresponds to an intensity $\sim 10^{29}$ W/cm^2, which is six orders of magnitude beyond current possibilities, and four orders of magnitude above the reach of the new facilities that will be available in the next decade.

Nevertheless, we are not too far, and it has been suggested that real electron-positron pairs may be produced in significant amount via laser-induced electromagnetic cascades even below the Schwinger limit. In this process, charged electron-positron pairs are produced and accelerated within the laser pulse, subsequently emitting hard photons which in turn decay into further electron-positron pairs, which are accelerated by the laser pulse itself and so on. This cascade effect possibly leads to a saturation of the laser intensity at the level $\sim 10^{26}$ W/cm^2 [23], which is just an order of magnitude above the level that may be reached in a decade. It might be expected that more efficient configurations can be found leading to real pair production at a somewhat lower scale [5, 22, 34, 46, 47]. In any case, the production of real pairs is hardly expected to be observable below the 10^{24} W/cm^2 intensity scale [5].

Although we cannot expect to succeed in the production of real pairs, at least until the next decade, we may be closer to detect the first signatures of the polarization of vacuum induced by the production and annihilation of *virtual* pairs of particles. In QED, this effect is predicted to be generated by the same radiative corrections

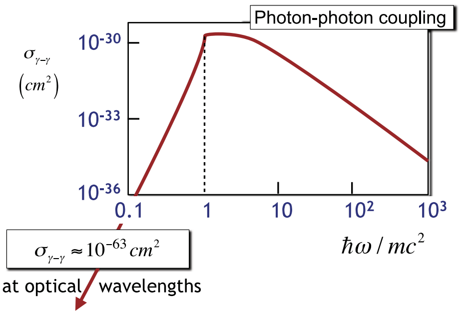

Fig. 9.1 Photon-photon cross-section $\sigma_{\gamma-\gamma}$ vs. photon energy (in units of the electron mass). The peak $\sigma_{\gamma-\gamma}$ occurs for a photon mass similar to the electron mass. At optical wavelengths, the cross-section falls down by about 30 orders of magnitude

that are responsible for photon-photon scattering. Although an experimental evidence of the latter has been obtained in the case of Delbruck scattering of a gamma ray of energy at the MeV scale from an atomic electric field [43], all the searches both for the scattering of *real* photons have only produced negative results, and no experimental evidence has been found so far of the interaction of light with light in the optical regime. This is due to the extremely tiny QED cross-section for the photon-photon scattering, in particular at optical wavelengths ($\sigma \sim 10^{-63}$ cm^2), as shown in Fig. 9.1.

Another possibility to gain experience with the nonlinear behavior of the quantum vacuum is to consider a gamma ray photon colliding with one, or a few, optical photons. This has been already done in the context of the SLAC-144 experiment. They observed collisions of a 46.6 GeV electron beam with a 527 nm Terawatt pulsed laser and subsequent positron production. Such positrons were arising from a combined process in which laser photons were backscattered by the electron beam first and then interact with several laser photons to produce an electron-positron pair. These results, in good agreement with QED predictions, were a clear experimental evidence for inelastic photon-photon scattering. In those experiments the peak laser intensity just arrived to 10^{18} W/cm^2 but the nonlinear QED effect was enhanced enough to be observed thanks to the backscattered photons [12, 13].

However, the process at the optical scale can have a very rich phenomenology, including the diffraction of light by light in the complete absence of matter. Moreover, it can be enhanced by additional contributions from new physics. In fact, while all Schwinger-type calculations assume that the lightest possible particle pair is the electron-positron, there are theories predicting the existence of axions and other mini-charged particles lighter than the electron. Extreme lasers can then represent a unique laboratory test for the existence, or not, of such particles. On the other hand, it has recently been argued that even the QED virtual electron-positron pair exchange can be tested at present PW facilities by searching for light by light diffraction in a head-on collision of two laser pulses [50]. This result lowers by several orders of magnitude the requirement on the intensity for the polarization of the vacuum to become observable, as compared to previous works. As far as we know, the latter is the best candidate to provide the first signature of the virtual pair creation mediating the interaction of light with light in the optical regime.

Summarizing, to our knowledge there are two key questions where lasers can be relevant for our understanding of the quantum vacuum. The first question is the existence of the Schwinger limit itself, whose experimental study would require laser peak intensities beyond $10^{29}\ \mathrm{W/cm^2}$. Such intensities are beyond the possibilities of standard CPA technology, although conceptually new laser schemes that are under consideration, such as Backward Raman Amplification, might allow for reaching the Schwinger limit in the future. In any case, a deeper theoretical understanding and modeling on the laser-electron coupling at such extreme fields is needed, particularly in the context of radiation reaction that can be dominant beyond $10^{26}\ \mathrm{W/cm^2}$. While we wait for such developments we can try to solve the second key question: which can be the first effect to be observed at the lower laser intensities that will be available now or in the near future? The proposal that we present in this chapter tries to answer this question. As we shall see, the quantum interaction of light with light may be observed at laser facilities in the Petawatt or multi-Petawatt regime much before the Schwinger limit, and its search can also be used to address fundamental questions such as the existence of mini-charged or axion-like particles.

The chapter is organized as follows:

In Sect. 9.2, we will briefly review the recent research in the field, that has opened the possibility of performing optical measurements of vacuum polarization effects using ultraintense lasers.

In Sect. 9.3, we discuss the mathematical formalism and introduce the two parameters that drive the nonlinear vacuum effects. We review the predictions for the values of the relevant parameters both in QED and in non-standard models of particle physics, such as the Born-Infeld theory or scenarios involving new mini-charged or axion-like particles. We show that, in the case of detecting the effect of vacuum polarization above the QED level, the possible measurement of both the relevant parameters can be used to discriminate among the different types of new physics.

In Sect. 9.4, we discuss the current experimental constraints on the relevant parameters that have been obtained by the PVLAS collaboration [9, 54] from the negative search of birefringence of the vacuum in an external magnetic field. These limits constrain the cross-section for photon-photon scattering in the near infrared to be smaller than $\sim 10^{-58}\ \mathrm{cm}^2$, but this value, even if it is extremely tiny, is still $\sim 5 \times 10^6$ times higher than the prediction of QED, so that there is still much room for new physics to emerge.

In Sect. 9.5, we discuss the main effect that is produced when two counter-propagating coherent light waves cross each other. In this case, the nonlinear quantum vacuum polarization makes each of the two beams to behave as a phase object for the other, thus producing a phase shift on its wavefront.

In Sect. 9.6, we review one of the consequences of the phase shift that is produced in the collision of two laser pulses of different waists: the wider beam is diffracted by the more concentrated one. We discuss the possibility of searching for this effect by counting the number of diffracted photons on a ring detector, and show that this can be used to measure or constrain the parameters that describe quantum vacuum polarization.

In Sect. 9.7, we discuss the sensitivity for such measurements that, in principle, can be achieved at several ultraintense laser facilities that are scheduled to become operative in the near future.

In Sect. 9.8, we draw our conclusions and future trends.

9.2 The Search for Quantum Vacuum Polarization

The interaction of light with light in complete absence of matter has still to be tested in the optical regime. In this regime a rich phenomenology of collective effects is expected to appear, due to the polarization of the quantum vacuum. In particular, in the last few years there has been an increasing interest in the phenomenological consequences of the quantum nonlinear corrections to the Maxwell equations due to the exchange of virtual particles and in proposing experimental tests that can also be used to search for new physics. Several different configurations have been proposed aimed at testing the nonlinear optical response of the vacuum, e.g. using harmonic generation in an inhomogeneous magnetic field [18], four-wave mixing [1, 6, 36, 44], resonant interactions in microwave cavities [11], or vacuum birefringence [3] which can be probed by x-ray pulses [19, 28], among others [38, 45].

In particular, the possibility of purely optical tests is especially promising, since it can exploit the extraordinary advancements in laser technology that have been achieved in the last two decades. Indeed, an example of this kind has been performed recently by the PVLAS collaboration. In their experiment, a laser beam travels within a slowly-varying magnetic field. The nonlinear correction to the Maxwell equations induced by the external magnetic field would then imply the emergence of birefringence and dichroism that would induce a rotation of the laser polarization [9]. The non-observation of such effects was used to set the current limit on the photon-photon scattering cross-section at optical wavelengths. Although these limits are still 7 orders of magnitude above the prediction of QED, they can be used to set the best laboratory constraints on several kinds of new physics scenarios, such as Born-Infeld theory or models implying new mini-charged or axion-like particles in suitable mass ranges [9, 20, 52]. A second class of purely optical tests of the nonlinear corrections to the Maxwell equations is based on exploiting the field of the laser pulses themselves, instead of making the pulses to travel across external electric or magnetic fields. The main advantage of this approach is the fact that the electromagnetic intensities that can be achieved by focusing ultrashort laser pulses are nowadays 10 orders of magnitude larger than the intensities of stationary external fields that can be obtained in the laboratory, such as the magnetic field that is used in PVLAS experiment. This improvement compensates the much smaller interaction length, which is limited by the duration of the ultra-intense laser pulse. This kind of motivations suggested a configuration in which two counter-propagating laser pulses cross each other, inducing a phase shift onto each other due to the nonlinear quantum effects that can be directly measured either for parallel or for orthogonal polarizations [24, 51, 52]. Very recently, this concept has been significantly improved by suggesting a configuration in which the crossing pulses have different waists and, instead of directly measuring the phase shifts, the number of diffracted photons is counted. On one hand, the diffraction of a probe laser by two additional counter-propagating ultra-intense pulses was proposed as a matter-less analogue to the Young double slit experiment [32, 37]. On the other hand, a simpler case of crossing of just two counter-propagating laser pulses [50], analogue to a matter-less single slit experiment, has been found to provide a much more sensitive and promising configuration for the search of light-by-light diffraction in vacuum and the test of the nonlinear corrections to the Maxwell equations [50]. This proposal will be reviewed in detail in Sect. 9.6 below.

9.3 The Effective Lagrangian for the Electromagnetic Fields in QED and Non-standard Models

In this section, we will briefly review the QED and non-standard model predictions for the interaction of light with light at optical wavelengths, following Ref. [52].

Optical photons have energies well below the threshold for the production of real electron-positron pairs, so that we can assume an effective Lagrangian for the electromagnetic fields **E** and **B** of the form

$$\mathscr{L} = \mathscr{L}_0 + \xi_L \mathscr{L}_0^2 + \frac{7}{4}\xi_T \mathscr{G}^2, \tag{9.1}$$

being $\mathscr{L}_0 = \frac{\varepsilon_0}{2}(\mathbf{E}^2 - c^2\mathbf{B}^2)$ the Lagrangian density of the linear theory, $\mathscr{G} = \varepsilon_0 c(\mathbf{E}\cdot\mathbf{B})$ and ε_0 and c the dielectric constant and the speed of light in vacuum, respectively. $\mathscr{L}_0^2$ and $\mathscr{G}^2$ are the only two Lorentz-covariant terms that can be formed with the electromagnetic fields at the lowest order above $\mathscr{L}_0$, thus they will describe the first correction to the linear evolution both in QED and non-standard models.

In QED, such terms arise due to the interchange of virtual charged particles running in loop box diagrams [14]. The resulting Lagrangian density [29] coincides with (9.1) with the identification $\xi_L^{QED} = \xi_T^{QED} \equiv \xi$, being

$$\xi = \frac{8\alpha^2\hbar^3}{45 m_e^4 c^5} \simeq 6.7 \times 10^{-30}\ \frac{\mathrm{m}^3}{\mathrm{J}}. \tag{9.2}$$

In non-standard models of Particle Physics, however, the two parameters ξ_L and ξ_T can acquire different values. In Born-Infeld theory [7, 8], that can derived from Superstring theory, one would obtain the relation $\xi_T^{BI} = 4\xi_L^{BI}/7$ [17], in general without a definitive prediction for the numerical value.

New mini-charged particles (MCPs) [2, 15, 16, 21, 25, 26, 30, 31], that would appear naturally in a large class of gauge models, would provide an additional contribution analogous to that from the electron-positron box diagram. There are different possibilities for MCPs as we will discuss below.

If the new MCPs are spin 1/2 fermions, and assuming that their mass m_ε is larger than the energy of the photons (the eV scale in optical experiments), we would obtain from Ref. [52]

$$\Delta\xi_L^{\rm MCP} = \Delta\xi_T^{\rm MCP} = \left(\frac{\varepsilon m_e}{m_\varepsilon}\right)^4 \xi, \tag{9.3}$$

where ε is the ratio of the charge of the particle with respect to the electron charge. The case of MCPs lighter than the photon energy would deserve a different treatment and in general would imply additional effects such as real MCPs production.

If the new MCP is a spinless boson of mass m_ε larger than the energy of the photons, from Ref. [52] we obtain

$$\Delta\xi_L^{\rm MCP0} = \frac{7}{16}\left(\frac{\varepsilon m_e}{m_\varepsilon}\right)^4 \xi, \qquad \Delta\xi_T^{\rm MCP0} = \frac{1}{28}\left(\frac{\varepsilon m_e}{m_\varepsilon}\right)^4 \xi. \tag{9.4}$$

On the other hand, if the MCP is a spin 1 boson, the result obtained from Ref. [52] is

$$\Delta\xi_L^{\rm MCP1} = \frac{261}{16}\left(\frac{\varepsilon m_e}{m_\varepsilon}\right)^4 \xi, \qquad \Delta\xi_T^{\rm MCP1} = \frac{243}{28}\left(\frac{\varepsilon m_e}{m_\varepsilon}\right)^4 \xi. \tag{9.5}$$

Let us now discuss the case of an axion-like particle (ALP) [4, 10, 27, 39–41], such as the particle needed to solve the strong CP problem in Peccei-Quinn theory [48]. We can allow both for a Light Pseudoscalar Boson or a Light Scalar Boson, depending on the coupling with the photons, that is described in the Lagrangian density by the terms $\mathscr{L}_P = -\sqrt{\hbar c}\, g_P \Phi_P \mathscr{G}$ and $\mathscr{L}_S = -\sqrt{\hbar c}\, g_S \Phi_S \mathscr{L}_0$, respectively. We can find the leading contribution to the effective Lagrangian when the photon energy is much smaller than the m_Φ scale, that can be cast in the form of Eq. (9.1) with an additional contribution given by

$$\Delta\xi_T = \frac{2\hbar^3 g_P^2}{7cm_\Phi^2}, \qquad \Delta\xi_L = 0, \tag{9.6}$$

in the case of pseudoscalars, or

$$\Delta\xi_L = \frac{\hbar^3 g_S^2}{2cm_\Phi^2}, \qquad \Delta\xi_T = 0, \tag{9.7}$$

in the case of scalars.

Figure 9.2 shows the theoretical predictions for ξ_L and ξ_T including the contributions from these different new particle ensembles.

Note that for masses smaller than the uncertainty on the momenta of the colliding photons, the computation of $\Delta\xi_L$ is more complicated and the production of real axions has also to be taken into account [20].

The generalized Lagrangian of (9.1) implies a set of modified Maxwell's equations for the average values of the electromagnetic quantum fields similar to those that have been obtained in Ref. [42], the only difference being the distinction between ξ_L and ξ_T. In any case, as we can expect on dimensional grounds, the amount of the effect of these nonlinear corrections turns out to be driven by the product

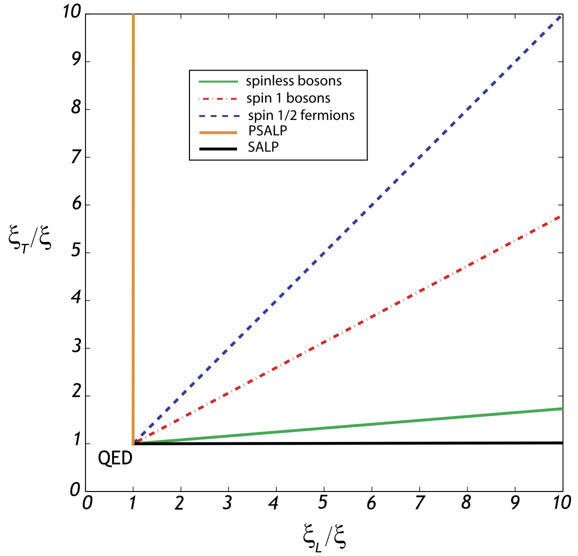

Fig. 9.2 Theoretical predictions for the parameters ξ_L and ξ_T entering the effective Lagrangian Eq. (9.1) in different new physics models. The *solid green line* describes the prediction including the contribution of a spinless MCP; the *dashed-dotted red line*dashed-dotted red line corresponds to adding a spin 1 MCP; the *dashed blue line* corresponds to adding a spin $1/2$ MCP; the *solid orange line* (parallel to the vertical axis) to adding a pseudo-scalar ALP and the *solid black line* (parallel to the horizontal axis) to a scalar ALP. Although we only show the region close to the QED prediction, marked by the labeled starting point shared by all the lines displayed, each model line can be extended for higher values of ξ_L and ξ_T

$\xi_{L,T}\,\rho$ of the relevant parameter with the energy density of the electromagnetic field.

9.4 Present Constraints

The current *laboratory* constraint on a combination of the parameters ξ_L and ξ_T that drive the nonlinear terms in the Lagrangian (9.1) have been obtained by the PVLAS collaboration [9, 54] from the search for birefringence of the vacuum in a uniform magnetic field background. Such limit is more reliable, although much less stringent, than the model-dependent *cosmological* constraints that have been derived for the masses and coupling constants of MCPs and ALPs. With our notation, the 95 % C.L. limit from PVLAS reads

$$\frac{|7\xi_T - 4\xi_L|}{3} < 1.5 \times 10^{-26}\ \frac{\mathrm{m}^3}{\mathrm{J}} = 2.2 \times 10^3 \xi. \tag{9.8}$$

Assuming $\xi_L = \xi_T$ as in QED, this results implies constraint $\xi < \xi^{\mathrm{PVLAS}} \equiv 1.5 \times 10^{-26}\ \mathrm{m}^3/\mathrm{J}$. This can be translated into a limit for the photon-photon scattering cross-section, e.g. $\sigma < 9.5 \times 10^{-59}\,\mathrm{cm}^2$ at $\lambda = 1064\,\mathrm{nm}$. Although such cross-section is extremely tiny, it is still $\sim 5 \times 10^6$ times higher than the prediction of QED for the same wavelength, so that there is still much room for new physics to emerge.

It is worth noting that the PVLAS experiment is only sensitive to the combination $|7\xi_T - 4\xi_L|$ and cannot be used to constrain the whole parameter space. In particular, a pure Born-Infeld theory, for which $\xi_T = \frac{4}{7}\xi_L$, cannot be constrained at all by the PVLAS results.

Finally, we note that, even for an external magnetic field as large as 10 T, the product that drives the quantum vacuum polarization effects is as small as $\xi\rho \sim 3 \times 10^{-22}$. It is then natural to explore the possibility of substituting the external magnetic field with the electromagnetic field of an ultraintense laser pulse, since in this case the product $\xi\rho$ can already be improved by 10 orders of magnitude ($\xi\rho \sim 4 \times 10^{-12}$ at the current record intensity that has been reached by HERCULES [53]). Of course, this gain is partly compensated by the much shorter interaction region, that would be limited by the temporal duration of the laser pulse itself instead of the macroscopic propagation distances that are used in the PVLAS experiment.

9.5 Phase Shift of Crossing Polarized Beams

There are several geometries to observe vacuum polarization. In the present section we consider just two counter-propagating linearly-polarized plane waves. The effect of the nonlinear terms in Eq. (9.1) in this case can be computed as in Refs. [24, 51, 52]. Let us call A and B the two waves, and describe the electromagnetic fields with the usual four-vector potential A^μ. In the absence of the nonlinear interaction terms driven by ξ_L and ξ_T, the linear evolutions of A and B would simply sum each other, so that $A^\mu_{\mathrm{lin}} = A^\mu_A + A^\mu_B$. Since the product $\xi\rho$ will be very small in all the experimental configurations that can be obtained in the near future, we can compute the solution of the full QED equations $\delta\Gamma/\delta A^\mu = 0$ by perturbing the linear propagation. The result which is relevant for our purposes is that each of the two waves acquires a phase-shift due to the crossing with the other [51, 52]. The phase shift of the wave B is

$$\Delta\phi_{L,T} = (a\xi)_{L,T} I_A k_B \tau_A, \tag{9.9}$$

where $k_A = 2\pi/\lambda_A$, $k_B = 2\pi/\lambda_B$, $I_A = \rho_A c$ is the intensity of the wave A and τ_A is the temporal duration of the interaction. The indexes L and T refer to the two beams having parallel or orthogonal linear polarizations, respectively. Following Ref. [50], we have fixed $a_L = 4$ and $a_T = 7$.

As we shall discuss in the next section, this formula can be generalized to the case of a Gaussian laser pulse by using the transverse intensity distribution $I_A(r)$ instead of a constant I. In this case, we will also assume that the time variation can be approximated by a step function, which will be argued to be a reasonable approximation in the cases that will be considered in the next section.

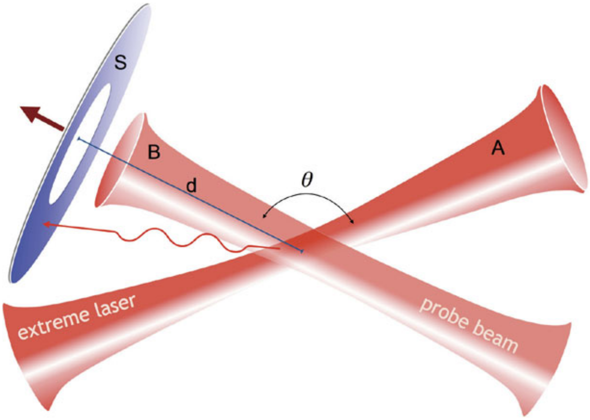

Fig. 9.3 Sketch of an experiment for searching light by light diffraction in vacuum. An ultra-intense laser pulse A and a wider probe beam B, both moving in a high vacuum, are focused to a region where they collide at an angle θ close to π. The diffracted part of the probe is then observed at a distance d on the ring screen S. In a minimal version, a single laser can produce both beams

As discussed in Refs. [51, 52], (9.9) can be used to perform a set of experiments aimed at measuring the phase shifts resulting from the crossing of two pulses for parallel and for orthogonal polarizations. If $\xi_L = \xi_T$ as in QED or in theories involving mini-charged spin $1/2$ fermions, $\Delta\phi_T$ turns out to be more sensitive to the effect of the vacuum polarization by a factor $7/4$ than $\Delta\phi_L$. More importantly, by performing the experiment with the two different configurations for the polarizations we will be able to test both parameters ξ_L, ξ_T appearing in the effective Lagrangian (9.1), distinguishing between QED and other models such as Born-Infeld theories. Finally, we note that (9.9) also implies that the high power pulse behaves like a birefringent medium, producing a relative phase shift $\Delta\phi_b = \Delta\phi_T - \Delta\phi_L = (7\xi_T - 4\xi_L)Ik\tau$ between the transverse an parallel polarizations of the low power beam.

However, instead of reviewing the proposal of searching for the direct phase shift or birefringence of a pulse due to the crossing with the other, that was discussed in Refs. [51, 52], we will proceed to study the scenario of Ref. [50], which turns out to be more sensitive for the search of the vacuum polarization at future Petawatt of multi-Petawatt facilities.

9.6 Light by Light Diffraction in Vacuum: An Optimal Scenario

The possibility of using photon counting to search for vacuum polarization effects based on signatures of three-photon scattering was suggested in Refs. [6, 36, 44]. In Ref. [32], this idea was applied to a matter-less double slit configuration in which a laser pulse is diffracted by a pair of counter-propagating pulses. A simpler, more efficient and most probably optimal scenario was proposed in Ref. [50], involving only two counter-propagating laser pulses. Here, we will review in detail this configuration, following closely Ref. [50], and applying their results to several facilities that will be available in the near future.

In this scenario, illustrated in Fig. 9.3, a polarized pulse A of waist w_A crosses an almost counter-propagating polarized laser pulse B of waist $w_B \gg w_A$, that will be used as the probe. We assume that the uncertainty in frequency $\Delta\nu_{A,B} \simeq 1/\tau_{A,B}$ of each beam is much smaller than the mean frequency $\nu_{A,B} = c/\lambda_{A,B}$, so that the pulses can be considered as monochromatic with a good accuracy. In fact, this approximation will be fully justified in all the practical cases that we will consider below. The uncertainties in the transverse components of the wavevector, $\sim 1/w_{A,B}$, are supposed to be negligible with respect to $k_{A,B}$ as well.

Let $A_A = A_A(0)\exp(-r^2/w_A^2)$ and $A_B = A_B(0)\exp(-r^2/w_B^2)$ describe the dependences of the non-vanishing components of the two waves on the radial coordinate $r \equiv \sqrt{x^2+y^2}$, orthogonal to the propagation direction chosen in the z-axis. The intensity of the pulse A in the colliding region will then have the transverse distribution $I_A(r) = I_A(0)\exp(-2r^2/w_A^2)$. As a consequence, the space-dependent phase shift of the wave B just after the collision with the beam A is

$$\phi(r) = \phi(0)\exp\left(-\frac{2r^2}{w_A^2}\right), \tag{9.10}$$

where $\phi(0) = (a\xi)_{L,T} I_A k_B \tau_A$ and we understand one of the sub-indexes L or T in (9.10).

As a consequence, after the crossing the shape of the pulse B becomes $A_B = A_B(0)\exp[-(r^2/w_B^2) + i\phi(r)]$. Taking into account that ϕ is expected to be very small at all the facilities that will be available in the near future, we can make the approximation $\exp[i\phi(r)] \simeq 1 + i\phi(r)$ and obtain

$$A_B = A_B(0)\left[\exp\left(-\frac{r^2}{w_B^2}\right) + i\phi(0)\exp\left(-\frac{r^2}{w_0^2}\right)\right], \tag{9.11}$$

where we have defined $w_0 \equiv (2/w_A^2 + 1/w_B^2)^{-1/2}$.

Since the field A_B propagates linearly after the collision, we can sum the free evolution of each term in (9.11) that can be computed within the paraxial approximation $\omega = c\sqrt{k^2 + k_\perp^2} \simeq c(k + k_\perp^2/2k)$ for the angular frequency, where $\mathbf{k}_\perp = (k_x, k_y, 0)$, assuming that $\Delta k_{x,y} = 1/w \ll k$. To be conservative, we require that the number of non-diffracted photons on the ring detector of inner radius r_0 and outer radius R is 100 times smaller than the value of the diffracted photons. This requirement can then be used to compute a safe value for the inner radius [50]:

$$r_0 = w_D w_U \sqrt{\frac{\log\left(\frac{10 w_B}{\phi(0) w_0}\right)}{w_D^2 - w_U^2}}, \tag{9.12}$$

where $w_U \equiv w_B\sqrt{1 + (2d/k_B w_B^2)^2}$ and $w_D \equiv w_0\sqrt{1 + (2d/k_B w_0^2)^2}$ are the widths of the non-diffracted and diffracted patterns at the distance d from the collision point.

The result for the number of diffracted photons hitting the ring detector, as computed in Ref. [50], is then

$$N_D^{\mathcal{N}} = \frac{8f\mathcal{N}}{\pi\hbar c}\frac{E_A^2 E_B w_0^2}{\lambda_B w_A^4 w_B^2}\left(e^{-\frac{2r_0^2}{w_D^2}} - e^{-\frac{2R^2}{w_D^2}}\right)(a\xi)_{L,T}^2, \tag{9.13}$$

where f is the efficiency of the detector, and $E_A = P_A\tau_A$ and $E_B = P_B\tau_B$ are the total energies of the two pulses.

The number of scattered photons is then proportional to $E_A^2 E_B$. This requirement can be obtained economically by producing both beams simultaneously, e.g. by dividing a single pulse of energy $E = E_A + E_B$ before the last focalizations. The maximum value for N_D can then be achieved for $E_A = 2E/3$ and $E_B = E/3$. Of course, this choice is not necessary in the case of facilities such as VEGA [55], that will provide two different high power pulses simultaneously.

The other parameters that can be adjusted in order to maximize N_D are the widths w_A and w_B of the two colliding beams. Their choice is constrained by the following requirements:

1. w_B should be much larger than w_A;
2. the pulse A must not spread in a significant way during the crossing;
3. the center of pulse A has to remain close to the central part of beam B during the interaction (we will allow that it can deviate at most by a 10 %);
4. the scattering angle θ should be close to π, but at the same time it should be large enough that the trajectories of the two beams out of the collision point are separated by a distance sufficiently larger than their width. We assume that such an angular distance is 6 times the divergence of the beam A, which is $\sim \lambda/\pi w_A$.

As shown in Ref. [50], these requirements can be fulfilled by the safe and optimal choices

$$w_A = \sqrt{60c\tau_B\lambda/\pi}; \qquad \pi - \theta \simeq 6\lambda/\pi w_A. \tag{9.14}$$

On the other hand, the best choice for the value of $w_B > w_A$ will be computed numerically by maximizing N_D as given by (9.13), Finally, the outer radius R will be chosen slightly larger than $\sqrt{2}w_D \sim 2\lambda d/\pi w_A$, by requiring that only a few percent of the diffracted wave is lost.

N_D can then be used to determine the values of the parameters ξ_L and ξ_T. To evaluate the best possible sensitivity, we will suppose that the background noise can be kept below the signal level, which may not be a trivial requirement. In this case, the best sensitivity would correspond to the detection of 10 diffracted photons, so that the zero result could be excluded within three standard deviations. The minimum values of ξ_L and ξ_T that in principle could be measured would then be given by (9.13), taking $N_D^{\mathcal{N}} = 10$ and all the optimization choices reviewed above. (In the numerical computations that we will present in the next section, we also include a small correction $\sin^4(\theta/2)$ that appears in the expression of $\phi(0)$ as shown in Ref. [52].)

9.7 Sensitivity at Selected Ultraintense Laser Facilities

Let us now study the possibility of searching for light by light diffraction as described in the previous section at different ultraintense laser facilities that will be available in the next few years.

Table 9.1 Limiting values of the parameters ξ_L and ξ_T that can be measured at different facilities

Facility	P (PW)	τ (fs)	λ (nm)	$\xi_L^{\lim}/\xi$	$\xi_T^{\lim}/\xi$	$\xi_T^{\lim}/\xi^{\mathrm{PVLAS}}$
VEGA	$1+0.2$	30	800	4.0×10^2	2.3×10^2	1.0×10^{-1}
PETAL	7	500	1053	24	14	6.3×10^{-3}
ELI 10 PW	10	30	800	14	8.0	3.6×10^{-3}
100 PW	100	30	800	0.42	0.24	1.1×10^{-4}

One of the systems we proposed for our calculations is the VEGA laser at the Spanish Pulsed Laser Centre (CLPU, Centro de Láseres Pulsados) at Salamanca [55]. VEGA laser is a CPA system working at 30 femtoseconds after compression. It will have, by the beginning of 2014, a PW line, 30 J in 30 fs at one Hz, synchronized with a 200 TW line, 6 J in 30 fs. The VEGA system is based on standard CPA technology using a Ti:sapphire amplifier. The laser is going to be very relevant because it is going to be running at one Hz (one shot per second) and has the possibility to be upgraded to 5 Hz. VEGA laser will be quite unique in using as probe a 200 TW laser. Of course the conclusions for VEGA can be easily adapted to any other system at short pulse PW level.

The next candidate for the search of quantum vacuum features will be ELI (the Extreme Light Infrastructure). As indicated in the ELI whitebook [56], ELI will be the first infrastructure devoted to the fundamental study of laser-matter interaction in the ultra-relativistic regime ($I > 10^{24}$ W/cm^2). In its first stage, ELI plans to arrive to the 10 PW level and in a second stage expects to pass over the 100 PW barrier.

Such systems correspond to high field lasers, with pulse durations close to 30 fs, or less. Nevertheless, there are other systems with longer pulses, the high energy lasers. For comparison, we have selected the PETAL system as the most representative in this category [57].

By performing the optimized computation discussed in the previous section, we can compute the limiting value of the parameters ξ_L and ξ_T that can be measured within 3σ for a single shot experiment, depending on the parameters of the laser pulses (power P, duration τ and wavelength λ). In Table 9.1, we list few facilities that will be available in the near future, and compute the minimal value of the parameters $\xi_L^{\lim}$ and $\xi_T^{\lim}$ that can be measured for a single shot experiment, as compared either to the QED prediction ξ, or to the current PVLAS limit ξ^{PVLAS}. We see that all the facilities under consideration are potentially able either to detect signals of new physics, such as axion-like or mini-charged particles, or to significantly improve the PVLAS limits. A 100 PW laser such as that considered in the last line of the table would be able to measure the QED effect. These results are also shown in graphical form in Fig. 9.4 (that can be compared with Fig. 9.2), where we plot the regions in the ξ_L–ξ_T plane that will be testable in a single-shot experiment with either orthogonal or parallel polarization at the same VEGA, ELI 10, and 100 PW facilities that appear in Table 9.1.

Let us first discuss the results of the computations for VEGA that appear in Fig. 9.4 and in the first line of Table 9.1. As we have mentioned above, VEGA

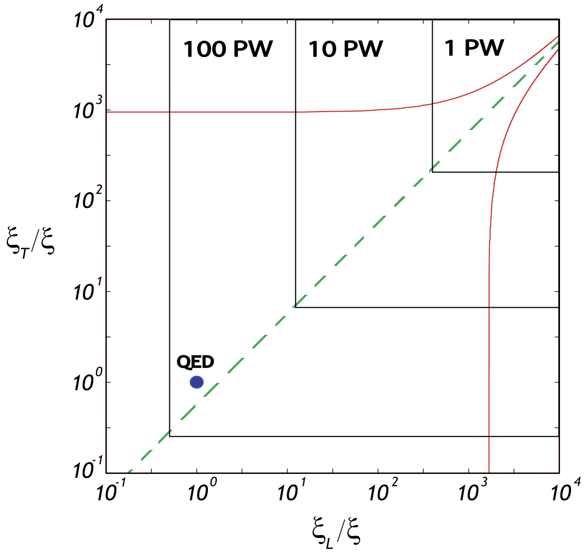

Fig. 9.4 Predicted sensitivity in the ξ_L–ξ_T parameter space (in logarithmic scale) for a single shot experiment searching for light by light diffraction at different (multi) PW laser facilities, corresponding to Table 9.1. The result labeled "1 PW" corresponds to VEGA. The outer region bounded by the *red solid lines* is excluded by the current PVLAS data. We also plot the prediction of the pure Born-Infeld theory (*green dashed line*). We see that the single shot experiment at a 100 PW facility will explore a region including the QED prediction, highlighted with the *blue point*. Observe that both scales have been normalized by the QED parameter ξ, so QED falls at the $(1, 1)$ point in the figure, only accessible with a 100 PW laser at single shot regime. Note that the sensitivity can be systematically improved by increasing the number of shots, as discussed in the text, so that in principle even VEGA could detect the QED effect, if the noise could be reduced below the signal level

will provide two synchronized laser pulses, one at 0.2 PW—which can be used as the probe pulse B—and the other at 1 PW, suitable for playing the role of pulse A. The limiting sensitivity for a single shot given in Table 9.1 and Fig. 9.4 is obtained with the following optimal choices for the experimental parameters:

1. the waist of the two pulses at the focus (coinciding with the crossing point) are $w_A = 12\ \mu\text{m}$ and $w_B = 59\ \mu\text{m}$, so that the focused intensities of the two pulses are $I_A = 4.6 \times 10^{20}\ \text{W/cm}^2$ and $I_B = 3.7 \times 10^{18}\ \text{W/cm}^2$;
2. the angle between the two beam directions is $\pi - \theta = 7.4°$;
3. the inner and outer radius of the detector are $r_0 = 0.23$ cm, $R = 0.52$ cm (for $d = 10$ cm);
4. the divergence of the diffracted wave that hits the detector is approximately 7 times larger than the divergence of the non-diffracted wave;
5. the efficiency of the detector is chosen to be 0.5, which is a realistic value in the near IR with present technology.

The choice of the parameters for ELI 10 and the possible 100 PW laser considered in Table 9.1 and in Fig. 9.2) is quite similar [58]. On the other hand, in the case of PETAL the optimization requires much larger focused waists, namely $w_A = 48$ µm and $w_B = 0.14$ mm, that may be a technological challenge.

Apart from VEGA, all the other facilities belong to the upcoming multi-PW lasers generation. There are two main reasons for choosing VEGA, among the several PW lasers available worldwide. The first is the fact that it automatically provides two pulses, which is of course an advantage for our experiment. The second reason is its high repetition rate, that is planed to be 1 Hz, and possibly even 5 Hz, as we have mentioned above. From (9.13), we see that the expected number of events is proportional to the number of repetitions $\mathscr{N}$, so that the limiting sensitivity $\xi_{L,T}^{\lim} \propto \mathscr{N}^{-1/2}$ improves as $\mathscr{N}^{-1/2}$ with respect to the single-shot values given in Table 9.1. In particular, after $\mathscr{N} \simeq 5.2 \times 10^4$ shots (less than one day run) VEGA will reach a sensitivity at the QED level for the measurement of ξ_T, since in this case $\xi_T^{\lim} = \xi$. The number of shots needed to measure also ξ_L at the QED level would be $\mathscr{N} \simeq 1.6 \times 10^5$. Of course, the measurement would only be reliable if the noise level, including all possible sources of background, can be kept below the level of the signal, which may not be a trivial requirement. A preliminary analysis of the possible sources of background indicates that VEGA may only reach sensitivity at the QED level if it operates in such an extreme vacuum that may be a challenge for the present technology. For more reasonable values of the pressure of the tube, it will be eventually able to find signals of new physics, or to improve the current limits of ξ_L and ξ_T from PVLAS by several orders of magnitude. On the other hand, the upcoming generation of the 10 PW facilities listed in Table 9.1 will most probably be able to detect the QED effect. A 100 PW facility would be able to detect the QED effect even in a single shot experiment.

As a result, this kind of experiment might provide the first signature of quantum vacuum polarization in the near future. It should be noted that the four-wave mixing configuration discussed in Ref. [36] has also been argued to be potentially sensitive to the QED effect (under extreme vacuum requirements) using PW lasers such as Astra Gemini. In such a proposal, three ultra-intense laser pulses are focused close to the diffraction limit and forced to collide at the same space-time point, possibly producing a signal of ultraviolet photons. However, the production and alignment of three ultra-concentrated and ultra-short laser pulses represent a greater technological challenge, as compared to our minimal scenario based on the crossing of only two pulses. Moreover, in the proposal discussed in Ref. [36] two of the incoming pulses are chosen to double the frequency of the laser source, which is not a trivial requirement from a technical point of view. In any case, even though our proposal is simpler and probably easier to perform, we think that both experiments deserve to be carried out since they can provide two independent tests of the quantum vacuum.

9.8 Conclusions

Ultra-intense laser pulses constitute a unique system in which an enormous amount of photons are packed in the same quantum state in the same microscopic volume. This allows for the possibility of studying the coherent interaction of light with light in vacuum due to the interchange of virtual particles, which is a prediction of the quantum theory. This kind of effects strongly depend on the particle content of the theory, so that any experiment searching for them can also be used to search for new physics, such as axion-like or mini-charged particles, that have been introduced to solve theoretical problems but are still wanted for observation. The first possible signal that may be detectable of such an interaction is the polarization of the quantum vacuum by the laser pulses itself. As we have seen, in principle this effect can be measurable even at the rate predicted by Quantum Electrodynamics (QED) with only the known particle content at a high repetition rate PW laser such as VEGA. We have described an experiment searching for light by light diffraction in vacuum in which two almost counter-propagating pulses cross each other. The optimal choice for the focused intensity of the most concentrated of the two pulses has been argued to be ‘just’ $5 \times 10^{20}\ \mathrm{W/cm^2}$, a value which is several orders of magnitude lower than the intensities at which another important basic process may become observable, the production of real electron-positron pairs from the vacuum. The study of the background noise, which is in progress, seems to indicate that in practice we will have to wait for the next generation of 10 PW laser for the process of light by light diffraction in vacuum to be observable at the QED rate. In any case, VEGA will already be able either to demonstrate the quantum vacuum polarization due to new physics, or to improve the current limits on photon-photon scattering in vacuum at optical wavelengths by several orders of magnitude. We believe that these results provide strong support to the use of ultra-intense lasers in fundamental research.

Acknowledgements We acknowledge support from Spanish Ministerio de Economía y Competitividad (through the projects Consolider Program SAUUL CSD2007-00013, FCCI: ACI-PROMOCIONA ACI2009-1008, and FIS2009-09522), and from the Spanish Junta de Castilla y Leon (project CLP421A12-1).

References

1. S.L. Adler, Ann. Phys. **67**, 599 (1971)
2. M. Ahlers, H. Gies, J. Jaeckel, A. Ringwald, Phys. Rev. D **75**, 035011 (2007)
3. E.B. Aleksandrov, A.A. Anselm, A.N. Moskalev, Zh. Eksp. Teor. Fiz. **89**, 1181 (1985)
4. P. Arias, J. Gamboa, H. Falomir, F. Méndez, Mod. Phys. Lett. A **24**, 1289 (2009)
5. A.R. Bell, J.G. Kirk, Phys. Rev. Lett. **101**, 200403 (2008)
6. D. Bernard et al., Eur. Phys. J. D **10**, 141 (2000)
7. M. Born, Proc. R. Soc. Lond. **143**, 410 (1934)
8. M. Born, L. Infeld, Proc. R. Soc. Lond. **144**, 425 (1934)
9. M. Bregant, et al., PVLAS collaboration, Phys. Rev. D **78**, 032006 (2008)
10. J.W. Brockway, E.D. Carlson, G.C. Raffelt, Phys. Lett. B **383**, 439 (1996)
11. G. Brodin, M. Marklund, L. Stenflo, Phys. Rev. Lett. **87**, 171801 (2001)

12. C. Bula et al., Phys. Rev. Lett. **76**, 3116 (1996)
13. D.L. Burke et al., Phys. Rev. Lett. **79**, 1626 (1997)
14. V. Costantini, B. De Tollis, G. Pistoni, Nuovo Cimento **2A**, 733 (1971)
15. S. Davidson, B. Campbell, D. Bailey, Phys. Rev. D **43**, 2314 (1991)
16. S. Davidson, S. Hannestad, G. Raffelt, J. High Energy Phys. **05**, 003 (2005)
17. V.I. Denisov, I.V. Krivchenkov, N.V. Kravtsov, Phys. Rev. D **69**, 066008 (2004)
18. Y.J. Ding, A.E. Kaplan, Int. J. Nonlinear Opt. Phys. **1**, 51 (1992)
19. A. Di Piazza, K.Z. Hatsagortsyan, C.H. Keitel, Phys. Rev. Lett. **97**, 083603 (2006)
20. B. Dobrich, H. Gies, J. High Energy Phys. **10**, 022 (2010)
21. M.I. Dobroliubov, A.Y. Ignatiev, Phys. Rev. Lett. **65**, 679 (1990)
22. N.V. Elkina et al., Phys. Rev. Spec. Top., Accel. Beams **14**, 054401 (2011)
23. A.M. Fedotov, N.B. Narozhny, G. Mourou, G. Korn, Phys. Rev. Lett. **105**, 080402 (2010)
24. A. Ferrando, H. Michinel, M. Seco, D. Tommasini, Phys. Rev. Lett. **99**, 150404 (2007)
25. H. Gies, J. Jaeckel, A. Ringwald, Phys. Rev. Lett. **97**, 140402 (2006)
26. E. Golowich, R.W. Robinett, Phys. Rev. D **35**, 391 (1987)
27. J.A. Grifols, E. Masso, R. Toldra, Phys. Rev. Lett. **77**, 2372 (1996)
28. T. Heinzl, B. Liesfeld, K.U. Amthor, H. Schwoerer, R. Sauerbrey, A. Wipf, Opt. Commun. **267**, 318 (2006)
29. W. Heisenberg, H. Euler, Z. Physik **98**, 714 (1936)
30. B. Holdom, Phys. Lett. B **166**, 196 (1986)
31. B. Holdom, Phys. Lett. B **178**, 65 (1986)
32. B. King, A. Di Piazza, C.H. Keitel, Nat. Photonics **4**, 92 (2010)
33. J.J. Klein, B.P. Nigam, Phys. Rev. B **135**, 1279 (1964)
34. I. Kuznetsova, J. Rafelski, Phys. Rev. D **85**, 085014 (2012)
35. S.A. Lee, W.M. Fairbank Jr., Measuring the birefringence of the QED vacuum, in *Laser Physics at the Limits*, ed. by H. Figger, D. Meschede, C. Zimmermann (Springer, Berlin, 2002), p. 189
36. E. Lundstrom, G. Brodin, J. Lundin, M. Marklund, R. Bingham, J. Collier, J.T. Mendonça, P. Norreys, Phys. Rev. Lett. **96**, 083602 (2006)
37. M. Marklund, Nat. Photonics **4**, 72 (2010)
38. M. Marklund, P.K. Shukla, Rev. Mod. Phys. **78**, 591 (2006)
39. E. Masso, Nucl. Phys. Proc. Suppl. **114**, 67 (2003)
40. E. Masso, R. Toldra, Phys. Rev. D **52**, 1755 (1995)
41. E. Masso, R. Toldra, Phys. Rev. D **55**, 7967 (1997)
42. J. McKenna, P.M. Platzman, Phys. Rev. **129**, 2354 (1963)
43. A.I. Milstein, M. Schumacher, Phys. Rep. **243**, 183 (1994)
44. F. Moulin, D. Bernard, Opt. Commun. **164**, 137 (1999)
45. G.A. Mourou, T. Tajima, S.V. Bulanov, Rev. Mod. Phys. **78**, 309 (2006)
46. E.N. Nerush, I.Yu. Kostyukov, A.M. Fedotov, N.B. Narozhny, N.V. Elkina, H. Ruhl, Phys. Rev. Lett. **106**, 035001 (2011)
47. E.N. Nerush, V.F. Bashmakov, I.Yu. Kostyukov, Phys. Plasmas **18**, 083107 (2011)
48. R.D. Peccei, H.R. Quinn, Phys. Rev. Lett. **38**, 1440 (1977)
49. J. Schwinger, Phys. Rev. **128**, 2425 (1962)
50. D. Tommasini, H. Michinel, Phys. Rev. A **82**, 011803(R) (2010)
51. D. Tommasini, A. Ferrando, H. Michinel, M. Seco, Phys. Rev. A **77**, 042101 (2008)
52. D. Tommasini, A. Ferrando, H. Michinel, M. Seco, J. High Energy Phys. **11**, 043 (2009)
53. V. Yanovsky, V. Chvykov, G. Kalinchenko, P. Rousseau, T. Planchon, T. Matsuoka, A. Maksimchuk, J. Nees, G. Cheriaux, G. Mourou, K. Krushelnick, Opt. Express **16**, 2109 (2008)
54. G. Zavattini et al., PVLAS collaboration, arXiv:1201.2309v1 (2012)
55. http://www.clpu.es/en/infrastructures/main-beam-line/phase-3.html
56. G.A. Mourou, G. Korn, W. Sandner, J.L. Collier (eds.), *ELI-Extreme Light Infrastructure, Science and Technology with Ultra-Intense Lasers Whitebook* (CNRS, Paris, 2011)
57. http://petal.aquitaine.fr/
58. http://www.extreme-light-infraestructure.eu

Index

K. Yamanouchi et al. (eds.), *Progress in Ultrafast Intense Laser Science X*,
Springer Series in Chemical Physics 106, DOI 10.1007/978-3-319-00521-8,